The Dissertation Committee for Nathan Joseph Bechle Certifies that this is the approved version of the following dissertation:

Evolution of Localization in NiTi Shape Memory Alloys and its Effect on Structures

Committee:

Stelios Kyriakides, Supervisor

Chad M. Landis

Kenneth M. Liechti

Krishnaswamy Ravi-Chandar

Desiderio Kovar

Evolution of Localization in NiTi Shape Memory Alloys and its Effect on Structures

by

Nathan Joseph Bechle; B.S.; M.S.

Dissertation

Presented to the Faculty of the Graduate School of

The University of Texas at Austin

in Partial Fulfillment

of the Requirements

for the Degree of

Doctor of Philosophy

The University of Texas at Austin

May 2016

Dedication

To my O-boys

Acknowledgements

I wish to express sincere gratitude to my advisor, Professor Stelios Kyriakides, for his devotion to my research. I have never met a person who takes more pride in their profession and this is clearly born out in the quality of his work. There is no doubt in my mind that I would not be the researcher I am today without his guidance and tutelage.

The work reported was conducted with the financial support of the National Science Foundation under grant no. CMMI-12000465. I would also like to acknowledge support from The University of Texas at Austin through a Thrust 2000-William H. Cunningham Endowed Graduate Fellowship in Engineering from the Cockrell School of Engineering courtesy of Mr. W.A. "Tex" Moncrief, Jr.

I wish to express my appreciation to all members of my Ph.D. committee as well as the remaining faculty of the Department of Aerospace Engineering and Engineering Mechanics. The departmental support staff made life much easier along the way, particularly Joe Pokluda, Scott Messec, Pablo Cortez, Ricardo Palacios, Travis Crooks, Lydia Tostado, Steve Sanders, and many more I am forgetting.

I would also like to thank my fellow graduate students and research colleagues for helping to keep me afloat all these years. Whether it was research discussions, heated mechanics arguments, or an in-depth baseball conversation, these guys were always there to keep me grounded and motivated. In order of appearance: Dr. Nikolaos Bouklas, Dr. Lin Yuan, Mathieu Leduc, Dr. Wen-Yea Jang, Dr. Liang-Hai Lee, Dr. Julian Hallai, Dr. Stavros Gaitanaros, Dr. Nicolas Tardif, Scott Haltom, Zach Wilson, John Mersch, Dongjie Jiang, and Martin Scales. Would not have been the same without you, fellas.

I would like to thank Dr. John Hermanson (sorry about the formal Dr. title), the person who introduced to me to scientific research as an undergrad and kept fueling that fire. He taught me how to approach scientific problems and showed me the creativity, ingenuity, and hard work it takes to solve them. He also invited me to play Ultimate.

Last, I would like to extend a special thank you to my family. The love and support from Ma and Pops have made me who I am. Matty, you are a little brother by name only. I look up to you and emulate my life after your philosophies more than you know. Domi, thank you for your support through this process. Oscar and Oliver, you continue to help define me as a person and find new ways every day to make me a proud father. I hope someday you boys can read this so you can figure out what Daddy was doing all those evenings and Saturdays.

Evolution of Localization in NiTi Shape Memory Alloys and its Effect on Structures

Nathan Joseph Bechle, Ph.D.

The University of Texas at Austin, 2016

Supervisor: Stelios Kyriakides

Nearly equiatomic NiTi can be strained in tension to several percent and fully recover upon unloading (pseudoelastic behavior). This property is derived from solid-state transformations between the austenitic (A) and martensitic (M) phases, which can be induced by either changes in temperature or stress. It is well established that stress-induced phase transformation can lead to localized deformation associated with the nucleation and propagation of the M-phase during loading and the A-phase during unloading. This partially unstable material behavior strongly influences the stability of NiTi structures. A requirement for the analysis and design of such structures is constitutive models that capture the material instability. Most efforts on modeling SMA behavior to date are based on uniaxial experiments. In an effort to expand knowledge to the multiaxial setting, results from a series of experiments on pseudoelastic NiTi tubes loaded under combined axial load and internal pressure are presented. Specimens were loaded under radial stress paths in the axial-hoop stress space using stereo digital image correlation for full-field monitoring of the evolution of transformation-induced deformation. Results spanning axial-to-hoop stress ratios from -1.0 to uniaxial tension revealed that, but for a narrow region near equibiaxial tension, transformation leads to localized helical deformation bands with helix angles that depend on the stress ratio. In

the process, the stresses remain nearly constant until transformation is completed. In the vicinity of equibiaxial tension, the material exhibits hardening and homogeneous deformation. Loci of the transformation stresses, while exhibiting minor anisotropy, traced an elongated trajectory in the axial-hoop stress space not captured by a von Mises representation. By contrast, the transformation strains exhibit significant anisotropy between axial and hoop dominant stress paths. Moreover, strains around the equibiaxial stress state, where material hardening and homogeneous deformation was observed, are significantly smaller than in the rest of the stress space. The strain anisotropy has a corresponding reflection on the energy dissipated during transformation with axial dominant stress paths dissipating significantly more energy than hoop dominant ones, with less dissipation observed in the neighborhood of equibiaxial stress.

Table of Contents

Chapter 1: INTRODUCTION

1.1 NiTi BACKGROUND AND MICROSTRUCTURE

Shape memory alloys (SMAs) exhibit two unique behaviors that make them an exciting class of engineering materials. *Pseudoelasticity* (also known as *superelasticity*) is the ability of a material to be strained well beyond the "proportional limit", yet fully recover upon the removal of stress. The so-called *shape memory effect* is when a material is seemingly permanently strained, but returns to the initial configuration when the temperature is increased above a transition level. The most common SMA that exhibits both of the aforementioned behaviors is nearly equiatomic NiTi (also known as nitinol). In NiTi, the responses are attributed to diffusionless solid state phase transformations between austenite (A), martensite (M), and R-phase (R) crystallographic structures.

The M phase is a B19' monoclinic structure that is thermodynamically stable at low temperatures and high stresses. The A phase is a B2 cubic structure which is stable at high temperatures and low stresses. The R phase is a rhombohedral distortion of the B2 cubic structure, and an intermediate martensitic phase with little effect on the mechanical response of NiTi. The high symmetry B2 to low symmetry B19', or A to M, transformation leads to 12 distinct lattice correspondence variants (LCVs) for the M orientation and can be induced with either changes in stress or temperature.

Figure 1.1 shows the temperature induced transformation absent of stress achieved through differential scanning calorimetry (DSC) for one of the tube stocks used in this investigation together with the corresponding lattice orientations. Tracing along the upper curve, the material begins in the M phase (stable at low temperatures) and transitions into the A phase as the temperature increases. The positive spike corresponds to the endothermic nature of the M→A transformation. Beyond a transition temperature,

the material stabilizes into the A phase. The boundaries of this power peak are idealized by construction tangent lines, and denoted as A_s and A_f for the austenitic start and finish temperatures, respectively. For this material, A_s = -9.6 °C and A_f = 12.1 °C. The bottom curve traces the reverse order when the material is cooled from the A phase with NiTi commonly transitioning to the R phase before eventually becoming fully martensitic below M_f. The power valleys are a result of the exothermic nature of the A→M transformation.

Consider the pseudoelastic experimental response of a NiTi tube subjected to uniaxial tension under isothermal conditions at a temperature above A_f shown in Fig. 1.2. Loading from ⓪ induces homogeneous elastic deformation of the parent A phase until ① at which point A becomes unstable and transformation to detwinned−M occurs. Under isothermal conditions, the transformation from A→M occurs at a constant stress traversing a stress plateau from ① to ② during which there is a coexistence of two deformation regimes. The transformed M regions are at a relatively constant strain value corresponding to the termination of the upper plateau at ② while the untransformed A regions remain at the strain level at the onset of transformation at ①. Upon termination of the upper stress plateau, saturation to the M phase has occurred, and further displacement leads to homogeneous deformation of the detwinned−M microstructure. There are small pockets of remaining A that transform at higher stress levels due to neighboring constraints. Significant stressing will lead to slipping of the detwinned−M and results in plastic deformation. Upon unloading, the M phase unloads elastically until a stress at which M is no longer stable ③ and transformation back to the A phase occurs. The reverse transformation occurs at a relatively constant stress level with the coexistence of two deformation regimes. At ④ the material has returned to the parent A phase and the

remaining deformation history is homogeneous with the specimen returning to the undeformed configuration at zero stress ⑤.

1.2 APPLICATIONS

Over the years the special properties of NiTi have been exploited in a variety of novel applications with some examples shown in Fig. 1.3. The shape memory effect is primarily used as an actuation mechanism. The first large scale application of NiTi was a constrained recovery Raychem Corporation Cryofit hydraulic tube coupling on the Grumman F-14 aircraft in 1969 (Kauffman and Mayo [1997], Van Humbeeck [1999], similar modern design in Fig. 1.3a [http://www.aerofit.com/sma_Couplings.html]). Other examples of shape memory actuation include space deployment devices such as the Frangibolt, helicopter blade tab control, heat-release safety valves (Wu and Schetky [2000], Fig. 1.3b [https://assuredautomation.com/]), adaptive variable-geometry chevron nozzles (Chau et al. [2006], Hartl et al. [2010]), automotive hatch vent release, and aircraft wing morphing (Mohd Jani et al. [2014]).

Applications that employ the pseudoelastic effect take advantage of large, recoverable deformations and energy dissipation. Commercial applications include recoverable eyeglass frames (Fig. 1.3e [http://www.samaterials.com/]), clothing accessories such as the underwire for brassieres and dresses, recoverable limbs on action figures, headphone bands, and cell phone antennas (Poncet [1994], Wu and Schetky [2000]). In civil engineering, NiTi is used for isolation/damping devices for buildings and bridges in regions affected by seismic activity (Van Humbeeck [1999], Fig. 1.3c Sharabash and Andrawes [2009], Asgarian and Moradi [2011], Ozbulut et al. [2011]). Biocompatibility and pseudoelasticity at body temperatures make NiTi an ideal material for biomedical applications which is currently the largest market for NiTi. Surgical

applications include self-expanding intraluminal stents (Fig. 1.3d [http://www.gi-supply.com/]) and replacement heart valves (Fig. 1.3e [http://www.corevalve.com/]), tissue ablation devices, guidewires for device deployment, tissue retrieval baskets, vena cava filters, bone anchor systems, and catheters (Poncet [1994], Duerig et al. [1999]). In the dental industry NiTi applications include pre-tensioned arch wires for braces and root canal drills and files (Duerig et al. [1999], Yoneyama and Miyazaki [2008], Mohd Jani et al. [2014]). More recent biomedical applications include orthopedic implants, artificial muscles, and prosthetic limbs (Mohd Jani et al. [2014]).

Although pseudoelasticity and the shape memory effect have been exploited in many practical applications, it is fair to say that at the present the use of NiTi as a structural component remains limited. One factor preventing the efficient engineering of NiTi is the lack of a robust constitutive model capable of representing the complex material behavior of NiTi.

1.3 MOTIVATION

NiTi was discovered at the Naval Ordnance Laboratory (NOL, hence the name nitinol) in 1959 by William J. Buehler while developing materials with high impact resistance and ductility for the nose cone of a reentry vehicle (Kauffman and Mayo [1997]). Buehler suspected that the material had a significant atomic structural change with minor temperature variations by noting changes in the acoustic damping of NiTi rods when dropping them on concrete flooring. The shape memory effect was discovered during a NOL management meeting in 1961 when a deformed rod was subjected to a flame from a lighter and immediately straightened out. The atomic changes were confirmed at NOL by Frederick E. Wang to be the result of a “shearing” between austenitic and martensitic orientations through the rearrangement of atoms. Early external

research efforts primarily focused on the temperature dependence of the metallurgical and material properties (Wasilewski [1971], Jackson et al. [1974]) and the crystallography of the martensitic transformation (Tas et al. [1972], Miyazaki et al. [1984], Matsumoto et al. [1987]).

Mechanics research has historically lagged behind the materials science of NiTi, with pioneering experimental work conducted by Miyazaki et al. [1981a] investigating the pseudoelastic tensile response of NiTi at various temperatures. Miyazaki [1981b] observed Lüders-like localized deformation in NiTi wires subjected to tension at room temperature. The fundamental research on the thermomechanical interactions of deformation and phase transformations came from Shaw and Kyriakides [1995]. An extensive experimental investigation into the tensile response of NiTi wire at a variety of temperatures, strain rates, and environmental conditions revealed the sensitive thermomechanical behavior. It was shown that in order to mitigate effects due to the latent heat of transformation, experiments to extract material parameters are best conducted under isothermal conditions. To ensure isothermal conditions, experiments are performed at a sufficiently slow strain rate which is highly dependent on the ambient medium. For a large temperature range in the pseudoelastic regime, NiTi exhibits localization where the A↔M transformation leads to inhomogenous deformation. During this stage the engineering stress traverses a flat stress plateau with the coexistence of multiple deformation regimes corresponding to the onset and termination of the transformation plateau. The deformation regimes are separated by a transition front with significant strain gradients and traverse the specimen at a constant velocity along the length dependent on the number of fronts, applied displacement rate, and the extent of transformation strain (also observed in NiTi thin strips in Shaw and Kyriakides [1997]).

Further mechanics-based research revealed the nature of the localized deformation and patterns on NiTi thin strips (Shaw and Kyriakides [1998], Liu et al. [1998], Daly et al. [2007], Hallai and Kyriakides [2013]), and more recently the helical deformation patterns observed with inhomogeneous deformation associated with transformation in tubular specimens (Li and Sun [2002], Feng and Sun [2006], Favier et al. [2007], Reedlunn et al. [2014], Bechle and Kyriakides [2014]). A further complication to the mechanical behavior was the tension-compression asymmetry observed initially in the shape memory regime on NiTi rods by Wasilewski [1971]. Experiments on NiTi in the pseudoelastic regime confirmed the asymmetry between tension and compression (Patoor et al. [1995], Jacobus et al. [1996], Orgéas and Favier [1998], Gall et al. [1999]). The origin of the stress and strain asymmetry is generally attributed to crystallographic texture (Patoor et al. [1995], Gall et al. [1999], Gall and Sehitoglu [1999], and Sehitoglu et al. [2000]). A significant difference in the tangent modulus during transformation between tension and compression was observed by Gall and Sehitoglu [1999] and Sehitoglu et al. [2000], and later Mao et al. [2010], Reedlunn et al. [2014], and Bechle and Kyriakides [2014]. For more detail on this asymmetry, see Chapter 2.

Driven by the needs of the aforementioned applications, significant efforts to develop constitutive models that capture the basic behavior have been undertaken. Most phenomenological NiTi constitutive models use the martensitic volume fraction as the internal variable within a thermodynamic framework with varying hardening rules to account for the phase transformation. Early efforts captured the recoverable transformation strain, but neglected the material instability and asymmetry (one dimensional: Liang and Rogers [1990], Brinson [1993]; three-dimensional: Liang and Rogers [1992], Boyd and Lagoudas [1996], Leclercq and Lexcellent [1996]). In 1D,

Govindjee and Kasper [1999] included the asymmetry by having separate tensile and compressive volume fractions. In 3D, Raniecki and Lexcellent [1998] and Qidwai and Lagoudas [2000] introduced transformation surfaces with J_3–type invariants to represent the tension/compression asymmetry. To account for the material instability, Abeyaratne, and Knowles [1993, 2006] introduced a double-well potential and Shaw [2002] used a strain gradient approach, but neither model included asymmetry. The current state of the art in NiTi constitutive models (for example Auricchio and Petrini [2004], Bouvet et al. [2004b], Popov and Lagoudas [2007], Arghavani et al. [2010], Lagoudas et al. [2012], Auricchio et al. [2014]) does not account for asymmetry in tension/compression together with stress-state dependent material instability. In order for a constitutive model to be applied to the variety of loadings, deformations, and stress states that will be required for current and future applications of NiTi, a constitutive model must be capable of capturing localization, tension/compression asymmetry, and the psuedoelasticy/shape memory effect. To aid in the development and calibration of such 3D constitutive models, more detailed experimental data is required.

1.4 OUTLINE

This dissertation presents the results of an extensive experimental study on the material behavior of NiTi. Emphasis is given to the material instabilities, evolution of deformation due to phase transformations, and the evolution of the phase transformation deformation in multiaxial stress states. The effect of the complex material response on structures is also demonstrated. Chapter 2 presents the underlying uniaxial material response with tension and compression experiments on tubes at various temperatures. Chapter 3 focuses on the effect of phase transformation to the response of two simple structures, a tube subjected to pure bending and the axial compression of a shell. Chapter

4 presents a more expansive record of the material behavior with tubes subjected to multiaxial stress states through combined axial tension and internal pressurization with a more thorough analysis of the multiaxial experimental results in Chapter 5. The main conclusions of the study are presented in Chapter 6 together with a summary of the results and remarks for future work.

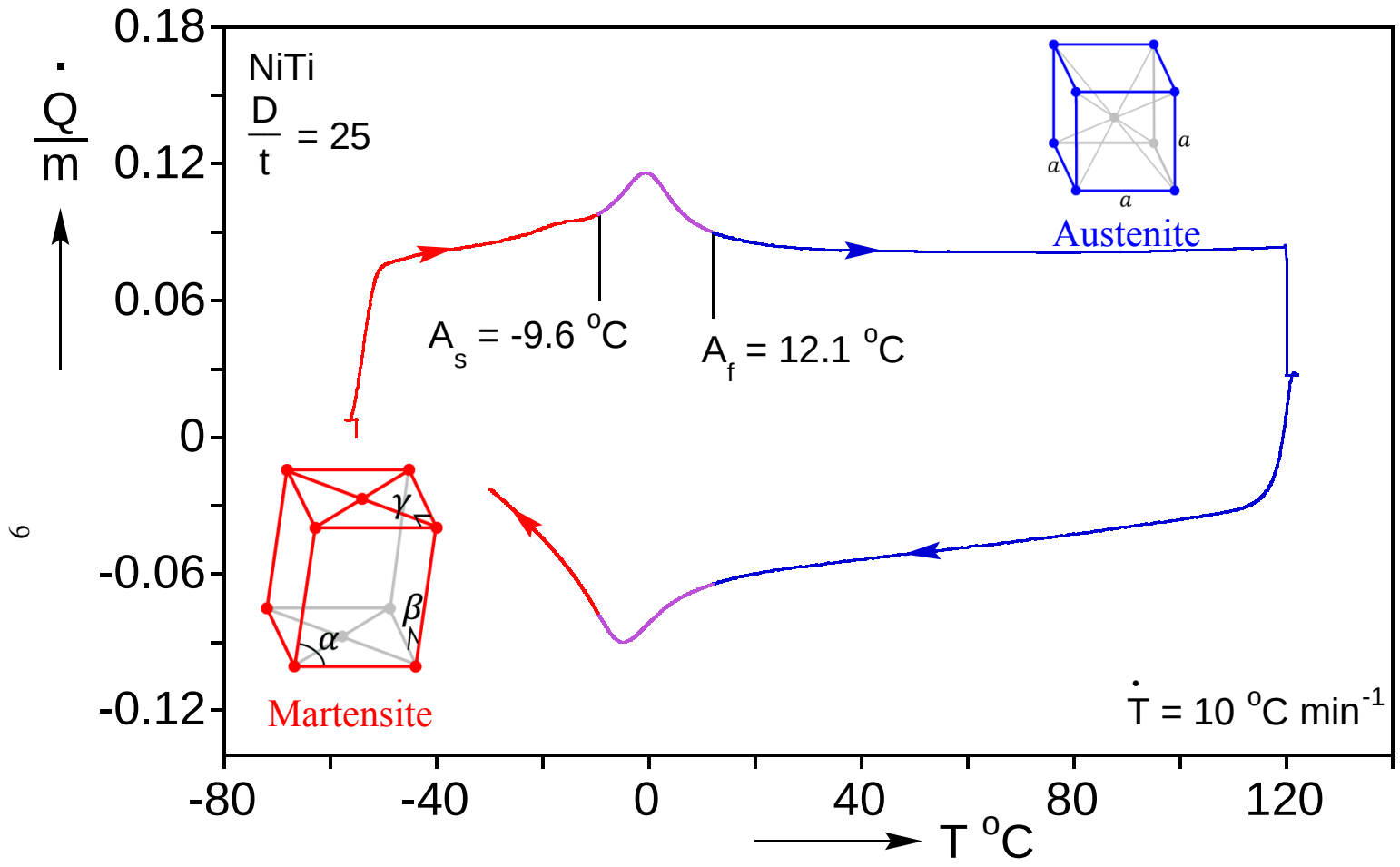

Fig. 1.1 Digital scanning calorimetry (DSC) thermogram of NiTi tube stock with corresponding crystallographic orientations.

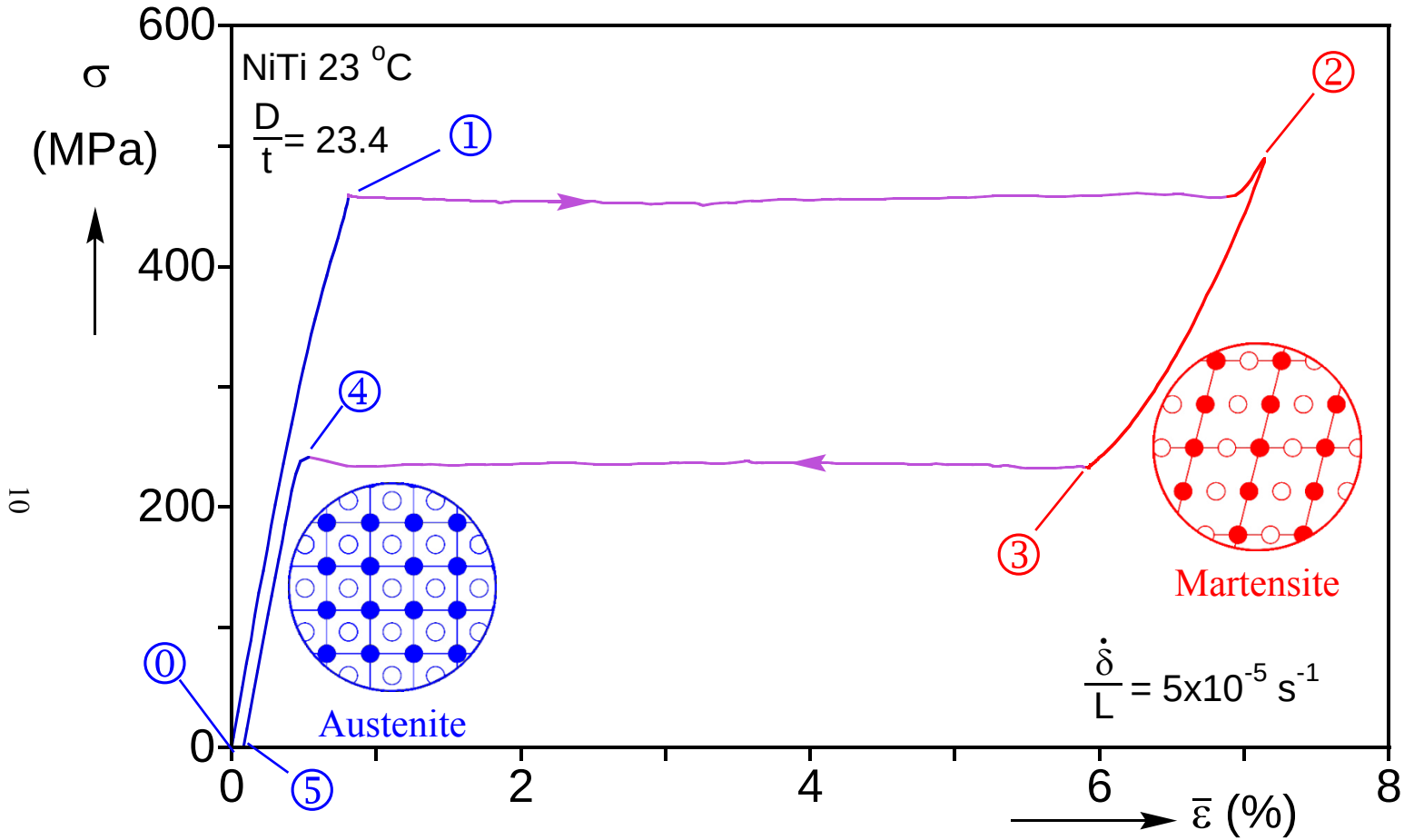

Fig. 1.2 Axial stress-average strain response for one of the NiTi tube stocks used in this investigation subjected to uniaxial tension in the pseudoelastic temperature regime with corresponding crystal lattice microstructures.

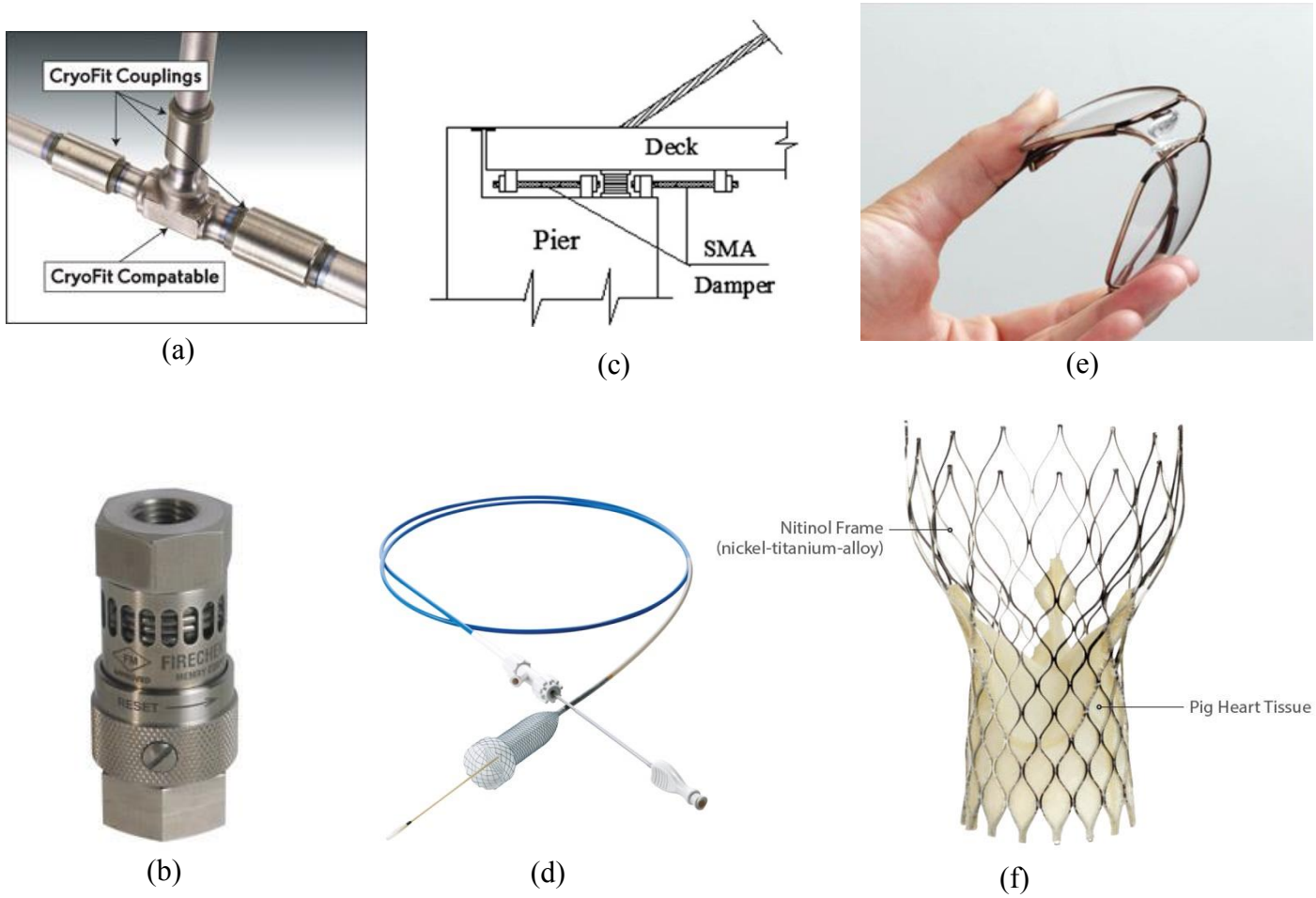

Fig. 1.3 Examples of NiTi applications using the shape memory effect: (a) CryoFit couplings, (b) heat activated pneumatic shutoff valve; and pseudoelasticity: (c) seismic damper, (d) stent, (e) eyeglasses, (f) replacement heart valve. (Citations in the text)

Chapter 2: UNIAXIAL MATERIAL BEHAVIOR[1]

Phase transformations are induced by either changes in stress or temperature. Furthermore, latent heats associated with the transformations tend to complicate the material response due to thermomechanical interactions. It is well known that the transformation stresses are strongly dependent on temperature which must be established for any SMA (Wasilewski [1971], Jackson et al. [1974], Miyazaki et al. [1981a, 1981b], Shaw and Kyriakides [1995]). In addition, in some temperature regimes, stress induced transformation leads to inhomogeneous deformations (Shaw and Kyriakides [1995, 1997, 1998], Liu et al. [1998], Li and Sun [2002], Feng and Sun [2006], Daly et al. [2007]). Another complication is a strong tension/compression asymmetry which is generally attributed to crystallographic texture (Patoor et al. [1995], Jacobus et al. [1996], Orgéas and Favier [1998], Gall et al. [1999], Gall and Sehitoglu [1999], Sehitoglu et al. [2000]).

This chapter presents the fundamental uniaxial response of NiTi in the temperature regimes of interest. Since one of the objectives of this study is to investigate the effect of the complex material behavior on the response of structures, the uniaxial experiments are conducted on the same tube stock as that which will be used for the structural experiments to be presented in Chapter 3.

2.1 EXPERIMENTAL SETUP

The tube stock used has a nominal diameter of 5.13 mm (0.202 in) and a wall thickness 0.635 mm (0.025 in). Tubes were used in the as-received condition supplied by

[1] Bechle, N.J., Kyriakides, S. (2014). Localization in NiTi tubes under bending. *Int'l J. Solids Struct*. **51**, 967-980. (Designed and performed experiments, analyzed data, and wrote the paper)

Memry Corp specified with the BB alloy (PN: 10579, LN: DM-8215, IN: C7-8775). The tube material is nearly equiatomic (50.82 at % Ni).

2.1.1 Material Calorimetry

The transformation temperatures of this material were determined through digital scanning calorimetry (DSC). DSC was performed using a Perkin Elmer DSC 6000 together with the Perkin Elmer Intracooler SP cooling accessory. Perkin Elmer Pyris software was used for machine control and data acquisition. Two samples were cut from the tube stock using a diamond saw blade. Each sample was cooled to -60 °C, held for 30 minutes, and then subjected to a temperature scan rate of 10 °C/min. Figure 2.1 shows the heat release rate of the sample compared to a reference material. The area under the peak represents the latent heat of the M to A transformation. Austenitic start and finish temperatures were determined using tangent construction lines to be A_s = -15.8 °C and A_f = 20.9 °C.

2.1.1 Tension Experimental Setup

The isothermal tensile and compressive responses of the tube stock in the range of temperatures of interest were measured in a screw-type testing machine. The custom experimental setups used to perform the tests are shown schematically in Figs. 2.2a for tension and 2.2b for compression.

In tension, a 114 mm (4.50 in) tube section is gripped between plate clamps with linear v-notches exposing a 40.6 mm (1.60 in) test section. To prevent crushing of the tube, snug-fit steel rods are inserted inside the gripped sections. The specimen is clamped by uniformly tightening four bolts integral to each grip using the same torque levels to

ensure uniform clamping. The torque level was determined empirically such that the required tension force can be achieved without slipping.

The specimen and grips setup is surrounded by a water bath with a transparent side for visualization as shown in Fig. 2.2a. The water temperature is maintained at the chosen level by connecting the bath to a temperature controlled circulating system. The temperature of the specimen is monitored with a thermocouple to ensure its isothermal condition. The overall elongation of the specimen is monitored using a custom-built submersible extensometer with a 25.4 mm (1.0 in) gage length. Details of the extensometer design and calibration appear in Appendix A. The evolution of localized deformation in the test section is monitored using digital image correlation (DIC).

(a) Digital Image Correlation

DIC is a non-contact experimental technique for determining full-field displacements of a deformed surface. Displacements are computed by tracking a stochastic pattern on a surface which is digitized into grayscale pixel intensities through an image sequence during the experiment. Through post-processing, the images of the deformed surface are compared against a reference image by passing the pixel intensities through a correlation algorithm. The distribution of pixel intensities is divided into subregions (referred to as facets in the ARAMIS software) spanning multiple pixels in both directions (say 15×15 pixels for example). The location of each facet in the deformed image is determined relative to the reference image by minimizing a correlation function. The function is commonly a normalized summation of the squares of the difference in pixel intensities. The local deformation and rotation of each facet is included in the correlation algorithm by assuming a uniform strain state in the facet region. Once the undeformed and deformed coordinates of the center of each facet are

determined, the corresponding displacement field permits the numerical calculation of the deformation gradient at each point. The calculation includes neighboring points (3×3 grid by default in ARAMIS) and assuming a homogeneous strain state over the computation region. It should be noted that in general the facets tend to overlap, with the spacing defined as the facet step in ARAMIS, thus the strain reference length in pixels is usually smaller than the facet size. ARAMIS outputs three strain measures, the Biot strain (which ARAMIS refers to as "technical" strain), logarithmic strain, and Green strain. The strain values reported in this work and the corresponding publications use the default ARAMIS output of Biot strain, $\boldsymbol{\varepsilon}^B$, as defined by Eq. 2.1 where F is the deformation gradient, and I is the identity tensor. The final results are smoothed by applying a 2D filter to accommodate the noise associated with computing numerical derivatives.

$$\boldsymbol{\varepsilon}^B = \sqrt{\boldsymbol{F}^T \boldsymbol{F}} - \boldsymbol{I} \tag{2.1}$$

The stochastic pattern was applied to the NiTi tubes by depositing a fine speckle pattern on the specimen (Fig. 2.3) that was photographed at regular time intervals (~2 s) with a high-resolution digital single-lens reflex (DSLR) camera (4288×2844) equipped with a timer. The tests were performed under displacement control that corresponds to a strain rate of 10^{-4} s^{-1}—when the deformation is homogenous. The load was measured with a dedicated 22.2 kN (5,000 lb) load cell. The transducer outputs were monitored with a computer-based data acquisition system running LabVIEW that was synchronized with the camera timer. Synchronization was performed by matching machine control initiation with imagery, and then interpolating in time using file time stamps for each image.

2.1.2 Compression Experimental Setup

The compression tests were performed in the same test bay as those for tension, but using a different setup designed to alleviate buckling of the specimen (Fig. 2.2b). Here the specimen is 40.6 mm (1.60 in) long. Instead of grips, the ends of the tubular specimen are inserted into tight fitting recess cavities machined into one-inch stainless steel rods, leaving a test section of 20.3 mm (0.8 in; $L/D \sim 4$). A square shoulder machined into the bottom of the cavity mates with the end of the tube, which was carefully faced off in a lathe. Access holes machined into the stainless rods allow passage of water from the temperature controlled water bath connected in a closed loop as shown in Fig. 2.2b. Infrared thermography was used in preliminary experimental design to select the flow rate required to keep the specimen at constant temperature The flow rate was controlled with an analog dial connected to the output of the circulating fluid bath. A thermocouple connected to the surface of the tube using a thermally conductive paste was used during the tests to verify the constancy of the specimen temperature.

The experiments were again performed at a slow displacement rate that results in an average strain rate of 10^{-4} s^{-1}. The overall compression of the specimen was monitored with a 12.7 mm (0.5 in) extensometer while DIC was used to monitor the evolution of deformation in the test section using the same camera and rate mentioned above.

Additional compression experiments were conducted on NiTi rods from Memry (PN: 10578, LN: DM-5833, IN: N1-2314) with the same nominal dimensions as the tube experiments explained above. The objective of the compression rod experiments was to investigate the onset, evolution, and effect of plasticity in compression. The prescribed displacement rate corresponded to a strain rate of 5×10^{-5} s^{-1}. (Experiments were

conducted at 23 °C and it can be assumed the rod stock has the same transformation temperatures as the tube stock.)

2.2 Experimental Results

2.2.1 Tension Results

Figure 2.4a shows the nominal stress-elongation response ($\sigma - \delta / L$) recorded at 23 °C where δ is the change in length recorded by the extensometer (gage length L). Figure 2.4b shows a set of full-field DIC contours of axial strain corresponding to the numbered bullets on the response in Fig. 2.4a (evaluated using the ARAMIS software). The unstressed material is in the austenitic phase (A) and thus the response traces the familiar closed hysteresis that is characteristic of pseudoelastic behavior (e.g., see similar isothermal responses in Shaw and Kyriakides [1995, 1997]). Under tension, A deforms elastically and homogeneously as depicted in image ①. At a stress of 381 MPa (55.2 ksi) the material starts to transform into the martensitic phase (M). M nucleates at one of the gripped ends due to the stress concentration. The phase change results in local macroscopic deformation that becomes apparent in image ②. With additional elongation, the M phase propagates from right to left as illustrated in images ③ - ⑥ generating two deformation regimes: a strain of 0.81% ahead of the front and 6.7% behind it. In other words, the strain values that correspond to the beginning and end of the top stress plateau. During this propagation of M, the stress remains nearly unchanged at 383 MPa (55.3 ksi).

Because of the circular geometry of the tubular specimen, the front separating the two deformation regimes (phases) is in the form of a multi-pronged helix that can be seen in images ③ and ④. (Similar helical patterns have been reported by Li and Sun [2002], Feng and Sun [2006], Favier et al. [2007], Reedlunn et al. [2014]). The spiral propagates

to the left rotating in a clockwise direction. Figure 2.5 shows an expanded view of the helical front that corresponds to image ④. Helical bands are tubular manifestations of inclined localized deformations in strips that are along the two characteristics of approximately $\pm 55^\circ$ to the axis of the tube (Bijlaard [1940], Hill [1952]; see also Shaw and Kyriakides [1997], Kyriakides and Miller [2000], Hallai and Kyriakides [2013]). The multiple fingers is a way of minimizing the bending deformation that can result from the asymmetry caused by a single inclined band.

Once about one half of the specimen length has been traversed by the fingered front, M nucleates for the first time at the opposite grip. As is apparent in images ⑤ and ⑥ , at this site bands propagate along both characteristics. The two fronts continue to propagate towards each other and by configuration ⑦ a chevron like island of A is left. Beyond this point, the two fronts start to interact and this causes the recorded stress to drop. The last sliver of A is seen in image ⑧, beyond which deformation in the specimen is homogenous once more (e.g., ⑨) and the stress has a strong positive modulus. Between points ⑧ and ⑨, M undergoes detwinning, and in addition randomly dispersed pockets of remaining A get transformed by the higher stress. The specimen was loaded to about 527 MPa (76.4 ksi) and a strain of 7.5% before unloading commenced.

Unloading follows a different trajectory than the stable branch of the response at the end of the stress plateau, presumably because the M volume fraction between points ⑧ and ⑨ has increased. As illustrated by images ⑩ and ⑪, the deformation remains homogenous until a stress of 119 MPa and a strain of 5.6% when M becomes unstable and transformation back to A commences. As is evident from image ⑫, A nucleates at the location of the termination of the A→M transformation and simultaneously the stress increases. Thus, as was recorded in similar experiments of others, a clear distinction

between the nucleation stress and the propagation stress develops for the M→A transformation. Interestingly, A develops into a single helical band that propagates along the length and simultaneously broadens as illustrated in image ⑬. The propagation takes place at a gradually increasing stress (152 MPa at ⑫ to 170 MPa just before ⑭). In the neighborhood of image ⑭, the spiral front has reached the LHS grip and is responsible for the stress undulation recorded. By this time A has consumed all but a narrow spiral of M in the left two-thirds of the specimen. Between ⑭ and ⑮ a single multi-pronged front has formed and is propagating towards the right spiraling in the opposite direction to that of the ones in the loading phase. By configuration ⑯, the reverse transformation has been completed, the specimen is once more homogeneous, and unloads to nearly zero strain along a similar path to that followed during loading.

Similar isothermal experiments were performed at three additional temperatures, 13, 33, and 43 °C and the results appear in Fig. 2.6 together with the 23 °C response. Pseudoelastic behavior characterized by closed hystereses (slightly open for 43 °C) is observed in all four cases.

The elastic moduli for tension and compression in the A and M phase are plotted vs. temperature in Fig. 2.7 designated as E_A and E_M. Values were determined from the extensometer measurements: E_A from the initial loading of the four responses in Figs. 2.6 and 2.12, and E_M is the slope at first unloading. The initial elastic modulus (E_A) increases with temperature while the modulus upon unloading (E_M) remains essentially unchanged.

In tension, the plateau stresses, σ_{PM} for the A→M transformation and σ_{PA} for M→A, are well defined in the results shown in Fig. 2.6 and are plotted vs. temperature in Fig. 2.8. The extents of the upper and lower plateaus did not vary much with temperature:

they are about 7% for the upper plateaus and 6% for the lower ones. Our setup masks the loading nucleation peak (see Shaw and Kyriakides [1997]), but captures the nucleation stress valley upon unloading (see Fig. 2.6) that is designated as σ_{NA}. It is seen to be lower than σ_{PA} but to follow a similar trend with temperature. As reported by others, the A→M stress plateau (σ_{PM}) increases nearly linearly with temperature as shown in Fig. 2.8, with a calculated slope of 5.89 MPa/°C. A corresponding increase is also recorded in the same figure for the initiation (σ_{NA}) and plateau stresses (σ_{PA}) of the M→A transformation, with calculated slopes of 5.53 and 6.41 MPa/°C, respectively.

The response at 43 °C is isolated in Fig. 2.9a with the corresponding axial strain contours from DIC in Fig. 2.9b. The empty regions in the DIC contours are a result of the condensation of bubbles at the elevated temperature. Despite the deviation from pseudoelasticity with the appearance of non-recoverable transformation strains, the response exhibits a flat stress plateau during both forward and reverse transformation. The DIC contours confirm the strongly inhomogeneous deformation, which again takes the form of helical bands inclined to the longitudinal axis and propagates along the length of the specimen.

2.2.2 Compression Results

A compressive stress-shortening response recorded in an experiment at 23 °C on a specimen with test section length-to-diameter ratio (*L/D*) of 3.9 is shown in Fig. 2.10a. The average strain was recorded using a 12.7 mm (0.5 in) extensometer while local deformation was monitored with DIC over the central 2.2*D* long section. Figure 2.10b shows a set of DIC color axial strain contours that correspond to the points marked on the response in Fig. 2.10a with numbered bullets. The response traces the expected closed

hysteresis but exhibits significant differences from the tensile behavior at this temperature:

- the A→M transformation stress is significantly higher
- but for a short duration early on, the A→M transformation is occurring at an increasing stress
- the strain reached before the upswing in stress is about half that in tension
- the M→A transformation stress is also significantly higher
- except for a section at small strains a significant part of the M→A transformation occurs at a monotonically decreasing stress.

In more detail, during the initial linearly elastic branch of the response, deformation is uniform as depicted by image ① in Fig. 2.10b. M transformation commences at a stress of about 600 MPa (87 ksi). This occurs in a more gradual manner than in tension, but even in image ②, past the stress knee, deformation remains uniform. Signs of inhomogeneous deformation start to appear at an average strain of about 1.36%, just past image ②, and remain until a strain of about 3.25% at image ⑧. Remembering that the rectangular images represent a cylindrical surface, in this regime deformation localizes starting from the upper left hand corner, forms a "triangular zone" and spreads diagonally to the other corner. We speculate that this may indicate an inclined elliptical diffuse front that joins two deformation regimes. To get a more quantitative impression of the strain gradients along this inclined path, in Fig. 2.11 the axial strain levels are plotted along three lines inclined at 35° to the axis of the tube for images ③, ⑤ and ⑧. The strain plots show a strain gradient along these directions that starts at about $\pm 0.5\%$ in image ③ grows to nearly $\pm 1\%$ in image ⑤ and is diminished in image ⑧. This strain distribution indicates that the specimen is undergoing some bending. In image ⑨ the strain gradient is

nearly eclipsed and in ⑩ deformation is homogeneous once more. Since, the stress at this point is higher than the stress between points ③ and ⑧ it appears that any bending that has taken place between these points is transformation induced rather than structural.

Upon unloading, deformation remains homogeneous through point ⑫ at about 440 MPa (64 ksi) when the stress transitions to a lower stress "plateau" during which M→A transformation occurs. Once more, a certain amount of strain gradient develops in the specimen; transformation is more pronounced in the lower right corner of the images and moves again in a nearly diagonal direction across to the other corner. The gradient is most pronounced in image ⑯ where a variation of the order of ±1% from the nominal strain exists along an inclined direction similar to that in Fig. 2.11. This unavoidably implies that the specimen again undergoes some bending. By image ⑱ transformation is completed, deformation is uniform, and the specimen unloads elastically following the initial loading trajectory (see similar results in Fig. 7 of Reedlunn et al. [2014]).

Although valid compression experiments are more difficult to perform than tension, and as a result are rather rare, the asymmetry between tension and compression for NiTi was reported as early as 1971 by Wasilewski. Among others, Vacher and Lexcellent [1992] reported asymmetry in CuZnAl followed by more careful experiments including triaxial loading by Jacobus et al. [1996] on NiTi. Gall and Sehitoglu [1999] and Gall et al. [1999] attributed the asymmetry to differences in detwinning strain and critically resolved shear stresses (Schmid factors) caused by crystallographic texture (see also Orgéas and Favier, 1998). The origin for the asymmetry in the localization of NiTi has been hypothesized to be due to more correspondence variance pairs (CVP's) available in tension than compression (Gall and Sehitoglu [1999] and Sehitoglu et al. [2000]). More recently Mao et al. [2010] using electron backscattering diffraction

confirmed differences in Schmid factors between tension and compression. They also noted a wider scatter in the Schmid factors for compression to which they attributed the more homogeneous nature of transformation in compression (see also Mao et al. [2008]). Currently, this is an unresolved topic in the community with further research required.

Similar isothermal compression experiments were conducted at 13, 33, and 43 °C. The four stress-displacement responses recorded are plotted together in Fig. 2.12. They all exhibit essentially monotonic behavior for both loading and unloading, while the hystereses traced shift to a higher stress as the temperature increases. It is noteworthy that at 43 °C the hysteresis did not close indicating that the pseudoelastic temperature regime has been exceeded. The initial elastic moduli of A (E_A) are seen in Fig. 2.7 to increase nearly linearly with temperature and are seen to be somewhat higher than the corresponding values in tension. Interestingly, the initial moduli at unloading (E_M) are even higher.

All of the compressive responses are essentially monotonic both during loading and unloading. In view of the absence of distinct stress plateaus, Fig. 2.8 only displays the "nucleation" stresses σ_{NM} and σ_{NA}. Since the transitions at both loading and unloading are smooth, these values were determined using tangent construction lines. Both stresses exhibit significant dependence on temperature. A comparison of Figs. 2.6 and 2.12 clearly shows that the strains induced by transformation in compression are significantly smaller than those in tension. However, in compression the termination of M transformation is not well defined and consequently we opt not to assign a stress value to it. The 43 °C test developed some permanent deformation and consequently the various variables deviate from the trends of the results from the other three temperatures. The nucleation stresses, σ_{NM} and σ_{NA}, follow a nearly linear trajectory in the 13 - 33 °C

temperature range, with calculated slopes of −12.21 MPa/°C and −11.25 MPa/°C, respectively.

During loading, the deformation in all four cases exhibited mild inhomogeneities for a relatively short part of the strain history. These were qualitatively and quantitatively similar to those reported above for the 23 °C experiment. The unloading deformation patterns were also similar for 13, 23 and 33 °C, but differed for 43 °C. The response of the 43 °C test is shown isolated in Fig. 2.13a along with a set of corresponding DIC axial strain contours that appear in Fig. 2.13b. The DIC images show a mild inhomogeneity developing between points ③ and ⑤ on the response. However, the unloading response maintains a strongly positive tangent modulus and simultaneously the deformation remains homogeneous throughout and the hysteresis did not close.

In summary, the tube compression results show the significant difference between tension and compression reported by previous researchers and are mainly attributed to crystallographic texture. Both the loading and unloading responses, but for limited strain ranges, maintain an essentially positive tangent modulus. Despite this, some relatively small amount of inhomogeneous deformation was observed for parts of the loading and unloading trajectories that resulted in some bending of the compressed tube. The largest variation of axial strain was of the order of ±1% from the mean value. Unlike the sharp fronts that develop in tension, here the evolution of localized deformation appeared to be less organized. The pseudoelastic behavior was terminated at a temperature between 33 and 43 °C and consequently upon unloading the highest temperature case exhibited some permanent deformation.

The axial compressive stress-nominal displacement response from experiments conducted on NiTi rods are shown in Fig. 2.14. The onset of M transformation was found

to occur at approximately 605 MPa with an M saturation stress of approximately 775 MPa, levels similar to the response of NiTi tubes. Experiments with loading beyond the M saturation stress revealed pseudoelastic behavior for stresses as high as 1.5 GPa (5 % strain). Upon unloading, the onset of the A transformation stress was found to be inversely proportional to the loading termination stress, while the A saturation stress remained relatively constant at about 295 MPa. NiTi rods stressed beyond 1.5 GPa began to deviate from linearity and result in permanent plastic deformation, with hysteresis that did not close. Following a loading termination stress at about 2.5 GPa (9.1 %), the onset of the A transformation stress was nearly zero and resulted in a permanent strain of nearly 6 %. One NiTi rod loaded to failure exhibited a 45° failure in shear at a nominal compressive stress of about 2.9 GPa and a strain of nearly 15 %.

2.3 CONCLUSIONS

Uniaxial tension and compression experiments were conducted under isothermal conditions in custom testing facilities on as-received tube specimens from the same batch of stock material. In the temperature range of 13 - 43 °C, under tension the material exhibits the well-known closed hysteresis with and upper and lower stress plateau. During the upper plateau material undergoes A→M transformation that results in localized deformation. Because of the tubular nature of the test specimens, localization was in the form of helical deformation patterns that propagate until the whole specimen is transformed. The stress then starts rising and further deformation is homogeneous. The material unloads homogenously until M→A transformation nucleates which again leads to helical localization patterns. For the temperatures examined the hysteresis loops closed except at 43 °C where a small permanent strain was induced.

The corresponding compressive responses exhibited significant differences from the tensile ones at all temperatures examined. The transformation stress is significantly higher than the one in tension and the induced strain is nearly half of the plateau strain in tension. Both the loading and unloading responses, but for limited strain ranges, maintain an essentially positive tangent modulus and the deformation remained essentially homogeneous. These differences have been attributed in the literature to crystallographic texture. The 43 °C response deviated from pseudoelasticity more severely than that of tension as the response did not close fully.

Separate compression experiments were performed on NiTi rods in order to establish the behavior of the material past the completion of M transformation. The response recorded a closed hysteresis for stresses up to 1.5 GPa (i.e., 2.5 times σ_{NM}). For higher stresses, the lower plateau shifts downwards and the hysteresis does not close fully. The loading response exhibits nonlinearity that can be attributed to a combination of further transformation of pockets of untransformed A and dislocation activity in the detwinned M phase. As the unloading stress increases, the permanent deformation increases. The NiTi rod failed in shear at a nominal compressive stress of 2.9 GPa and a strain of about 15 %.

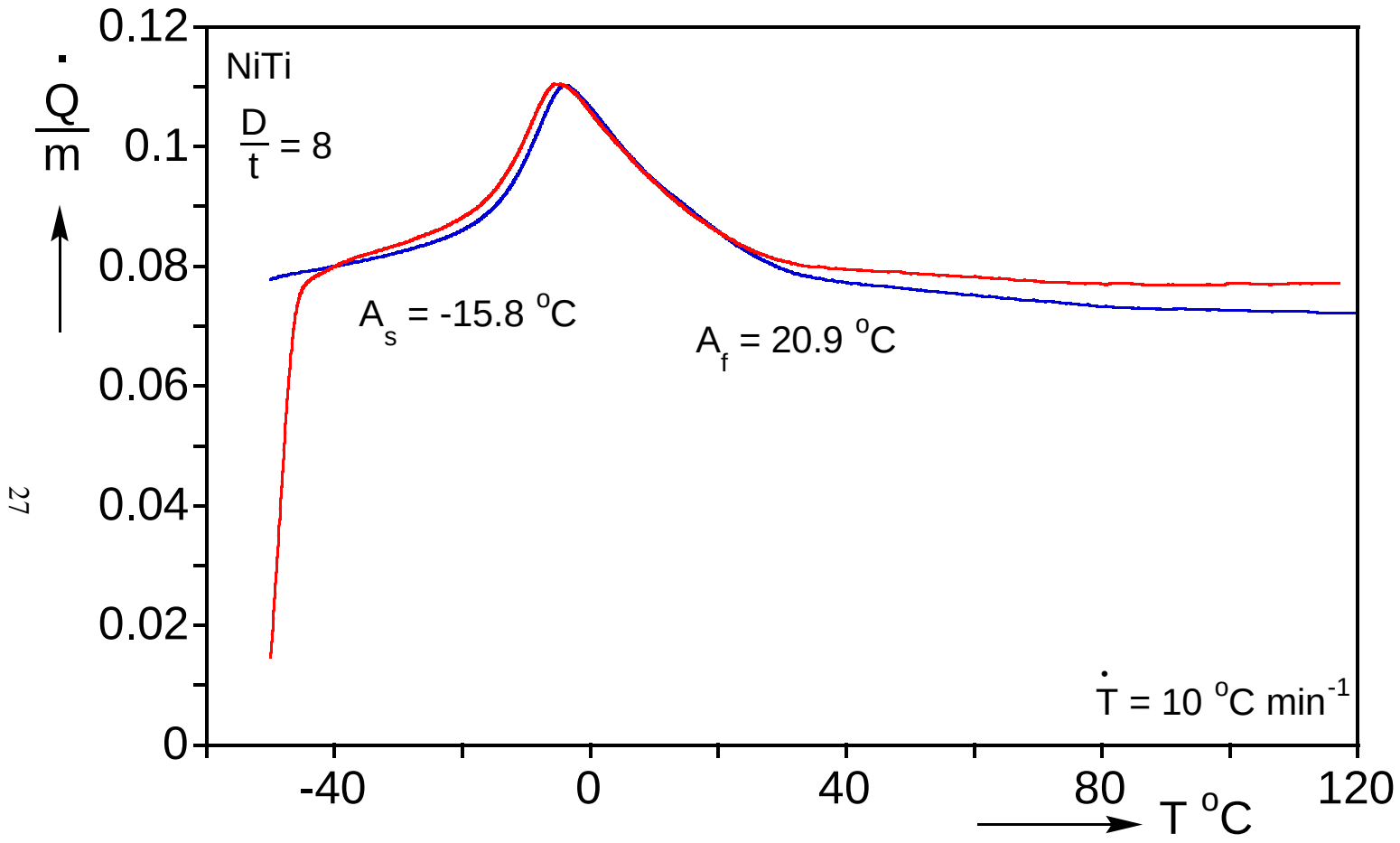

Fig. 2.1 DSC themogram of NiTi tube stock used in tension, compression, and bending experiments.

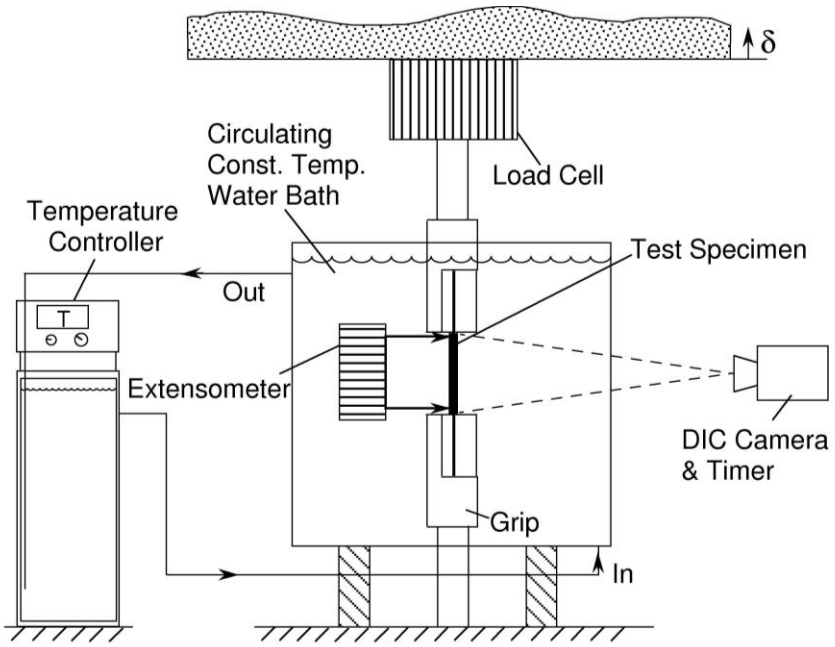

(a)

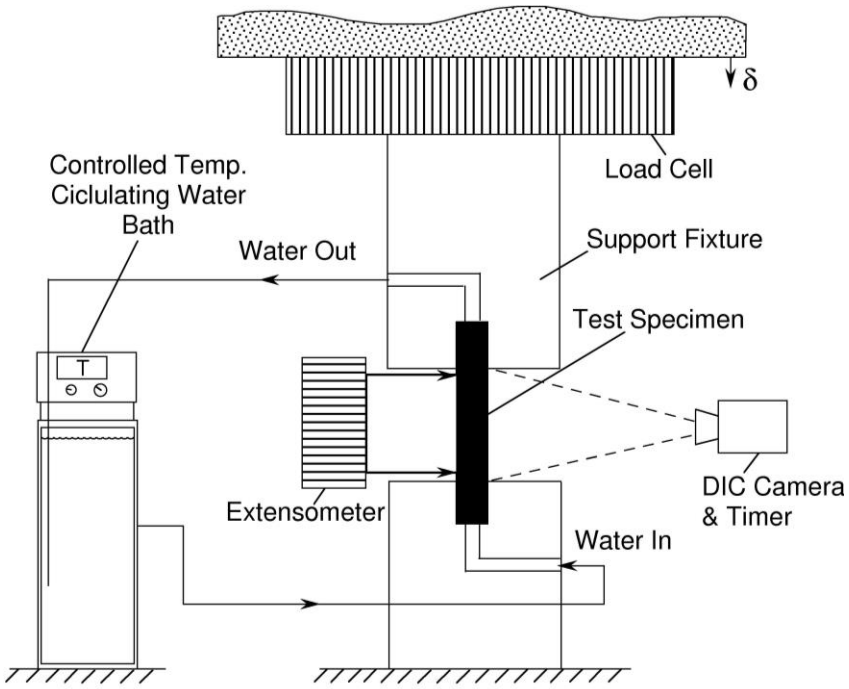

(b)

Fig. 2.2 Custom experimental setups for isothermal (a) tension and (b) compression tests on tubes.

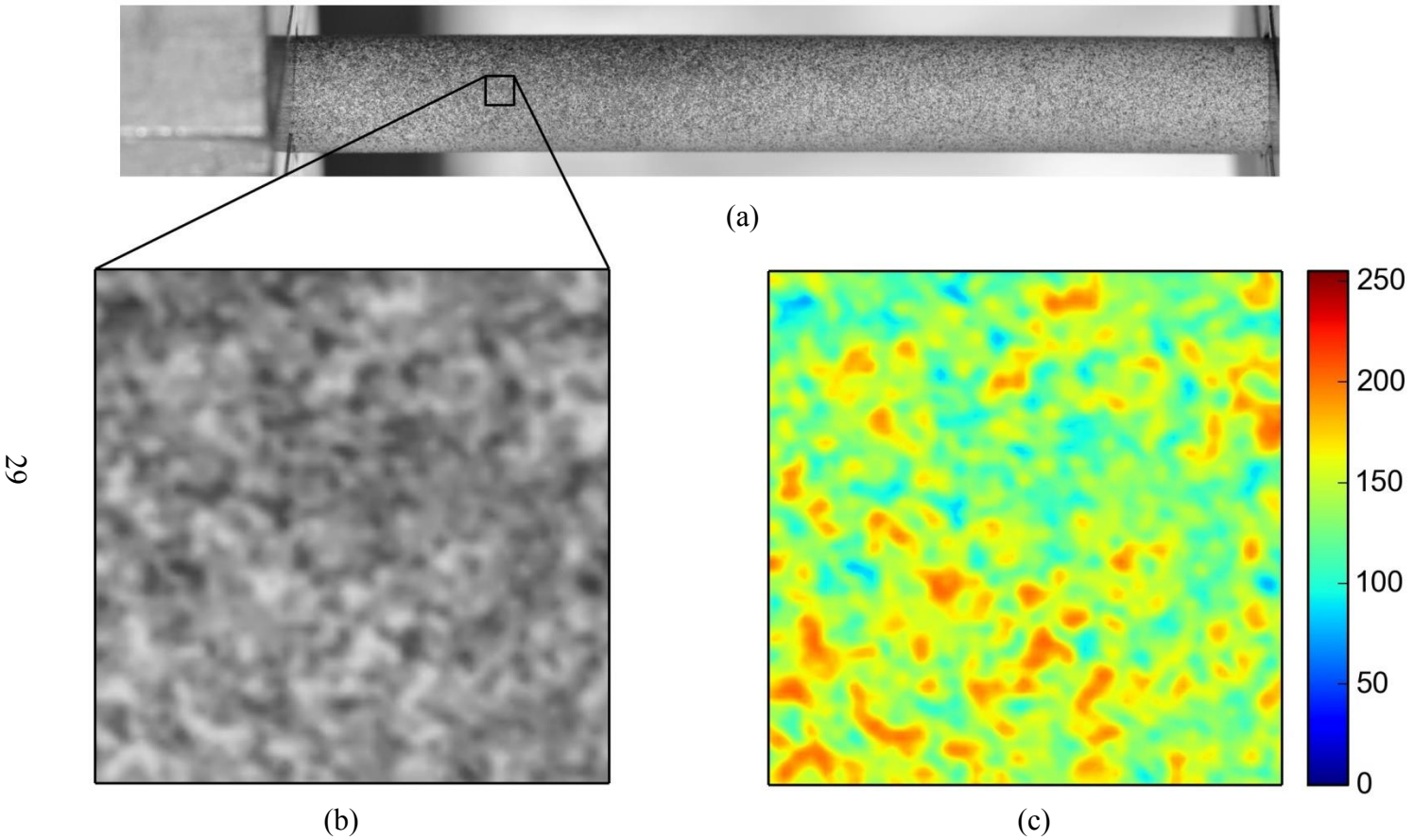

Fig. 2.3 (a) Grayscale reference image displaying sample speckle pattern on tension specimen, (b) 100×100 pixel subset, (c) corresponding grayscale levels.

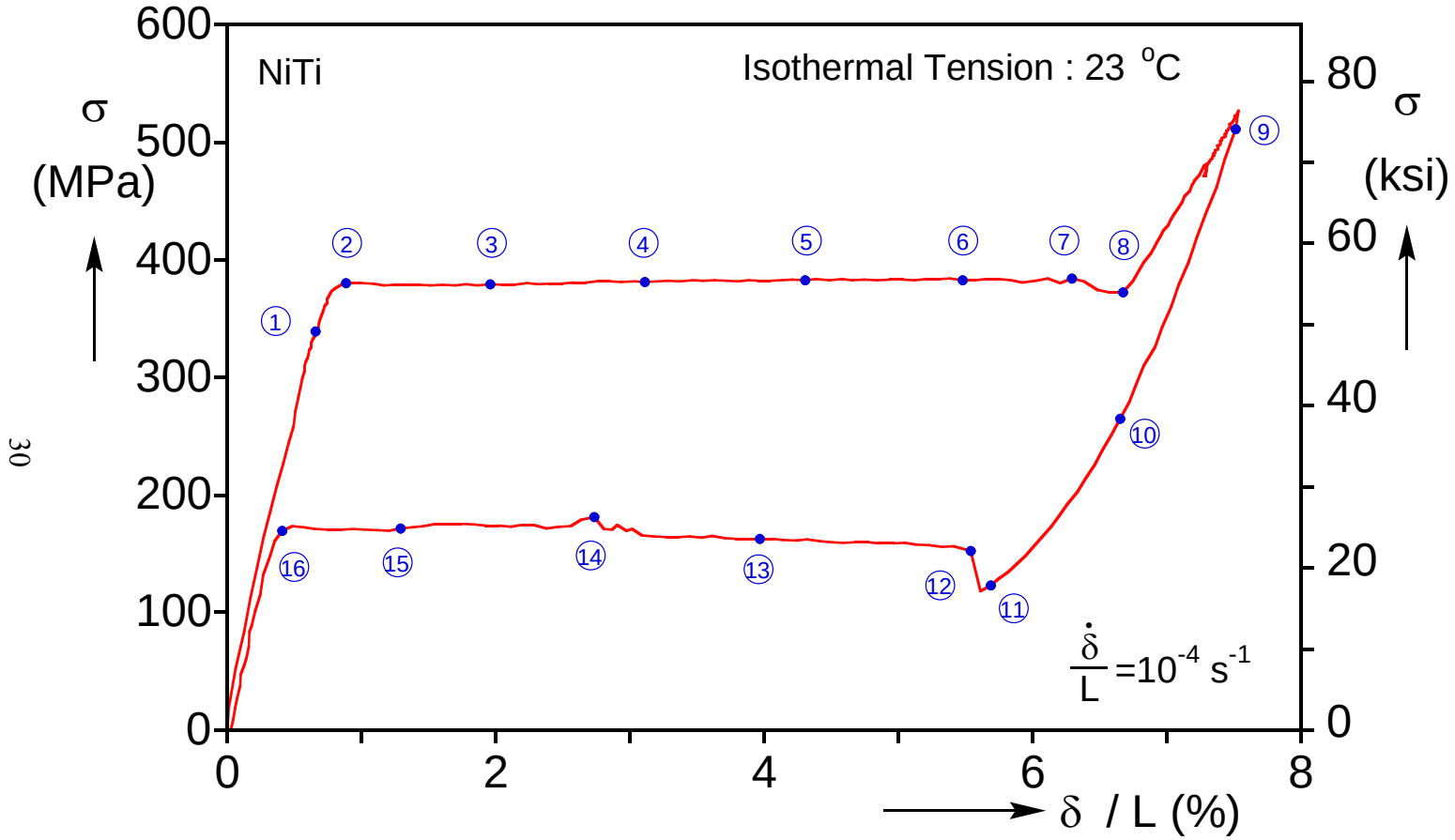

(a)

Fig. 2.4a (a) Isothermal pseudoelastic tensile stress-elongation response of a NiTi tube at 23 °C.

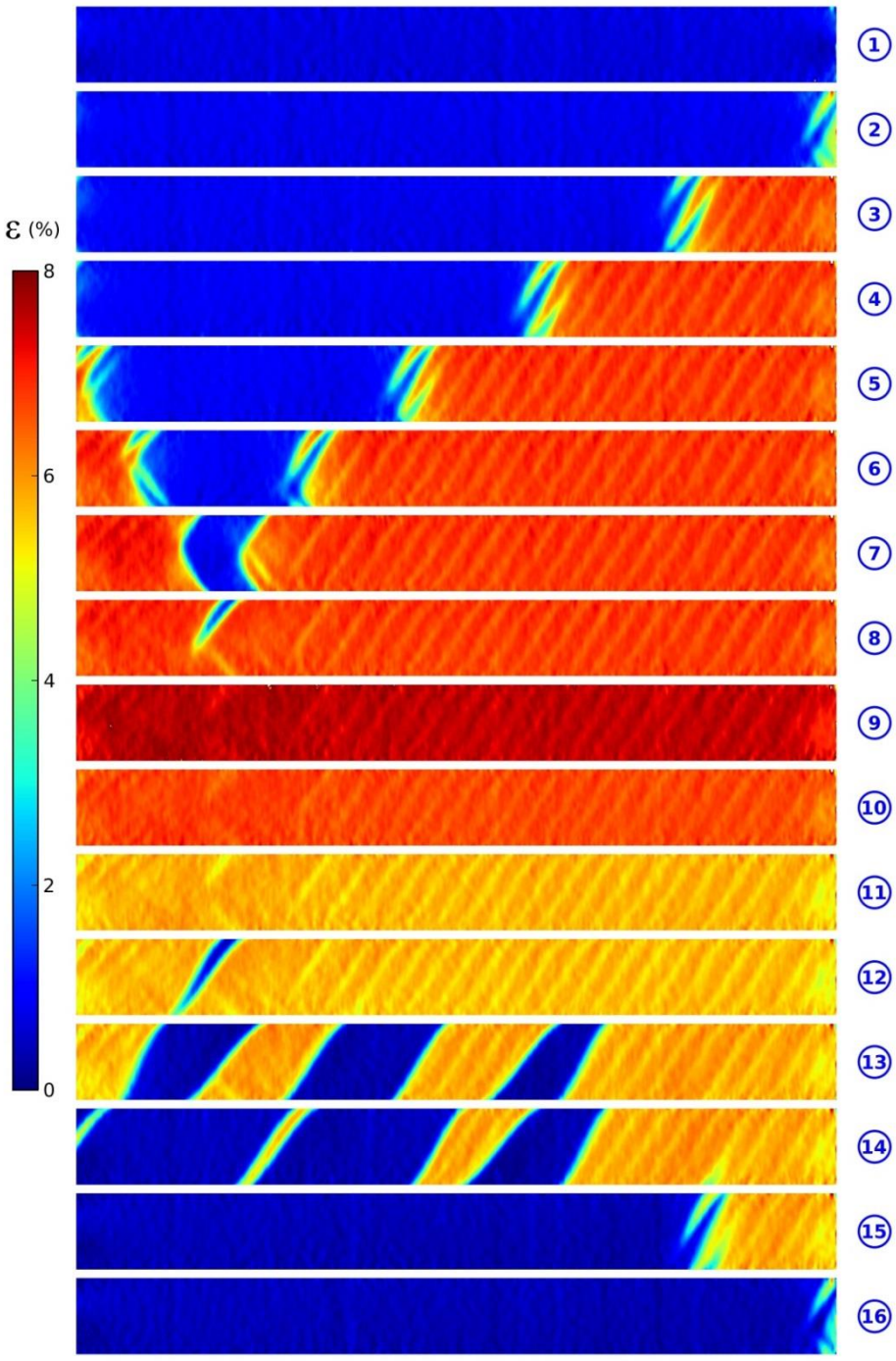

(b)

Fig. 2.4b (b) Set of axial strain contours from DIC corresponding to the numbered bullets marked on the response in 2.4a.

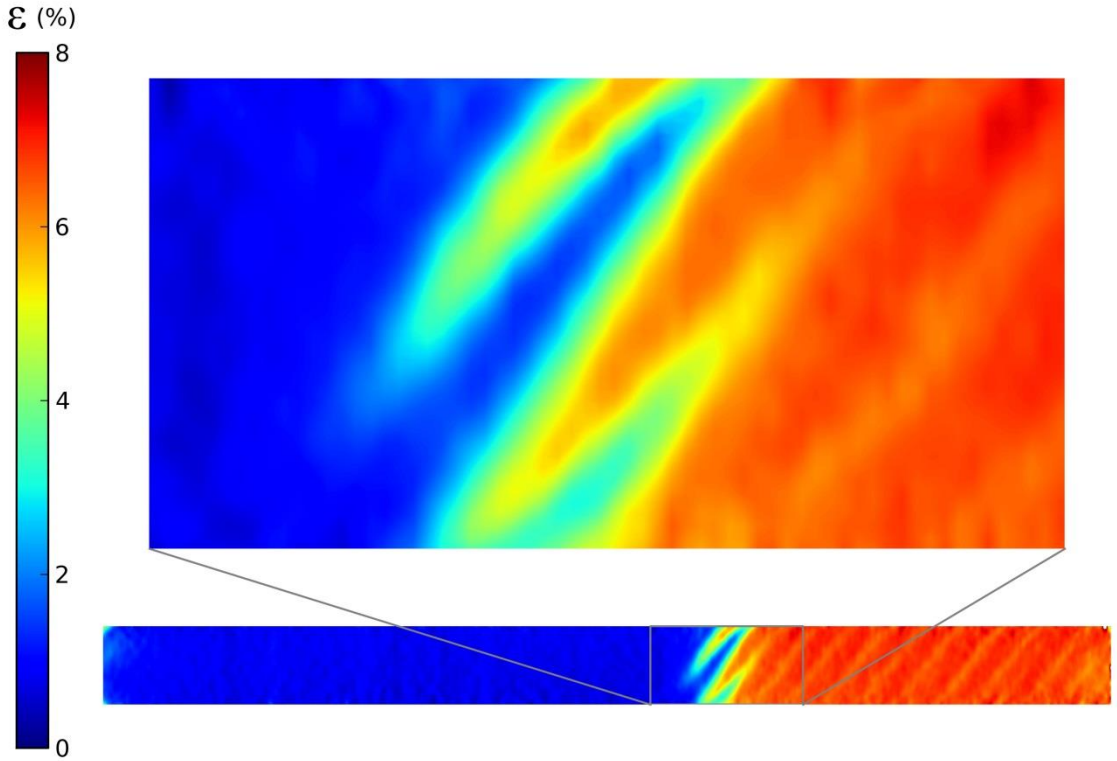

Fig. 2.5 Expanded view of image ④ in Fig. 2.4 illustrating the helical deformation pattern through which A→M transformation spreads

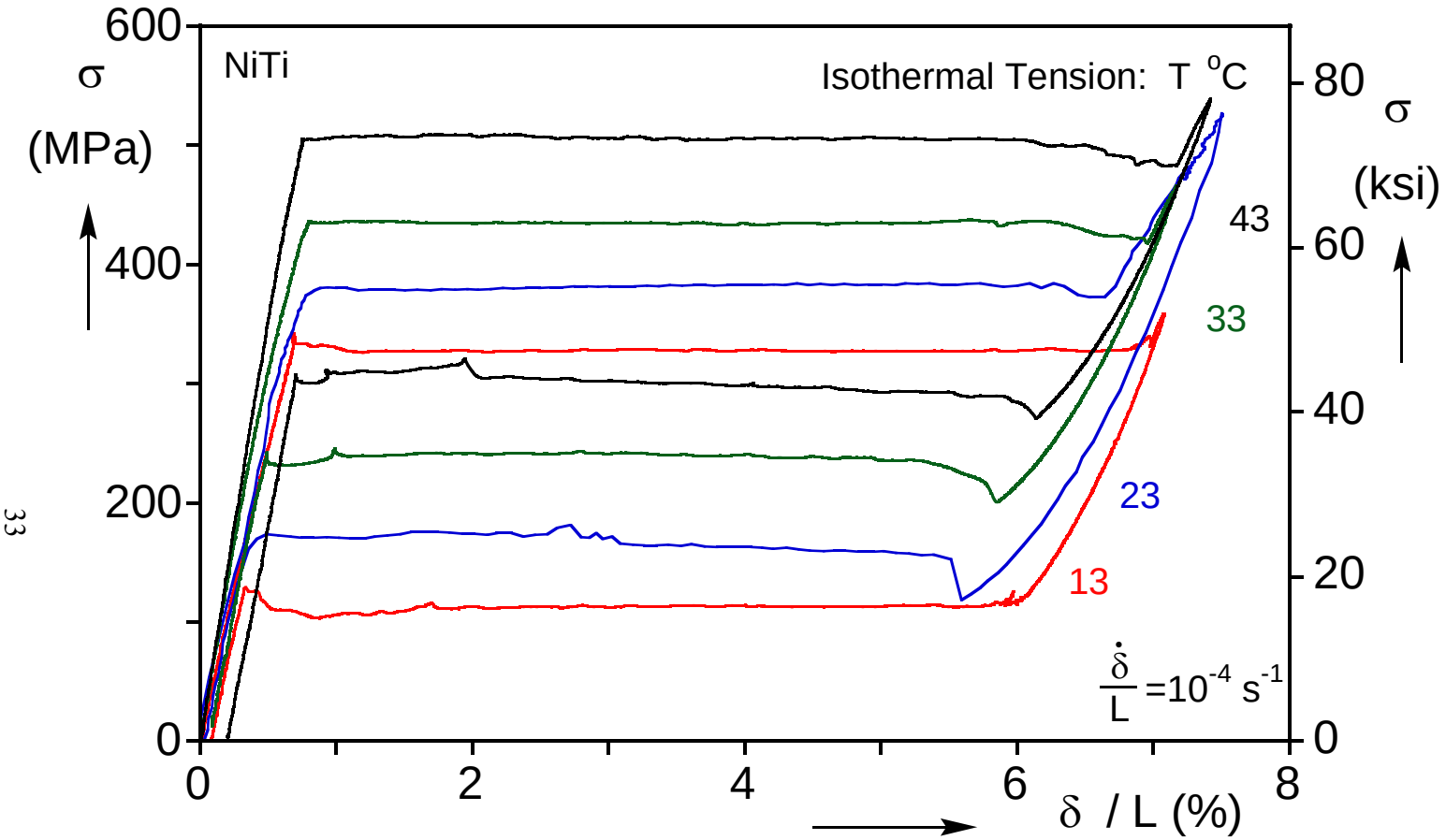

Fig. 2.6 Pseudoelastic tensile stress-elongation responses of NiTi tubes at 13, 23, 33, and 43 °C

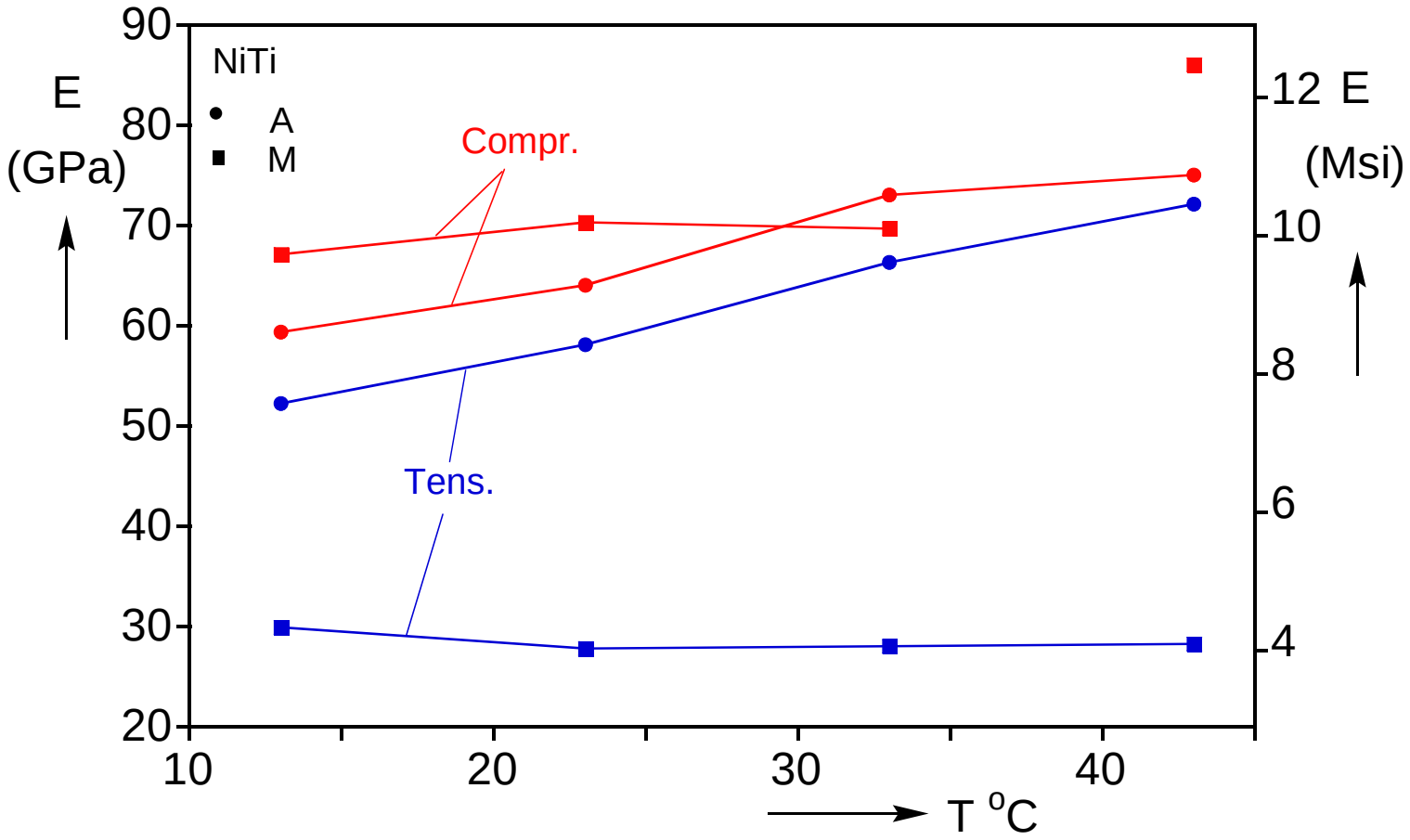

Fig. 2.7 Loading and unloading initial moduli for A and M phases vs. temperature from tension and compression tests on NiTi tubes.

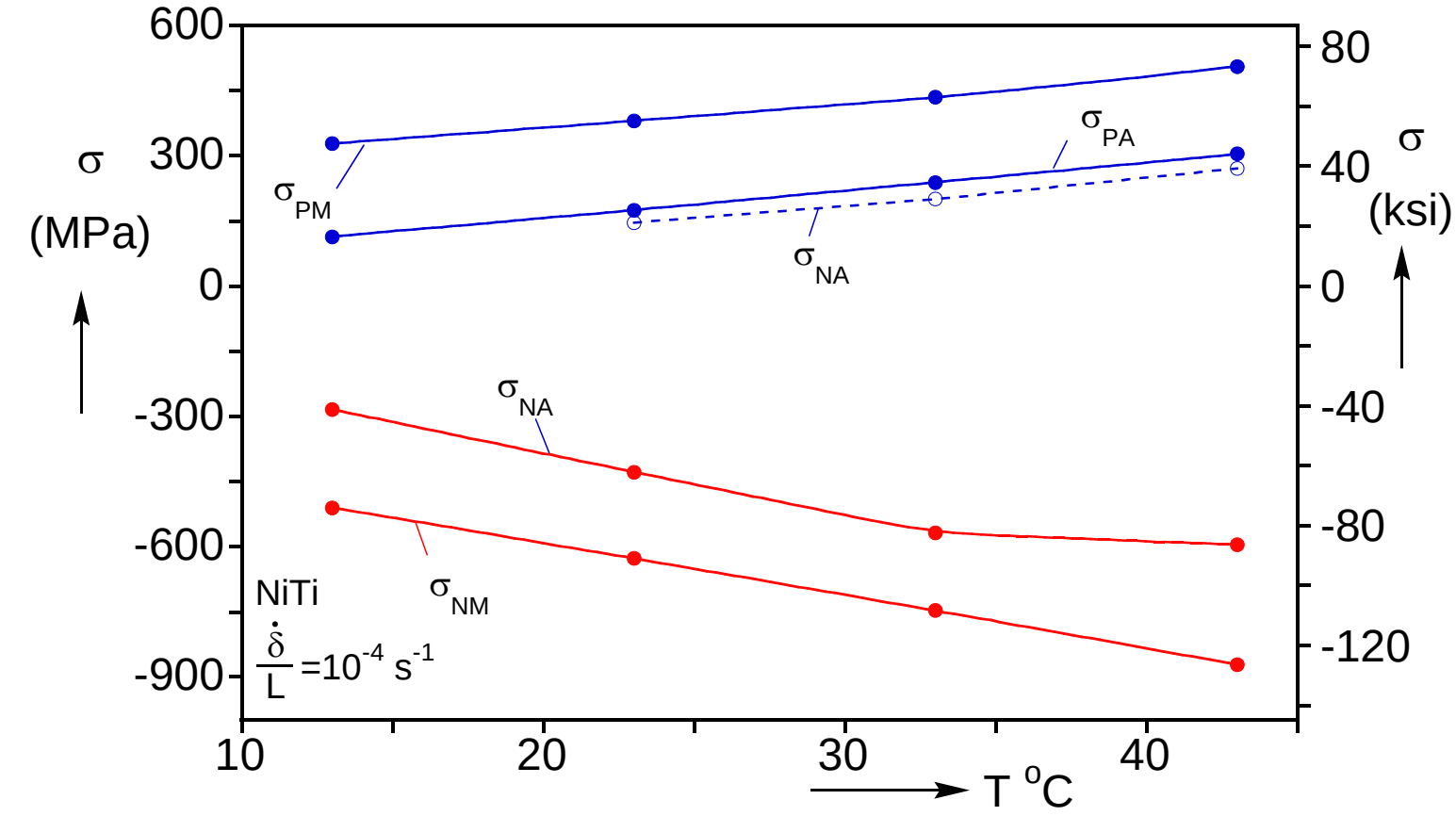

Fig. 2.8 Transformation stresses vs. temperature for loading and unloading from tension and compression tests on NiTi tubes.

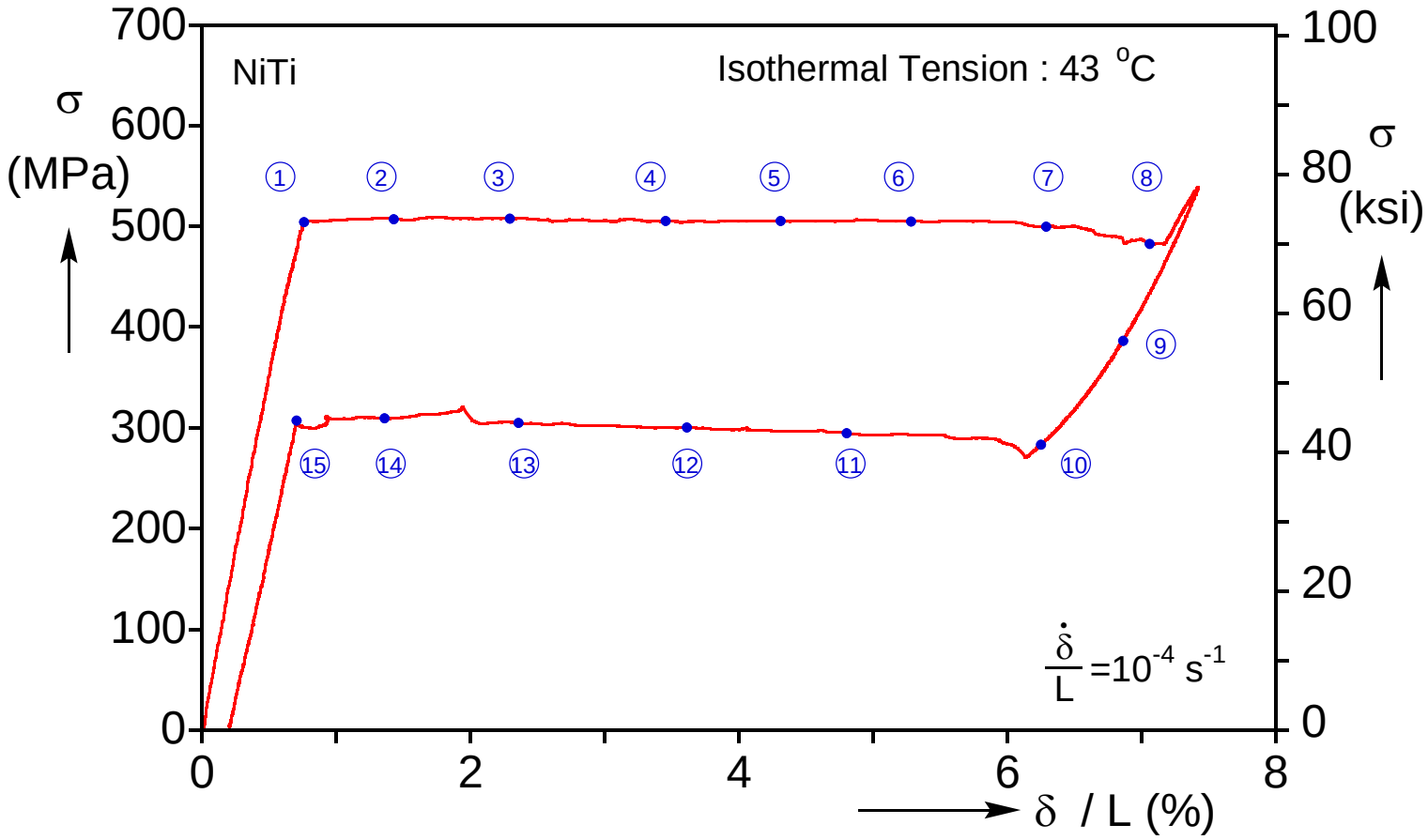

Fig. 2.9a (a) Isothermal pseudoelastic tensile stress-elongation response of a NiTi tube at 43 °C.

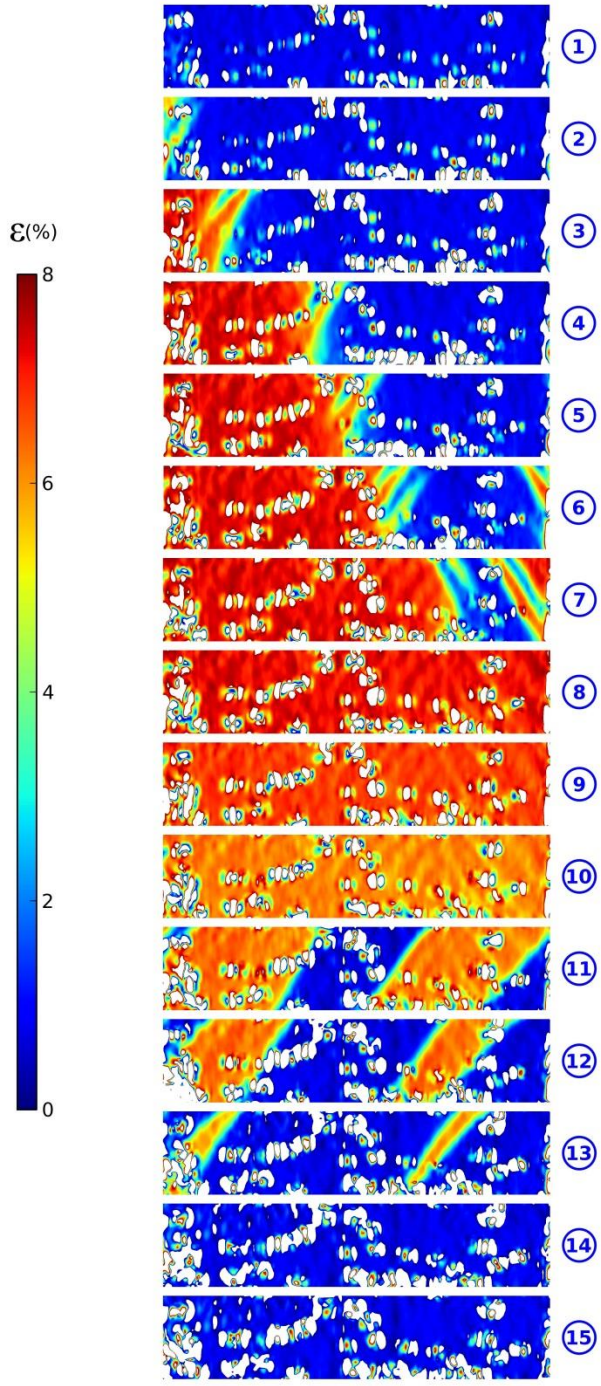

(b)

Fig. 2.9b (b) Set of axial strain contours from DIC corresponding to the numbered bullets marked on the response in 2.6a.

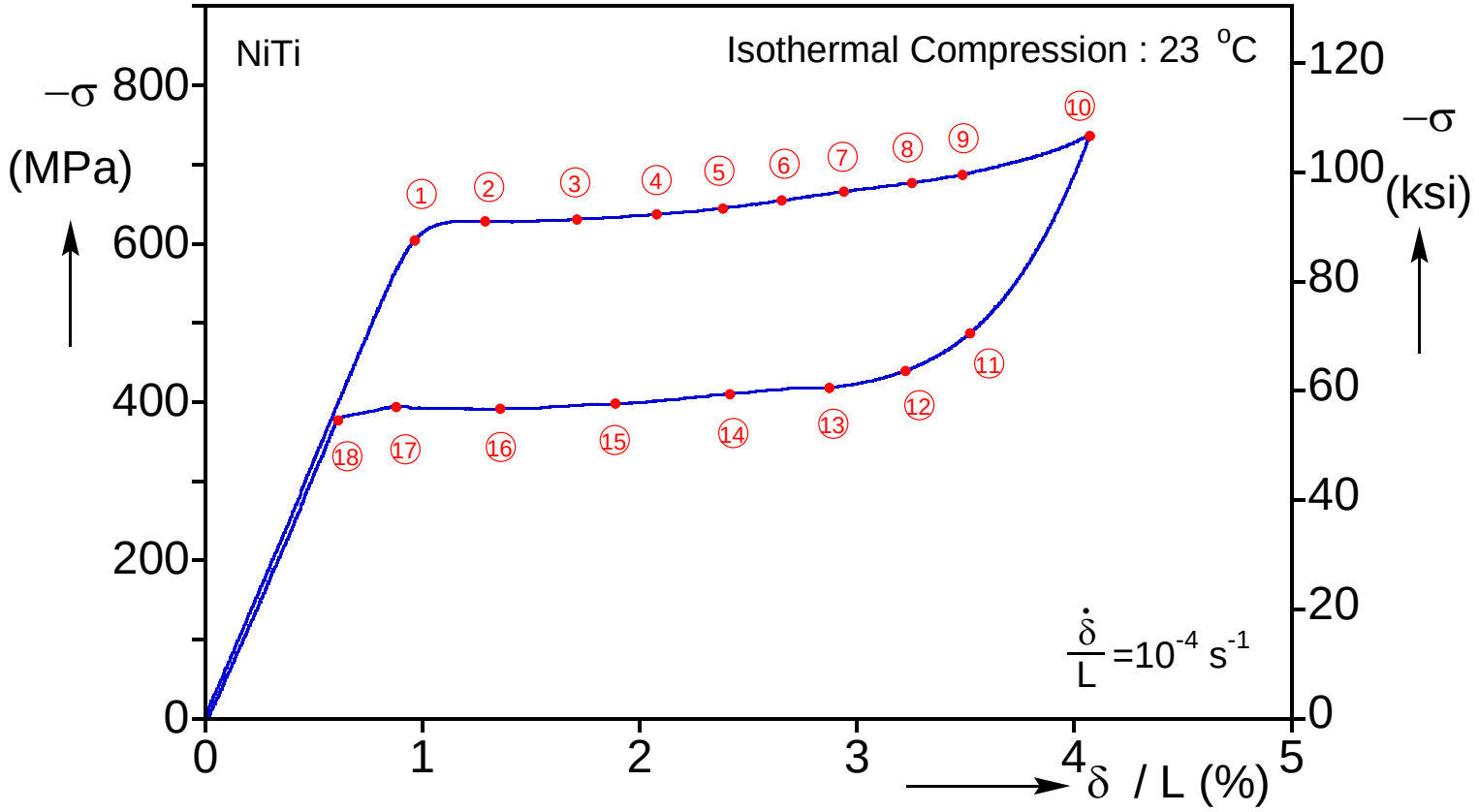

(a)

Fig. 2.10a (a) Isothermal pseudoelastic compressive stress-displacement response of a NiTi tube at 23 °C.

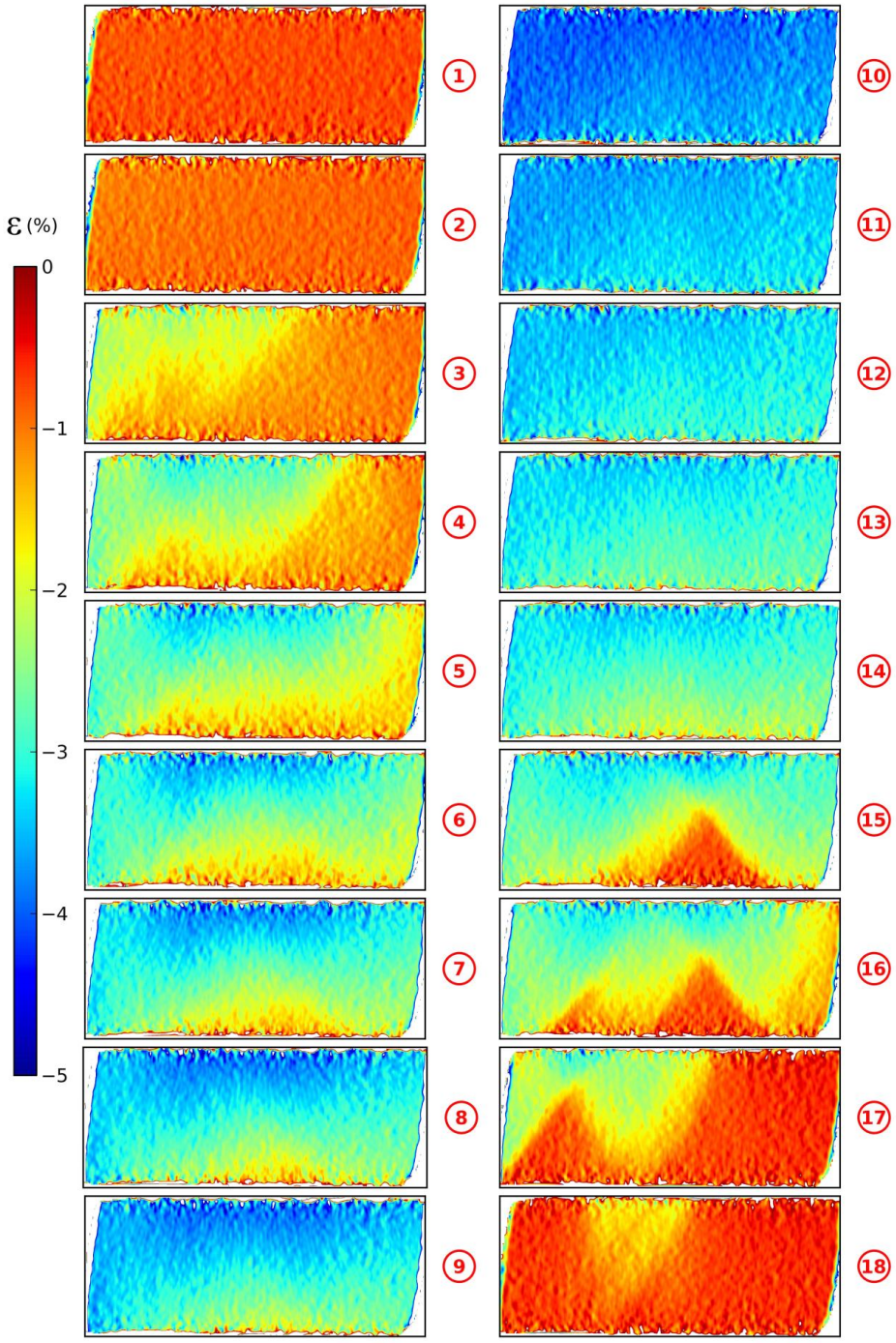

(b)

Fig. 2.10b (b) Set of axial strain contours from DIC corresponding to the numbered bullets marked on the response in 2.8a.

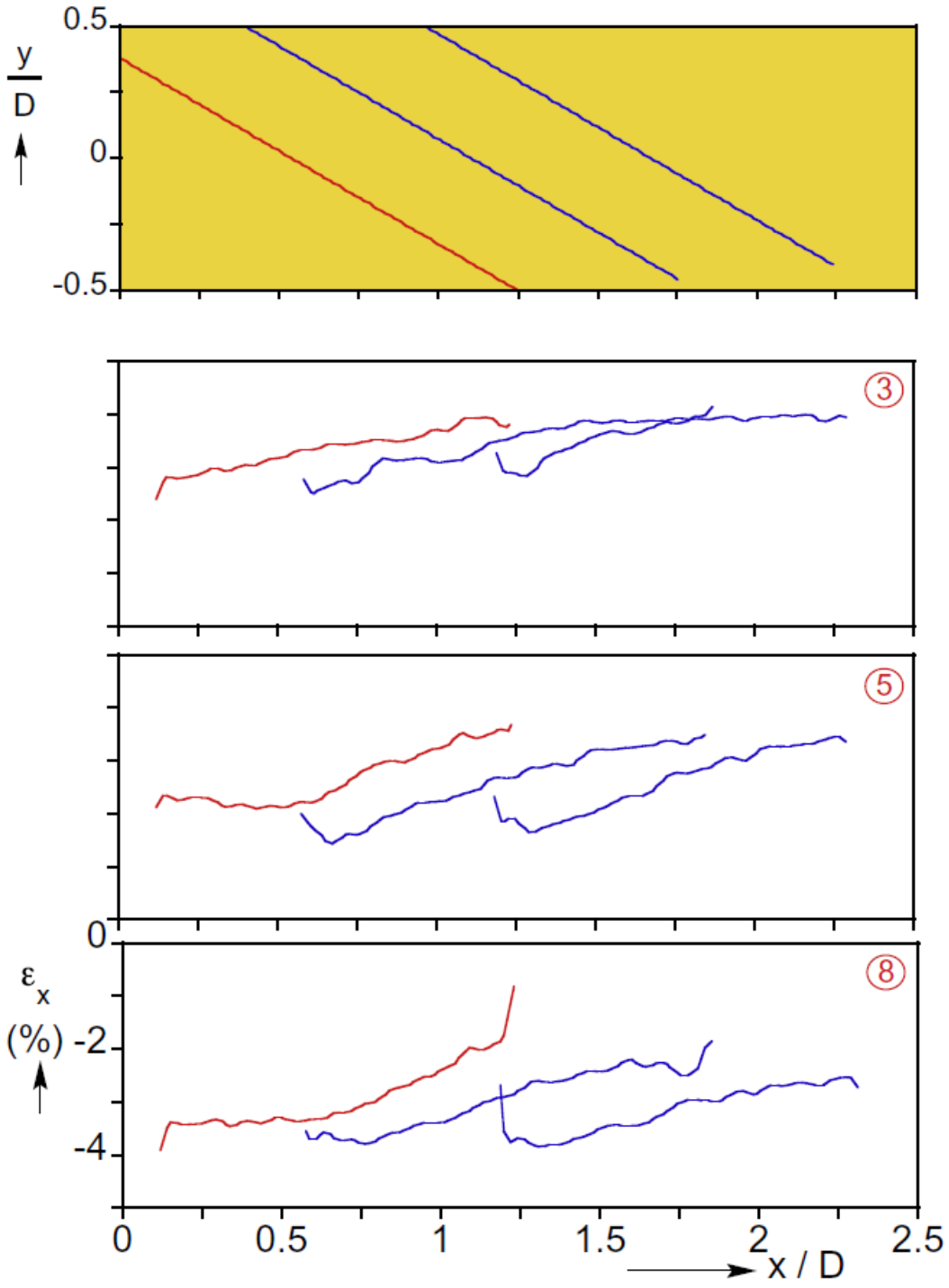

Fig. 2.11 Axial strain variation along three lines inclined at 35° to the tube axis corresponding to contours ③, ⑤, and ⑧ in Fig. 2.8. .

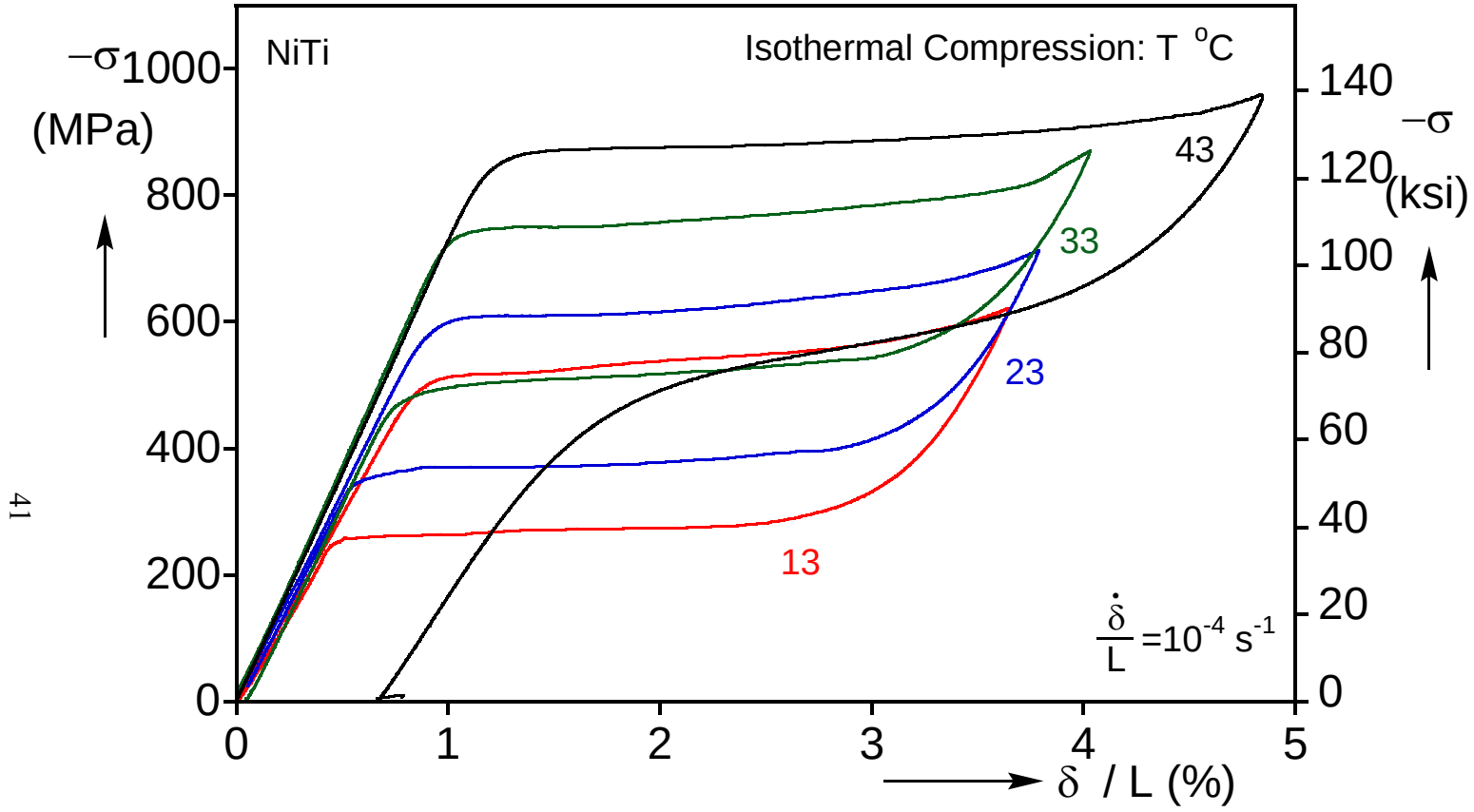

Fig. 2.12 Compressive stress-displacement responses of NiTi tubes at 13, 23, 33, and 43 °C.

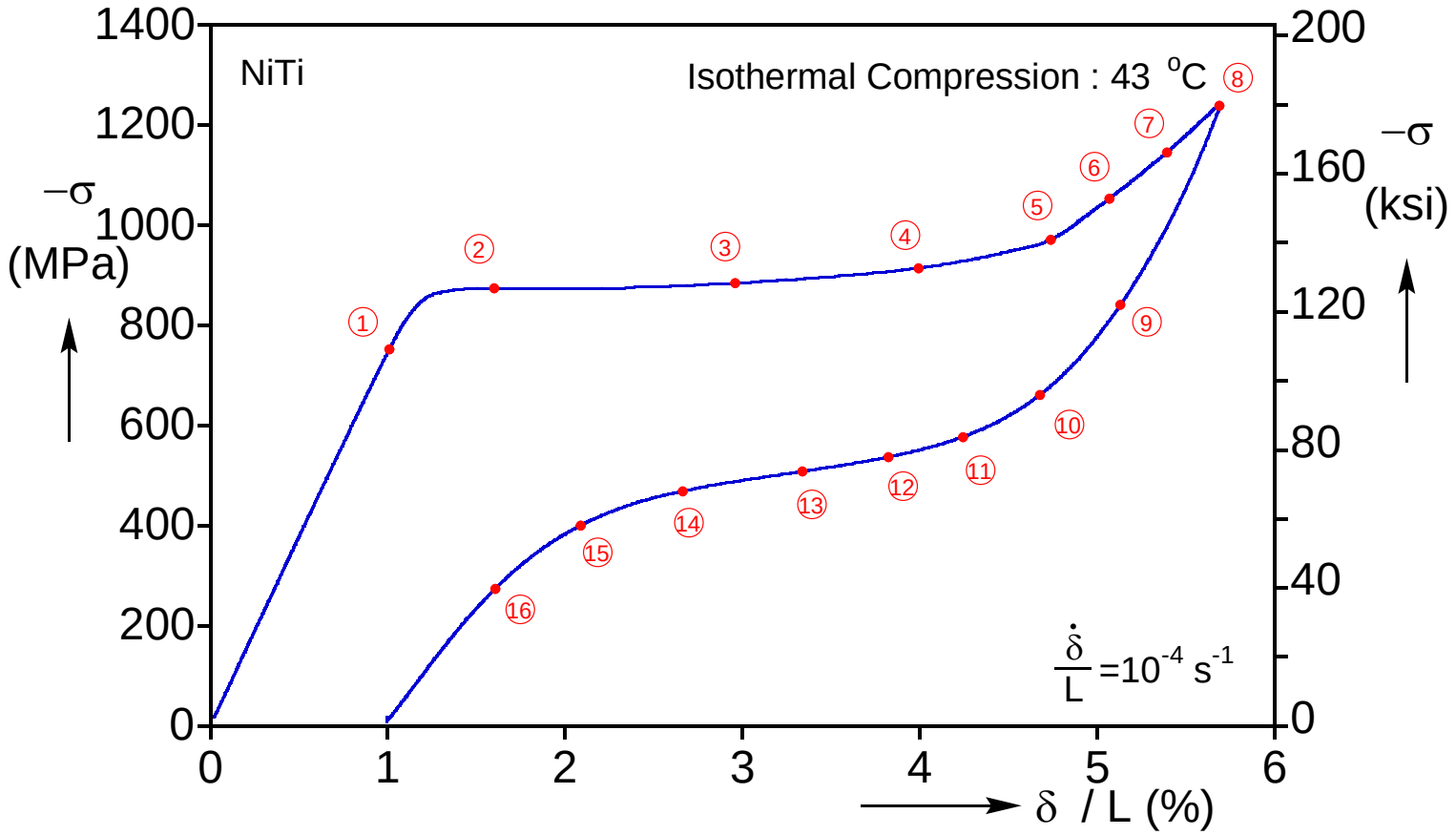

(a)

Fig. 2.13a (a) Compressive stress-displacement response of a NiTi tube at 43 °C.

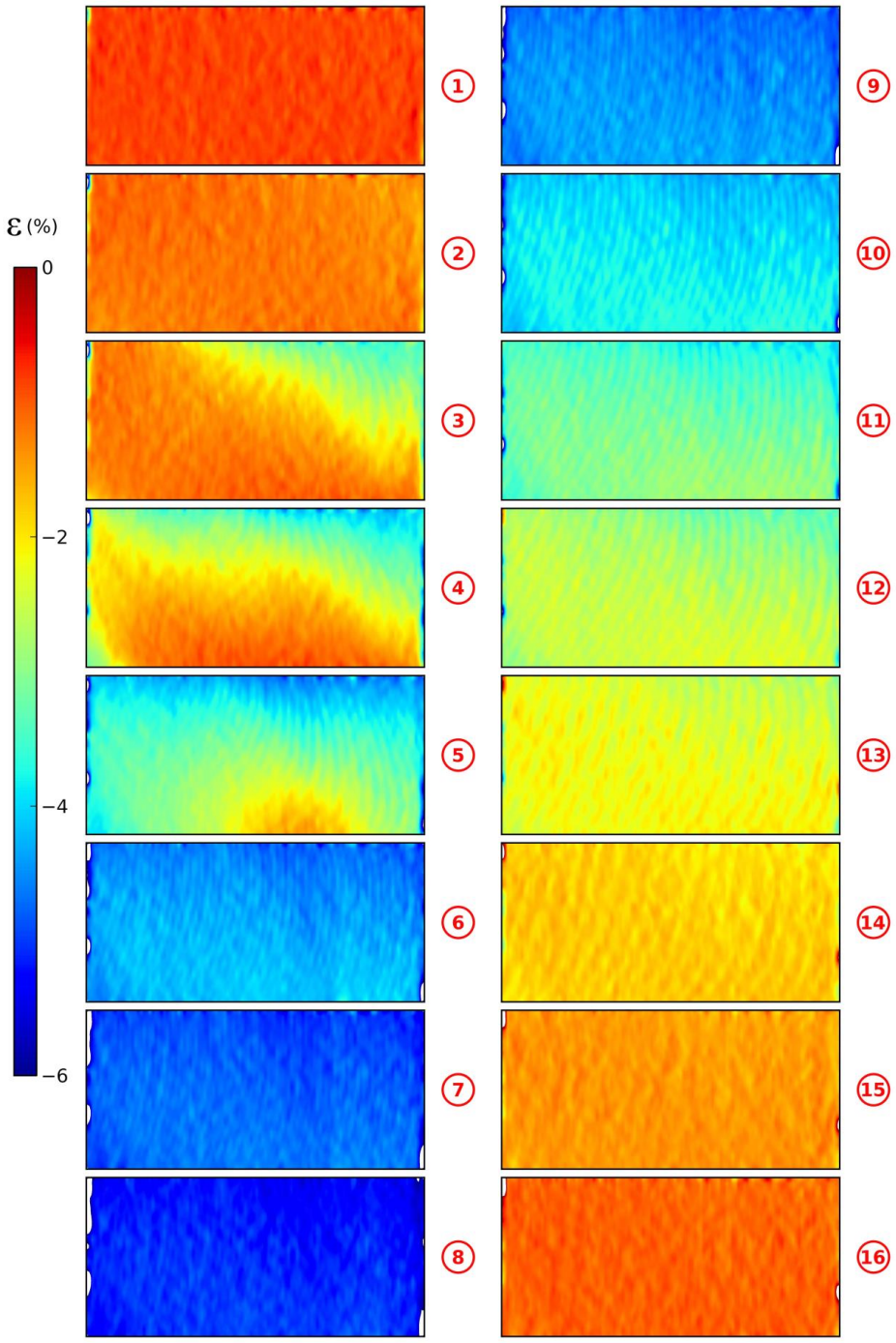

(b)

Fig. 2.13b (b) Set of axial strain contours from DIC corresponding to the numbered bullets marked on the response in 2.8a.

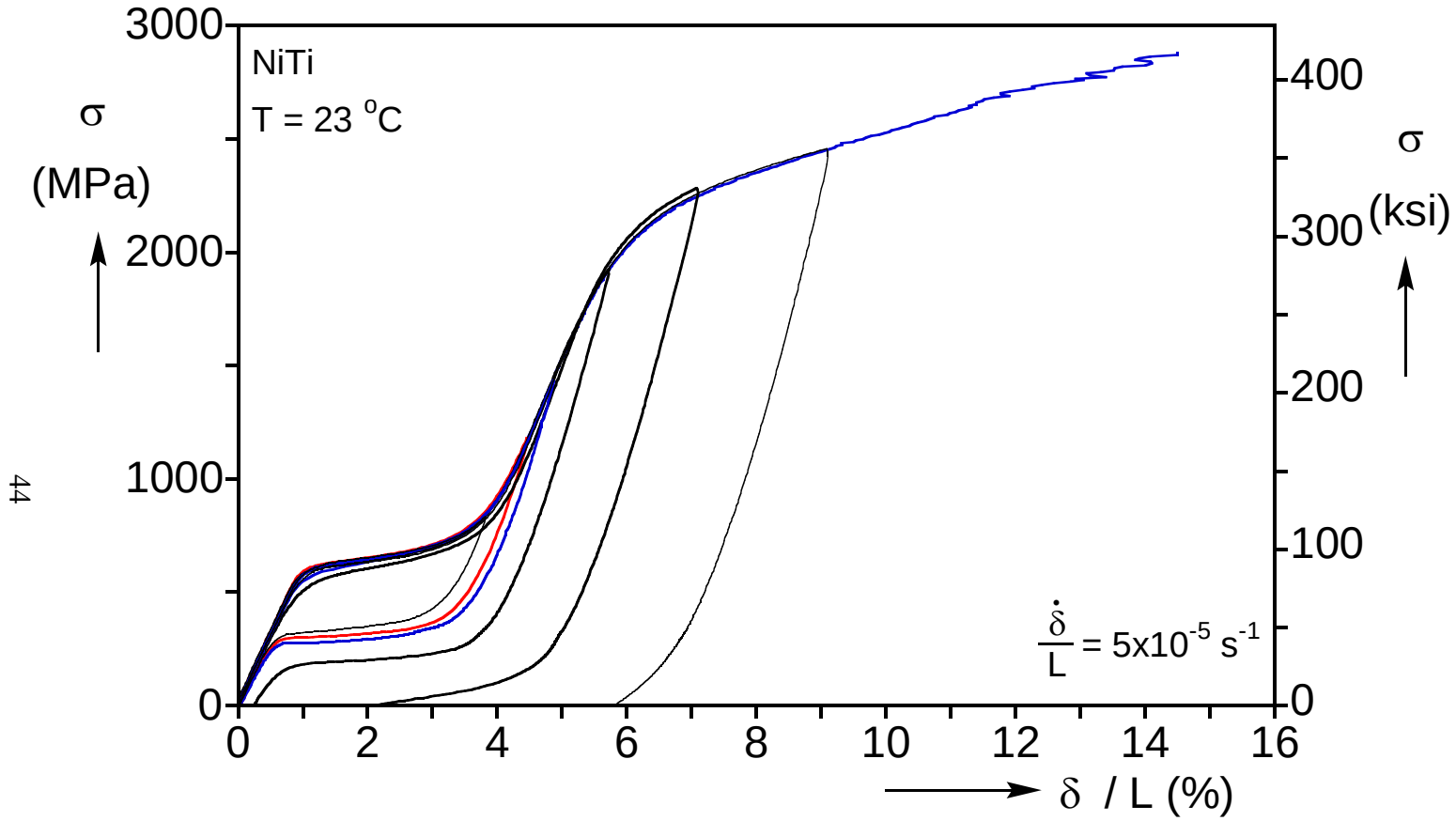

Fig. 2.14 Compressive stress-displacement responses of NiTi rod at 23 °C.

Chapter 3: NiTi STRUCTURAL RESPONSES[2] [3]

During the past 15 years, although the inhomogeneous nature of the A↔M phase transformations associated with pseudoelasticity has been well documented by several researchers (e.g., Shaw and Kyriakides [1995, 1997], Li and Sun [2002], Sun and Li [2002], Feng and Sun [2006], Favier et al. [2007]), the effect on SMA structures remains, by and large, elusive. Parallel work on steel structures that exhibit Lüders banding has revealed that the localized deformation associated with it leads to complex interactions with structural instabilities (e.g., Corona et al. [2002]; Aguirre et al. [2004]; Kyriakides et al. [2008]). For example, in the case of bending of tubes that exhibit Lüders bands this interaction can lead to premature collapse (Hallai and Kyriakides [2011a, 2011b]). Even though Lüders banding is a dislocation driven material instability, its macroscopic effect is inhomogeneous deformation over a certain strain range. Despite obvious micromechanical differences between the phase transformations that govern SMA behavior and the Lüders banding phenomenon, the macroscopic effect, for example in a tensile test, is indeed very similar (Hallai and Kyriakides [2013]). In view of these similarities, in this chapter we aim to understand the effect of inhomogeneous deformations associated with phase transformations on the response of two simple NiTi structures, the pure bending of a tube and the axial compression of a cylindrical shell.

---

[2] Bechle, N.J., Kyriakides, S. (2014). Localization in NiTi tubes under bending. *Int'l J. Solids Struct*. **51**, 967-980. (Designed and performed experiments, analyzed data, and wrote the paper)

[3] Jiang, D., Bechle, N.J., Landis, C.M., Kyriakides, S. (2016). Buckling and recovery of NiTi tubes under axial compression. *Int'l J. Solids & Struct.* **80**, 52-63. (Designed and performed experiments, analyzed experimental data, and wrote experimental section)

3.1 PURE BENDING OF NiTi TUBES

Bending of NiTi tubes in the pseudoelastic temperature regime is complicated by the inherent phase transformations and the associated localized deformations. Furthermore, inducing bending strains up to 7% requires significant rotations of the ends. Although several efforts to conduct such bending experiments have been reported in the literature, Berg's experiments (Berg [1995a, 1995b]) on NiTi wires appear to be the primary ones that achieved the bending curvature required to complete the phase transformations. Perhaps because of different objectives to the ones of this investigation, these experiments were performed under moment control. Consequently, the expected moment plateaus and the associated events could not be tracked as the response jumped across the plateaus when the unstable phase transformations initiated. In addition, since the loading rate was not controlled, latent heat effects may have influenced the results recorded.

3.1.1 Bending Facility

The main interest of the present study is the investigation of the effect of localized deformation associated with phase transformations on the response of SMA tubes at pseudoelastic temperatures under pure bending. Thus, the first task was to design a rotation-controlled pure bending device in which NiTi tubes similar to the ones analyzed under tension and compression (Chapter 2) could be bent under isothermal conditions.

(a) Design Requirements

The custom-built miniature four-point bending device developed for this purpose is shown in Fig. 3.1 (see also Fig. B1 and Appendix B for more details of the bending device). The design was influenced by larger scale bending machines in our labs and adapted to the needs of SMA materials such as the relatively large rotations required to

induce strains of more than 7% (e.g., see Corona and Kyriakides [1988], Hallai and Kyriakides [2011a], and an earlier version of a miniature bending device in Nacker [2009]). The machine has a moment capacity of 25.4 N-m (225 in-lb) and can accommodate specimen end rotations up to 70° (for a 5 mm (0.2 in) diameter, 76 mm (3 in) long rod translates to a radius of curvature of 31 mm (1.25 in) and a max bending strain of 8%). Bending experiments were to be conducted isothermally, thus the device needed the capability of operating at very slow rates and/or incorporating a fluid temperature control system. Because of the expected bending-induced instabilities, the bending device was designed as a relatively "stiff machine" where the energy stored in the machine is always a small fraction of that stored in the test specimen.

(b) Stepper Motor

Motion for the device is supplied by a Pacific Scientific T23NRLC-LNN-NS-00 stepper motor. The motor has a 1.8° step resolution and is powered by a Danaher Motion P70360-SDN drive. The drive connection is the National Instruments UMI-772 Universal Motion Interface, and the motion was controlled using NI Motion Assistant software integrated into LabVIEW. The stepper motor rate is chosen such that the extreme fiber strain rate of the specimen is 10^{-4} s^{-1} for uniform curvature bending by accounting for the gear ratio, pitch of the ACME power screws, hub sprocket dimensions, and specimen dimensions. The stepper motor drive shaft is geared up to the "turnbuckle" as shown in Fig. B2.

(c) Turnbuckle Assembly

The device is comprised of two free-spinning hub sprockets mounted on a stiff support structure 165 mm (6.5 in) apart. Two steel roller chains that wrap around and

terminate on the sprockets are connected to ACME threaded rods, which through a "turnbuckle" transforms rotary motion to linear motion (Fig. B2). The stepper motor shaft engages the turnbuckle through two spur gears with a ratio of 5. A spur gear is bolted to a steel flange which is welded to the left end of the turnbuckle cylinder. The turnbuckle cylinder is mounted in a housing through two press-fit ball bearings that allow free rotation. The turnbuckle cylinder has a right- and a left-hand threaded ACME nut connected at each end. Correspondingly, the threaded rods, whose rotation is prevented, run in each nut so that rotation of the turnbuckle causes them to either contract or extend equally, and in the process either pull or release the chains. The chains wrap around idler sprockets and terminate at the hub sprocket assembly.

(d) Hub Sprocket Assembly

The NiTi tubular specimen, typically 114 mm (4.5 in) long, is snug fit and bonded into 9.53 mm (0.375 in) diameter case-hardened and ground finished extension tubes leaving a test section 76 mm (3.0 in) long. The extension tubes in turn engage two low-friction Pacific Bearing Company FL06 Polytetrafluoroethylene (PTFE) linear bearings anchored to pillow blocks on each sprocket as shown in Fig. B3 and B4. Rotation of the sprockets induces couples to the extension tubes and pure bending to the specimen. The linear bearings allow the inward axial motion of the extension tubes that is required for the large curvatures to which the specimen is bent.

(e) Transducers

In-line miniature Sensotec Model 31 load cells measure the tension in the chains, which is proportional to the moment applied to the specimen. See Figure B5 for the calibration of the load cells. The rotation of each hub sprocket is monitored with a

Shaevitz R30D rotary transducer (RVDT) connected to the rear of the shafts on which they ride. See Figure B6 for the calibration of the RVDT's. The load cell and RVDT transducers were powered, amplified, and balanced with dedicated signal conditioning hardware.

(f) Circulating Bath

As in the tension and compression mechanical tests from Chapter 2 conducted on the same NiTi tubes, the bending experiments are performed under isothermal conditions. This is achieved by passing constant temperature water (or glycol) through the tubes. To this end, flexible rubber hoses connected to the extension tubes and a temperature controlled circulating bath form a closed loop as shown in Fig. 3.2. The liquid flow rate is selected so as to keep the specimen at essentially constant temperature. This was confirmed with an infrared camera.

(g) Data Acquisition and Control

The data acquisition and control systems of the experiment are shown schematically in Fig. 3.2. A LabVIEW-based data acquisition system is used for real-time monitoring and storing of the signals from the four machine transducers. A FLIR ThermoVision SC6000 infrared camera running at 30 frames/min is used to record full-field temperature profiles of the deforming specimen. The camera is operated from a laptop that runs FLIR ExaminIR software. To aid with infrared contrast, a flat chamber connected to a second temperature controlled circulating bath is placed behind the specimen. This background chamber is typically kept at +/- 2 °C from the specimen testing temperature. A high-resolution DSLR camera (4288×2848 pixels) operated by a

timer that runs on the same laptop as ExaminIR takes full-field images of the deforming tube at a rate of 30 frames/min.

A FLIR ThermoVision SC6000 infrared camera is used to record full-field temperature profiles of the transforming specimen. The camera is connected to a 50 mm focal length lens with a 18.3°×14.7° angle field of view for all experiments. The infrared detector is capable of being operated in near infrared sensor assembly (NIR) – using an indium gallium arsenide array for a spectral range of 0.9-1.7 μm, mid-wavelength sensor assembly (MWIR) – using an indium antimonide array for 3-5 μm, or long-wavelength infrared sensor assembly (LWIR) – using a quantum well infrared photodetector array for 8-9.2 μm. The LWIR sensor array is used for room temperature fluctuation radiation levels. A factory preset calibration for the LWIR setting in a -10 to 50 °C temperature range is used for all experiments. The pre-test experimental procedure consists of: a cool-down period of approximately 15 minutes to allow the sensor array to reach temperatures of about 70 Kelvin, the initialization of the factory calibration, and sensor balancing using a black anodized aluminum plate (emissivity of 0.95) as an external constant temperature source. Specimens were coated with flat white and black paint providing an emissivity of 0.92-0.94.

FLIR ExaminIR software is used to operate the camera through Gigabit Ethernet communication. The 14-bit digital data transfer capacity of the camera is 50 MHz which permits frame rates up to 126 Hz at the full resolution of 640×512 pixels, with higher frame rates requiring windowing. High speed is not necessary for the present experiments, thus frame rates are on the order of 30 frames/min with full pixel resolution. ExaminIR captures and stores the digital infrared data, which is then exported as a CSV format for post-processing.

3.1.2 Isothermal Bending at 23 °C

An isothermal experiment at 23 °C is now used to illustrate the main features of the behavior of the NiTi tubes studied under pure bending. Figure 3.3 shows the measured moment-end rotation response ($M/M_o - \bar{\theta}/L\kappa_o$) and Fig. 3.4 a photographic sequence of twenty configurations showing the evolution of bending in the tube. Here $\bar{\theta}$ is the average of the rotations of the two sprockets and the normalizing variables are defined as follows:

$$M_o = \sigma_{PM} D_o^2 t, \quad \kappa_o = 2\varepsilon_o D \tag{3.1}$$

where σ_{PM} is the stress of the upper plateau and ε_o is the strain at the start of M transformation in tension at this temperature (see Fig. 2.8), and $2L$ is the length of the test section ($D_o = D - t$, see Table 3.1). Initially, the material is in the A phase, the response is stiff, and the tube bends with a constant curvature as illustrated in image ①. At a curvature of about $1.2\kappa_o$ and a moment of about $1.1M_o$, the bending stiffness starts to decrease. The bending stress has reached a level that causes transformation and M starts to nucleate in the specimen. When the curvature reaches about $1.6\kappa_o$, the moment starts tracing a somewhat ragged plateau at a level of about $1.2M_o$ that lasts until a normalized rotation of about 6. In this setup the clamped ends provide sufficient stress concentration to cause M to nucleate at or near the ends and in this case M nucleated first on the LHS. It is worth observing that, because of the material asymmetry, the curvature at the onset of the moment knee corresponds to extreme fiber strains that exceed those observed in uniaxial tension.

The thermomechanical processing of the tube left behind a thin layer of a brittle black oxide that shatters at some strain and in the process provides a means of visualizing the localized deformation patterns. Nucleation takes the form of local bands inclined to

the axis of the tube analogous to the fingered patterns observed in tension (Chapter 2) and very similar to the ones reported in bending experiments on steel tubes with Lüders bands (e.g., see Fig. 9 Aguirre et al. [2004]; Fig. 17 Hallai and Kyriakides [2011a]). A difference from Lüders banding in bent tubes is that for NiTi they appear only on the tensioned side. Here the first such bands develop close to the LHS end in the neighborhood of ② at $1.6\kappa_o$. As deformation progresses, the bands tend to organize themselves into diamond-shaped pockets that can be seen on the tensioned sides of images ③ to ⑩ in Fig. 3.4. The diamond patterns can be seen more clearly in three expanded and truncated images of the bent tube in Fig. 3.5. On closer inspection, one can observe that in image ⑤ transformation propagated to the right of the three full diamonds via inclined bands while in image ⑥ a fourth full diamond has emerged. Such diamond patterns on NiTi tubes were first observed in bending experiments by Nacker [2009]. Figure 3.6 shows a photograph of one of his specimens after unloading with a full complement of such patterns from Nacker [2009].

The surface temperature of the tube was monitored and recorded using infrared thermography throughout the bending history at a rate of 30 frames/min. The record in Fig. 3.7 shows the temperature to remain essentially constant very close to 23 °C for the duration of the experiment. However, local temperature spikes (valleys) of the order of 1 °C at the sites where M (A) nucleates (see image ④) and at the main propagating transformation fronts such as those in Figs. 3.5 and 3.6 were observed. In other words, the record confirms the evolution of local deformation in the specimen, but also that local nucleation of M (or A) occurs at other sites during the moment plateaus but does not spread.

Accompanying the local deformation is Brazier ovalization [1927] and possibly wrinkling of the wall of the tube. The combination of the three leads to localization of curvature that is first seen in image ③ and more prominently in ④ and beyond. To quantify the variation of curvature along the length of the tube, the top and bottom edges were tracked using a grayscale threshold image processing scheme as shown in Fig. 3.8. This scheme was used to establish the slope $\theta(s)$ along the length of the tube. Figure 3.9a shows a set of plots of $\theta(s)$ corresponding to a select number of deformed configurations from Fig. 3.4 (based on the top edge). Remembering the relationship for curvature, $\kappa = d\theta/ds$, the slope trajectories clearly show the coexistence of two curvature regimes: a larger curvature in the main transformed region(s), and a lower curvature elsewhere. The smaller curvature approximately corresponds to the value at the beginning of the moment plateau in Fig. 3.3 (~1.5 κ_o) and the larger one to the curvature at the completion of transformation (~7 κ_o). These curvature values remain essentially constant while the specimen response traverses the upper moment plateau.

Up to image ⑤ deformation is mainly concentrated in the left half of the specimen and in the process nearly 40% of the span has been bent to the larger curvature (see ⑤ in Fig. 3.9a). In the neighborhood of image ⑤, localized deformation initiates close to the right end developing a similar diamond pattern. This new zone of transformation, in turn, propagates towards the center of the specimen as can be seen in ⑥. Thus the slope contour corresponding to ⑦ is seen to have developed two higher slope (and curvature) sections at the ends connected with a low slope section near the center. Throughout this non-homogeneous deformation regime, the low and high curvatures are smoothly joined by transition sections that are of the order of 2D long, where transformation takes place. Continued rotation causes both high curvature regimes to propagate towards the center.

In image ⑧, close to the end of the moment plateau, a section in the center of the specimen remains at the lower curvature.

Beyond this point the moment starts to rise. Estimates of the strain indicate that the A→M transformation in tension must be close to completion and consequently the observed upswing in the moment is expected. However, the end rotations have reached very high values contributing to an increase in the friction in the four linear bearings in which the end tubes slide (see Fig. 3.1). While the structural response appears as expected, despite our efforts to correct for friction (see Appendix C) this is a nonlinear effect that we could not fully account for; thus the reported moment at the highest levels of rotation may have some error. Furthermore, using the whole set of diagnostics at our disposal, we can report that some transformation is taking place beyond point ⑨. By point ⑩, the whole specimen is uniformly bent (see Fig. 3.9a) and the diamond patterns have now consumed the whole tube. Soon thereafter the specimen is unloaded.

Unloading is achieved by reversing the direction of rotation of the stepper motor, which flips the direction of translation of the tubes inside the linear bearings. The latter reverses the direction of the frictional force on the extension tubes and results in the sudden dynamic drop in moment that can be seen in Fig. 3.3. Subsequently, the specimen unloads with a gradually decreasing stiffness and uniform curvature (images ⑪ - ⑬). At a curvature of about $5.5\,\kappa_o$ and a moment of $0.65\,M_o$ the stiffness has become very small indicating that M→A transformation has commenced. The resultant localization follows in a nearly reverse order from that followed during loading. A first nucleates near the center of the specimen where the stress is lower (remember that the ends have a higher stress due to the constraints offered by the extension tubes). This local transformation results in lower local curvature that can be seen in image ⑮ and in the corresponding

slope trajectory in Fig. 3.9b. Continued unloading causes an outward expansion of the lower curvature zone as illustrated in image ⑯ and the corresponding slope trajectory. As this takes place, the moment hovers at about $0.59\,M_o$ while the smaller curvature is at about $1.29\,\kappa_o$ and the larger one at $5.2\,\kappa_o$; these curvature values correspond approximately to those at the end and beginning of the lower moment plateau (~ points ⑲ and ⑭). Beyond point ⑲ the specimen returns to uniform curvature that is maintained until the moment is zero. The last unloading is along the same linear trajectory as the one followed during loading, and the hysteresis closes fully, an indication that the material was not strained beyond its pseudoelastic regime.

To visualize the localization patterns, a separate experiment was performed on the same tube stock at the same temperature, in which the specimen was additionally speckled for DIC measurements. This allows monitoring of the evolution of such diamond deformation patterns (T3-B-07 in Table 3.1) using digital image correlation (DIC). For this purpose, a fine speckle pattern was deposited on the undeformed SMA tube. The in-plane deformation of the specimen surface was captured with a digital camera (4288×2848 pixels) at 2 s intervals. Bending was conducted again isothermally at 23 °C at the same rate with the moment-rotation response shown in Fig. 3.10. Figure 3.11 shows two sequences of deformed images with superimposed axial strain contours generated from the record using ARAMIS, with numbered bullets corresponding to the Fig. 3.10. Localization again initiated on the LHS and is depicted in image ① as a single diamond on the tensioned side, with a strain level of the order of that at the termination of the upper stress plateau in tension. In the region of the specimen that has localized deformation, a higher compressive strain is observed on the outer fibers at the bottom due to the localization of curvature. In images ④ and ⑤, the diamond patterns have

propagated towards the mid-span of the tube, and similar ones have started developing on the RHS. The corresponding higher compressive strains remain limited to the outer fibers in regions of the tube where tension localization is observed. In image ⑥, the higher curvature regime has spread further and the overall deformation now appears balanced between the left and right sides with a central section remaining in the lower curvature regime and uniform strain across the length. Beyond image ⑦, the moment takes an upswing and in image ⑧ the whole length of the tube is seen to be deformed to the higher curvature. The top surface is covered by the diamond patterns while the bottom is in nearly uniform compression.

To visualize the non-planar nature of the deformation across the specimen depth, three strain profiles along sections are shown in Fig. 3.12 (correspond to image ⑧ from Fig. 3.11). The compressive strain along all three profiles is linearly varying. However, section 1, which corresponds to the center of the diamond pattern, exhibits a sharp change in strain at the apex of the transformation front. Section 2 remains nearly linear through most of the cross-section, but a sharp change in strain occurs again at the interface. In section 3, located between two diamond patterns, the effect of the interface does not occur until nearly the top edge of the specimen.

Returning to Fig. 3.11, it is also interesting to observe that some material at the inner fibers have negligible strain. Some fluctuation in the compressive strain is observed along the length. It is worth mentioning that similar diamond patterns were recently reported in Reedlunn et al. [2014] from bending experiments on similar NiTi tubes (e.g., see Fig. 11). What was not reported is the localization of curvature reported here, presumably because the relatively small slenderness ratio of their specimens suppressed it.

Overall, the diamond deformation patterns are very similar to the ones seen in calculated bending configurations with superimposed strain contours in Hallai and Kyriakides [2011b] in their modeling of bending of tubes with Lüders bands. The difference with NiTi is that the patterns only develop on the tensioned side.

Similar isothermal bending experiments were performed at three additional temperatures, 13, 33, and 43 °C, in which the same experimental procedure was followed and the same imagery was recorded. The moment-rotation responses recorded appear in Fig. 3.13 together with the one from 23 °C discussed above. For a more clear interpretation of the results, the moments and rotations are normalized by the variables M_{o23} and κ_{o23} in (2.1) respectively based on $\sigma_{PM}(23^{\circ})$ and $\varepsilon_o(23^{\circ})$ (Fig. 2.8). All cases exhibit an initial linear branch during which deformation is homogeneous and the tubes bend uniformly. The linear branches terminate into knees associated with the onset of transformation to M. The moment at the knees exhibits the same dependence on temperature as transformation stress in tension, $\sigma_{PM}(T)$ (the knee for 13 °C is somewhat lower). Subsequently, the moments trace relatively flat plateaus during which two curvature regimes co-exist: one that corresponds to the value at the onset of transformation and a second near its termination. The extent of the moment plateaus is nearly independent of temperature reaching a normalized rotation of about 6. With the termination of the moment plateaus, the tubes return to uniform curvature. A jump in moment was recoded upon unloading in all cases due to friction in the bearings. Initially, the unloading exhibits uniform curvature until reverse transformation commences. Moment plateaus are again traced indicating inhomogeneous bending. Three of the plateaus now follow the temperature dependence of the reverse transformation stress in tension, $\sigma_{PA}(T)$, while the moment corresponding to 13 °C is slightly lower. Three of

the hystereses close, indicating complete pseudoelastic behavior whereas the response at 43 °C unloads with some residual curvature (as was the case for the compression and to some degree the tension tests in Chapter 2).

The moment-end rotation response for an isothermal bending experiment at 43 °C is isolated in Fig. 3.14 with corresponding bending configurations in Fig. 3.15. During loading, transformation induces localization as the moment traces a nearly constant plateau indicative of inhomogeneous deformation, confirmed in the slope profiles in Fig. 3.16a. Interestingly, unloading was essentially monotonic and the tube deformation is uniform as shown in Fig. 3.16b.

3.1.3 Thin Walled Bending Experiments

In completing the section on bending the following comment is worth making. In the present experiments, the main structural effect of localized deformation induced by transformation reported was localization of curvature that was transient and recoverable. However, bending of tubes is also accompanied by ovalization and wrinkling. Both of these can lead to local buckling in the form of inward kinks on the compressed side of the tube. The NiTi tubes used in the experiments of the preceding section had diameter-to-thickness ratios (D/t) of about 8.25. This low value limited the extents of both ovalization and wrinkling despite the high curvature induced by the phase transformation. Higher D/t NiTi tubes under bending will experience much higher values of ovalization and wrinkling and consequently more prone to structural instabilities (see Hallai and Kyriakides, [2011a, 2011b]). The D/t dependence of such potential instabilities is worth further investigation.

To this end, NiTi tubes with a nominal D/t of 19 were subjected to bending using the same experimental facilities. The tubes were nearly equiatomic (50.86 at % Ni) NiTi

tubes with A_s = 2.6 °C and A_f = 28.3 °C established from DSC using a similar procedure that outlined in Chapter 2 (see Fig. 3.17). The tube stock used had a nominal diameter of 5.13 mm (0.202 in) and a wall thickness 0.254 mm (0.010 in). Tubes were used in the as-received condition (hot rolled, cold drawn, and centerless ground) supplied by Memry Corp specified with the BB alloy (PN: 10603, LN: DM-8936, IN: C7-9762).

Bending was conducted again isothermally at 23 °C with the moment-rotation response shown in Fig. 3.18. Figure 3.19 shows a sequence of deformed images with numbered bullets corresponding to those in Fig. 3.18. Localization again initiated on the LHS as the response traverses a nearly constant moment plateau. In this case, the thinner walled tube begins to ovalize, which leads to the formation and growth of a dimple on the compressed side (image ②). Further deformation beyond this point amplifies the dimple, as can be seen in images ②-④, which leads to an abrupt collapse of the specimen. The collapsed section folds, forming sharp edges which lead to failure. Image ⑤ shows the fractures along the front and back faces. Interestingly, the remainder of the specimen abruptly unloads and returns to the original, straight configuration. Upon unloading, despite collapse and fracture, the specimen provides springs back to the undeformed structural configuration, albeit with partial fractures at the LHS. Figure 3.20 shows isothermal bending experiments at 3, 13, and 23 °C on the same thinner walled tube stock. In all three cases, the specimen failed in a similar manner to the one described above.

3.2 Axial Compression of NiTi Tubes

This study is aimed at the exploitation of the unique behavior of NiTi in novel structural applications and particularly on the interaction of these material nonlinearities with structural nonlinearities. Motivated by energy absorption applications, Nemat-

Nasser et al. [2006] conducted exploratory experiments on buckling and recovery of SMA shells under quasi-static axial compression and impact (see also similar recent results in Tang and Li [2012]). The buckling and postbuckling responses of NiTi shells with a diameter-to-thickness ratio (D/t) of 36 in the pseudoelastic and shape memory temperature regimes were recorded. The former shells developed what appears to be a mode-2 shell-type buckling that recovered upon unloading. The latter shells buckled in a similar mode but did not recover significantly upon unloading. Recovery occurred when the temperature was increased to above the transformation temperature. This work revisits the axially loaded tube/shell buckling problem with the objective to use careful, accurate experiments on NiTi tubes to better understand and quantify the interaction of the pseudoelastic material response with shell buckling and postbuckling nonlinearities.

The buckling experiments are performed on nearly equiatomic (50.86 % Ni) NiTi tubes. The following transformation temperatures were established for the material using DSC as outlined in Chapter 2: A_s = -9.6 °C and A_f = 12.1 °C (See Fig. 3.21). Tubes were used in the as-received condition (hot rolled, cold drawn, and centerless ground) supplied by Memry Corp specified with the BB alloy (PN: 10603, LN: DM-9467, IN: C7-9762). Specimens were extracted from a NiTi tubular stock with specified outer diameter of 6.35 mm (0.25 in) and a wall thickness of approximately 0.25 mm (0.010 in)–the exact dimensions of the specimens are listed in Table 3.2 ($\Xi_0 \equiv$ wall eccentricity).

The mechanical properties of the tubular stock under uniaxial tension and compression were established at 23 °C using the isothermal tensile and compressive test set-ups presented in Chapter 2. The responses are very similar to those previously reported for the same alloy and processing but different dimension tubes. However, the transformation stresses in both tension (σ_{PM}) and compression (σ_{NM}), listed in Table

3.2, are somewhat higher (compare with results in Fig. 2.8). Another difference is that for the present tubes, uniform compression terminates soon after the onset of transformation due to buckling of the specimen—because of the much higher tube *D/t*.

3.2.1 Experimental Setup

Buckling specimens approximately three diameters long $(L \approx 3D)$ were extracted from the tubular stock using a lathe to face them off to ensure parallelity of the ends. The specimens were then compressed between hardened steel platens under displacement control in a screw-type testing machine. The A→M transformation is exothermic, and the reverse is endothermic with the latent heats released/absorbed potentially changing the temperature of the specimen and thus altering the transformation stress (see Fig. 2.8). To limit any such thermomechanical interactions, compression was performed at the very slow rate of $5\times10^{-5}\,\mathrm{s}^{-1}$ when deformation is homogeneous.

Several buckling experiments were performed on specimens of similar dimensions. In some of them the tube was coated with a fine speckle pattern and the deformation over the full length was monitored with 3-D digital image correlation (DIC; 5 MP cameras, images taken every 2 s). Although DIC provides accurate measures of deformations before buckling, its performance in the postbuckling regime is not optimal because the large out-of-plane deformations associated with the buckling mode lead to loss of correlation. Consequently, we have chosen to mainly present results from an experiment in which the buckling deformation was monitored with time-lapse photography using a 12 MP digital camera (4 s frequency). In such experiments, the specimen was coated with a thin layer of non-reflective paint for better visualization.

3.2.2 Buckling and Recovery

The nominal stress-shortening ($\sigma - \delta / L$) response recorded in an experiment with the tube parameters listed in Table 3.2 is shown in Fig. 3.22 (L is the specimen initial length thus δ / L represents the average compressive strain in the tube while deformation is uniform). The response exhibits an initial stiff and nearly linear branch during which the mainly A-phase deforms elastically. A gradual reduction in stiffness starts at approximately 650 MPa, an indication that transformation to M has initiated. Transformation continues at an accelerating rate leading to further reduction in the recorded stiffness, and reaches a maximum at 725 MPa (depicted by a caret "^"). It is noteworthy that the material response in the vicinity of the onset of transformation, drawn in the figure with a dashed line, does not exhibit a visible maximum. We can thus conclude that the maximum in the structural response must be related to structural instability. With continued compression, the stress varies slightly between 723 and 724 MPa followed by a drop in the recorded stress, which is a sign that the structure is starting to collapse. At a normalized displacement of 3.34% the compression is terminated and the specimen is unloaded at the same displacement rate. As expected, the unloading leads to a near closing of the hysteresis, but a small permanent deformation is recorded.

The associated events are best visualized with the help of a sequence of images from the photographic record. Figure 3.23 shows 20 images that correspond to the numbered bullets on the response in Fig. 3.22. Image ① shows the initial unloaded specimen. Image ② corresponds to the beginning of the gradual reduction in stiffness associated with the onset of the M transformation; the specimen appears uniformly deformed. In image ③, close to the end of the local stress plateau that has formed, the first

signs of buckling at the top of the specimen appear. The m = 3 buckling mode becomes more clearly visible in images ④ and ⑤.

It is well established that the first instability of inelastic circular tubes like the present one is axisymmetric wrinkling (see Bardi and Kyriakides [2006]; Bardi et al. [2006] and references therein). The wrinkle amplitude is initially very small but grows with increasing load, in the process reducing the stiffness of the structure (see section 3.2.3). At some stage a non-axisymmetric mode characterized by m circumferential waves becomes preferred leading to localized deformation and collapse of the structure. The average strain difference between the two instabilities depends on the structure D/t and the inelastic tangent modulus of the material. This can also be influenced by initial imperfections. Wrinkling is not visible in the photographic record in Fig. 3.23 perhaps due to its very small amplitude. However, local wrinkles were observed to develop at the ends of similar tubes whose deformation was monitored by 3-D DIC as described in section 3.2.3.

The sequential development of axisymmetric wrinkling and the associated stress plateau followed by shell buckling that leads to collapse is one of several differences with the results of Nemat-Nasser et al. [2006] and Tang and Li [2012]. Furthermore, the assertion that wrinkling is related to the shell L/D is not quite correct as wrinkling precedes shell buckling for all but for very short shells in which boundary effects tend to dominate the behavior. Wrinkling can, of course, be masked by large enough imperfections in geometry, misalignment, and in boundary conditions, any of which may have influenced the behavior observed in the two works. The presence of such imperfections is also supported by the initial nonlinearity observed in several of the

compressive responses reported in these references, and by the generally low maximum stresses achieved.

Returning to the response in Fig. 3.22, in the descending part of the loading response between points ③ and ⑤, a single three-wave buckling mode is seen to be localizing near the top of the specimen. As in all localization problems, beyond point ③ the additional applied displacement feeds the growth of the amplitude of this lobe. This occurs with the load dropping by about 20%, which results in unloading in the rest of the structure. In the neighborhood of point ⑤, the growth in the amplitude of the first lobe slows down, presumably because the local bending strains have reached levels where the material response stiffens again due to the near completion of the M transformation. This causes a second lobe below the first one, rotated by 60°, to begin developing. In images ⑥ to ⑨ the amplitude of the second lobe grows while the stress drops to 495 MPa. It is interesting to observe that beyond point ⑥, the first lobe appears relatively unchanged. At point ⑨, the compression is held for a few minutes to enable observation of the specimen and subsequently unloading is commenced at the same displacement rate.

The apparent arrest of deformation in the first lobe before it is fully collapsed by folding, and the development of a second lobe, and presumably more, is to some degree in contrast with the concertina folding collapse mechanism of elastoplastic shells (see also Nemat-Nasser et al. [2006]). In typical elastoplastic metals, the first lobe tends to fold up causing self-contact of the walls of the shell. The collapse is arrested, the load increases initiating collapse of a second lobe, and the process repeats (see Fig. 3 in Bardi and Kyriakides [2006]). The result is an undulating force-displacement response characteristic of elastoplastic tubular energy absorbers. For a steel or Al-alloy shell with a D/t similar to the one of the NiTi tube in Fig. 3.22, the mean value of the crushing stress

will be significantly lower than the collapse stress. The higher crushing stress and the associated smaller deformation in the SMA shell buckling lobes is ostensibly related to the stiffness recovery of the material following the completion of the A→M transformation. The net effect is a higher energy absorption for SMA shells over that of elastoplastic metal ones with the additional benefit of being reusable.

Unloading from points ⑨ to ⑭ results mainly in a gradual reduction of the amplitude in the lower lobe and to a smaller degree in the upper one. This occurs with a monotonic decrease in the stress, but with a progressively reducing stiffness. Between points ⑭ and ⑰ both lobes gradually straighten out with the lower one essentially vanishing at ⑰. Interestingly, the recorded force develops a local minimum in this neighborhood and then rises to a local maximum just before configuration ⑲. In other words, the final straightening of the top lobe has the potential to snap back; here this occurs in a controlled manner due to the displacement-controlled unloading.

Beyond point ⑲, the specimen has reverted mostly back to the A-phase, so it unloads with approximately the same slope as the initial loading branch of the response. However, the recorded permanent "deformation" of about $0.002L$, indicates that at least part of the structure has undergone some unrecoverable deformation. This is corroborated by the following related observations: (i) visual inspection of the specimen at the end of the experiment revealed small amplitude axial ridges in the upper part of the specimen, corresponding to the extrados of the mode-3 buckling mode; (ii) on reloading the stress reached a maximum value 20% lower than the 725 MPa value as shown with the responses in Fig. 3.24. Furthermore, the local stress plateau of Fig. 3.22 is missing as the mode-3 buckling mode was excited directly, apparently from the residual imperfection left from the first loading cycle.

3.2.3 Axisymmetric Wrinkling

To visualize the evolution of the axisymmetric wrinkling buckling mode, a specimen was coated with a fine speckle pattern to accommodate DIC measurements. The response of the speckled NiTi tube subjected to axial compression under the same experimental conditions as above is shown in Fig. 3.25. A sequence of normalized radial displacement profiles $\left(u_r / R_o\right)$ and corresponding contours computed from 3D DIC are shown in Fig. 3.26 with the numbered bullets as labeled in Fig. 3.25. The onset of transformation results in a significant decrease in the tangent stiffness and a small axisymmetric feature is visible near the top of the specimen in image ①. It should be noted that in all such experiments, the initial axisymmetric wrinkle (and corresponding mode-3 buckle) initiated at either the top or bottom of the specimen due to the constraint associated with the frictional contact between the specimen faces and the steel platens. By image ②, the top axisymmetric wrinkle amplitude has grown and an additional wrinkle becomes visible at the bottom of the specimen. The amplitude of the top wrinkle continues to grow as a second wrinkle appears in the upper section of the specimen in images ③ to ④. By image ④, the second wrinkle at the top is growing in amplitude and beginning to become non-axisymmetric. In this vicinity, the response in Fig. 3.25 experiences a global maximum. Additional wrinkles appear in image ⑤, however, the amplitude of the second wrinkle from the top has increased significantly and is now forming into a non-axisymmetric lobe characteristic of the unstable mode-3 buckle. The response in Fig. 3.25 shortly after this point experiences a significant drop in stress as the specimen collapses in a near identical manner to that reported in Section 3.2.2.

We close this section with the following additional comments:

• Despite the rather stiff nature of our test set-up, the system stiffness influenced to some degree the recorded stress-displacement response. Local measurements of average strain from the DIC experiments were used to estimate the system's influence and the responses shown were appropriately corrected.

• In additional experiments on similar SMA tubes, specimens were compressed further than those presented above. Although a third lobe started developing, at some stage, one of the ridges of a fully formed lobe failed by cracking. For example, first signs of cracking were observed at a displacement of $\delta \approx 0.046L$ for the experiment shown in Fig. 3.27 where the stress is seen to drop suddenly. Consequently, the experiments in Figs. 3.22, 3.24, and 3.25 were terminated well before this level of compression was reached.

3.3 Summary and Conclusions

This chapter reported experimental results that show the interactions between NiTi SMA material nonlinearities with structural behaviors. Results from two structures are reported, a tube under pure bending and a shell under axial compression.

3.3.1 Pure Bending

The response of pseudoelastic NiTi tubes under bending was reported at several temperatures using a custom miniature bending device and diagnostic facilities. The tension/compression asymmetry of NiTi had a corresponding reflection on the bending results. Bending leads to localized nucleation of M. On the tension side this takes the form of deformation bands inclined to the axis of the tube. As bending progresses, the bands coalesce into diamond-shaped pockets with a constant periodicity, similar to ones reported to occur in bending of steel tubes with Lüders bands. By contrast, no localized

deformation patterns were apparent on the compressed side. When a sufficient length of the tube is so transformed, structural localization develops in the form of higher local curvature. Two curvature regimes coexist and with continued end rotation the higher curvature spreads along the length of the tube. While this is taking place, the moment hovers about a nearly constant level. When the higher curvature has spread throughout the length of the tube, most of the material has transformed to M and the tube continues to bend uniformly with a rising moment. Upon unloading, the tube deformation remains uniform until transformation back to A commences. This also leads to localization of curvature that follows a reverse process to that of loading. During the coexistence of two curvature regimes the moment remains again nearly constant. When all material has transformed back to A, the tube returns to uniform curvature and unloads elastically back to the straight configuration.

Bending at other temperatures within the pseudoelastic regime results in similar behavior tracing moment-rotation hystereses with shifted moment plateau levels (higher or lower). It was observed that the moment at the onset of both A and M transformations has a similar temperature dependence as the transformation stresses in tension.

The effect of the phase transformation induced localization on bending of tubes with a higher *D/t* was also investigated using NiTi tubes with a nominal *D/t* of 19. Transformation led to localized diamond deformation patterns and in turn ovalization of the cross-section. At the location of the apex of a diamond pattern, the ovalized cross-section developed a dimple on the compressed side of the specimen. Further deformation amplified the dimple growth eventually resulting in a folding of the cross section and abrupt collapse and failure by fracture. Upon unloading, the specimen returned to the undeformed, straight configuration despite the fractures. Similar dimple growth and

subsequent collapse and failure were observed on isothermal bending experiments at 13, 23, and 33 °C.

3.3.2 Axial Buckling and Recovery

The second problem investigated is the buckling and recovery of pseudoelastic NiTi tubes under compression and the associated energy absorption. Under compression, NiTi tubes with D/t = 23.6 initially deform uniformly following the elastic modulus of the parent A-phase. The reduction in stiffness caused by the material nonlinearity associated with the onset of transformation to the M-phase, leads to the development of initially periodic axisymmetric wrinkles. The wrinkled structure remains stable, but at larger strain levels, wrinkling gives way to a non-axisymmetric buckling mode, in this case characterized by three circumferential waves. This mode is unstable; with the loading decreasing, it localizes first into a single lobe followed progressively by others. In the presented experiments the structure was unloaded following the full development of a second lobe.

While the events described are reminiscent of those associated with plastic buckling of structural metal shells, the pseudoelastic behavior of NiTi resulted in some important differences. Under compression, phase transformation occurs essentially homogeneously, with a nearly monotonically increasing stress. However, transformation terminates at a significantly smaller strain level than tension and is followed by a stiff, saturation-type response that evolves into the linear elastic modulus of the M-phase. This material stiffening has two main effects. First, the growth of the first mode-3 lobe is arrested without it folding up. This triggers localization into a second lobe and potentially more, with the initial growth and subsequent arrest of deformation being repeated in each. Second, this progressive partial collapse of lobes without them folding in the

manner of elastoplastic shells, occurs at a much higher stress level relative to that at the onset of collapse, than in concertina folding of conventional metals.

On unloading, the deformation is recovered in the reverse order to that followed during loading. Reverse transformation occurs at a relatively high stress producing a nearly closed hysteresis, which of course is a feature unique to NiTi SMAs. This recovery and the significant energy absorbed during the load/unload cycle are exciting features of this behavior.

It is worth noting that the tubes used in our experiments developed a small amount of permanent deformation during loading, which resulted in a slightly incomplete closure of the hysteresis. Furthermore, the material was prone to damage that under excessive deformation led to fracture. Both of these issues are thought to be influenced by the thermomechanical processing of the NiTi tubes used and we expect that they could be reduced or alleviated.

Exp. No.	T °C	D mm (in)	t mm (in)	$2L$ mm (in)	σ_{PM} MPa (ksi)	ε_o (%)
T2-B-01	13	5.12 (0.2016)	0.615 (0.0242)	76.2 (3.00)	328 (47.6)	0.690
T3-B-04	23	5.11 (0.2010)	0.625 (0.0246)	76.7 (3.02)	381 (55.2)	0.827
T2-B-05	33	5.12 (0.2016)	0.617 (0.0243)	77.7 (3.06)	435 (63.1)	0.810
T3-B-05	43	5.12 (0.2014)	0.622 (0.0245)	76.5 (3.01)	506 (73.4)	0.755
T3-B-07	23	5.12 (0.2014)	0.622 (0.0245)	77.1 (3.04)	381 (55.2)	0.827

Table 3.1 Geometric and material properties of tubes used in the bending experiments

D mm (in)	t mm (in)	Ξ_o (%)	L mm (in)	T °C	σ_{PM} MPa (ksi)	σ_{NM} MPa (ksi)
6.320 (0.2488)	0.2680 (0.01055)	5.7	19.62 (0.7725)	23	445 (64.5)	-725 (105)

Table 3.2 Compression test specimen parameters

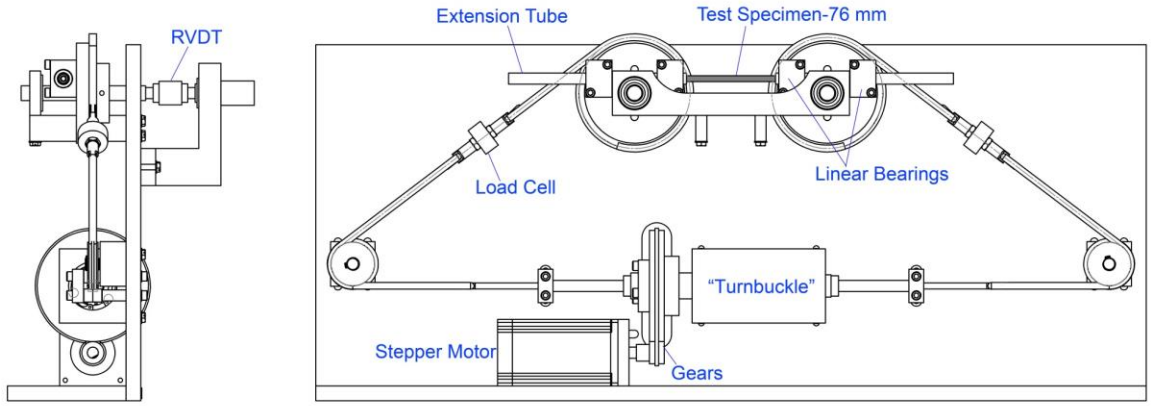

(a)

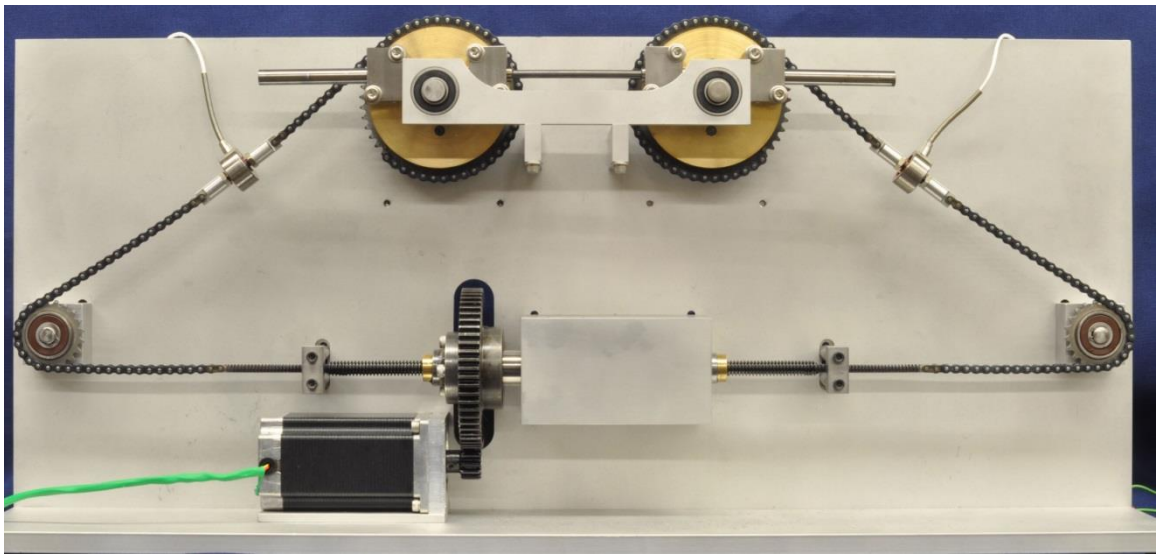

(b)

Fig. 3.1 Custom miniature bending device used to conduct pure bending of NiTi tubes. (a) Scaled drawing and (b) photograph.

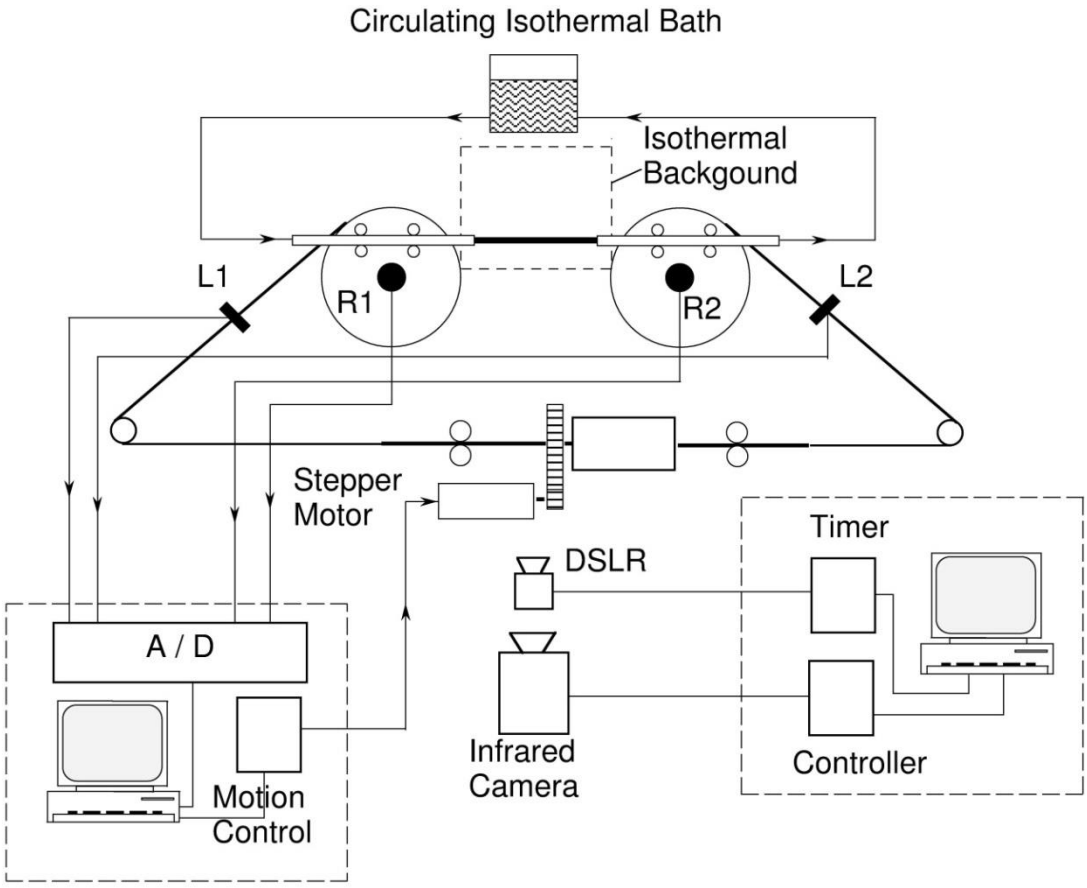

Fig. 3.2 Schematic of data acquisition and control systems as well as the digital and infrared imagery used to conduct isothermal bending experiments on NiTi tubes.

. .

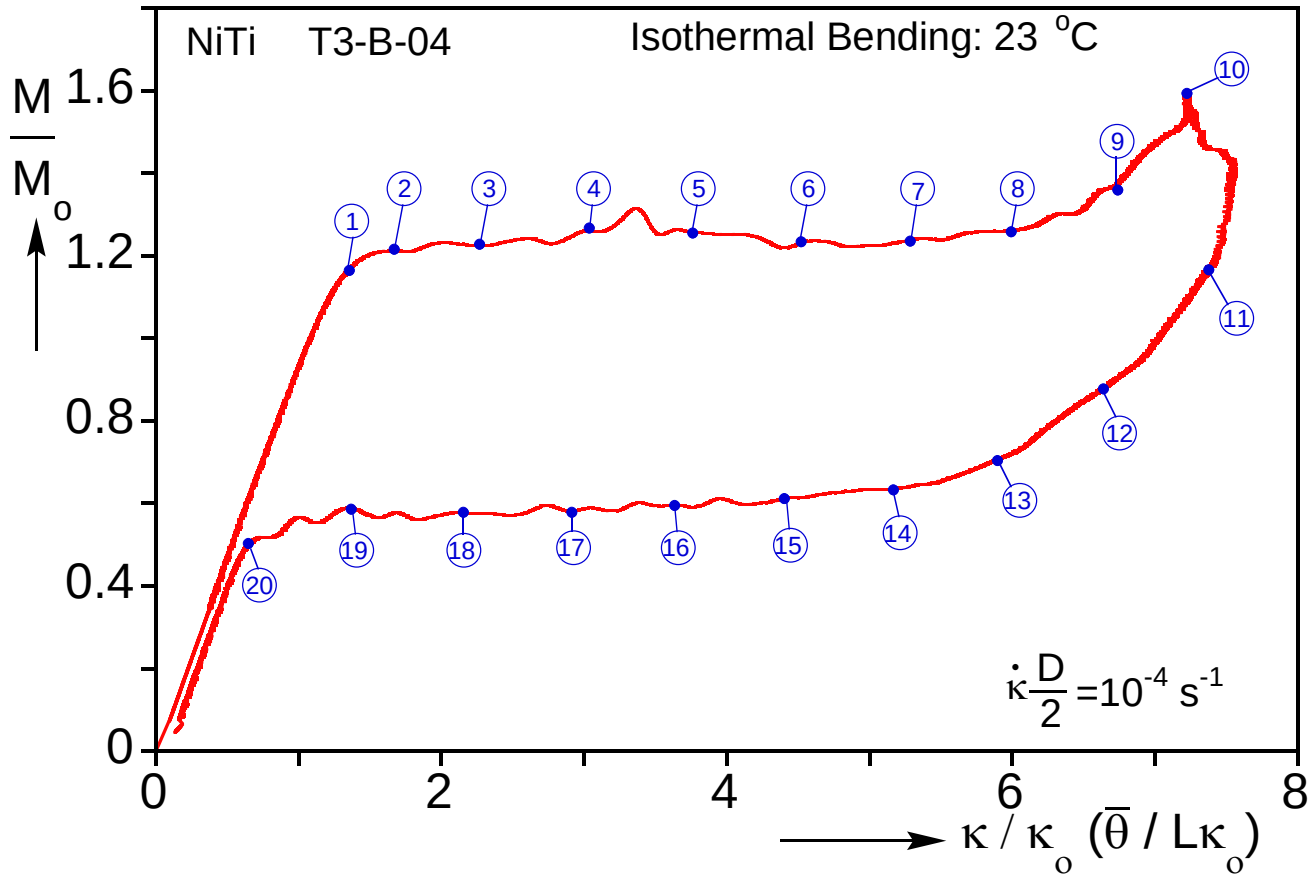

Fig. 3.3 Moment-end rotation response recorded in an isothermal pure bending experiments on a NiTi tube at 23 °C.

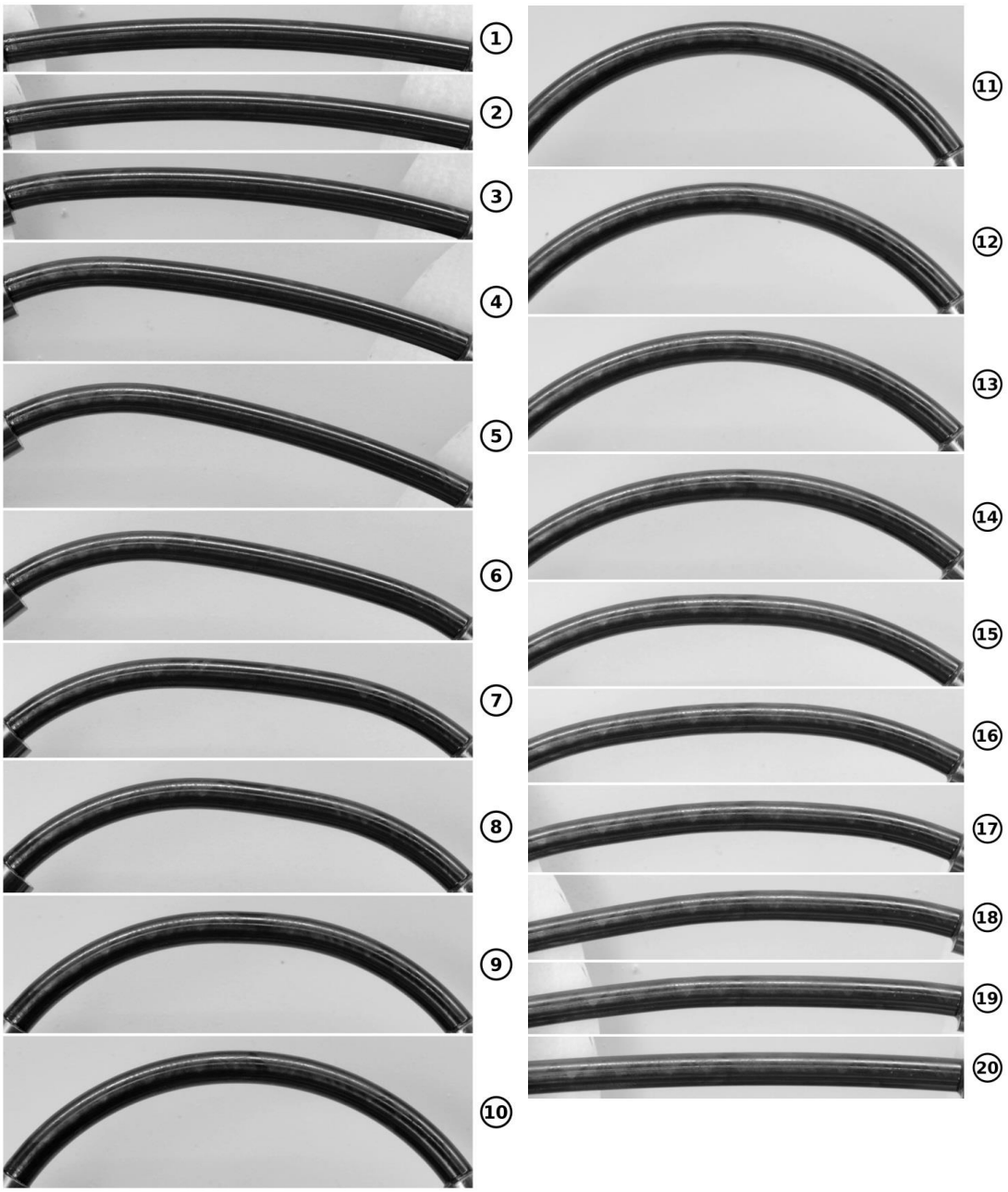

Fig. 3.4 Set of tube bending configurations corresponding to the numbered bullets marked on the response in Fig. 3.3.

Fig. 3.5 Expanded view showing the evolution of diamond deformation patterns on the tensile side of the tube in Figs. 3.3 and 3.4.

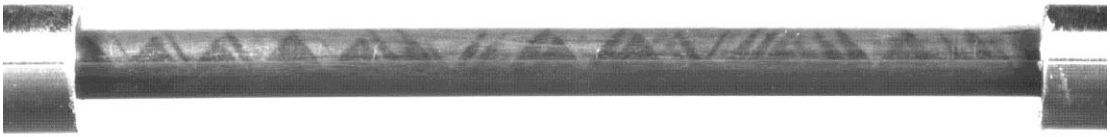

Fig. 3.6 An unloaded specimen from Nacker [2009] showing diamond patterns of a brittle oxide layer induced by bending on the tensioned side of a NiTi tube.

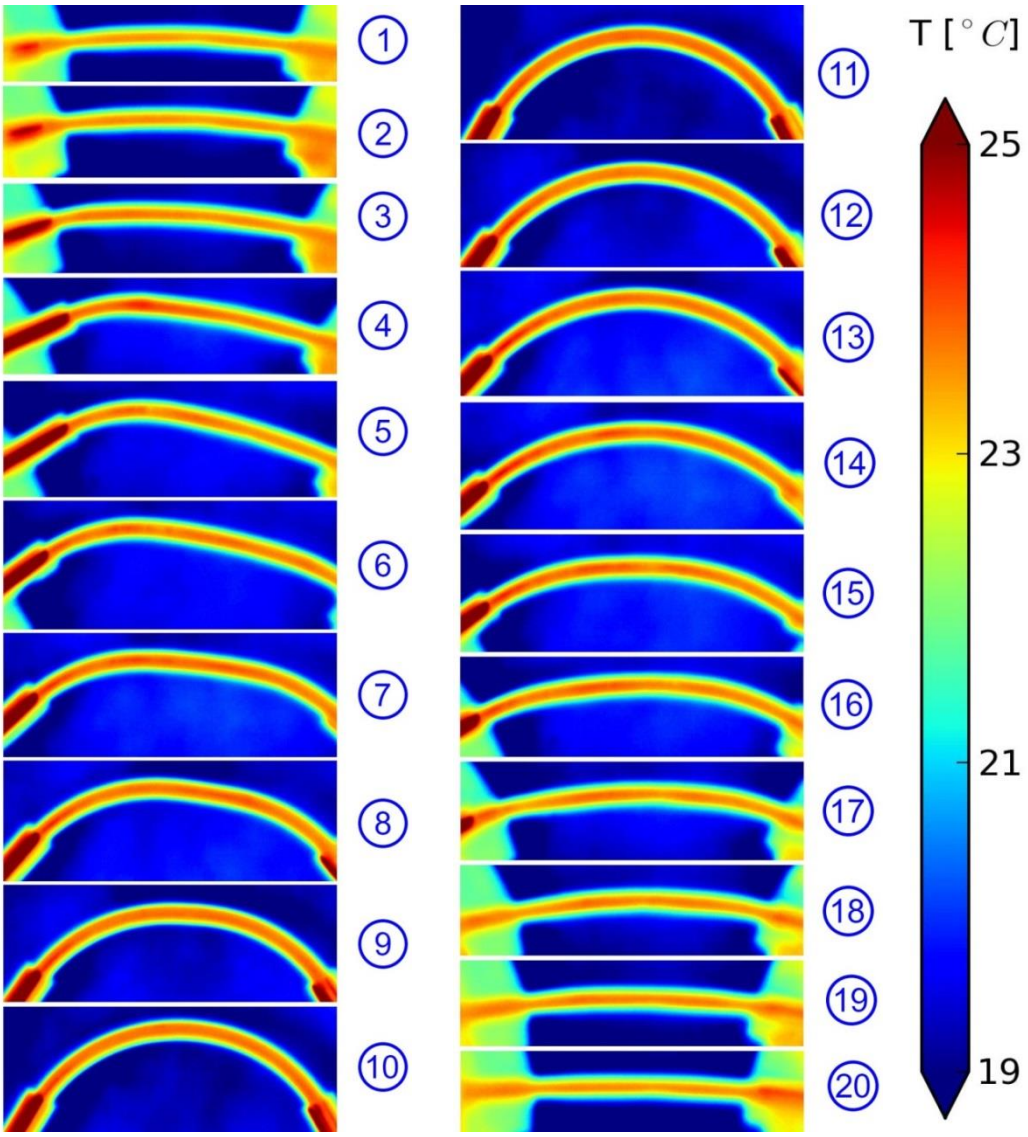

Fig. 3.7 Set of infrared thermograms from tube bending experiment corresponding to the numbered bullets marked on the response in Fig. 3.3.

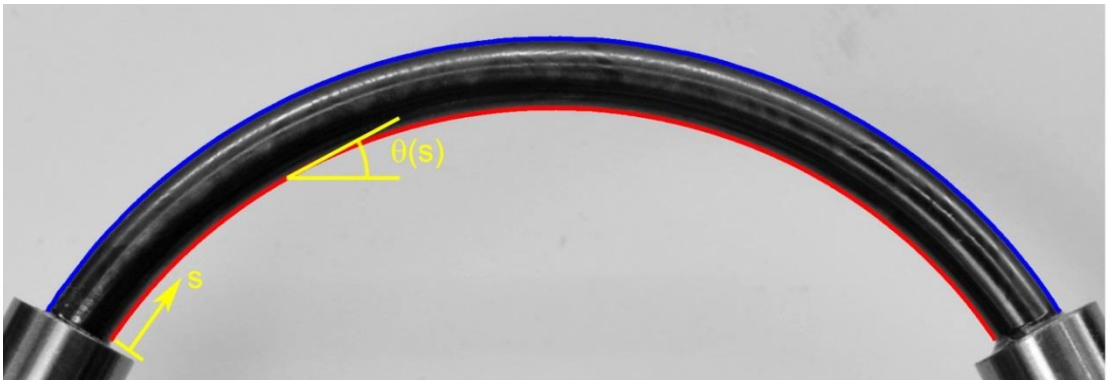

Fig. 3.8 Edge detection image processing scheme using pixel intensity to map top and bottom edge of tube during bending.

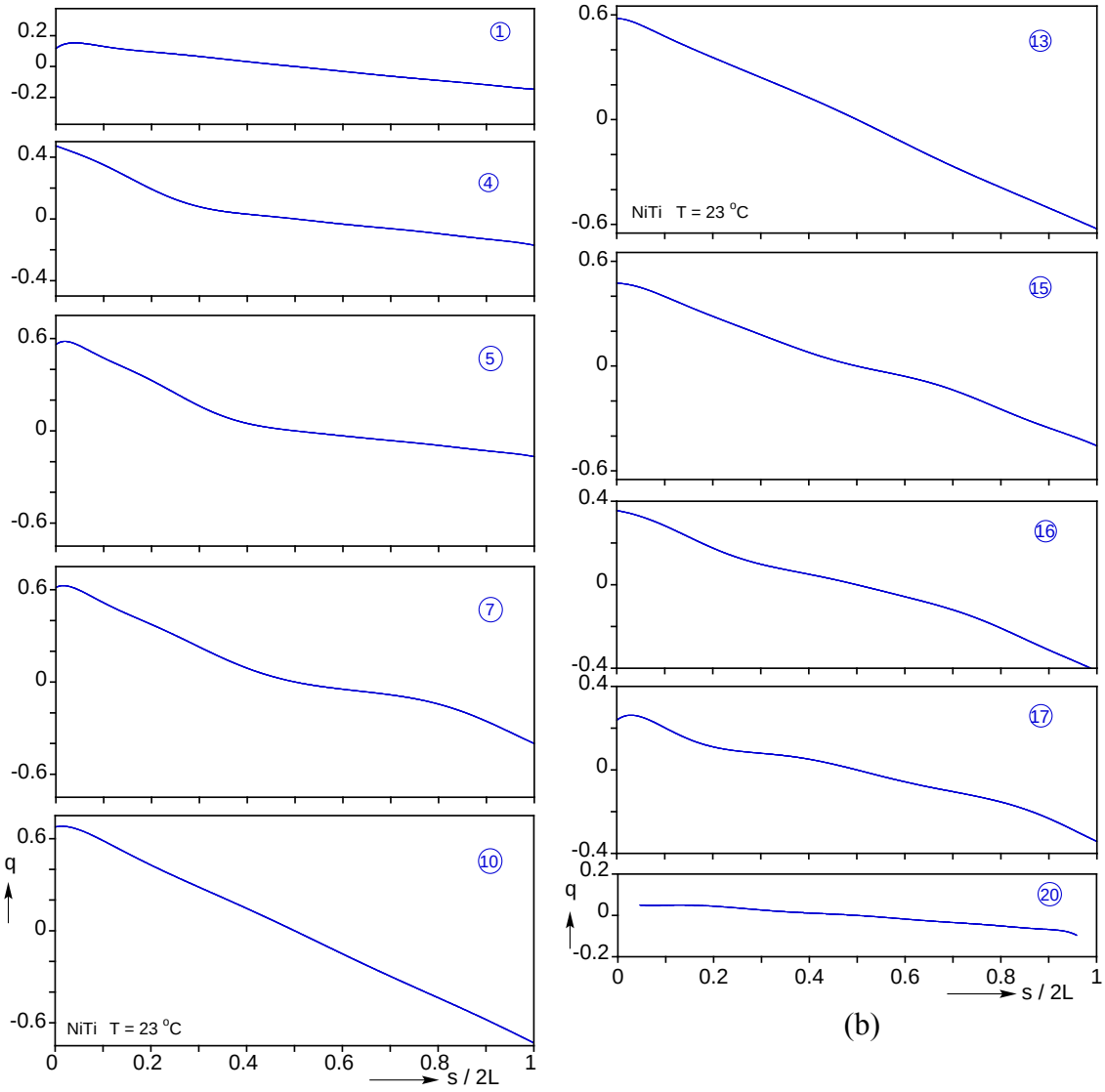

Fig. 3.9 Plots of the slope along the top edge of a NiTi tube at different stages of bending corresponding to the configurations in Fig. 3.4 that quantify the coexistence of two curvature regimes. (a) Loading and (b) unloading.

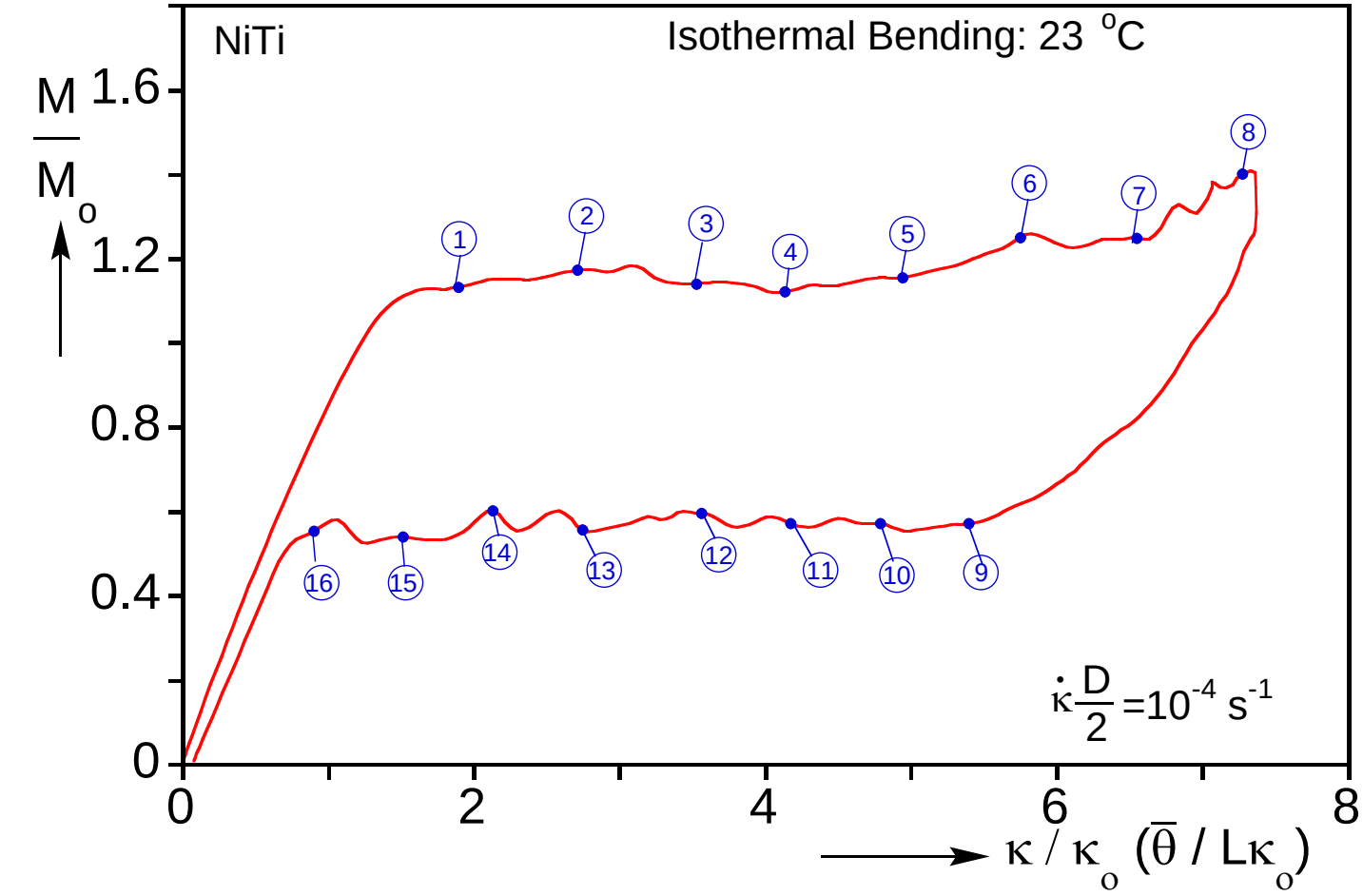

Fig. 3.10 Moment vs. curvature response for isothermal bending experiment of NiTi tube.

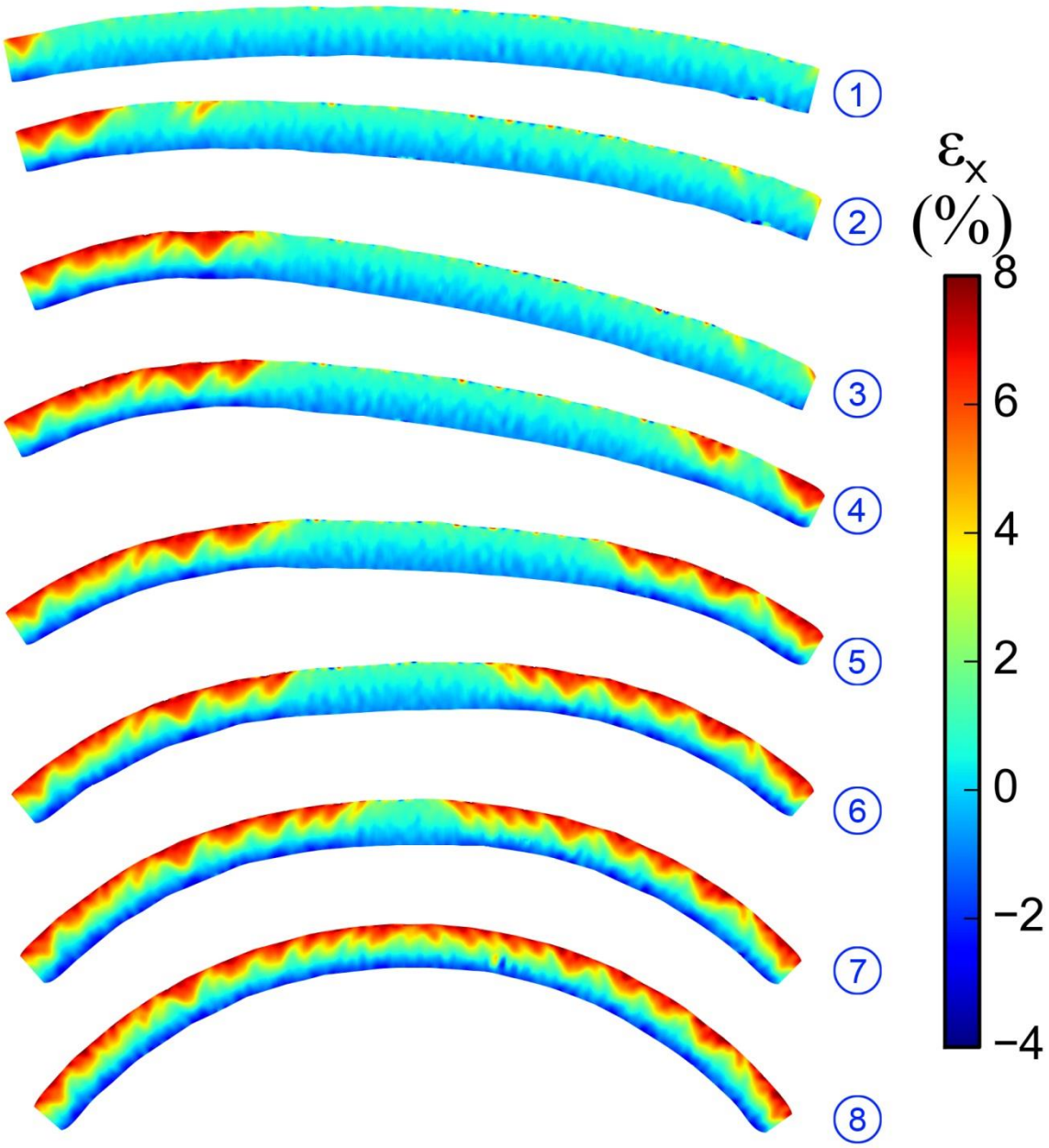

(a)

Fig. 3.11a Set of axial strain contours from DIC showing evolution of localized deformation patterns recorded during (a) loading and (b) unloading of a pure bending test on a NiTi tube at 23 °C with numbered bullets corresponding to those in Fig. 3.10.

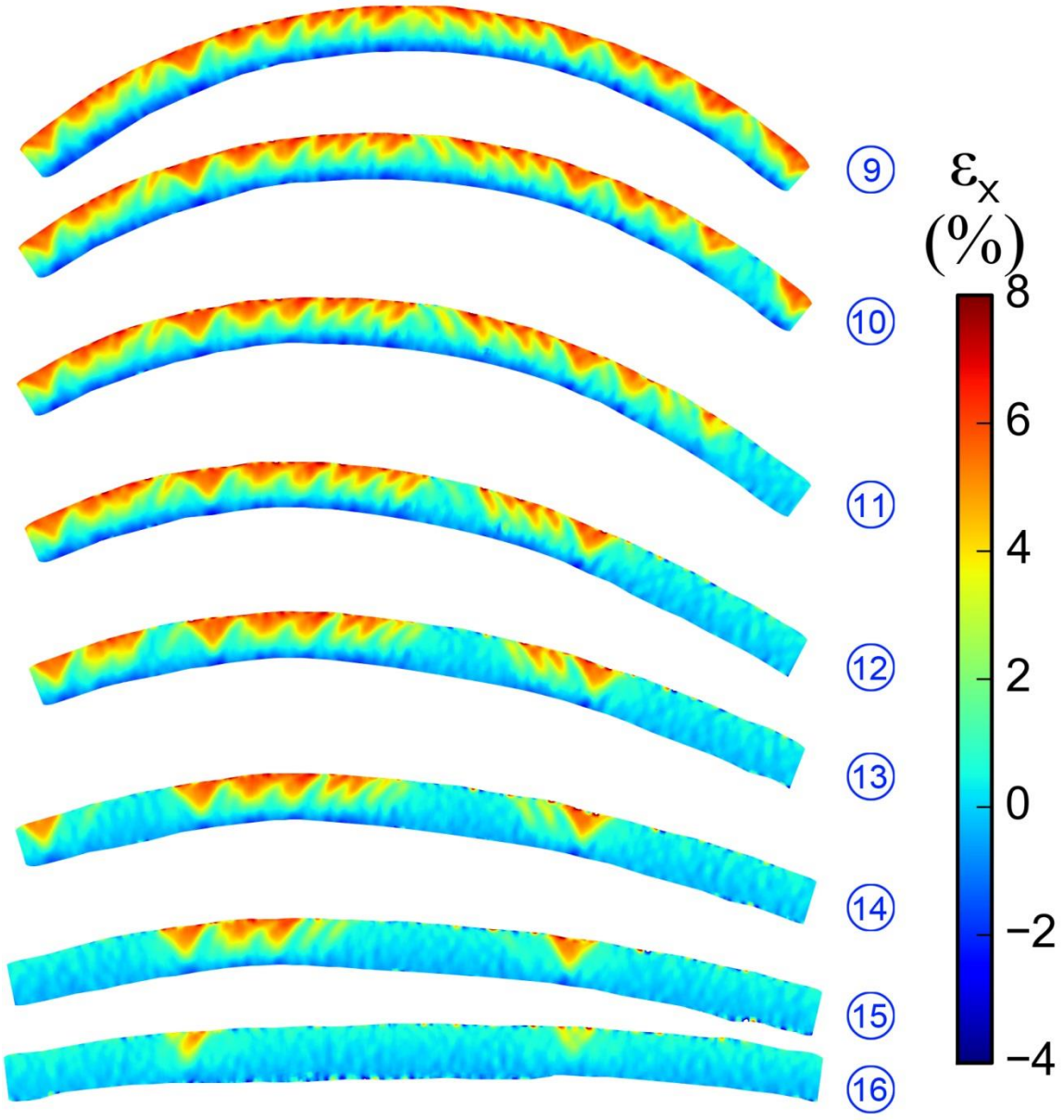

(b)

Fig. 3.11b Set of axial strain contours from DIC showing evolution of localized deformation patterns recorded during (a) loading and (b) unloading of a pure bending test on a NiTi tube at 23 °C with numbered bullets corresponding to those in Fig. 3.10.

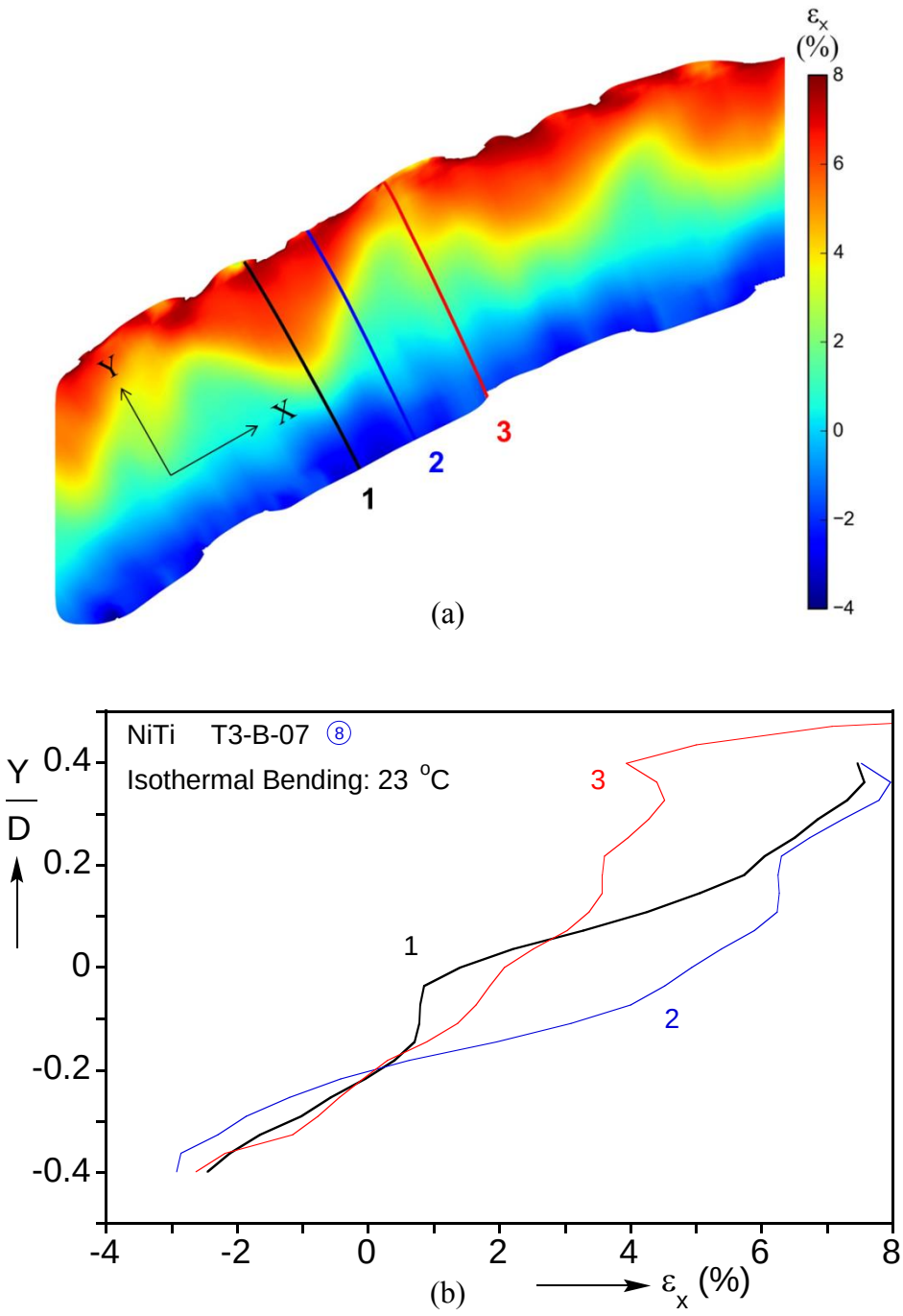

Fig. 3.12 Section lines through the depth of the specimen (a) in the reference coordinate system corresponding to image ⑧ from Fig. 3.11. (b) Axial strain profiles along section lines in (a).

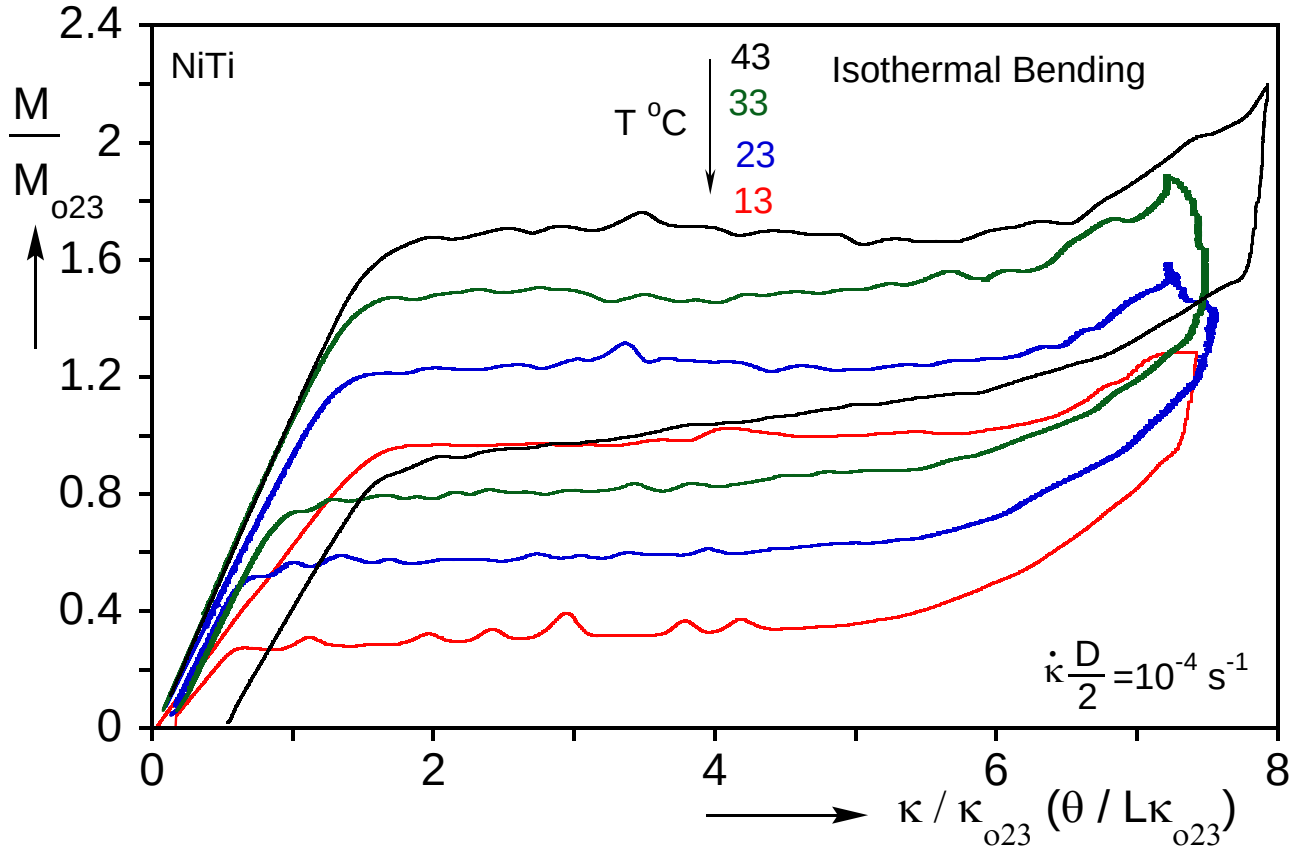

Fig. 3.13 Moment-end rotation responses of NiTi tubes at 13, 23, 33, and 43 °C.

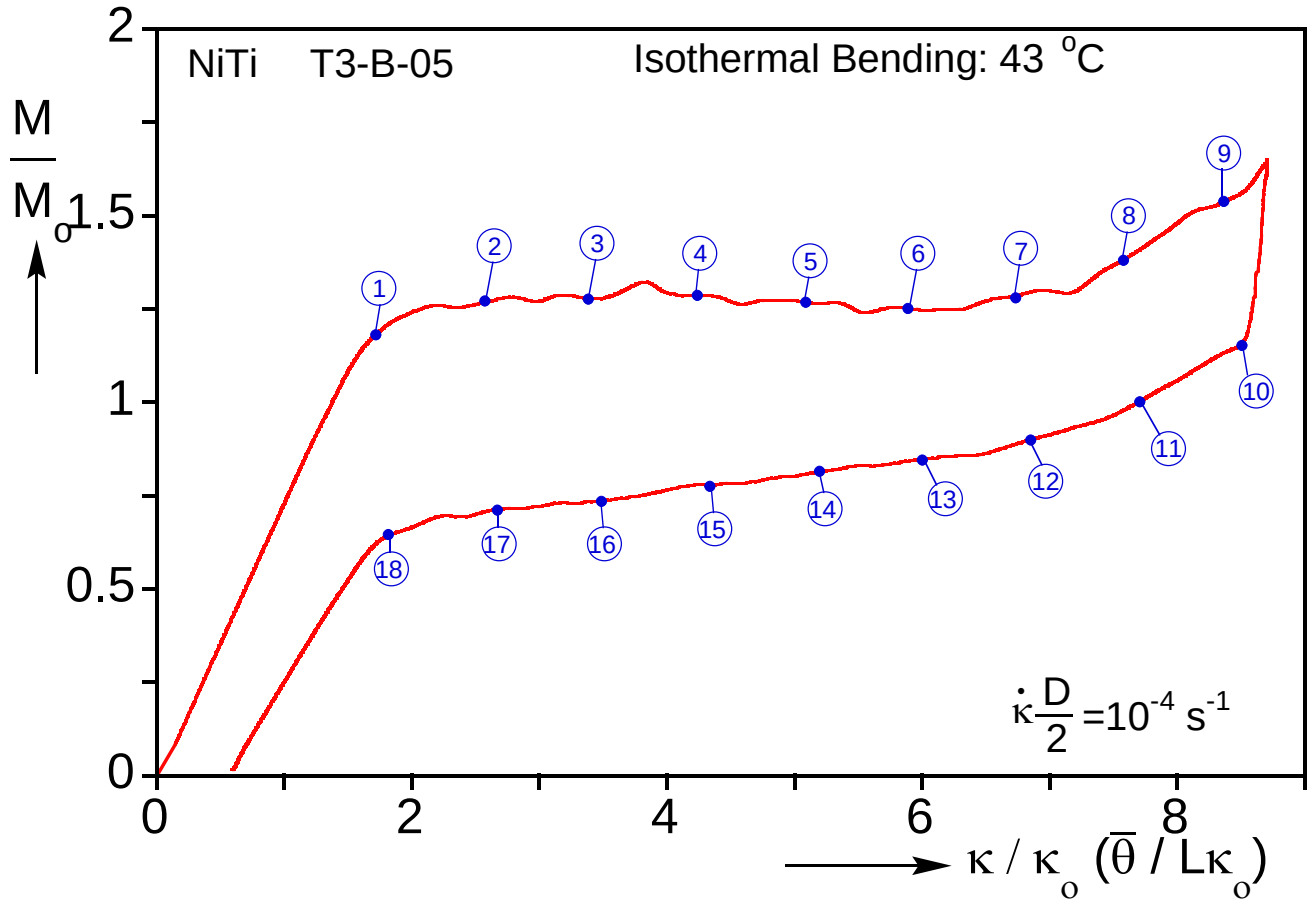

Fig. 3.14 Moment-end rotation response recorded in an isothermal pure bending experiments on a NiTi tube at 43 °C.

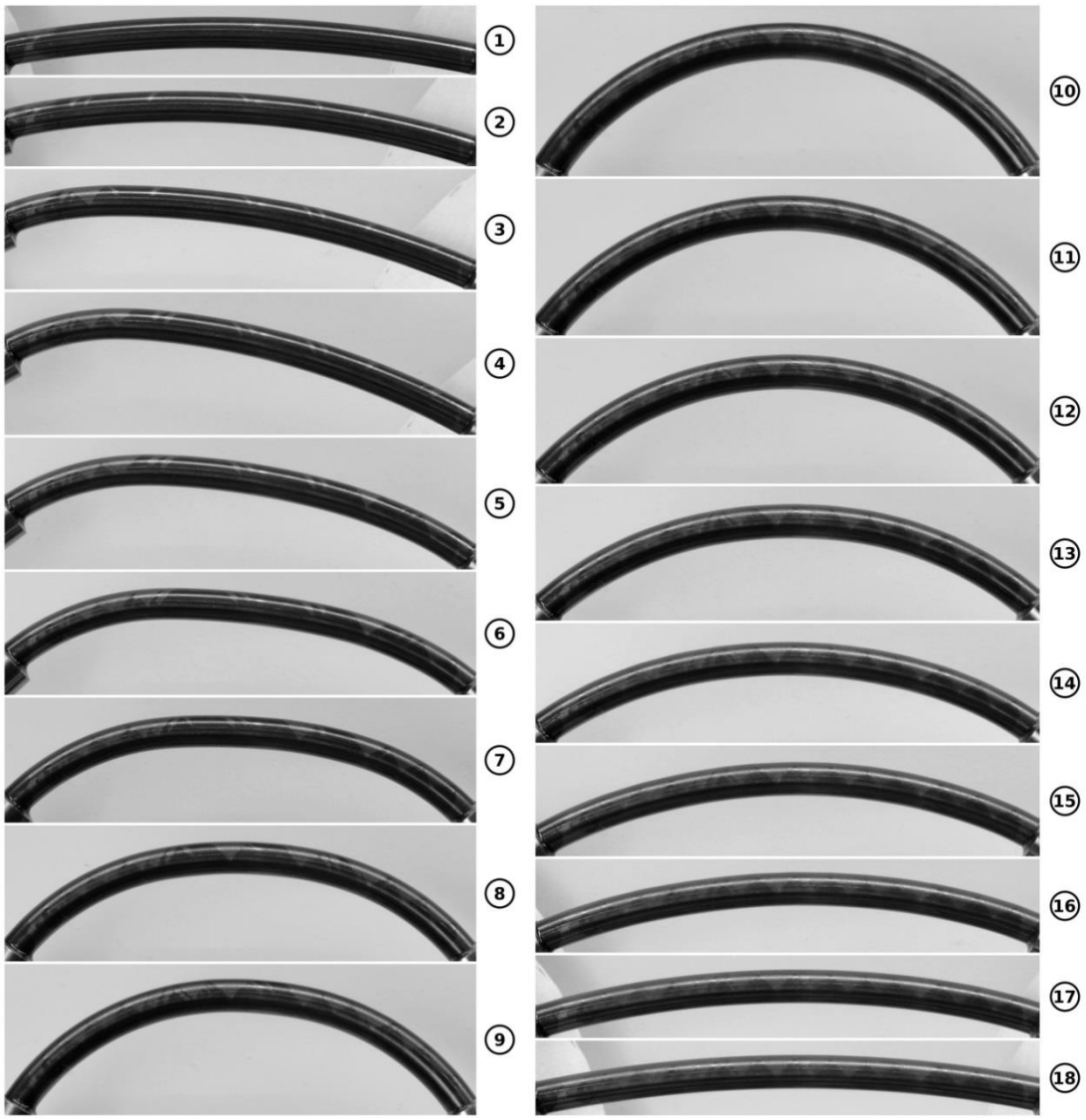

Fig. 3.15 Set of tube bending configurations for isothermal bending experiment at 43 °C corresponding to the numbered bullets marked on the response in Fig. 3.14.

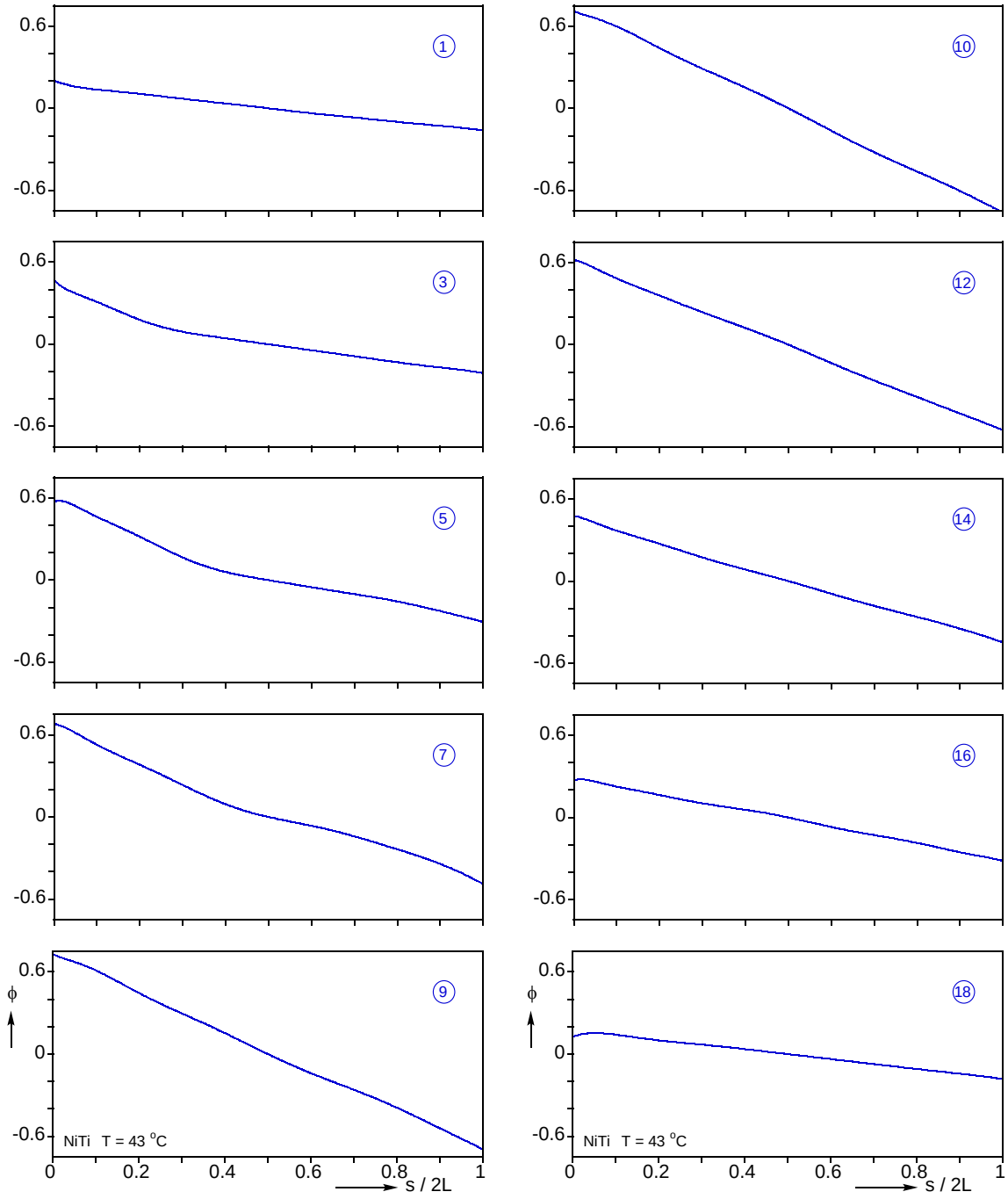

(a) (b)

Fig. 3.16 Plots of the slope along the top edge of a NiTi tube at different stages of bending corresponding to the configurations in Fig. 3.15 that quantify the coexistence of two curvature regimes during (a) loading, but uniform bending during (b) unloading.

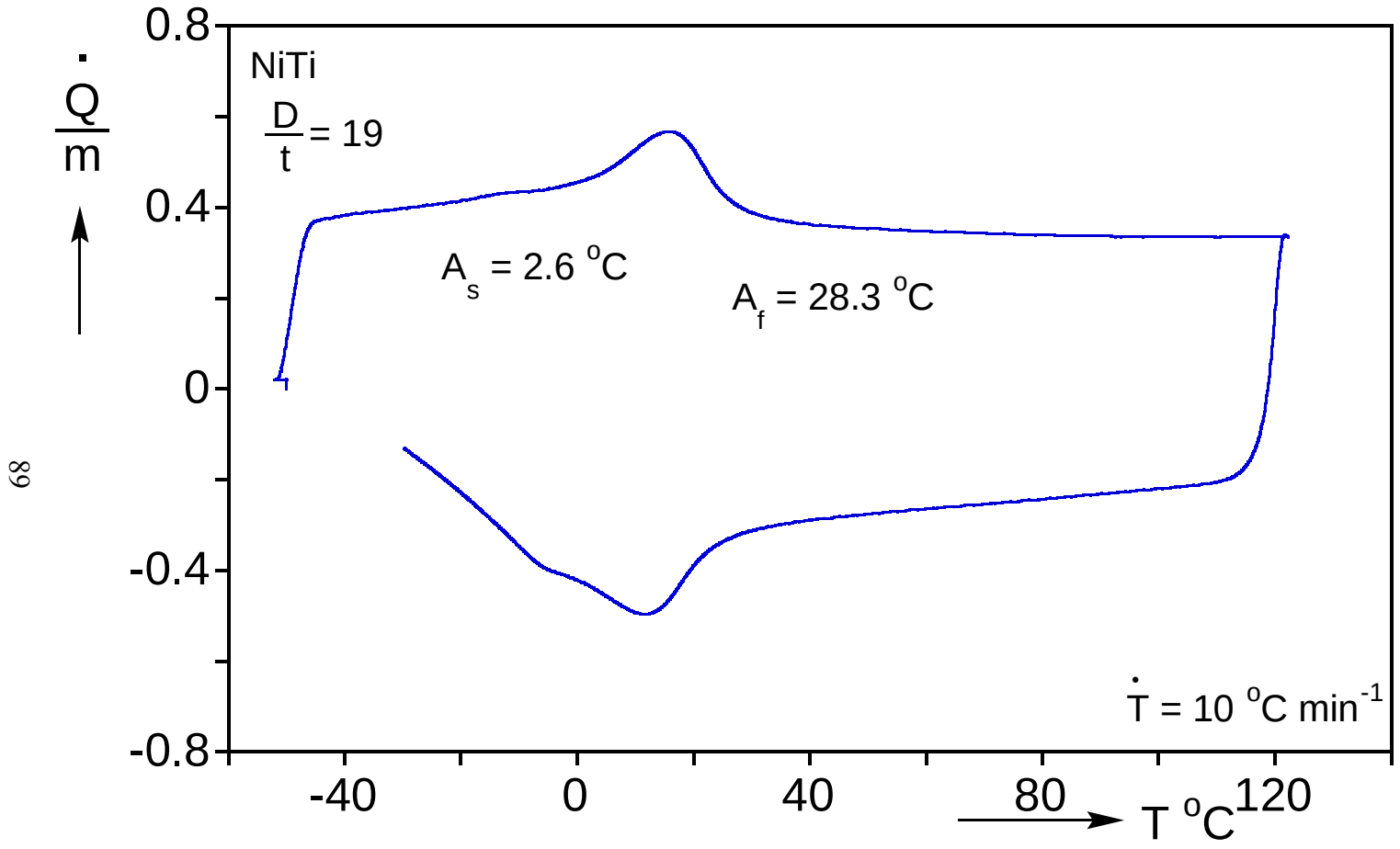

Fig. 3.17 DSC thermogram of NiTi tubes tested in bending at 13, 23, and 33 °C

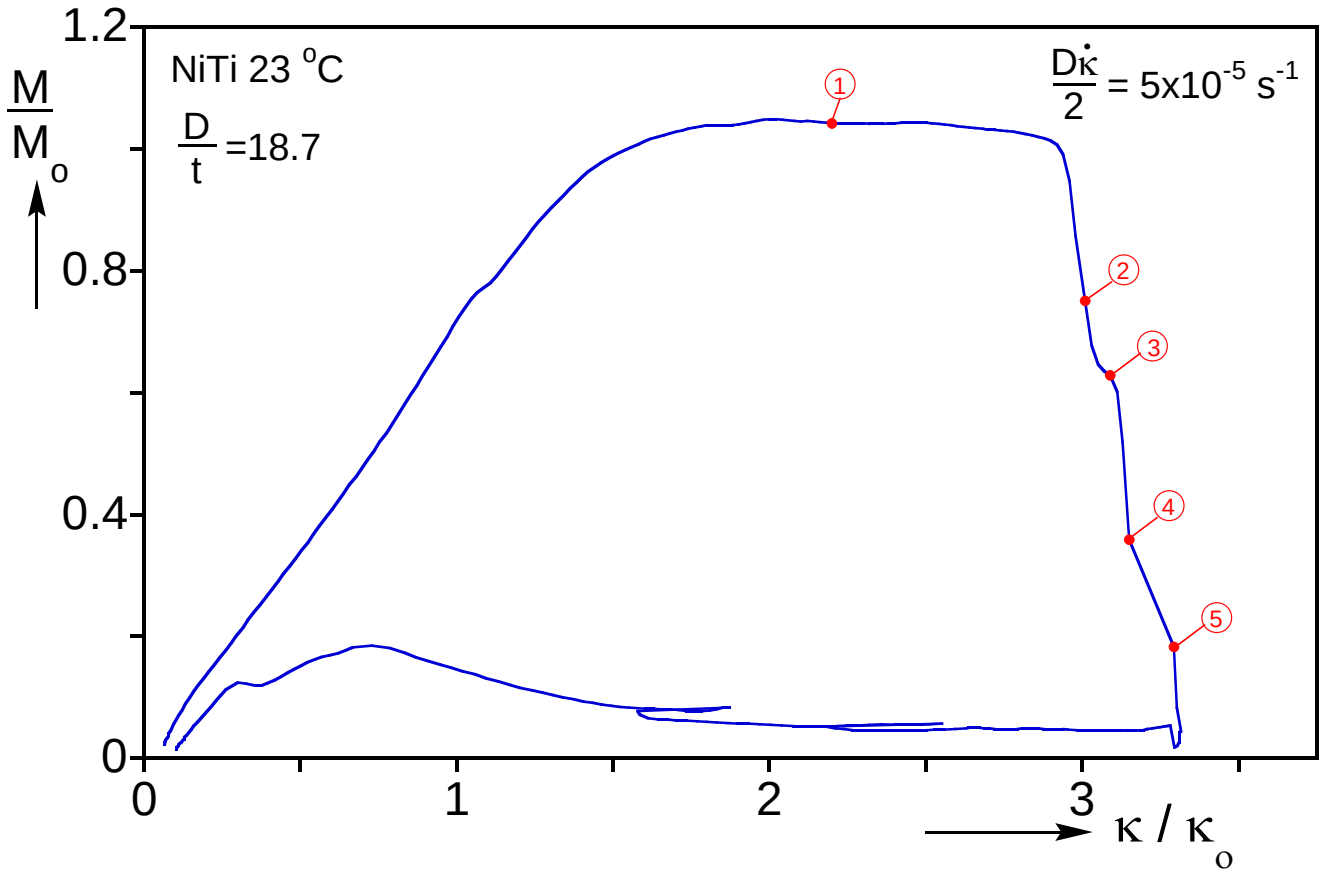

Fig. 3.18 Moment-end rotation responses of NiTi tube at 23 °C showing structural collapse.

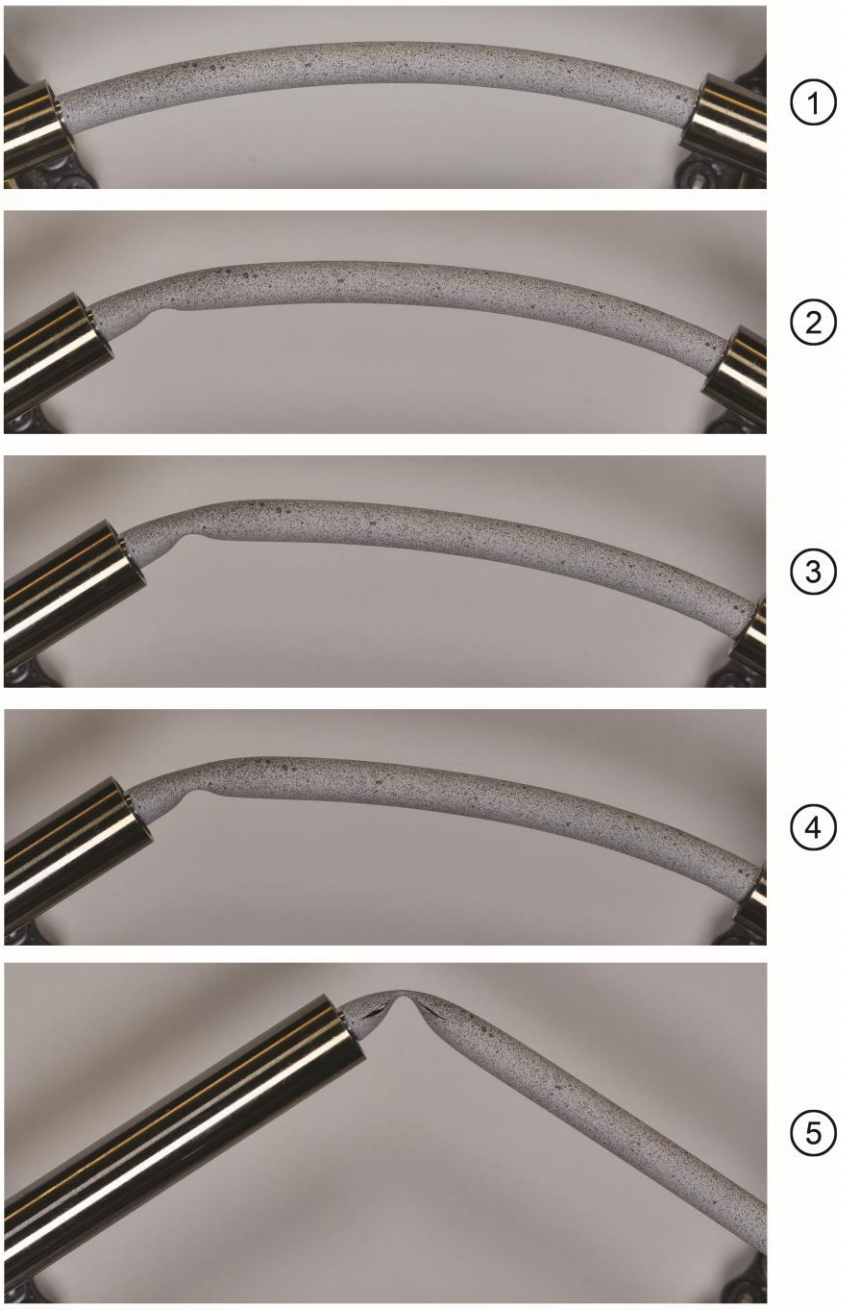

Fig. 3.19 Deformed configurations of bending collapse with numbered bullets corresponding to Fig. 3.13.

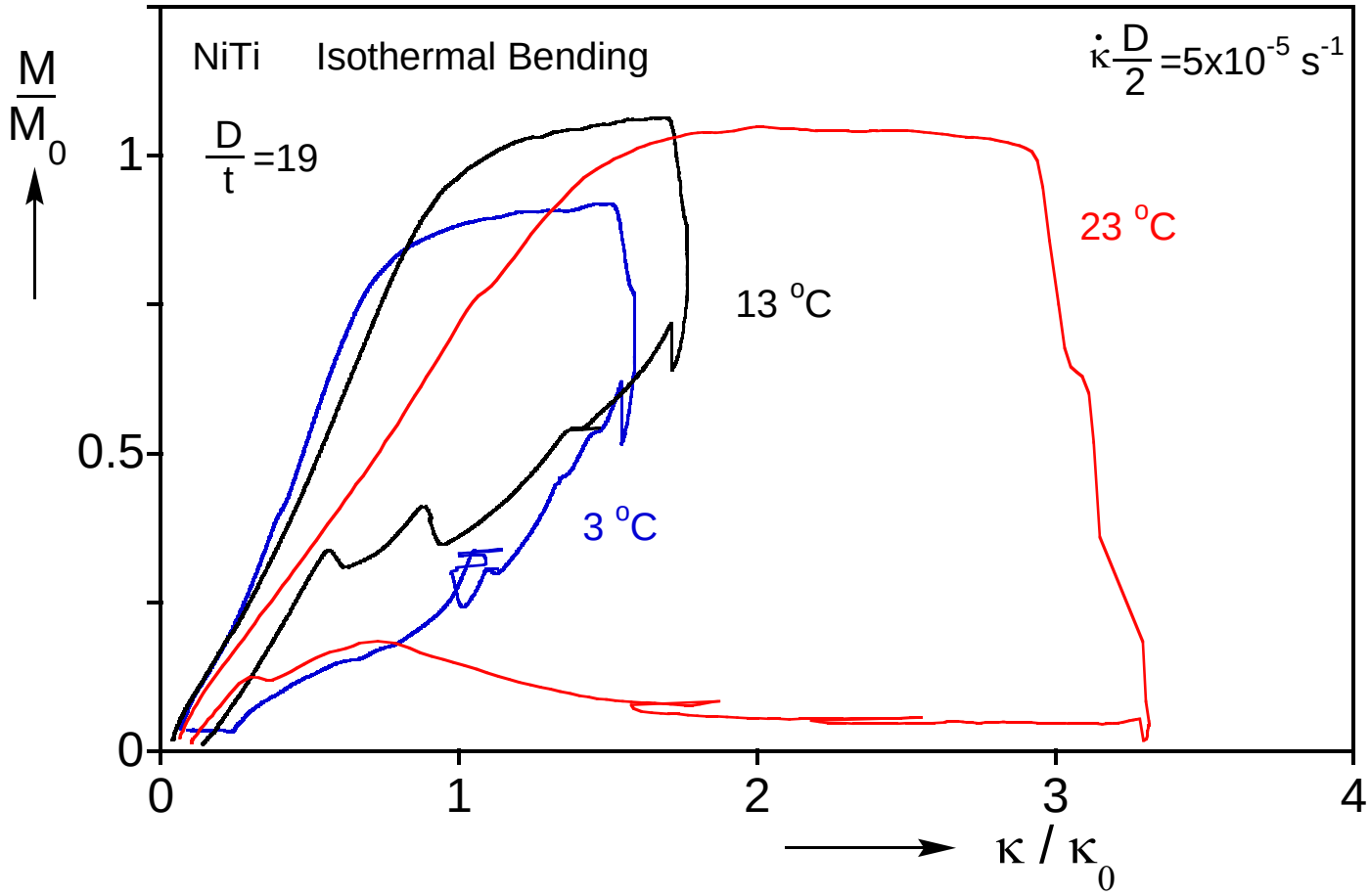

Fig. 3.20 Moment-end rotation responses of NiTi tube at 3, 13, and 23 °C showing structural collapse.

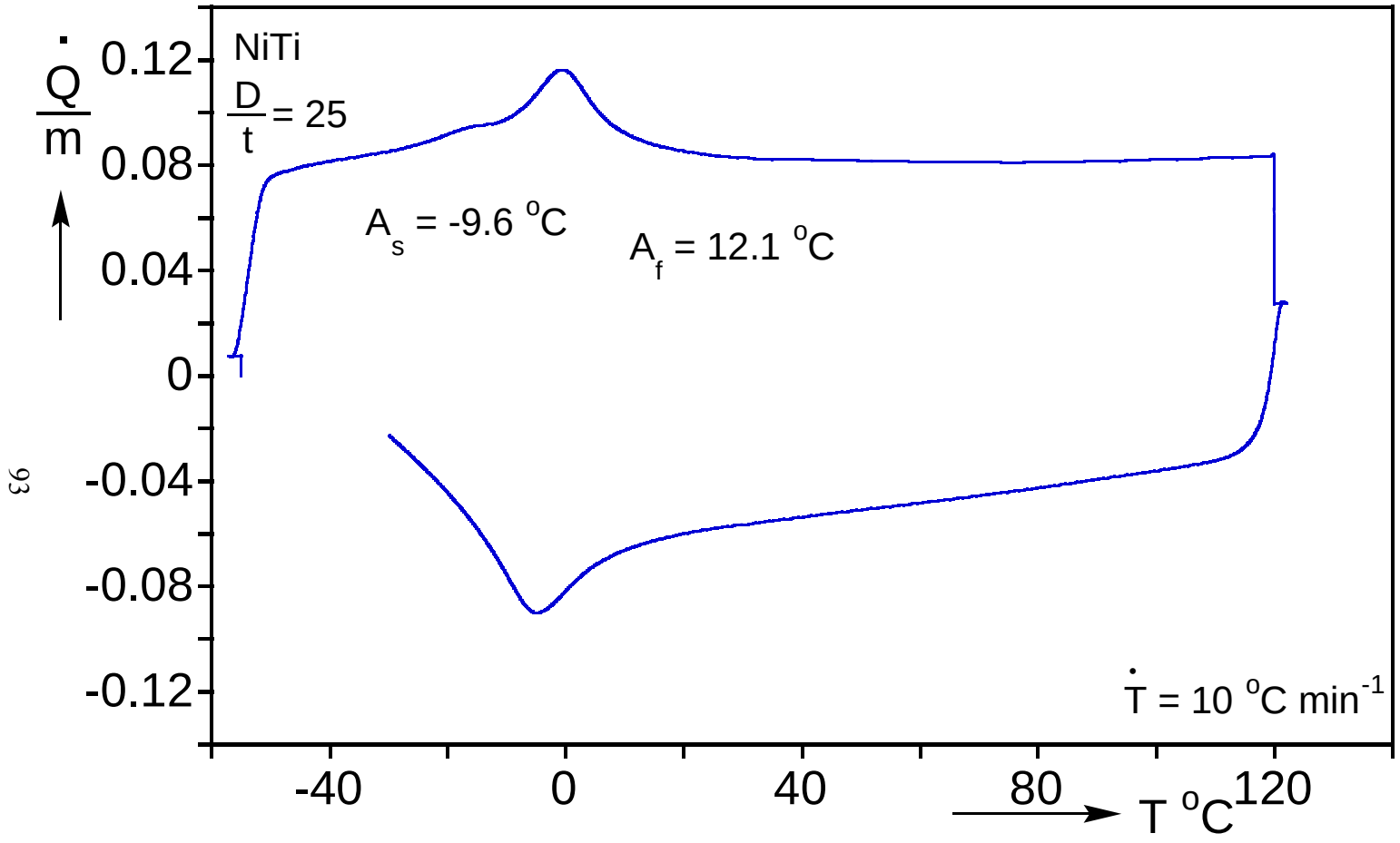

Fig. 3.21 DSC thermogram performed on NiTi tube stock used in axial compression of cylindrical shell experiments.

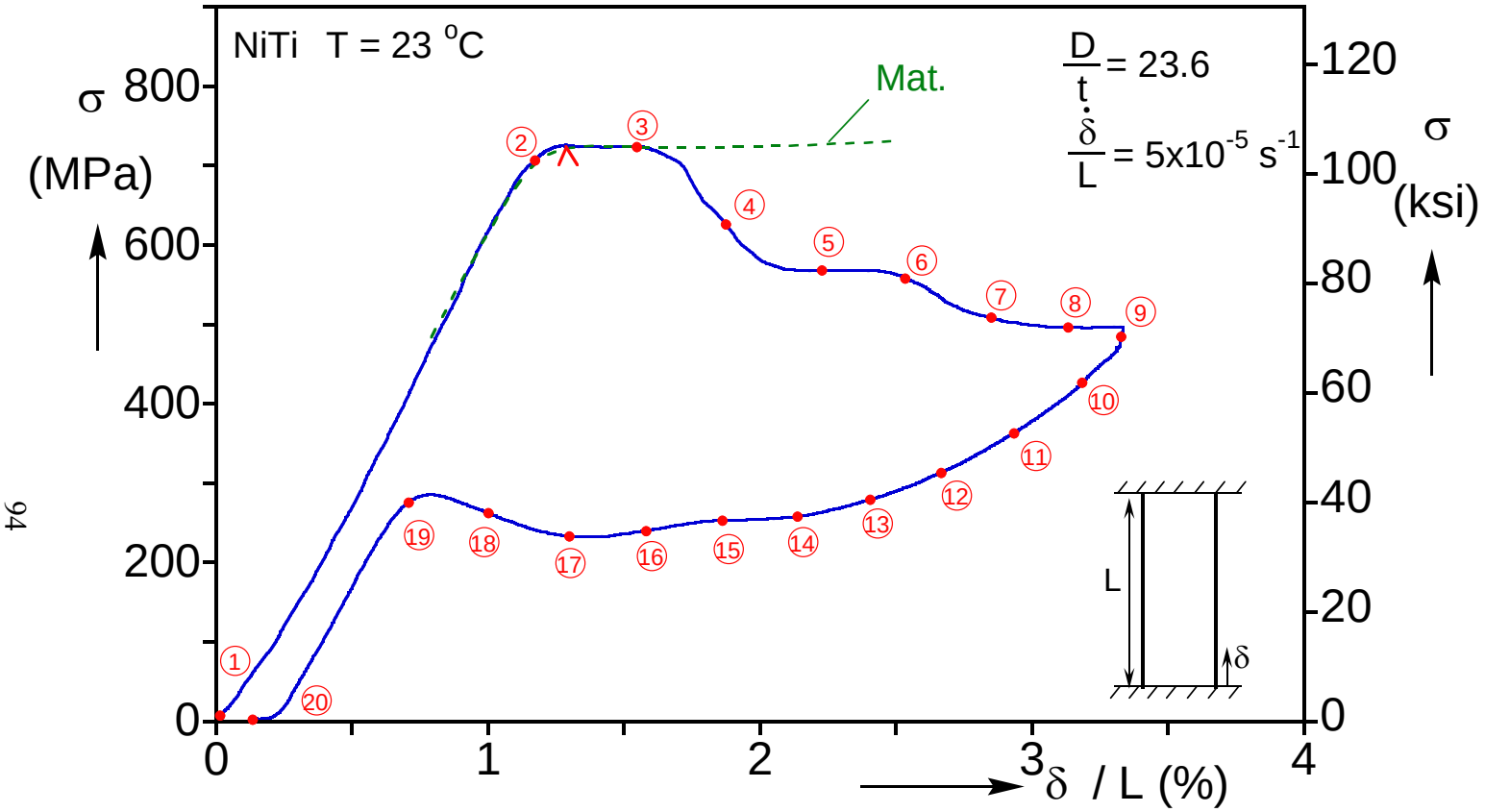

Fig. 3.22 Compressive axial stress-shortening buckling and recovery response recorded in an experiment on a pseudoelastic NiTi tube with $D/t = 23.6$.

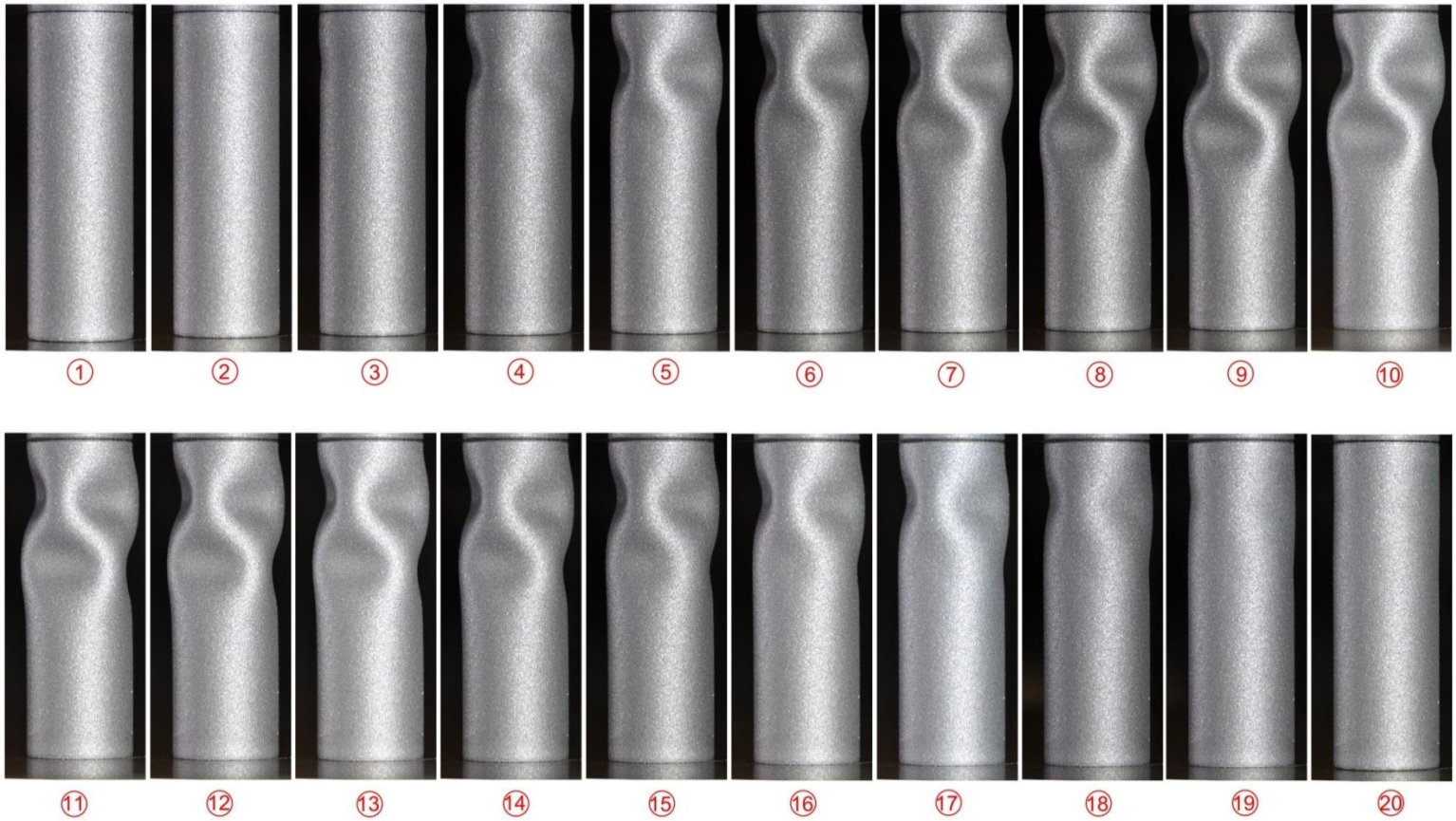

Fig. 3.23 Sequence of photographic images showing the evolution of a mode-3 buckling mode during loading (①-⑨) and the recovery of the deformation on unloading (⑨-⑳).

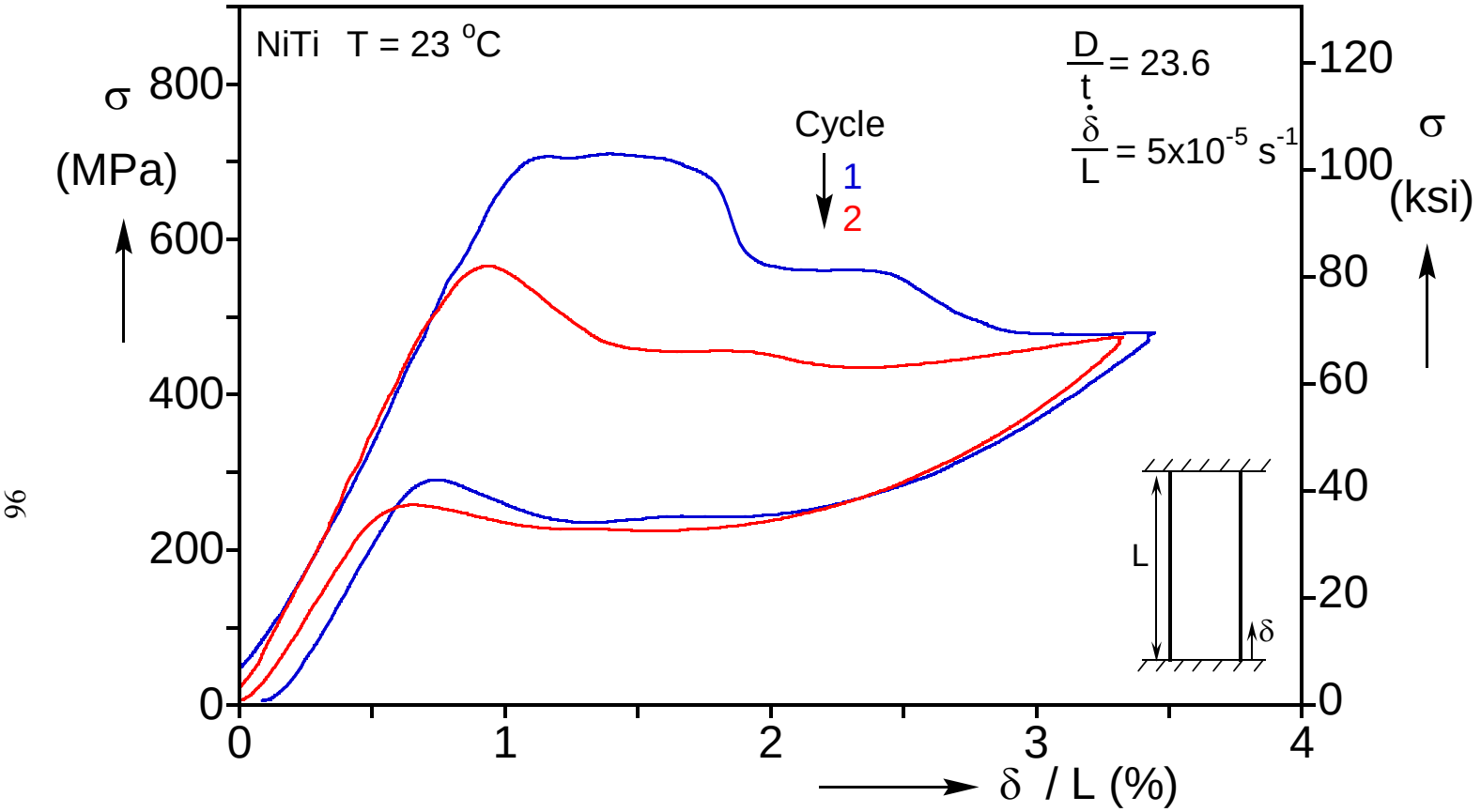

Fig. 3.24 Compressive axial stress-shortening buckling and recovery response. Included is the response of a second load/unload cycle that shows some degradation induced in the first cycle.

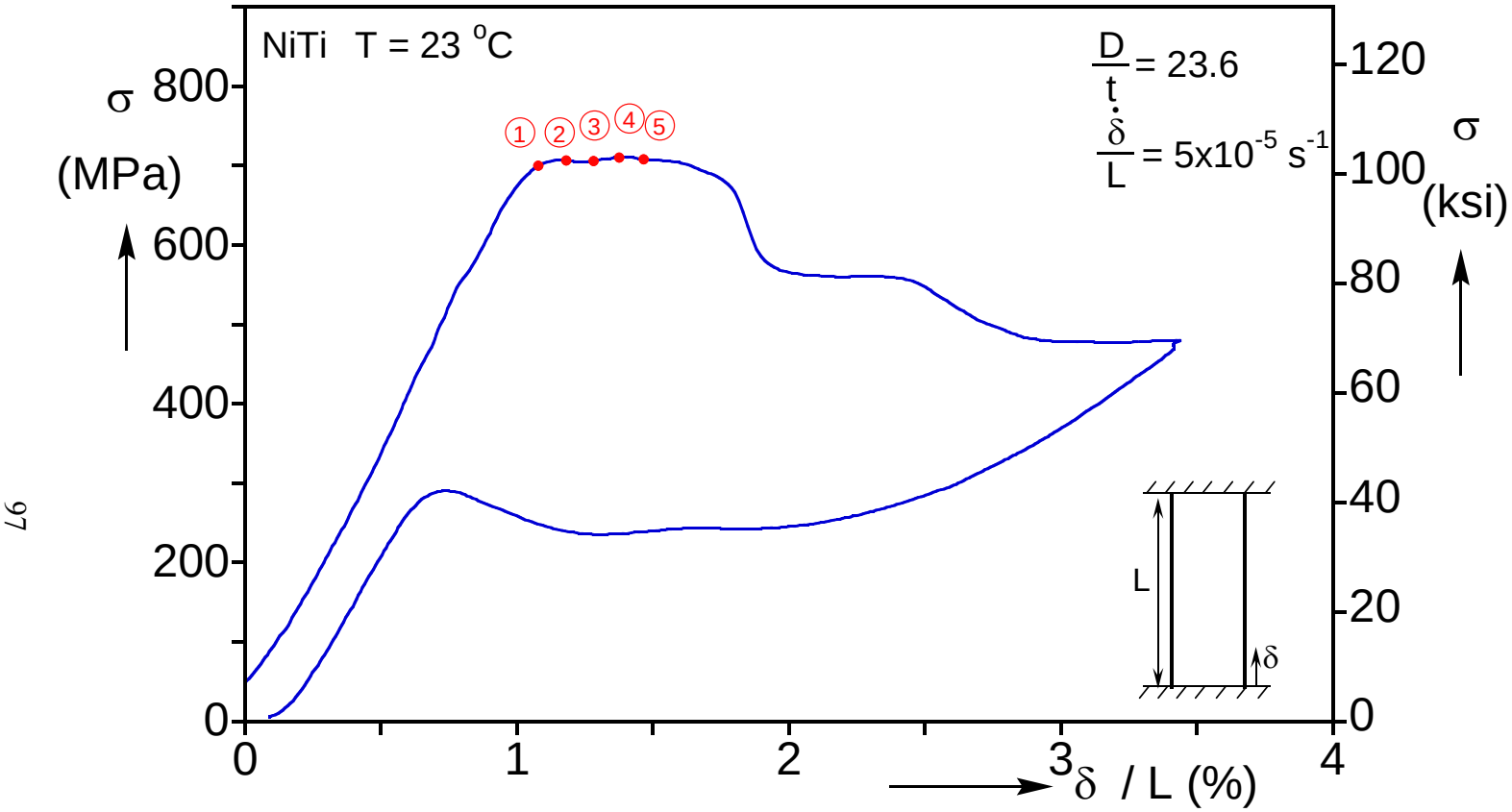

Fig. 3.25 Compressive axial stress-shortening buckling and recovery response recorded in an experiment on a pseudoelastic NiTi tube using DIC.

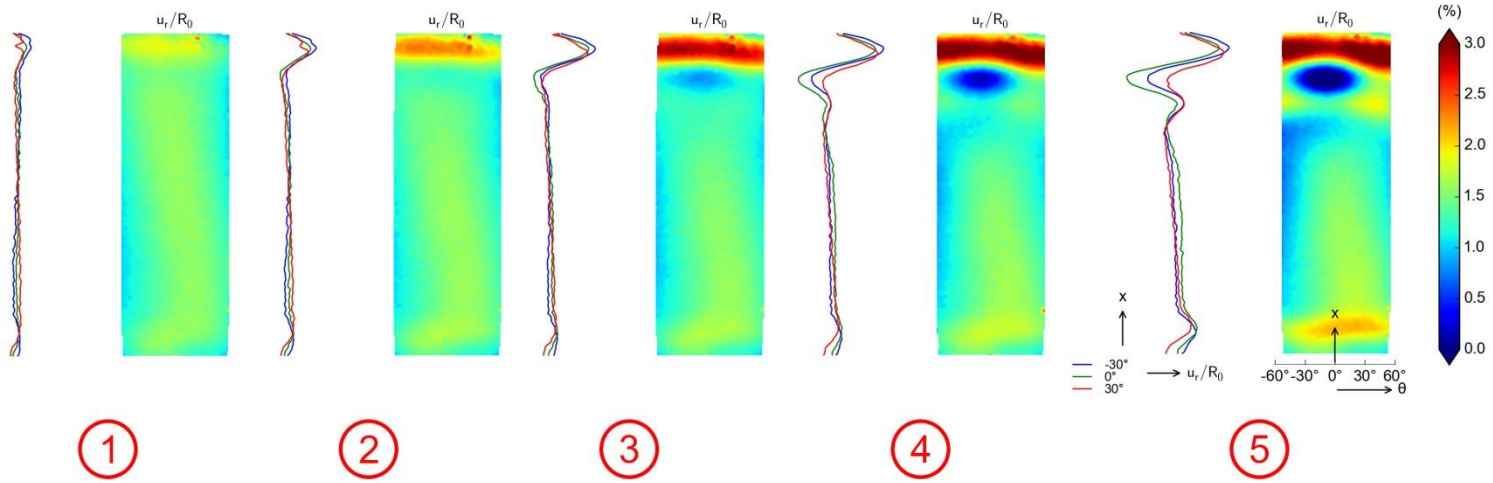

Fig. 3.26 Sequence of normalized radial displacement profiles and corresponding contour images from DIC with numbered bullets from Fig. 3.19. The sequence shows the evolution of a stable wrinkling buckling mode and transition to an unstable mode-3 buckling mode.

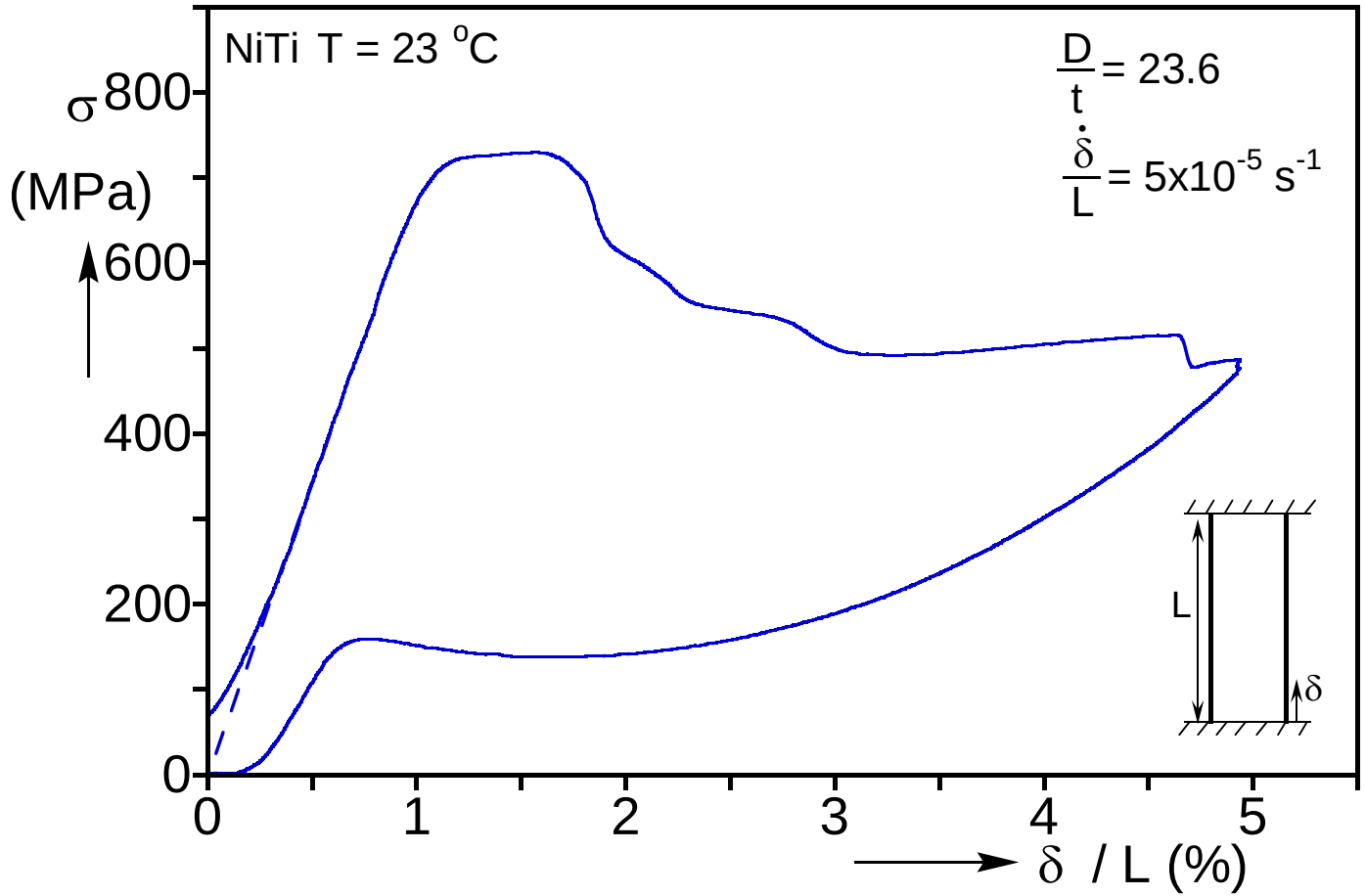

Fig. 3.27 Compressive axial stress-shortening buckling response recorded in an experiment on a pseudoelastic NiTi tube. The abrupt drop in stress at $\delta \approx 0.046L$ is associated with a failure by fracture at the extrado of a buckling lobe.

Chapter 4: MULTIAXIAL MATERIAL BEHAVIOR–EXPERIMENTS[4]

The previous chapters have demonstrated that the nonlinearities associated with deformation induced by phase transformations in NiTi have a significant impact on the behavior of NiTi structures. This dissertation is part of a longer term research objective to develop constitutive models that adequately represent these material nonlinearities so that the structural events reported can be simulated numerically. The uniaxial results presented in Chapter 2 provide the foundation for the requirements of such an effort; however, an essential additional component is the characterization of the material under multiaxial stress states. To this end, this chapter presents experimental results of NiTi tubes subjected to combined internal pressure and axial loading.

Efforts to establish the response of NiTi under biaxial stress states are limited and those performed have mainly concentrated on establishing the onset of transformation under tension and shear, usually using tubes under combined tension and torsion. Based on the uniaxial behavior, inhomogeneous deformations are also expected under multiaxial stress states, thus placing unique experimental demands. Additionally, and the stresses and strains involved are rather large and require specialized experimental setups and diagnostic measures. Furthermore, as pointed out in Chapter 2, the effect of latent heat must be accounted for. Some of these experimental challenges have been considered in individual studies, but very few experiments have been reported that address the whole set for NiTi under biaxial stress states. Lim and McDowell [1999], Lexcellent et al. [2002], Thamburaja and Anand [2002], Bouvet et al. [2004], and Grabe and Bruhns

[4] Bechle, N.J., Kyriakides, S. (2016 *in press*). Evolution of localization in pseudoelastic NiTi tubes under biaxial stress states. *Int'l J. Plasticty*. (Designed and performed experiments, analyzed data, and wrote the paper)

[2009] performed multiaxial experiments, but were unable to capture or did not report localized deformations. Helm and Haupt [2001] and McNaney et al. [2003] reported localization in tension dominated stress states, but did not record the evolution of deformation during transformation. Sun and Li [2002] conducted non-proportional, corner stress paths, reporting inhomogeneous deformation in tension dominant experiments and homogeneous deformation for torsion dominant stress states. A transformation surface was also generated, noting the deviation from von Mises; however, there was a sharp corner in the transition from tension controlled to torsion controlled corner paths.

The main conclusions from the literature on the multiaxial behavior of NiTi are: (i) NiTi under shear exhibits a monotonically increasing response with limited or no localization. (ii) Tension dominant stress states lead to localization and shear dominant ones do not. (iii) The nucleation of M transformation surface does not follow a von Mises type trajectory.

This study aims to address the need for a more complete picture of how pseudoelastic NiTi behaves under biaxial stress states, particularly the response during transformation. To this end, a custom internal pressure-axial load testing facility has been developed and used to conduct a series of experiments on NiTi tubes in the axial-hoop stress space. For each stress path the specimen is loaded under nearly isothermal conditions to the "completion" of martensitic transformation and unloaded. Stereo Digital Image Correlation (DIC) is used to monitor and capture the real-time deformation of the specimen. The issues of interest include: (i) How does biaxiality influence the onset of M transformation during loading and the onset of A transformation during unloading. (ii) Identify any prevalent anisotropies in stress or strain. (iii) How does the material deform

during transformation under different stress states. (iv) How is the hysteresis or energy dissipated influenced by biaxiality.

4.1 Experimental Setup

The experiments are conducted on tubular specimens from a nearly equiatomic NiTi tubular stock (50.9 at % Ni) supplied by Memry Corporation. The tubes are produced by drawing followed by thermomechanical processing that enhances the special properties of this alloy. The tube stock is then finished by centerless grinding to a specified outer diameter. This is the same tubular stock that was used in the axial buckling study in Section 3.2. The tubes had a specified outer diameter of 6.35 mm (0.25 in) and a wall thickness of approximately 0.25 mm (0.010 in)–the exact dimensions of the specimens are listed in Table 4.1. The following transformation temperatures were established for the material using digital scanning calorimetry: A_s = -10 °C and A_f = 12 °C (see Fig. 3.21). The experiments were performed at room temperature (23 °C) at which the material is in the austenitic phase and exhibits pseudoelasticity.

The biaxial testing facility consists of a screw-type axial testing machine that operates in conjunction with a 690 bar (10,000 psi) precision metering syringe pump using water as the pressurizing fluid. The pump has an independent controller that allows either pressure or volume control. A unique feature, essential to the present application, is that the syringe pump can dispense very small volumes at precise flow rates. The specimen is mounted in the testing machine via custom stainless-steel housing grips as shown in Fig. 4.1. The upper housing is connected to a 5 kN (1000 lb) load cell while the lower one is anchored to the crosshead of the testing machine. Careful alignment of the two housings is performed prior to mounting the specimen.

The ends of the specimen are clamped in the housings using self-centering 1-inch locking assemblies as shown in Fig. 4.2. Solid spacers that allow the required contraction on clamping are used to fill the space between the locking assemblies and the specimen. The specimen is protected from crushing by steel plugs inserted into the clamped ends to react the clamping force. Centered holes drilled along the length of the plugs allow free flow of the pressurizing fluid. Double O-rings are used to seal the plug against the specimen and against the housing as shown schematically in Fig. 4.2.

One-eighth-inch high-pressure tubing and connectors are used to connect the pump to the lower housing. The hydraulic circuit is completed with valves at the entrance and the exit (exhaust) as shown schematically in Fig. 4.1a (see also photograph of setup in Fig. 4.1b). The pressure in the system is monitored with a pressure transducer calibrated to 10V at 10 ksi.

The specimens were cut from a 1.525 m (5 ft) long tube stock to a length of 114 mm (4.50 in). The ends were faced off in a lathe and deburred to ensure that the O-rings are not damaged during the insertion of the end plugs. Clamping leaves a 50 mm (2 in) test section. A fine black speckle pattern was painted on a white undercoat on the test section to enable monitoring the deformation during the experiment using stereo Digital Image Correlation (DIC).

We report on experiments in which the specimens were loaded along radial stress paths such that the nominal axial (x) and hoop (θ) stresses are related via

$$\sigma_x = \alpha\sigma_\theta, \quad \alpha = \text{const.} \tag{4.1}$$

This is achieved by connecting the axial and pressure loading systems through feedback as follows. Let F and P be respectively the force measured by the load cell and the internal pressure. The axial and circumferential stresses are then

$$\sigma_x = \frac{F}{2\pi Rt} + \frac{PR}{2t} \text{ and } \sigma_\theta = \frac{PR}{t}, \tag{4.2}$$

where R and t are respectively the undeformed mid-surface radius and wall thickness of the tube. Thus, for example, if the load cell reads zero force, it means that the specimen is reacting the pressure end-cap load and consequently develops an axial stress of $PR/2t$ $(\Rightarrow \alpha = 0.5)$. Pressurization was performed by prescribing the fluid flux into the closed system (volume control). The axial testing machine is operated under load control with the pressure signal as external command using a TestProfiler method in Instron's Bluehill 3 software. The pressure is used in Eqs. (4.1) and (4.2) to establish a target value of force that corresponds to the chosen value of α. The target value of force is compared to the current set point and the difference becomes the command signal that ramps the force in a chosen time step (typically 1 s). In this manner the force is continuously updated so that it follows the measured pressure at the desired ratio. Experiments were performed for $-1.0 \le \alpha \le \infty$.

During the test the pressure, displaced volume, axial load, and machine displacement were monitored using a LabVIEW based data acquisition system. Each channel is sampled at 10 kHz and the signals are averaged over 1000 samples and stored at a rate of 10 per second.

Because inhomogeneous deformations were anticipated to develop for parts of the loading histories, a full-field deformation monitoring scheme was adopted. Stereo digital image correlation (DIC) was used to record the surface deformation history over the full 50 mm length of the test section and approximately one third of its circumference. An ARAMIS based DIC system with two 5 MP cameras was used. A facet size of 24×24 pixels ($\sim 0.28 \times 0.28$ mm) and spacing of 12 pixels (~0.14 mm) were used covering the field of view (FOV). Typically a stage was recorded every 5 seconds. Post-processing of

the recorded stages allows determination of the axial and circumferential engineering strains ε_x and ε_θ.

As is well established, the latent heat associated with transformation-induced deformation can heat/cool the specimen, changing the recorded stress. It is thus imperative that, in material characterization experiments, stresses be recorded under isothermal conditions (Shaw and Kyriakides [1995], Bechle and Kyriakides [2014]). This is usually accomplished by performing the tests in a circulating liquid bath at a slow strain rate or, in the case of compression, by passing a liquid through the specimen at a constant flow rate. Because of constraints placed by the optical diagnostic techniques used in the present experiments, surrounding the specimen with water was not possible; instead, the strain rate was maintained at a slow enough level to ensure that any released heat was dissipated by conduction and radiation. In the biaxial experiments performed, the rate of loading was determined by the rate at which water was pumped into the system, which was typically at 0.02 ml/min.

The adequacy of this arrangement was checked by monitoring the temperature of the deforming specimen with a thermocouple. For select experiments, the temperature of the full test section was monitored with an infrared camera. For most of the experiments, the 0.02 ml/min flow rate proved to be adequate in that temperature changes were kept below ±1 °C. However, for higher values of the stress ratio α, the required volume change is relatively small. In such cases, volume-control pressurization is not ideal, causing the induced, mainly axial, localized deformation to develop rather rapidly. This is turn results in modest increases/decreases in the local temperature of up to ±3 °C. Such temperature changes will be reported in the results that follow. See Section 5.3 for a more thorough investigation into the thermomechanical interaction.

4.2 REPRESENTATIVE RADIAL STRESS EXPERIMENTS

Results from two representative experiments are now used to describe the material response to radial $\sigma_X - \sigma_\theta$ loading histories. In order to connect to the uniaxial experiments reported in Chapter 2, we start with the uniaxial tension experiment. Results from a radial biaxial experiment with $\sigma_X = 0.375\sigma_\theta$ will follow.

(a) Uniaxial Tension Test: $\sigma_\theta = 0$

In this case the specimen was pulled under displacement control at a rate that induced an axial strain rate of 5×10^{-5} s^{-1} when deformation was homogeneous. Figure 4.3 shows the nominal stress-mean strain ($\sigma - \bar{\varepsilon}$) responses recorded in the axial, *x*, and hoop, θ, directions. The "mean" strain in each direction represents the spatial average over the full 320×60 facet FOV monitored (measurement accuracy $\bar{\varepsilon}_X \sim |0.04\%|$, $\bar{\varepsilon}_\theta \sim |0.09\%|$). Figure 4.4 shows 20 sets of full-field DIC contours of axial and hoop strain corresponding to the numbered bullets on the responses in Fig. 4.3. The FOV has a hoop span of about 6 mm of the unwrapped circumference, which is a consistent dimension for the hoop span of all DIC contours in this chapter.

The overall behavior is similar to the results reported in Section 2.2. However, this section will be used to describe the diagnostic measures for deformation that will be referenced throughout the discussion of the biaxial experiments. Consequently, the results are analyzed in some detail. The response exhibits an initial stiff and nearly linear branch during which the A phase deforms elastically and homogeneously as depicted in images ①. From this part of the response the elastic modulus, E_A, is measured to be 65.7 GPa (9.53 Msi) and the Poison's ratio, $\nu_A = 0.424$ (see additional results in Fig. 4.33). A small reduction in the modulus is observed at stress values higher than 400 MPa indicating that some small amount of material is starting to transform (see Shaw and Kyriakides [1995]).

However, the deformation remains homogeneous up to a stress of 458 MPa when two helical higher deformation band-like patterns initiate from the two gripped ends (②) (compares with transformation stress of 381 MPa of the tension test in Chapter 2). The two helixes follow opposite directions, presumably along the two Hill [1952] characteristics, but the bands make the same angle with the axial direction. They grow by forming helical patterns around the tube surface (③) with their strain quickly growing to levels close to 7% that is associated with martensitic transformation. The tips of the propagating helical bands are relatively sharp while, behind, the bands tend to broaden. As expected, the gradual propagation of M takes place with the stress remaining nearly constant.

The major events can be summarized as follows:

- By image ④, propagation of the tip of the top band is halted and a set of additional helical patterns initiate from the transformed region behind the leading band with approximately the same orientation as the parent front. The multi-helical front propagates as shown in images ⑤-⑧. Such multi-helical patterns are often preferred as they tend to minimize structural distortion to the tubular specimen.

- In the neighborhood of image ⑨ ($\bar{\varepsilon}_x \sim 6.5\%$), the top and bottom fronts are about to coalesce and this leads to the tracing of the customary stress valley.

- By point ⑩, the stress has taken an upswing and the corresponding images show the deformation to be again uniform at a level of just over 7%.

Unloading commences at this point at the same displacement rate. Initially, deformation is once more uniform (⑪ and ⑫). At a stress of 234 MPa (33.9 ksi) M→A transformation initiates at the lower end in the form of a multi-helical front with a single pointed band connecting it to the bottom end (see image ⑬; see detailed study of such

fronts in Feng and Sun [2006]). In images ⑬ and ⑭ the front propagates leaving behind material that has transformed to A at a strain corresponding to the end of the lower plateau. At $\bar{\varepsilon}_x \sim 4.5\%$, close to image ⑭, an additional front appears in the FOV at the top of the specimen developing again a multi-helical front with the opposite chirality (see ⑮). The two fronts propagate simultaneously until the strain is down to $\bar{\varepsilon}_x \sim 1.4\%$ when they begin to interact (image ⑱), eventually forming a single inclined band that can be seen in image ⑲. Their coalescence is accompanied by the usual small stress peak. Subsequently the specimen, now fully transformed to the A-phase, unloads with the A elastic modulus, returning to zero stress at a strain of 0.08% (this residual strain is of the order of the accuracy of the DIC measurements.)

A more quantitative measure of the extent of inhomogeneity in the specimen is established as follows. A number of equally spaced "bins" of strain levels spanning the range of strains recorded are first generated. For each DIC data set, the bins are populated with the number of points with the corresponding strain range from the entire 320×60 facet field. The resultant frequencies are then smoothed using a Gaussian filter to form a continuous distribution, and the smoothened frequency distributions are normalized such that the peak frequency is unity. Figure 4.5 shows such histograms of axial strain corresponding to the 20 images in Fig. 4.4. The histogram for image ①, in which the deformation is homogeneous, exhibits a relatively narrow unimodal distribution corresponding to the current strain level. For image ③, a bimodal distribution begins to develop with the second mode centered around a strain of about 7%, due to coexistence of two deformation regimes. As M propagates through the specimen, the amplitude of the higher strain mode grows while that of the lower strain gradually reduces. On the completion of the transformation (⑩), the small strain peak disappears and the

distribution becomes unimodal again. The peak centered around 7% strain reaches its highest amplitude and its narrowest form. Such histograms have been generated for both axial and hoop strains for each experiment. (Note that the histograms are based only on the DIC FOV.)

An alternative method of relating the temporal and spatial evolution of transformation is as follows. The axial position of the front(s) is established from the image record. Used together with the time of the image an x-t diagram of the evolution of the front is constructed. In tension experiments on small diameter SMA rods and strips (Shaw and Kyriakides [1995, 1997]) and steel strips that develop Lüders bands (Butler [1962]; Kyriakides and Miller [2000]), such diagrams revealed that fronts propagated continuously until the whole specimen was transformed. The velocity of the front, c, could then be related to the applied displacement rate, $\dot{\delta}$, and the transformation (or Lüders) strain, $\Delta\varepsilon^t$, as follows:

$$c = \frac{\dot{\delta}}{n\Delta\varepsilon^t} \tag{4.3}$$

where n is the number of active propagating fronts. The evolution of transformation in the tubular specimen is complicated by transitions from single to multi-helical fronts, temporary halts of propagation at specific sites, transformation outside the FOV, etc. Such complications made tracking of the evolution of fronts during the A→M stress plateau difficult. However, the M→A transformation progressed in a more orderly manner, which enabled tracking of the position of the center of the front in the FOV and construction of the x-t diagram shown in Fig. 4.6. Included is the average strain corresponding to the time axis (note that $\bar{\varepsilon}_x$ is not directly proportional to time). The diagram is broken up into several data sets corresponding to distinct events observed in the FOV. Data sets 2 and 3 correspond to the upward propagation of the multi-helical

front at the lower end of the specimen. The two data sets trace linear trajectories with slopes, or speed of propagation, much lower than the value of a single front propagation yielded by (4.3)—with $\Delta\varepsilon^t = 0.054$. This is an indication that additional transformation activity is taking place outside the FOV (with data set 2 also seeing the effect of simultaneous single and multi-helical fronts).

Data set 4 corresponds to the appearance and propagation of the upper front in the FOV. Its velocity is lower than the corresponding part of set 3, but interestingly the average of the propagation velocities of 3 and 4 is close to the value yielded by (4.3) for $n = 2$. Data sets 5 and 6 correspond to the propagation of the upper and lower multi-helical fronts toward each other (e.g., images 16 and 17 in Fig. 4.4). The speed of the lower one is significantly higher than that of the upper one, but the average speed again approximately coincides with that yielded by (4.3) for $n = 2$. Thus, unlike observations of fronts made on strips and small diameter rods where fronts tended to propagate simultaneously at essentially the same speed, in the present tubular experiment coexisting fronts were observed to propagate at different speeds.

The orientation of banded localized deformation has received significant attention over the years and the present set of biaxial experiments offer a means for evaluating various propositions. The orientation of the bands is determined at the nucleation of transformation. In the uniaxial tension case, two bands initiate from the ends of the specimen and enter the FOV. Figure 4.7 shows an expanded view of the band at the lower end of the FOV. The inclination of the band to the axis of the tube, ϕ, is taken to be that of the bisector of the edges of the inclined fingers. In this case $\phi = 55.8°$, a value that corresponds to inclinations measured in tension tests on NiTi strips (Shaw and Kyriakides

[1998]) and steel strips that develop Lüders bands (Kyriakides and Miller [2000]; Hallai and Kyriakides [2013]).

A separate tensile experiment was performed that was monitored with an infrared camera in order to assess temperature changes induced by latent heats of the transformations. The specimen was coated with a matte black paint and DIC lights were not used to minimize IR noise and avoid any potential additional heating. The specimen was pulled at the same displacement rate as that used in the test in Fig. 4.3, with the net extension of the specimen monitored with a non-contacting laser extensometer. The stress-average strain response recorded has plateaus with very similar stress levels and extents. Additionally, the deformation patterns that can be inferred from the thermographic record are also similar. The slow propagation of fronts coupled with relatively small temperature changes and the thin wall of the specimen results in a diffuse temperature profile. During the A→M transformation an increase of about 0.9 °C was observed at front edges with a maximum temperature increase of 1.4 °C at the coalescence of propagating fronts. The M→A transformation profile was again diffuse, although less so than that of the forward transformation, with front temperatures of -0.7 °C and a minimum of -1.8 °C at coalescence (see Section 5.3 for a more detailed analysis of the thermomechanical interactions).

(b) Radial Biaxial Experiment: $\sigma_x = 0.375\sigma_\theta$

This is a radial biaxial experiment loaded under volume control as outlined in Section 4.1 and, as such, is representative of the rest of the biaxial experiments in this study. The water was pumped into the specimen at a rate of 0.02 ml/min and the induced radial stress history is included in Fig. 4.8. During homogeneous deformation, this

induced a hoop strain rate of 2.8×10^{-6} s^{-1}. Figure 4.9 shows the nominal stress-mean strain $(\sigma-\bar{\varepsilon})$ responses recorded in the axial and hoop directions. DIC images were taken at 6 s intervals and Fig. 4.10 shows 20 select sets of axial and hoop strain contours corresponding to the numbered bullets on the responses in Fig. 4.9. Figure 4.11 shows the corresponding histograms of hoop strain. Both responses trace closed hystereses, with $\sigma_\theta-\bar{\varepsilon}_\theta$ being significantly larger. Because α is relatively small, the axial strain is dominated by the Poisson effect and as a result it is negative. The initial linear moduli of the responses of biaxial experiments are listed under $\sigma_\theta/\varepsilon_\theta\big|_A$ and $\sigma_x/\varepsilon_x\big|_A$ in Table 4.1 and are included in Fig. 4.33. A gradual reduction in stiffness commences at a hoop stress of about 500 MPa (72.5 ksi), presumably due to some transformation to M, but deformation remains uniform at least up to $\sigma_\theta=542$ MPa (image ①). Subsequently, transformation to M accelerates, forming gradual knees in the two responses that ease into nearly flat stress plateaus. At $(\sigma_\theta,\bar{\varepsilon}_\theta)=$ (549 MPa, 0.78%), localized deformation in the form of a sharp tipped band has entered the FOV (seen in image ② at $\sigma_\theta=$ 556 MPa) at an inclination of 32.7° to the axis of the tube. It is interesting to observe that, unlike the pure tension test, here nucleation occurs at gradually increasing stresses. Because of this rounding, we have adopted two methods for establishing the nucleation of transformation. The first is based on the "inelastic" work ΔW^t, which is a measure of the nonlinearity of the response. The second is based on the intersection of two tangents at the knee of the response as shown in Fig. 4.12. The nucleation stresses $\{\sigma_{xNM},\sigma_{\theta NM}\}$ listed in Table 4.1 are based on the second criterion.

The initial band develops into a multi-pronged one that, by image ③, has evolved into a triangular island with a hoop strain of about 5% while the rest of the FOV remains relatively undeformed at the strain of the stress knee (0.85%). While this island of

transformed material grows, a second narrow helical band of transformation develops from the top right with the same orientation as the initial band but propagating in the opposite sense as shown in image ④.

The two transformed zones grow and coalesce near the mid-height of the specimen at $\bar{\varepsilon}_\theta \approx$ 2.52%. The coalescence leaves behind a diamond shaped island of A near mid-height (image ⑤). Subsequently, transformation switches to mainly broadening of the upper zone with less change in the lower one, followed by a new narrow band at the top, which can be seen fully developed in image ⑦. Beyond point ⑨, most of the remaining islands of A have transformed and the stress takes an upswing. Loading is terminated at point ⑩ at $\sigma_\theta =$ 626 MPa. In Table 4.1 we report the extent of the transformation plateaus as $\Delta\varepsilon^t_{\theta M}$ and $\Delta\varepsilon^t_{xM}$. They represent the difference in strains at the beginning and end of the plateau established by the extrapolations shown in Fig. 4.12.

Unloading is conducted at the same flow rate and commences at point ⑩ and deformation is once more nearly uniform through point ⑪. However, some weak striped lower strain patterns near the middle of the specimen become discernible. An abrupt knee forms at $\sigma_\theta \approx$ 340 MPa as M→A transformation initiates in the specimen. Three parallel narrow islands of transformed material appear and can be seen in the middle of image ⑫ at the location mentioned earlier. Clearly these are sites that were the last to transform to M and had required somewhat higher stress to complete transformation. It appears that on unloading they start to transform to A at a somewhat higher stress than the rest of the specimen. The stress stabilizes at about 335 MPa and soon thereafter additional transformation fronts appear first at the top and then at the bottom of the FOV. These are also zones that transformed late to M. It is also interesting that all transformation zones and fronts have the same orientation, which also corresponds to what was observed

during the M transformation. In image ⑬, a triangular island of A has formed at the bottom and an approximately V-shaped one at the top. In images ⑮ and ⑯ these two zones have propagated towards the center with clear inclined fronts. Simultaneously the central striped islands of A have started growing so that by image ⑰ a single inclined zone of M remains. It continues to narrow until in image ⑲ at $(\sigma_\theta, \bar{\varepsilon}_\theta) = (322$ MPa, 0.62%) it has been reduced to a single narrow band. Transformation is completed soon thereafter when the hysteresis closes and further unloading follows the trajectory traced during loading.

One other variable that we will be tracking is the strain energy expended during the load unload cycle, W^t. It represents the areas enclosed by the two hystereses, which in this case is 12.93 MPa (Table 4.1).

The deformation histograms in Fig. 4.11 give an overall picture of the extent and evolution of inhomogeneous deformation in the FOV. In ① and ② the distribution is unimodal centered around $\bar{\varepsilon}_\theta$ of about 1%, at the beginning of the stress plateau. Subsequently, it becomes bimodal with a second peak centered about a strain of 5% that corresponds to nearly the end of the plateau. The larger strain peak gradually becomes the major mode during A→M transformation with the small strain peak disappearing in ⑨. The reverse transformation exhibits similar strain distributions following the reverse order.

In this experiment the temperature was monitored with an infrared camera. During A→M transformation, a temperature change of 1.2 °C was recorded at the edges of propagating fronts while a maximum temperature increase of 2.2 °C was recorded at the coalescences of transformation fronts. This temperature change may have contributed to the observed increase in the stresses. During the reverse transformation, a diffuse

cooling front of -1.2 °C developed that initially followed the propagating fronts at the bottom and top of the FOV. From points ⑯ to ⑲ this temperature decrease spread to the whole central section.

In summary, for this stress ratio, nucleation of M and A transformation resulted in less abrupt stress transitions, but their evolution led to inhomogeneous deformation.

4.3 RADIAL STRESS BIAXIAL EXPERIMENTS

We now review results from the rest of the radial stress biaxial experiments, concentrating on a select number of experiments whose behavior is representative of those of neighboring stress ratios. Along the way, we will be tracking some of the main parameters of the responses and listing them in Table 4.1. The trends of the key parameters in the biaxial stress space examined will be presented and discussed in summary in Section 4.5 of this chapter with analysis of the experiments in Chapter 5.

(a) $\alpha = 0$ $(\sigma_X = 0)$

This is a uniaxial test in the hoop direction and as such serves as a complement to the uniaxial tension test described in Section 4.2a. This specimen was also loaded at a volume rate of 0.02 ml/min which induced a hoop strain rate of 4×10^{-6} s^{-1} during the homogeneous parts of the deformation (details about the effect of the testing facility stiffness on the induced strain rate appear in Appendix D). The end-cap effect was compensated by feedback producing a purely σ_θ stress state as shown in Fig. 4.8. The recorded $\sigma_\theta - \bar{\varepsilon}_\theta$ response is shown in Fig. 4.13a and accompanying sets of twelve hoop and axial strain contours in Fig. 4.13b. The load-unload cycle produced a closed hysteresis similar to that for $\sigma_X - \bar{\varepsilon}_X$ one in Fig. 4.3. The initial elastic modulus, E_A, is 66.8 GPa and the Poisson's ratio, ν_A, is 0.426, both values close to those of the uniaxial

tension test. A mild nonlinearity in the response is observed above 340 MPa, but in image ①, at 454 MPa, the FOV remains uniformly strained. At 458 MPa the stiffness undergoes a rapid drop forming a knee and a single dextral (right-handed) helical band initiates on the lower LHS of the specimen. This band initiated close to the middle of the specimen outside the FOV. Table 4.1 reports the transformation stress ($\sigma_{\theta NM}$) to be just under 470 MPa, which compares with the corresponding value of 459 MPa for the axial tension test (Table 4.1). This band can be seen more developed with the hoop strain reaching more than 5% in image ② somewhat later. It has an inclination of 29.1° to the axis of the tube, which is somewhat smaller than the complement of the 55.8° angle of the initial band inclination under uniaxial tension (Table 4.1). With increased deformation the band broadens and a second band appears near the top end while the stress stabilizes at about 472 MPa. Image ③ shows the lower third of the specimen transformed, and the helical band at the top to have grown significantly. In image ④ the transformed zone in the lower part of the specimen continued its growth and the helical band above it has broadened further while the stress has gradually increased to 478 MPa. This increase may have been caused by a temperature increase of approximately 1.6 °C resulting from the released latent heat (recorded with an infrared camera in a separate experiment under the same loading and environmental conditions). With additional deformation, the existing bands broaden and several secondary bands develop. Transformation is essentially completed by $\bar{\varepsilon}_\theta \approx 5.4\%$ at a stress of 485 MPa, but small residual islands of A (e.g., image ⑤) transform at somewhat higher stress. Loading is terminated at ⑥ at $(\sigma_\theta, \bar{\varepsilon}_\theta) =$ (509 MPa, 5.66%). Interestingly, the transformation strain, $\Delta\varepsilon^t_{\theta M}$, is 4.76%, which is significantly lower than the corresponding value of 6.17% for the uniaxial tension experiment. The

corresponding axial strain is strictly due to the Poisson effect and consequently the contours show the same patterns.

During unloading, the specimen initially deforms homogeneously until the stress drops to 323 MPa when a single dextral band of A appears near the center of the FOV. It can be seen somewhat later in image ⑧ together with a second band. The first band appears to have initiated from the site that transformed last during the forward transformation. A stress plateau develops during which bands of A grow until the whole specimen is back to A. Unlike loading, several multi-pronged patterns develop during unloading that can be seen in images ⑨ and ⑩. The last island to transform is a band that appears to be at the same location as the one that nucleated first during loading. As unloading progressed the temperature dropped by -1.6 °C and on its completion the stress has dropped to 363 MPa. Beyond this point the specimen unloads with modulus E_A. The hysteresis energy $W^t = 10.21$ MPa, which compares with 13.49 MPa for the axial tension test (Table 4.1, Fig. 4.36). Since the transformation stresses in the two directions have similar values, this difference is primarily due to the smaller hoop direction transformation strains.

Our experimental setup facilitated the conduct of a number of experiments with negative values of α. This was achieved by reducing the length of the test section in order to ensure that axial compression did not lead to buckling. We place these experiments in two groups with similar behavior.

(b) $-0.25 \le \alpha \le -0.50$

The first group involves experiments with stress ratios of -0.25, -0.375, and -0.50. We briefly discuss results for $\sigma_x = -0.375\sigma_\theta$, which are representative of all three. The length of the test section was reduced to 38 mm (1.5 in) and pressurization was conducted

at a volume rate of 0.015 ml/min. The induced radial path is shown in Fig. 4.8. The recorded stress-average strain responses are shown in Fig. 4.14a and sets of corresponding strain contours in Fig. 4.14b. The axial and hoop stress-average strain responses trace closed hystereses characterized by nearly flat stress plateaus and transformation leads to inhomogeneous deformation. A major difference from responses for positive α, is that both the axial stress and strain are compressive. Transformation starts at $(\sigma_x, \sigma_\theta)_{NM}$ = (-155, 416) MPa as the two responses develop rather sharp knees. Simultaneously, a single sinistral (left handed) band of transformed material initiated from the upper gripped end of the specimen with an inclination of 30.5° to the axis of the tube (see image ①). The band gradually broadens and lengthens covering first the upper part of the FOV (see image ②), but gradually propagating towards the lower end as shown in images ④ and ⑤. Interestingly, in this case transformation evolved through this single band. Residual islands of A at the top and bottom transform when σ_θ is increased to 458 MPa (image ⑥).

On unloading, the specimen deforms uniformly down to σ_θ = 243 MPa, when transformation to A initiates from the zones that transformed last during loading in the upper and lower corners of the FOV (see image ⑧). The hoop and axial stresses trace plateaus at approximately 234 MPa and -87 MPa, respectively, while inclined transformation zones propagate from the upper and lower corners inwards. In essence, the transformation bands follow a nearly reverse evolution to that followed during loading. Both hystereses close and further unloading follows the loading responses. The hysteresis energy is now 10.27 MPa.

Overall, the results for α of -0.25 and -0.50 exhibit similar trends. Their responses are similar to those of α = -0.375 with the main variables listed in Table 4.1.

As the axial stress becomes more compressive, the hoop transformation stress decreases and $\Delta\varepsilon_x^t$ increases. The hysteresis energy for α = -0.25 is nearly the same as for 0, but increases for the two lower values of α (see Section 4.5). For -0.50, transformation induced deformation is mainly through the evolution of a single band, similar to what is observed in Fig. 4.14b for -0.375. By contrast, -0.25 exhibited more multi-helical localization patterns that resemble those observed for $\alpha = 0$.

(c) $-0.75 \le \alpha \le -1.0$

The second group of experiments with compressive axial stresses includes stress ratios of -0.75, -0.88, and -1.00. The length of the test section was reduced to 32 mm (1.25 in) and pressurization was conducted at a volume rate of 0.015 ml/min. We first discuss results from $\sigma_x = -0.75\sigma_\theta$ that are representative of the three in this group. The induced radial path is included in Fig. 4.8 (a brief deviation observed in this radial path is due to temporary loss of feedback control during unloading). The recorded stress-average strain responses are shown in Fig. 4.15a and sets of corresponding strain contours in Fig. 4.15b (note that because of the shorter test section, the field of view has been reduced to 16.4×6.5 mm). The nucleation of M during loading and A during unloading induce quite sharp stress knees. In fact, a small stress peak develops at the nucleation of M. Transformation progresses by inhomogeneous deformation reflected in both strain contours. It takes the form of multi-pronged sinistral helixes of M that appear nearly simultaneously both at the lower and upper ends of the FOV (image ②). Interestingly, the lower cluster has more prongs than the upper one, but both sets of helixes are inclined at about 38° to the tube axis. This inclination is somewhat larger than the angles measured for single nucleation bands from the other negative stress ratio experiments (Table 4.1). In images ③ and ④ the helixes grow gradually transforming the rest of the test section

with the stresses remaining essentially unchanged. The helixes meet in image ⑤ and the stresses start to increase indicating the completion of the unstable part of the transformation.

During unloading, the specimen deforms uniformly down to $(\sigma_x, \sigma_\theta)$ of about (-148, 199) MPa, when transformation to A initiates at the top end with multi-helical bands of both chiralities (see image ⑧). This deformation pattern propagates downwards (image ⑨) with the stresses remaining essentially unchanged. The propagation continues until $(\bar{\varepsilon}_x, \bar{\varepsilon}_\theta) \approx (-1.85, 3.18)\%$ when the sinistral bands decay and simultaneously dextral bands initiate from the bottom of the FOV (seen somewhat later in image ⑩). This switch appears to be necessary for compatibility between the top and bottom helixes. Further transformation is by upward propagation of the lower helixes and is completed a little after image ⑪ with the stresses dropping to (-143, 192) MPa. The two hystereses have closed and further unloading is by uniform deformation of A. The hysteresis energy W^t is 10.52 MPa a value that is in line with those of the other negative stress ratio experiments.

The results for α of -0.88 and -1.0 have the same trends. The transformation stresses continue to drop as α becomes more negative. Transformation induces inhomogeneous deformation with the stresses remaining essentially constant both during loading and unloading. For α = -0.88, A transforms by multi-pronged sinistral helixes that emanate from the top and bottom ends and propagate towards the middle. In the case of -1.0 the multi-pronged helixes are of both chiralities (see Fig. 4.16). On unloading, M transforms mainly with multi-pronged sinistral helixes for -0.88 but for -1.0 single inclined bands develop like those reported for larger α. It is worth pointing out that multi-pronged helical bands with dual chirality appear to be more common for shorter

specimens as a means of staying straight as dictated by the length constraint (e.g., see Feng and Sun [2006], Reedlunn et al. [2014] for tubes and Shaw and Kyriakides [1998] for strips transforming under axial tension). The extents of the hoop strain plateaus decrease and those of axial strain increase somewhat as α becomes more negative. The transformation energy in these two cases is at a similar level as that of the other negative stress ratios.

(d) $0 < \alpha \leq 0.50$

Experiments with lower positive values of α were conducted for 0.05, 0.25, 0.375, and 0.50. Overall the behavior recorded was similar to that of $\alpha = 0.375$ described above. The trends observed and highlights can be summarized as follows. All cases exhibit closed $\sigma_\theta - \bar{\varepsilon}_\theta$ hystereses with relatively flat upper and lower stress plateaus. The axial hystereses exhibit negative strain, the extent of which decreases as α increases. The onset of M transformation is less abrupt than those of the two uniaxial loading cases, inducing a somewhat rounded stress knee. Transformations leads to inhomogeneous deformation in the form of inclined bands that start with an inclination that hovers around $\phi = 30°$ to the axis of the tube, but ϕ drops to about 25° for $\alpha = 0.50$ (see Fig. 4.17). As the loading continues, the higher deformation bands grow, gradually covering the whole specimen while the stress remains nearly constant (small increase may have been caused by small increases in temperature due to the released latent heat). Both nucleation stresses, σ_{xNM} and $\sigma_{\theta NM}$, increase with α (Table 4.1). The hoop transformation strain, $\Delta\varepsilon^t_{\theta M}$, remains nearly unchanged while $\Delta\varepsilon^t_{xM}$ gradually decreases as α increases.

On unloading, the specimens initially deform homogeneously. Transformation back to A initiates with rounded transitions to relatively flat stress plateaus are being traced. The transformation stresses $(\sigma_{xNA}, \sigma_{\theta NA})$ increase with α. During the lower

stress plateau the deformation is inhomogeneous with its evolution following approximately the reverse order to that followed during loading. The hysteresis energy, W^t, increases with α reaching 12.93 MPa for 0.375 but drops to 12.37 MPa for 0.5 (Table 4.1).

(e) $\alpha = 0.60$

The responses and the deformation images for $\sigma_x = 0.60\sigma_\theta$ shown in Fig. 4.18 appear to set different trends than those of the lower values of α reported thus far. The transition "knees" in the two responses are more gradual and the two stresses monotonically increase/decrease during transformation. Following the trend set thus far, transformation nucleates at even higher stresses $(\sigma_x, \sigma_\theta)_{NM} = (361,\ 596)$ MPa. Furthermore, the first signs of inhomogeneous deformation are the form of relatively weak axial bands such as those seen in image ② and more intense in image ③. Therefore, the band inclination ϕ is reported as 0° in Table 4.1. It is noteworthy that these initial bands are not registered in the corresponding axial strain contours. Inclined bands of higher strain emanate from the top and bottom of the FOV around a hoop stress of 606 MPa, and a strain of 1.85% just before image ④. In this image, a single dextral narrow band has also developed near the lower end. The inclined bands propagate towards the center (image ⑤) where they meet, forming a diamond shaped island of relatively undeformed material that can be seen in image ⑥. Transformation is completed around $(\sigma_\theta, \bar{\varepsilon}_\theta) = (629$ MPa, 4.74%) but loading continued to a hoop stress of 673 MPa. In the process the axial response traces a higher stress than in lower stress ratios (due to the higher α) but a smaller strain.

On unloading from ⑦, the specimen deforms homogeneously down to $(\sigma_\theta, \bar{\varepsilon}_\theta) =$ (390 MPa, 4.05%), just beyond point ⑧. An island of lower strain has nucleated at the site

of the termination of forward transformation. This island develops into two sinistral inclined bands that can be seen in image ⑨. The bands broaden and lengthen as can be seen in image ⑩. In image ⑪, most of the FOV has been transformed to a hoop strain of about 0.42% but a weak narrow band of higher strain remains in the center of the FOV. In image ⑫, this band is the only zone of higher strain that remains and is reminiscent of a similar band in image ② during loading. This band is seen to be disappearing in image ⑬ very close to the point where the response rejoins the initial linear modulus of A. The axial deformation reflects the hoop strain patterns except that the weak longitudinal bands at the end are not registered.

In summary, the M nucleation stresses have increased for this stress ratio as have the stresses at the completion of transformation with the difference between nucleation and completion increasing over those of smaller α (due to monotonic increase in stresses during transformation). The transformation is completed in smaller strains and W^t is smaller. The initial angle of transformation is essentially 0°.

(f) $\alpha = 0.85$

We now consider results for $\alpha = 0.85$ (Fig. 4.19), which turns out to be very similar to those of 0.75. Transformation nucleates at higher stresses than in smaller values of α forming a gradual transition knee at $(\sigma_x, \sigma_\theta)_{NM} = (553,\ 614)$ MPa. Transformation takes place with increasing stress (Table 4.1) and is completed in smaller strains than previous stress ratios. Localized deformation in the form of a weak axial band is seen in the hoop contour in image ② during the stress knee. It grows axially as seen in image ③ and progressively consumes the entire FOV as seen in images ④, ⑤, and ⑥. Transformation appears completed by $(\sigma_\theta, \bar{\varepsilon}_\theta) \approx$ (685 MPa, 3.53%), but the stress was taken to 735 MPa and hoop strain of 3.89% before commencing unloading (⑦). As

pointed out earlier, the axial strain has been decreasing as α increased. For this particular stress ratio, no axial hysteresis is traced and, in tandem, the hoop strain localization does not register in the axial strain contours. Reducing the DIC scale to 0 to 1.0% confirms this lack of localization (Fig. 4.19c). The Poisson effect of the dominant hoop transformation strain appears to be a near perfect complement to the corresponding axial transformation strain.

On unloading, transformation to A commences at approximately $(\sigma_\theta, \bar{\varepsilon}_\theta) \approx$ (469 MPa, 3.13%). It takes the form of axial bands of lower strain that emanate from the bottom of the FOV. In fact, it appears that A nucleates at the site that transformed last during loading (compare images ⑥ and ⑨). The lower strain zone propagates upwards following essentially the reverse path to that followed during loading. Soon thereafter the specimen unloads with the initial linear loading modulus and the hysteresis closes. As was the case for loading, no change in the axial strain is registered in the unloading strain contours.

In summary, the nucleation stresses have increased and more pronounced hardening is observed during forward and reverse transformation. Transformation involves inhomogeneous deformation with a 0° orientation. It is completed in smaller hoop strain and no change in the corresponding axial strain. In addition, the hysteresis energy, W^t, has reduced from the local maximum value that occurred for α = 0.375.

(g) $1.0 \leq \alpha \leq 1.20$

Four sets of results near the equibiaxial stress ratio are discussed together, α = 1.0, 1.07, 1.15 and 1.20, because of common features exhibited by their behavior. In the case of α = 1.0 (see Fig. 4.20), the transformation stresses have continued to increase while the axial strain is now positive. However, the extent of the dominant hoop

transformation strain has decreased and consequently so has the transformation energy W^t. It is noteworthy that despite the equibiaxial state of stress, the axial transformation strain is significantly smaller than that in the hoop direction, $(\Delta\varepsilon_x^t, \Delta\varepsilon_\theta^t) = (0.94, 2.18)\%$, another sign of the anisotropy exhibited by the transformation strain pointed out earlier from the results of the two uniaxial stress experiments. Transformation induces even more gradual transition knees and pronounced hardening. For example, σ_θ increases by 101 MPa between nucleation of M and termination of transformation. The more dominant hoop strain contours exhibit very mild inhomogeneity with an axial orientation that broadens and spreads to the entire FOV (see images ③-⑤). In the axial strain contours, inhomogeneity is diffuse and a preferred orientation cannot be discerned. Reducing the DIC strain scale to 0-1.75% reveals weak features with diffuse strain gradients that are on the order of $\Delta\varepsilon_x^t$ (Fig. 4.20c). Grolleau et al. [2011] in a hydraulic bulge test on a circular NiTi sheet noted a hardening behavior and no localization at the apex.

In the case of α = 1.07 (Fig. 4.21) the axial response becomes dominant for the first time. Transformation induces gradual transition knees and monotonically increasing stresses. The results indicate that the responses develop equal hoop and axial transformation strains for a value of α between 1.0 and 1.07. The transformation strains remain relatively small as does W^t. The axial strain contours appear to be homogenous during both loading and unloading, which is confirmed by finer DIC scales. The hoop strain contours exhibit a mild inhomogeneity with a predominantly axial orientation. An axial feature first seen in image ② gradually spreads to the whole FOV. In this case loading may have been terminated before transformation to M was completed. Thus the

$(\sigma_x, \sigma_\theta)_M$ values reported in Table 4.1 originated from a second experiment with the same stress ratio that was taken to somewhat higher stresses.

The results for α = 1.15 are similar to those of 1.07. The responses remain monotonic, the size of the hoop hysteresis is reduced further, and W^t remains relatively low. The axial strain is essentially homogeneous with the contours exhibiting diffuse patterns with no identifiable preferred orientation. The hoop strain contours display a mild inhomogeneity with predominantly axial orientation.

Figure 4.22 shows the results for α = 1.20, where the hoop hysteresis has almost disappeared (similar to axial response for α = 0.85). The axial response maintains its monotonic nature with the axial transformation strain recording an increase. The transformation stresses remain relatively high, and W^t registers an increase over the previous three stress ratios. The axial deformation is essentially homogenous exhibiting very mild features oriented in the transverse direction. The hoop strain is very small and homogeneous except for a suspect axial region on the left edge of the FOV. At a reduced strain scale of 0-1.0% the hoop contours confirmed homogeneity outside this edge region prompting the conjecture that it may be an edge effect caused by the small values of strain involved.

In summary, all results close to the equibiaxial stress state exhibit responses with monotonically increasing stresses and, as a result, a significant difference is registered between the values at the onset and completion of transformation. The transformation strains are both positive and at their smallest achieving equal values around a stress ratio of about 1.05. The hysteretic energy recorded is at its lowest. Deformation is essentially homogeneous with mild features appearing for some cases that are mainly in the transverse direction for the axial strain and in the axial direction for the hoop strain.

(h) $\alpha = 1.26, \alpha = 1.30$

The two stress ratios of 1.26 and 1.30 represent the transition to axially dominant deformations and to increasingly more inhomogeneous deformations. Furthermore, the hoop hysteresis has now switched to negative strain. Figure 4.23 shows the results of 1.30, which are representative of both cases. Figure 4.23a shows that transformation continues to lead to rounded transition knees followed by rising stress responses. The transformation stresses $(\sigma_x, \sigma_\theta)_{NM} = (669,\ 525)$ MPa are of the same order of magnitude as those in the equibiaxial neighborhood (Table 4.1). Deformation remains essentially homogeneous (see image ②) until the axial strain reaches about 1.35% when mild inhomogeneity is observed at the top and bottom of the FOV. It consists of patterns nearly orthogonal to the tube axis at the top and slightly inclined ones at the bottom. They can be seen in a more advanced state of development in image ③. The mild inhomogeneity is not registered in the hoop strain profiles presumably because their magnitude is significantly smaller. As the loading progresses, the transformation patterns become stronger with islands forming at the top and bottom (see image ④), gradually spreading towards the center (see image ⑤). The patterns remain primarily in the transverse direction, but several ones with slight inclinations can also be seen in images ③ and ④. No inhomogeneity is registered in the hoop strain profiles throughout the loading in the strain scale of Fig. 4.23b. Reducing the DIC scale to -1.0% - 1.0% reveals very weak features on the order of the DIC strain resolution (see Fig. 4.23c). Inhomogeneous deformation is completed by $(\sigma_x, \bar{\varepsilon}_x) \approx (710$ MPa, 4.32%) when the stress develops an increasing trend. Loading is terminated at $(\sigma_x, \bar{\varepsilon}_x) = (765$ MPa, 5.16%) (image ⑥). This experiment was also monitored with an infrared camera, which recorded a temperature increase of 1.6 °C at active transformation fronts.

As in all cases, during unloading the deformation initially is homogeneous (see image ⑦). Upon unloading, as transformation to M starts, a gradual stress knee is traced. The transformation stresses based on the tangent constructions are $(\sigma_x, \sigma_\theta)_{NA} =$ (415, 325) MPa. First signs of inhomogeneous deformation appear at $(\sigma_x, \bar{\varepsilon}_x) \approx$ (413 MPa, 3.58%) when weak, nearly transverse patterns appear at the sites last transformed during loading. They can be seen somewhat later in image ⑧. As unloading progresses, the patterns strengthen and spread throughout the FOV as observed in images ⑨ and ⑩. The patterns are mostly in the transverse direction, but some have small inclinations. As was the case during loading, the hoop strain contours remain homogeneous at the scale of Fig. 4.23b. At the end of transformation at point ⑫, the axial stress dropped down to 369 MPa. During the evolution of transformation the temperature of active fronts dropped by 0.7 °C.

Overall, for these two stress ratios, the transformation strains have increased over those near the equibiaxial stress ratios and the hysteresis energies are also on a rising trend. The band initiation angles have been registered as 90°.

(i) $1.52 \leq \alpha \leq 8.0$

We now report on results from a group of five radial paths with stress ratios that range from 1.52 to 8.0. They share many features that will be outlined through the representative case of $\alpha = 4.0$ (see also the response for $\alpha = 2.0$ in Section 5.3). Figure 4.24 shows the recorded stress-average strain responses and the corresponding strain contours from DIC for $\alpha = 4.0$. The responses trace closed hystereses with rather sharp transition stress knees followed by relatively flat plateaus for both loading and unloading. The transformation starts at $(\sigma_x, \sigma_\theta)_{NM} =$ (541, 138) MPa and leads immediately to inhomogeneous deformation. In image ② just after the onset of transformation, a sinistral

helical band of higher strain starts at the upper end, and wraps around the specimen with its sharp front appearing below. The axial strain in the band is about 7% (corresponding to the strain at the end of the stress plateau) while the rest of the specimen remains approximately at 0.84% (strain at nucleation of M). The inclination of the front to the axis of the tube is about 60°. Image ③ shows the helical band to have propagated one more time around the specimen, the front reaching the lower third of the length of the FOV while behind it the band has widened. In image ④ the end of the band has widened further and its front has reached the lower edge of the FOV. Subsequently, transformation takes place by widening of the now stationary band as seen in image ⑤. In image ⑥, at $\bar{\varepsilon}_x =$ 6.97%, a single sliver of A remains which, soon thereafter, transforms leading to the termination of the stress plateau and the observed upswing in the stress (point ⑦). It is interesting that the axial stress at the end of the plateau has reached 553 MPa, an increase of 12 MPa over the stress at the nucleation of M. The hoop strain contours are negative replicates of the axial strain but at much smaller levels.

On unloading from ⑦, deformation remains homogeneous until point ⑧ at $(\sigma_x, \bar{\varepsilon}_x) =$ (256 MPa, 6.12%). A sinistral multi-helical front of A enters the FOV at the lower end just before image ⑨. It propagates upwards developing into a front with helixes of both chiralities. In image ⑩ a second multi-helical front enters the FOV from the top. The two fronts of A propagate towards each other as seen in image ⑪. In image ⑫ the two fronts have evolved into "chevron-like" patterns where transformation takes place along both characteristics. In image ⑬, but for a small sliver, the specimen has transformed back to A while the stress drops to 221 MPa.

For stress ratios of 2.0 and higher the induced change in the specimen volume becomes increasingly smaller. Due to experimental constraints the flow rate was kept at

0.02 ml/min thus the induced strain rate increased. This meant that radiation and conduction could not dissipate the latent heat of transformation fast enough causing small increases in temperature during loading and decreases during unloading. The changes in temperature were larger than the approximately ±1 °C value reported for experiments with α < 1.3. Thus for example, in the case of α = 2.0 a temperature increase of 2.6 °C was recorded at the propagating fronts of transformation during loading and a decrease of 2.1 °C during unloading. In both cases the temperature changes nearly doubled in the latter parts of the stress plateaus when transformation fronts interacted with each other and eventually coalesced. Section 5.3 presents a more detailed description of the thermomechanical interactions for α = 2.0.

The corresponding values for the α = 8.0 stress ratio were 3.0 °C and -2.8 °C at discrete transformation fronts and again nearly double in the latter parts of the stress plateaus. Although thermal imaging was not performed for 4.0, we expect the temperature changes to be of the same order as these two sets of values. Since the transformation stress is temperature dependent, we consider the small increase in the stress during loading and decrease during unloading in Fig. 4.24 to be mainly caused by thermal heating and cooling.

The results for stress ratios of 1.52, 1.79, 2.0, and 8.0 exhibit broadly similar behaviors. As α increases, transformation results in more abrupt stress knees and both transformation stresses progressively decrease. It is important to point out that the values of the M nucleation stresses are not affected by latent heat effects so they correspond to 23 °C. Transformation progresses with the stress remaining essentially constant. Small increases in stress during A→M and decreases during M→A transformation appear to be mainly due to mild heating and cooling resulting from latent heats. In all five cases

transformation resulted in inhomogeneous deformation in the form of inclined bands of transformed material. The initial inclination of the bands was about 60° to the axis of the tube dropping to approximately 55° for uniaxial tension. Multi-helical transformation fronts were observed for α of 4.0 and 8.0 during unloading. The strains at the termination of transformation increase with α until α = 2.0 at which point the strains remained similar to the values recorded for uniaxial tension. The hysteretic energy exhibits the increasing trend observed for α of 1.0 and higher reaching a maximum value at 2.0. The energy exhibits a deceasing trend for higher stress ratios.

4.4 NON-RADIAL STRESS BIAXIAL EXPERIMENTS

4.4.1 Experimental Setup

Non-radial stress biaxial experiments were performed on the same NiTi tubular stock using the same biaxial testing facilities as those outlined in Section 4.1. Four "corner" stress paths were conducted as shown in Fig. 4.25. The present experiments were conducted prior to the complete implementation of the feedback control system outlined in Section 4.1, thus the loading involved first pressurization under fixed axial displacement (plane strain pressurization) to a chosen value of pressure, followed by axial stretching under fixed pressure until the completion of transformation. The reverse process was followed for unloading. During plane strain pressurization, the axial displacement was held constant while a constant volume flux was prescribed into the system at 0.02 ml/min. Specimens were pressurized to hoop stresses of: I: 154 MPa, II: 304 MPa, III: 456 MPa, and IV: 616 MPa. After the plane strain pressurization, the pump was set to constant pressure mode, and the axial displacement was prescribed at a rate that induced an axial strain rate of 5×10^{-5} s^{-1} when deformation was homogeneous.

4.4.2 Results

(a) Experiment I ($\sigma_\theta = 154$ MPa)

The axial and hoop nominal stress-mean strain responses for experiment I along with the corresponding axial and hoop strain contours are shown in Fig. 4.26. During the initial pressurization, the deformation remained uniform. During axial loading, transformation to M commences at $\sigma_X = 527$ MPa (image ①), and a flat axial stress plateau is traversed. Transformation deformation takes the form of a single sinistral helical band that begins at the bottom of the specimen, and gradually helically traverses the entire length by image ⑨. Transformation is completed by image ⑩ when the deformation returns to being uniform. Upon unloading, deformation is uniform until $\sigma_X = 305$ MPa (image ⑪), at which point transformation back to A begins. A transformation deformation initiates at the top (location of M transformation termination), but this time is in the form of a multi-pronged helical front as seen in image ⑫. Subsequently, a second front forms at the bottom. The two fronts evolve as they propagate along the specimen length as the stress remains essentially constant. Transformation back to A completes and the specimen returns to the undeformed configuration. The axial response $(\sigma_X - \bar{\varepsilon}_X)$ displayed the customary hysteresis; however, there was no hysteresis in the hoop response $(\sigma_\theta - \bar{\varepsilon}_\theta)$.

(b) Experiment II ($\sigma_\theta = 304$ MPa)

The responses for experiment II along with the corresponding axial and hoop strain contours are shown in Fig. 4.27. During the initial pressurization, the deformation was again uniform. Transformation to M commences when the axial stress reaches 592 MPa, followed by a flat axial stress plateau. Deformation takes the form of an inclined

multi-pronged helical front that begins at the bottom. A second similar front becomes visible at the top in image ②. Both fronts propagate toward the center of the specimen where they coalesce and the deformation becomes uniform ⑩. Upon unloading, deformation is uniform until $\sigma_X = 358$ MPa (image ⑪) at which point transformation back to A begins. A transformation occurs in nearly the reverse manner to that of M transformation, with two additional fronts, one each at the top and bottom, visible by image ⑭. The fronts propagate along the specimen length as the stress remains nearly constant. Transformation back to A completes and the specimen returns to the undeformed configuration. Similar to experiment I, hysteresis is only present in the axial response.

(c) Experiment III ($\sigma_\theta = 456$ MPa)

The responses for experiment III along with the corresponding axial and hoop strain contours are shown in Fig. 4.28. Again, deformation during the initial pressurization was uniform. During axial loading, transformation to M commences at $\sigma_X = 626$ MPa (image ①) with weak inhomogeneous deformation in the form of a collection of inclined helical bands throughout the specimen length. This localization pattern is resembles that observed in the radial stress path experiment for $\alpha = 1.3$. Additionally, the stress knee is less abrupt and the stress exhibits a gradual increase during transformation. The specimen returns to uniform deformation by image ⑩. Upon unloading, axial deformation remains uniform throughout with a monotonically decreasing response. The hoop strain remained uniform until around image ⑭ at which point axial features become visible. The full axial load/unload cycle resulted in an overall increase in the hoop strain and a corresponding hysteresis. Plane strain pressure

unloading results in axial features in the hoop strain contours. The material returns to the undeformed configuration upon unloading with as both hystereses close.

(d) Experiment IV (σ_θ = 616 MPa)

The responses for experiment IV along with the corresponding axial and hoop strain contours are shown in Fig. 4.29. In this case, M transformation takes place during the initial pressurization, commencing at $\sigma_\theta = 491$ MPa (image ①). Transformation produces a gradual stress knee followed by hardening. Localized deformation initiates near the center of the specimen as a pocket of M with slight axial orientation expands both axially and circumferentially around the tube. The inhomogeneous deformation is essentially completed by the end of the pressurization (image ⑤). Interestingly, the axial strain remained essentially homogeneous during the pressurization.

During axial loading, ε_x increases while ε_θ decreases, with both deformations remaining uniform. During unloading of the axial stress, the strains follow the opposite trend and deformations are uniform. The complete cycle results in a monotonic axial response, and an increase to the width of the hoop hysteresis. Deformation during depressurization is initially uniform, but at $\sigma_\theta = 316$ MPa, a relatively abrupt knee forms. Transformation to A commences with axial features visible in the hoop strain contours in image ⑰. Axial strains remain uniform throughout. Both responses trace a closed hysteresis.

4.5 Discussion of Results

4.5.1 Radial Biaxial Experiments

We now take an overall view of the radial biaxial experimental results and try to establish trends. Figures 4.30 and 4.31 show selected $\sigma_x - \bar{\varepsilon}_x$ and $\sigma_\theta - \bar{\varepsilon}_\theta$ responses for

$\alpha \leq 1.0$ and $\alpha \geq 1.0$ respectively. For all stress ratios, transformation resulted in stress-strain hystereses that closed on unloading. In other words, in this part of the $\sigma_x - \sigma_\theta$ space the material continues to exhibit the pseudoelastic behavior previously observed under uniaxial tension. Figure 4.32 shows representative strain contours for nine stress ratios along the A→M transformation plateau and the corresponding histograms which quantify the degree of inhomogeneity. Note the transition from hoop dominant inhomogeneous deformation for small stress ratios (bimodal distribution in Fig. 4.32b), to homogeneous deformation around equibiaxial tension (nearly unimodal), to axially dominant inhomogeneous deformation for large alphas (return to bimodal).

The A phase was found to be isotropic and linearly elastic. The average values from the uniaxial tension and hoop experiments resulted in elastic modulus $E_A = 66.3$ GPa and Poisson's ratio $\nu_A = 0.425$. Figure 4.33 plots the measured initial stiffnesses of the axial and hoop stress-strain responses for the 26 biaxial experiments. Included in the figure are constructions based on the average values given above. The constructions agree well with the measured experimental stiffnesses.

Returning to Fig. 4.30, for stress ratios ranging from -1.0 to 1.0 the hoop hysteresis dominates. As α is increased from -1.0, the transformation stresses gradually increase while the dominant hoop strain decreases. For $\alpha \leq 0.60$, M nucleates mostly as a narrow helical band of higher strain accompanied by a loss in stiffness in the form of a sharp stress knee. Transformation spreads most often through axial propagation and broadening of such bands with the stress remaining essentially constant. The deformation inside the bands typically corresponds to that at the end of the stress plateau while the rest of the specimen, still in the A phase, is at the strain at the beginning of the plateau.

On unloading, the M phase initially deforms homogeneously. When the stress drops sufficiently, A nucleates forming again helical or multi-helical bands. A lower stress plateau is traced during which the bands propagate and broaden. In several cases the evolution of deformation follows the reverse order to that followed during loading. However, the lower stress of this transformation, coupled with structural effects, lead to other deformation patterns like multi-helical fronts for some cases.

The axial and hoop stress at the "nucleation" and "completion" of M and A transformations are plotted against each other in Fig. 4.34. Each pair of stresses was established by the "tangent" construction method defined in . The stresses corresponding to nucleation of M are fitted with the Cazacu et al. [2006] (CPB06) "yield" surface as outlined in Section 5.1. For completeness, the other three sets of data are fitted in a similar fashion and are included in the figure. Since for $-1.0 \le \alpha \le 0.5$ transformation occurred with small increase in stress, the nucleation and completion stresses are very close to each other.

Figure 4.35a shows axial vs. hoop strain plots at the nucleation and completion of M transformation from the 26 radial experiments conducted. It is interesting to observe that the extent of strain induced by the transformation of M starts with large values for the negative and small values of α and decreases as the biaxial stress state is approached.

As α increases from 0.75 to 1.0, the transformation stresses increase while the transformation strains decrease. The sharp transformation stress knee is replaced by a gradual reduction in modulus followed by hardening behavior until the completion of M (Fig. 4.30). Furthermore, transformation deformation is now mostly homogeneous with weak, mainly axial, patterns developing in the dominant hoop strain (Fig. 4.32). As a consequence of the exhibited hardening, the stresses at the nucleation and completion of

M in Fig. 4.34 are separated. For α = 0.85, the axial response did not develop a hysteresis and for higher values of α the axial hystereses have positive strain values (Figs. 4.30 and 4.35a). It is worth noting that at the equibiaxial stress state, the induced transformation strain is at its smallest. Furthermore, the axial strain is smaller than the hoop value, a sign of strain anisotropy.

Unloading in this stress ratio regime follows the same trends as loading. Nucleation of A is through a rounded stress transition knee followed by monotonically decreasing responses and mainly homogeneous deformation. Once more, the surfaces corresponding to nucleation and completion of A in Fig. 4.34 are separated. The associated transformation strains plotted in Fig. 4.35b follow a similar trend as those of the forward transformation but have smaller values.

Figure 4.31 shows select responses for $\alpha \geq 1.0$. Once again, transformation results in fully recoverable deformation with all hystereses closing. For lower values of α, in the neighborhood of 1.0, the responses are similar to those just outlined. Nucleation is associated with rounded stress transitions followed by hardening behavior for both loading and unloading. The axial and hoop transformation strains become equal at a stress ratio of about 1.05, but their values remain at their lowest level (Fig. 4.35a). Transformation develops essentially homogeneously with very weak, now in the transverse direction, patterns starting to appear in the axial strain at α = 1.20 and more prominently at 1.30. For 1.20 the hoop response traces essentially no hysteresis and appears to be the dual to the disappearance of the axial hysteresis for α = 0.85.

As the stress ratio increases beyond 1.30, transformation nucleates with increasingly sharper stress knees and its evolution occurs with minimal change in stress. The transformation is once more strongly inhomogeneous, developing helical bands of

transformed material that propagate and broaden. Similar behavior is observed during the transformation to A on unloading, but the unloading patterns are often different from those developed during loading. As illustrated by the results in Fig. 4.35, the transformation strains increase with α. Thus for the uniaxial tension case, the M transformation strain reaches a value of about 6.9% which compares to 5.4% developed for the uniaxial hoop test ($\alpha = 0$). This transformation strain anisotropy occurs even though the transformation stresses in the two directions have very similar values.

The energy dissipated by transformation, W^t, plotted against the angle $\tan^{-1}\alpha$ in Fig. 4.36 provides another global interpretation of NiTi behavior under biaxial stress states. For the negative values of α, up to the pure hoop stress case, the energy remains nearly constant. It increases somewhat for small values of α reaching a maximum at 0.375, and then drops to a minimum in the neighborhood of $\alpha = 1.0$. The energy then increases significantly to a maximum value at $\alpha = 2.0$ and drops again for larger stress ratios. Since the stresses at the beginning and end of the two transformations are seen in Fig. 4.34 to trace nearly symmetric loci, the large difference in W^t between $\alpha < 1.0$ and $\alpha > 1.0$ is another symptom of the anisotropy in the transformation strains.

4.5.2 Non-Radial Biaxial Experiments

Four non-radial stress paths were investigated using the same biaxial setup as that for the radial stress experiments. When hoop stress levels were low, axial deformation under biaxial stress states results in transformation deformations similar to the high α radial biaxial responses with flat stress plateaus (experiment I and II). For cases when the hoop stress was larger, transitions were observed between transformation deformations. Experiment III initially localized with inclined helical bands, but transitioned to axial features. Experiment IV transitioned between localization to homogeneous and returned

back to localization upon unloading. All cases exhibited closed axial hysteresis, with the hoop response in experiments I and II not developing a hysteresis.

4.6 SUMMARY AND CONCLUSIONS

NiTi tubes were loaded under radial stress paths in the $\sigma_x - \sigma_\theta$ plane and results for 26 biaxiality stress ratios of $-1.0 \le \alpha \le \infty$ have been reported. The most striking result is that, outside of a narrow region spanning equibiaxial tension, transformation leads to localized helical deformation bands with inclinations that are dependent on the stress ratio. During transformation, the stresses remain nearly constant. In the vicinity of equibiaxial tension, the material hardens and deformation is homogeneous. By contrast, the transformation strains exhibit significant anisotropy between axial and hoop dominant stress paths. Moreover, strains around the equibiaxial stress state, where material hardening and homogeneous deformation was observed, were significantly smaller than in the rest of the stress space. The strain anisotropy had a corresponding influence on the energy dissipated during transformation with axial dominant stress paths dissipating significantly more energy that hoop dominant ones, and less dissipation in the neighborhood of equibiaxial stress. These are features that constitutive models for NiTi must be able to address.

Exp	α	$(\tan^{-1}\alpha)^{\circ}$	D mm	t mm	$\left.\frac{\sigma_x}{\varepsilon_x}\right\|_A$ GPa	$\left.\frac{\sigma_\theta}{\varepsilon_\theta}\right\|_A$ GPa	ϕ°
1	-0.999	-44.96	6.319	0.273	47.9	45.0	38.1
2	-0.878	-41.29	6.319	0.273	45.6	44.5	37.7
3	-0.749	-36.84	6.319	0.273	43.7	48.4	38.3
4	-0.499	-26.50	6.324	0.272	37.4	53.4	32.1
5	-0.374	-20.50	6.324	0.272	32.4	57.2	30.5
6	-0.249	-13.96	6.323	0.272	25.3	60.6	31.0
7	0.001	0.07	6.323	0.272	-0.3	66.8	29.1
8	0.046	2.63	6.310	0.272	-7.5	67.8	35.1
9	0.250	14.06	6.323	0.275	-89.0	72.8	31.5
10	0.375	20.56	6.323	0.271	-269.3	78.4	32.7
11	0.500	26.57	6.318	0.272	579.4	87.1	24.1
12	0.599	30.92	6.319	0.272	306.8	89.5	0
13	0.750	36.87	6.320	0.273	167.9	98.4	0
14	0.849	40.34	6.322	0.281	139.9	109.0	0
15	0.999	44.98	6.319	0.277	122.4	124.0	-
16	1.069	46.92	6.322	0.281	106.1	129.1	-
17	1.148	48.95	6.319	0.277	106.7	145.1	-
18	1.199	50.16	6.326	0.275	105.4	142.8	-
19	1.263	51.63	6.319	0.267	101.6	169.2	90
20	1.298	52.39	6.319	0.272	99.6	166.4	90
21	1.518	56.62	6.319	0.267	89.6	232.1	61.9
22	1.789	60.80	6.319	0.267	83.4	372.1	62.4
23	1.998	63.41	6.323	0.271	84.9	623.1	57.5
24	3.995	75.95	6.323	0.275	73.2	-85.4	60.3
25	7.983	82.86	6.323	0.271	71.0	-28.6	60.0
26	UT	90	6.318	0.270	65.7	0.0	55.8

(a)

Table 4.1a Geometric and test parameters for radial biaxial experiments performed on NiTi tubes.

Exp	α	σ_{xNM} MPa	$\sigma_{\theta NM}$ MPa	σ_{xNA} MPa	$\sigma_{\theta NA}$ MPa	$\Delta\varepsilon^{t}_{xM}$ (%)	$\Delta\varepsilon^{t}_{\theta M}$ (%)	W^{t} MPa
1	-0.999	-312.3	314.6	-178.3	179.8	-2.435	4.430	9.99
2	-0.878	-287.9	328.6	-161.2	185.3	-2.461	4.560	10.50
3	-0.749	-263.7	353.7	-148.3	199.2	-2.447	4.637	10.52
4	-0.499	-192.5	386.9	-112.2	226.0	-2.427	4.756	10.21
5	-0.374	-155.0	415.5	-88.9	239.1	-2.371	4.780	10.27
6	-0.249	-103.7	417.7	-61.1	245.3	-2.060	4.261	9.65
7	0.001	0.2	469.8	0.0	277.0	-2.189	4.657	9.56
8	0.046	22.9	484.2	11.1	283.8	-2.194	4.629	10.11
9	0.250	130.3	517.0	80.7	325.4	-1.882	4.700	11.20
10	0.375	212.9	569.5	123.8	333.1	-1.763	4.608	12.93
11	0.500	295.5	590.9	181.3	364.7	-1.387	4.316	12.37
12	0.599	360.7	596.3	226.5	379.8	-1.056	4.026	11.09
13	0.750	432.5	587.4	335.0	443.8	-0.340	3.345	8.49
14	0.849	552.8	614.0	386.2	454.4	-0.004	2.921	6.51
15	0.999	596.2	593.6	466.5	459.7	0.936	2.178	7.12
16	1.069	608.4	574.5	453.0	426.9	1.455	0.852	6.72
17	1.148	628.9	542.5	454.4	398.3	2.132	0.566	8.21
18	1.199	636.4	522.5	448.8	388.0	3.080	0.260	9.68
19	1.263	668.4	521.4	456.7	367.6	3.517	-0.305	11.42
20	1.298	668.8	524.7	414.9	324.6	3.751	-0.457	13.71
21	1.518	656.6	433.3	377.8	249.6	5.022	-1.402	18.43
22	1.789	629.6	350.7	332.9	186.5	5.404	-1.834	19.87
23	1.998	626.1	314.4	284.6	144.9	6.146	-2.391	25.58
24	3.995	541.5	137.7	240.5	62.4	6.357	-2.773	21.67
25	7.983	516.0	66.6	233.5	31.1	6.427	-2.875	19.46
26	UT	458.5	0	232.2	0	6.171	-2.926	13.49

(b)

Table 4.1b Geometric and test parameters for radial biaxial experiments performed on NiTi tubes.

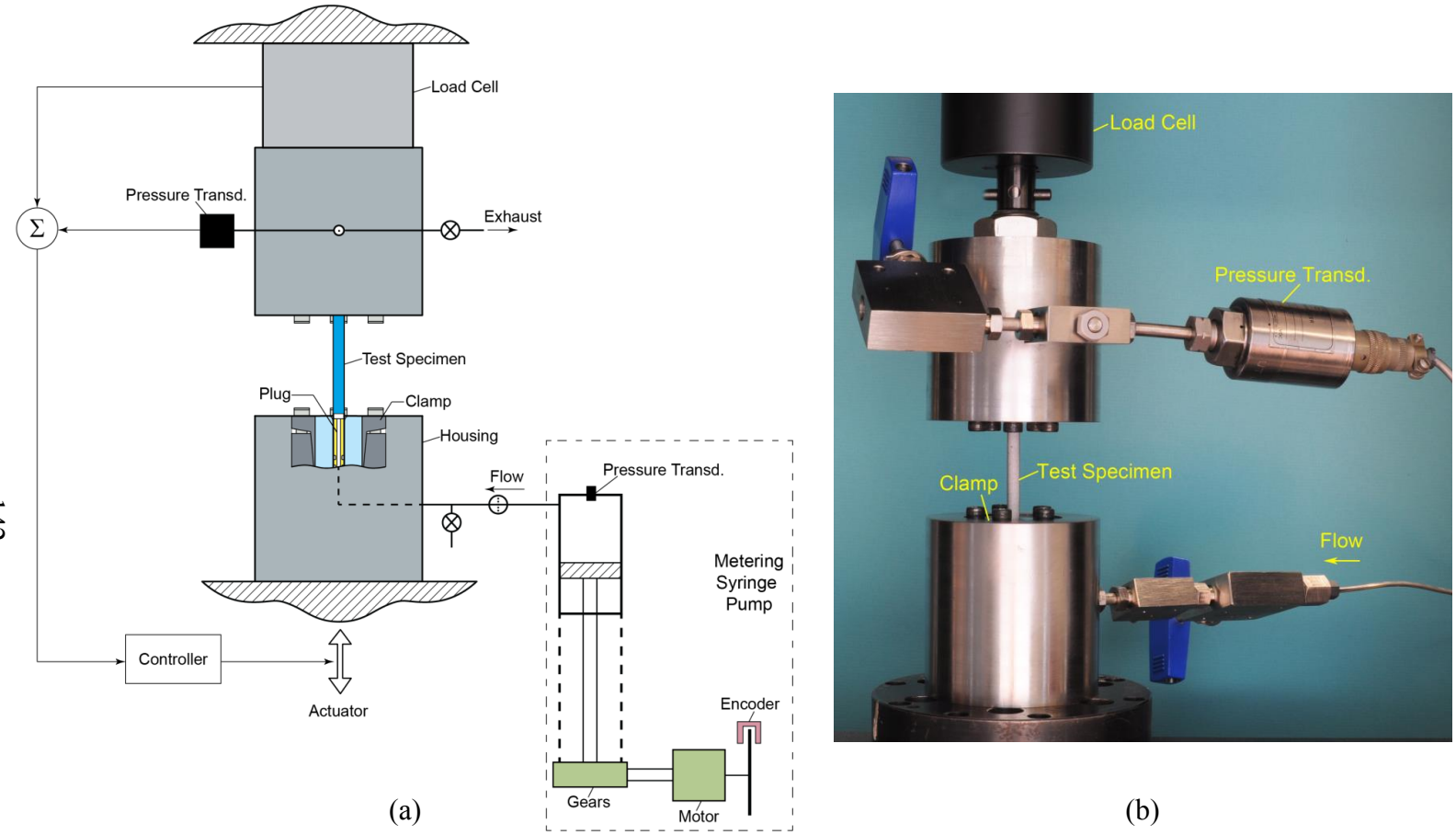

Fig. 4.1 Internal pressure-axial load biaxial test facility. (a) Schematic and (b) photograph of the grips and specimen.

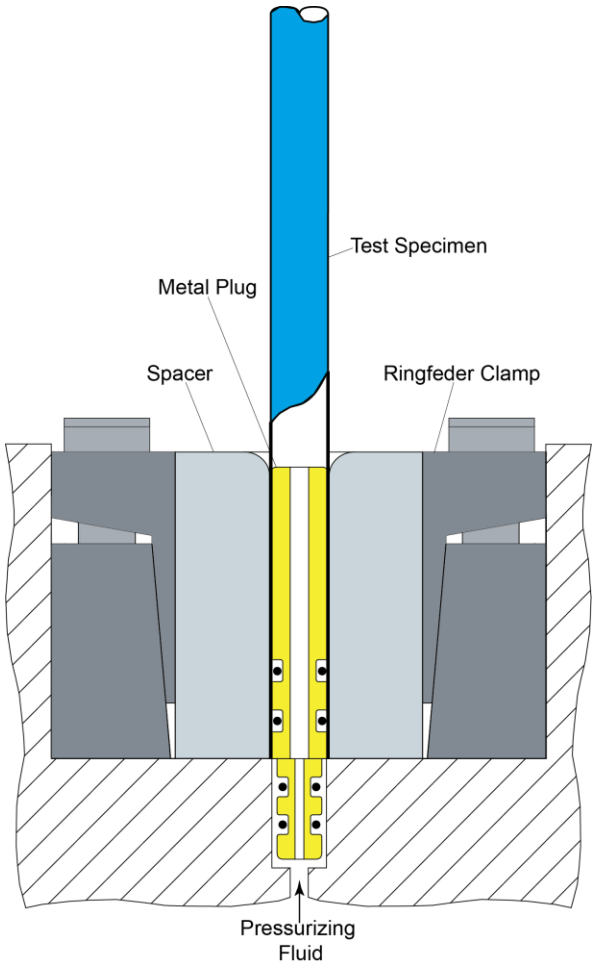

Fig. 4.2 Detail of gripped end of the 6.35 mm NiTi tubular specimen.

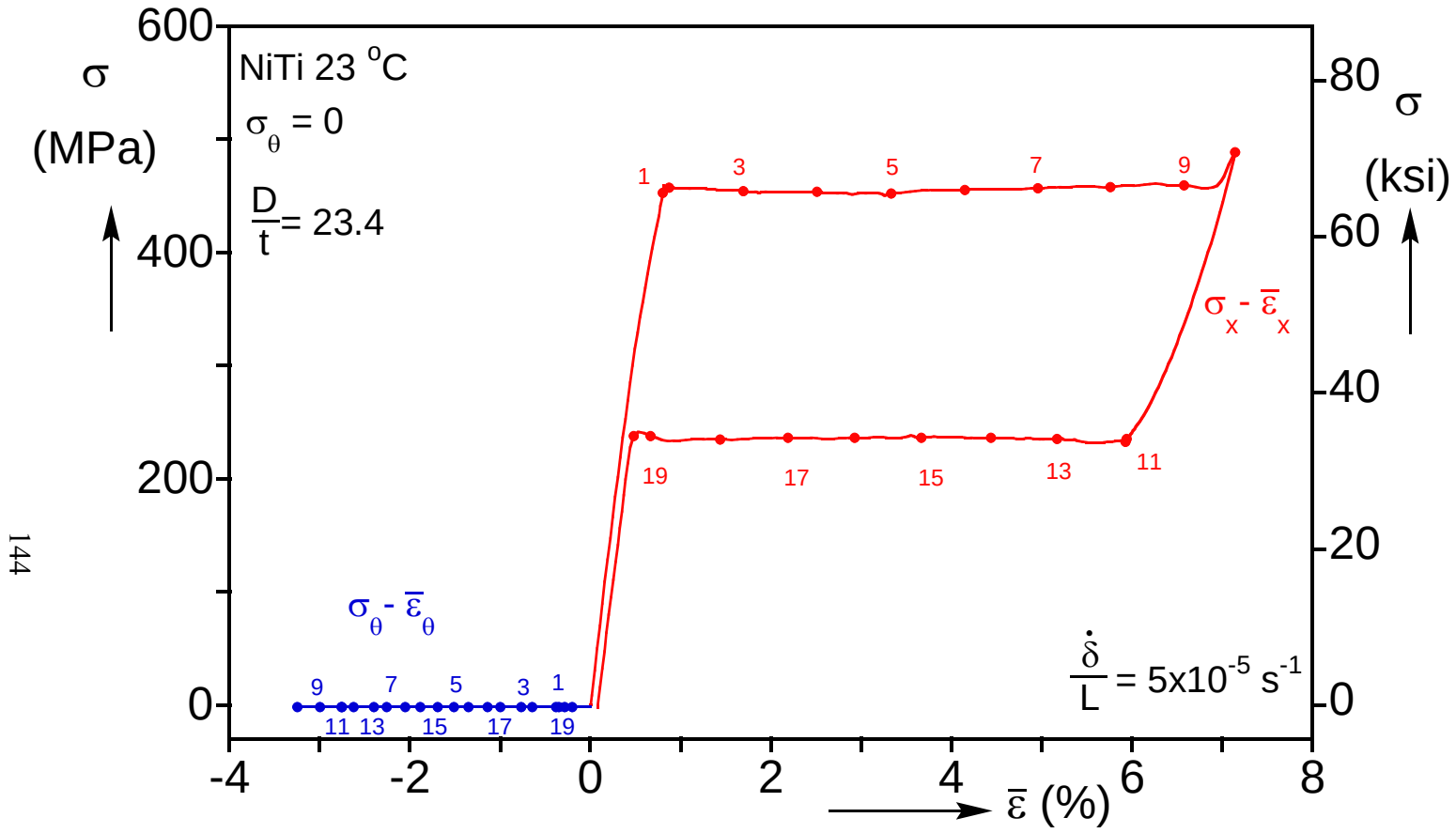

Fig. 4.3 Stress-average strains recorded in an isothermal uniaxial axial tension test on a NiTi tube at 23 °C.

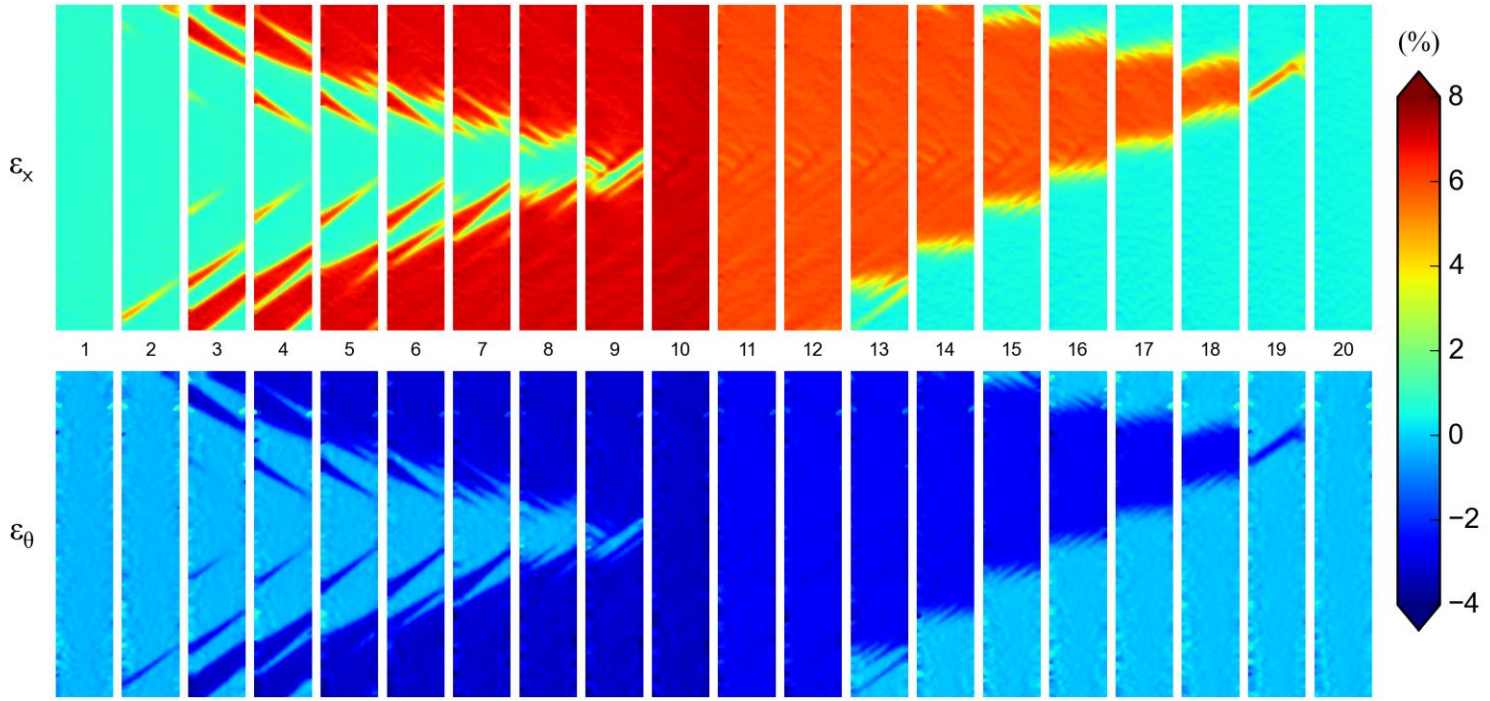

Fig. 4.4 Sequences of axial and hoop strain contours from DIC corresponding to the numbered bullets marked on the tensile responses in Fig. 4.3. The FOV has a hoop span of about 6 mm of the unwrapped circumference.

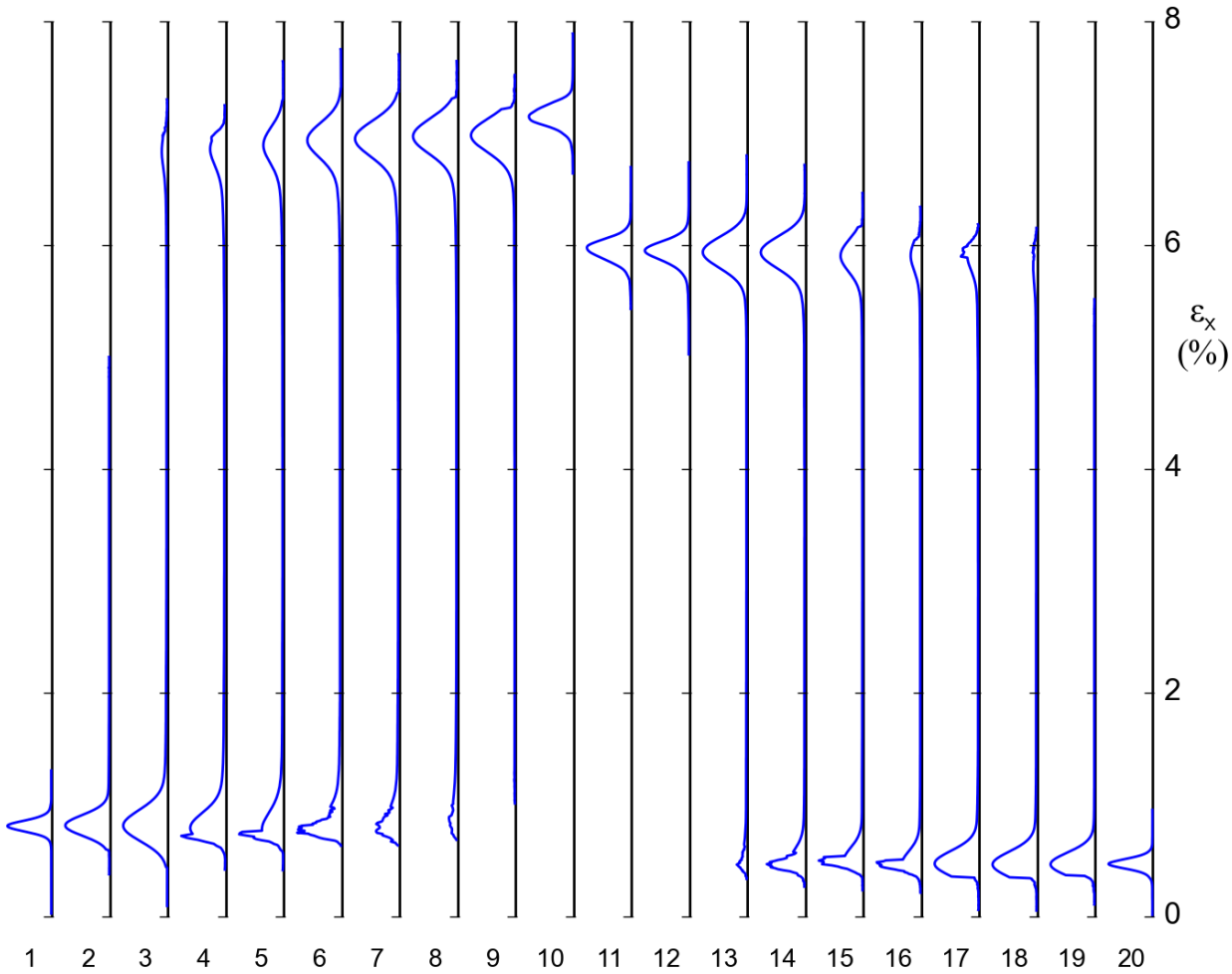

Fig. 4.5 Histograms of axial strain that show the degree of strain inhomogeneity in the FOV for the 20 strain images in Fig. 4.4.

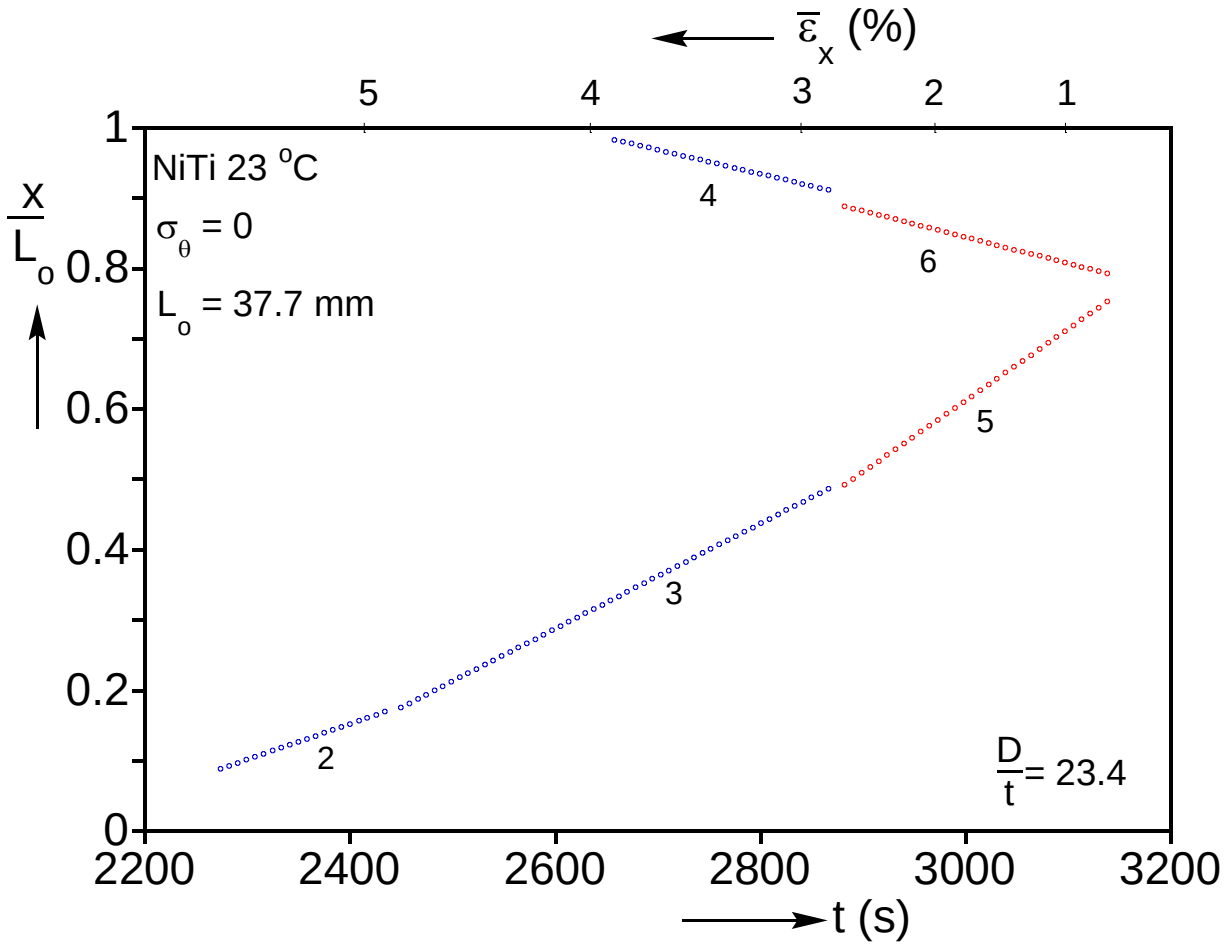

Fig. 4.6 Position (x) of transformation fronts vs. time (t) during the unloading of the uniaxial tension experiment in Fig. 4.3.

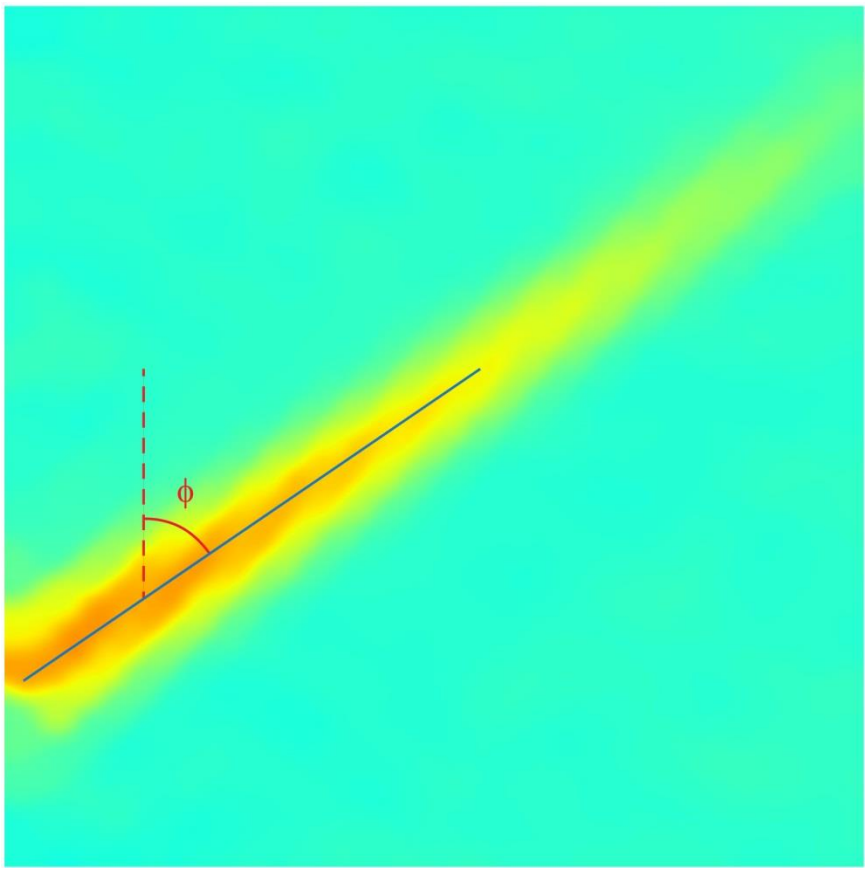

Fig. 4.7 Expanded view of an inclined helical martensitic transformation front

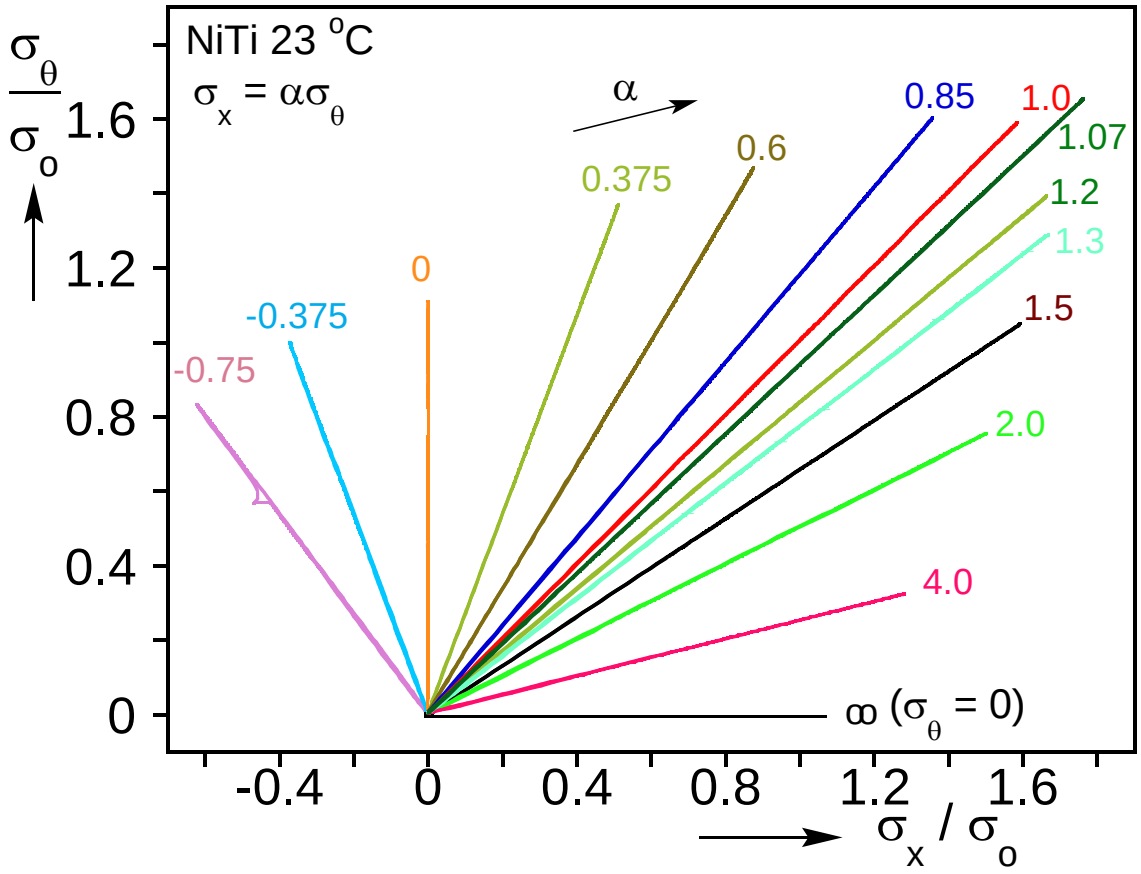

Fig. 4.8 Prescribed radial stress paths from representative experiments on NiTi tubes using setup in Fig. 4.1 and 4.2.

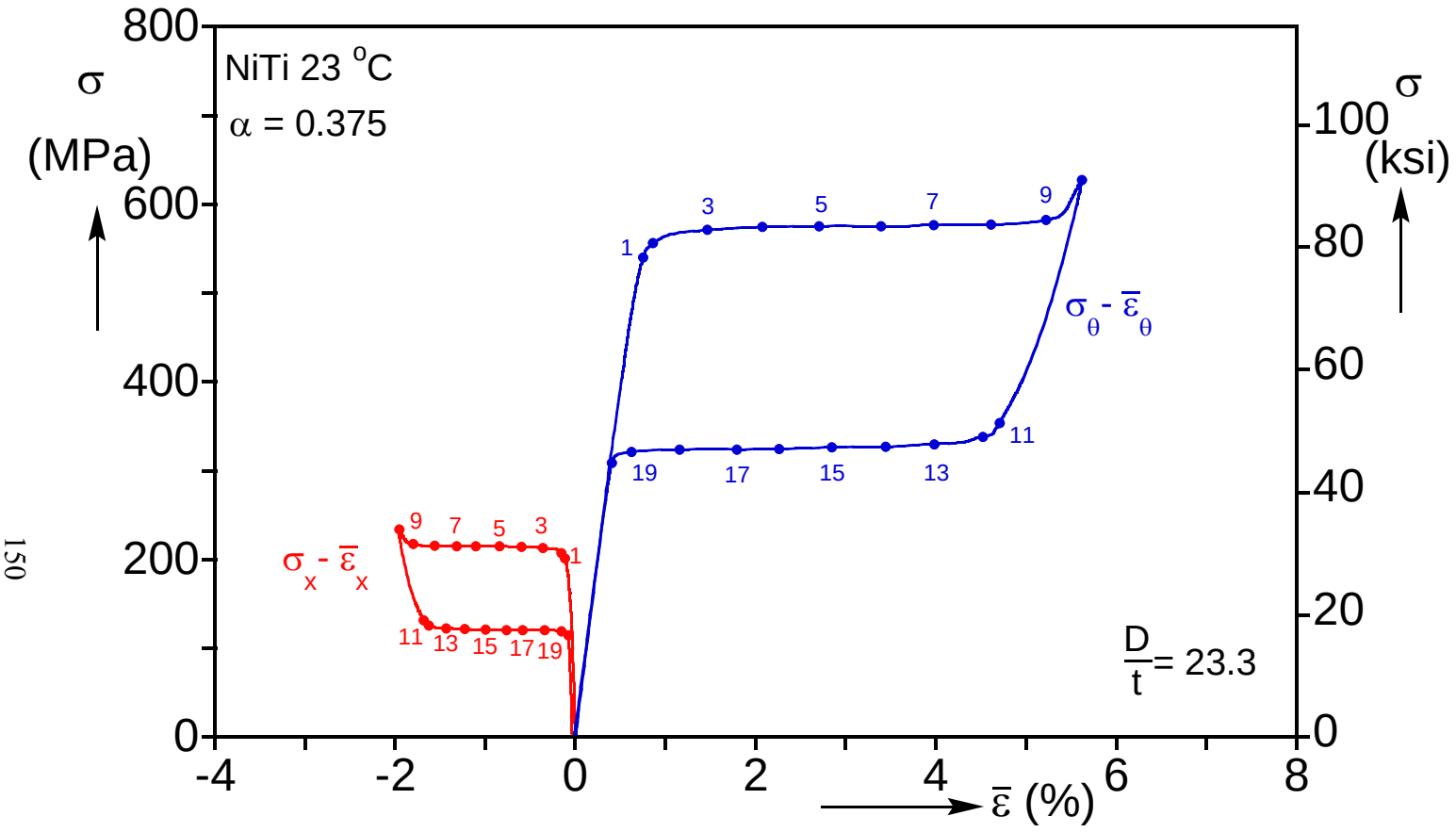

Fig. 4.9 Stress-average strains recorded in biaxial test with $\sigma_x = 0.375\sigma_\theta$.

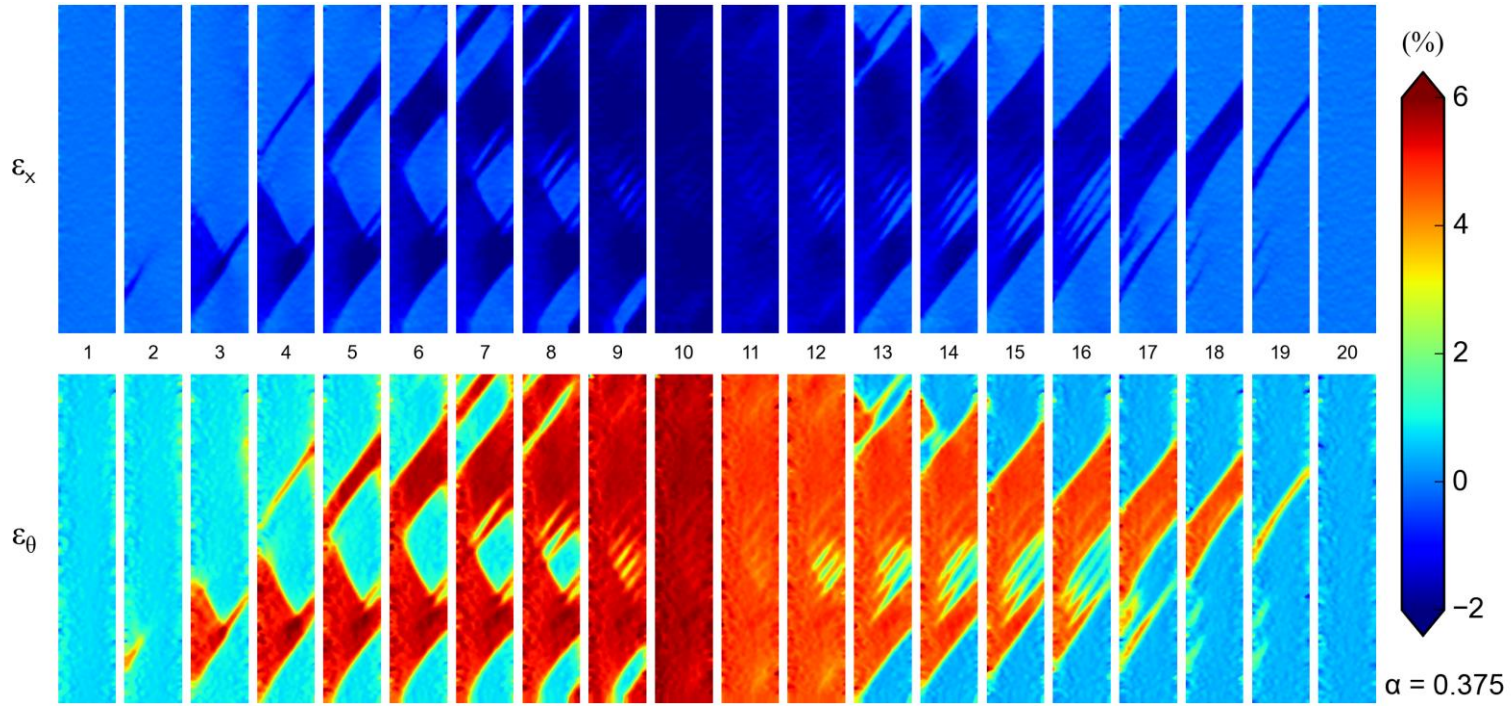

Fig. 4.10 Sequences of axial and hoop strain contours from DIC corresponding to the numbered bullets marked on the responses in Fig. 4.9.

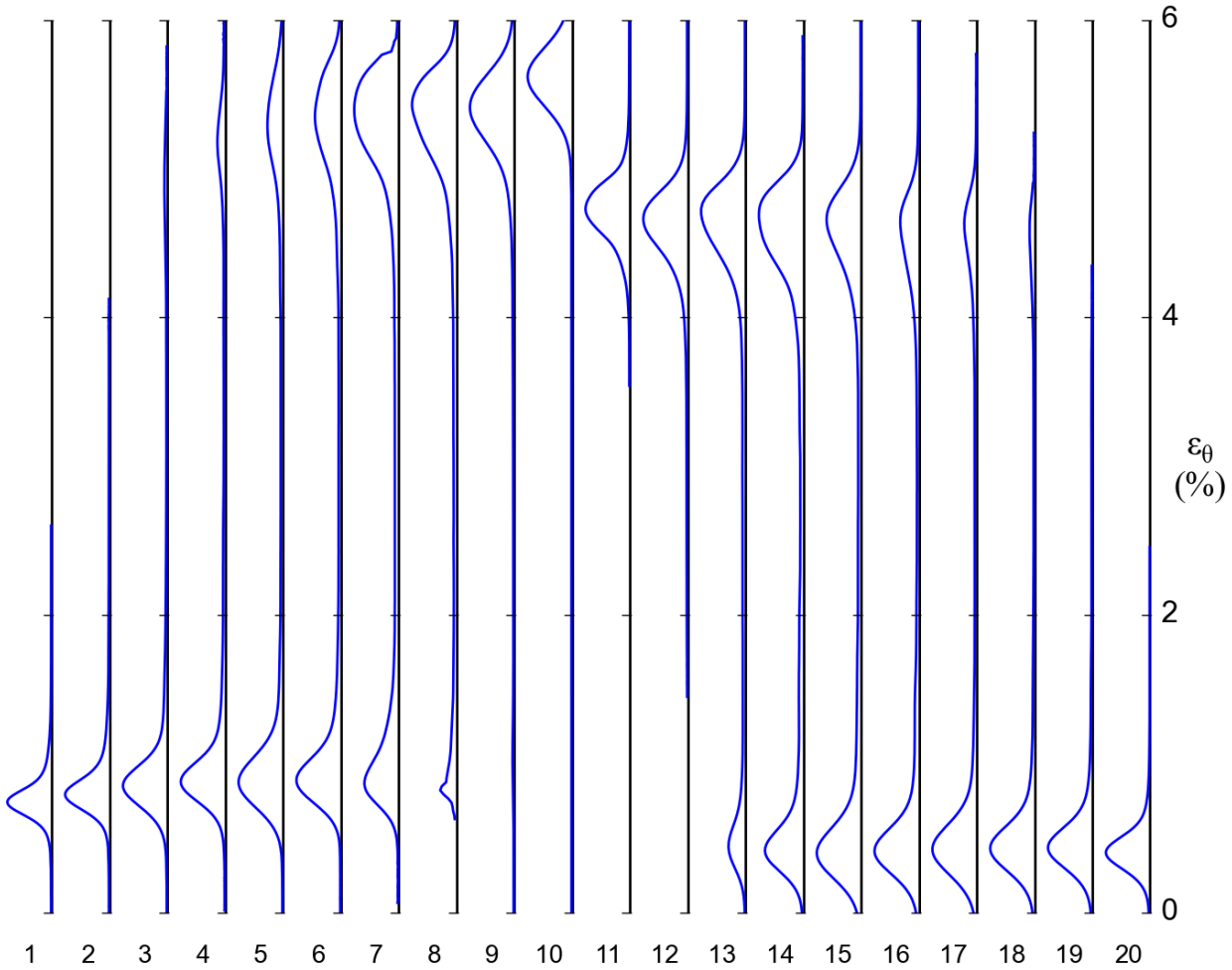

Fig. 4.11 Histograms of hoop strain that show the degree of strain inhomogeneity in the FOV for the 20 strain images in Fig. 4.10.

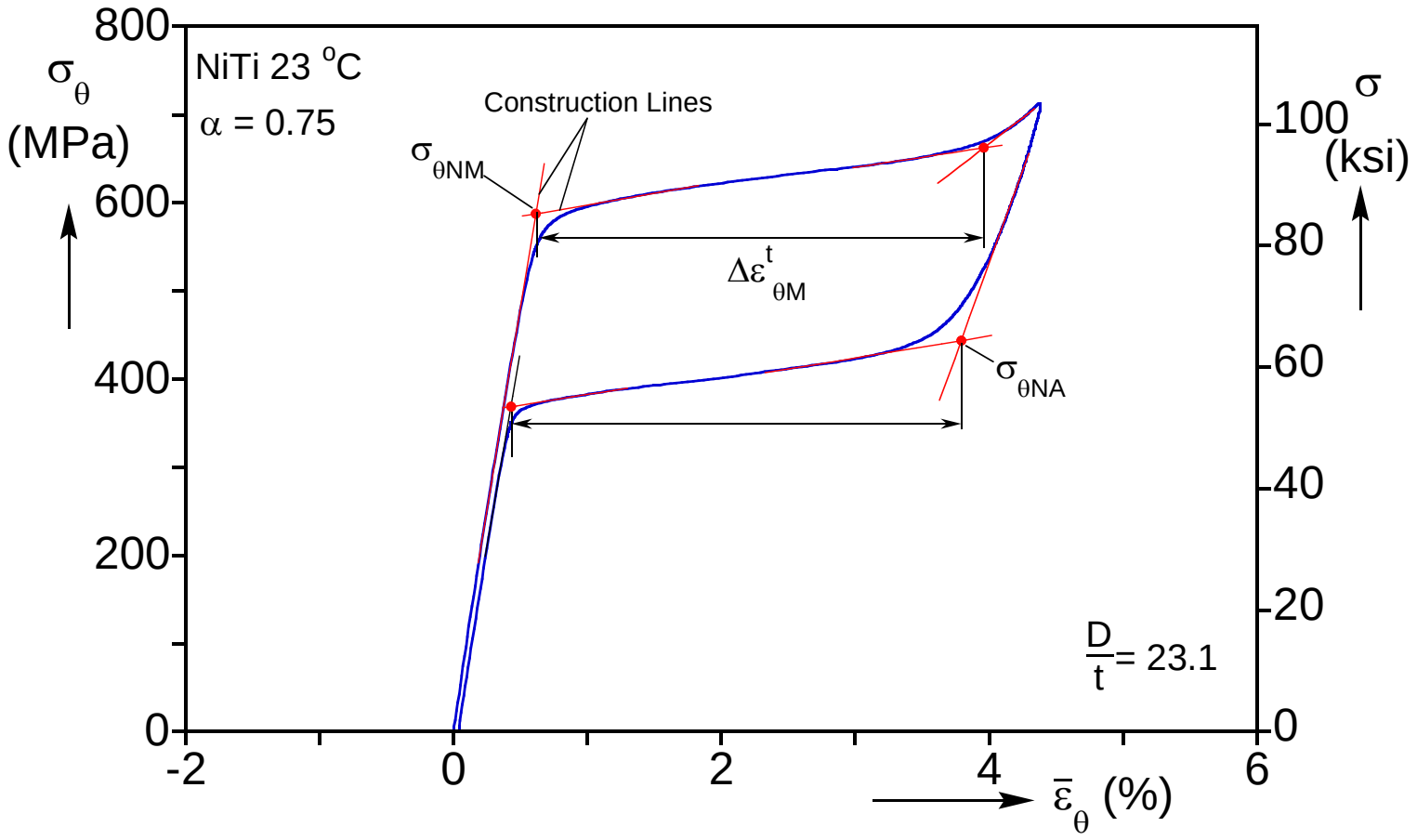

Fig. 4.12 Tangent construction lines for determining the onset and completion of transformations.

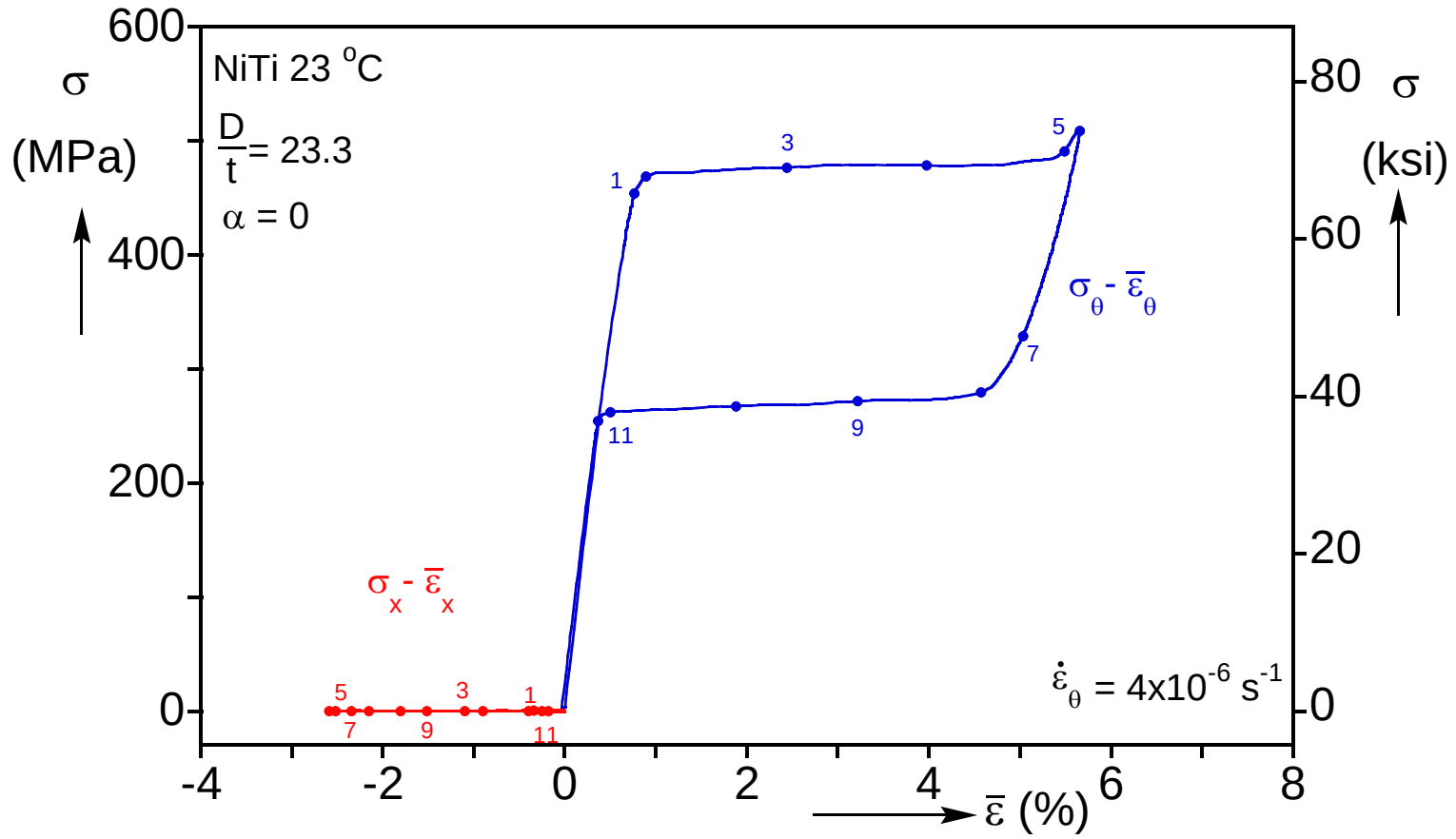

(a)

Fig. 4.13a Results from a uniaxial hoop tension test. (a) Stress-average strain responses.

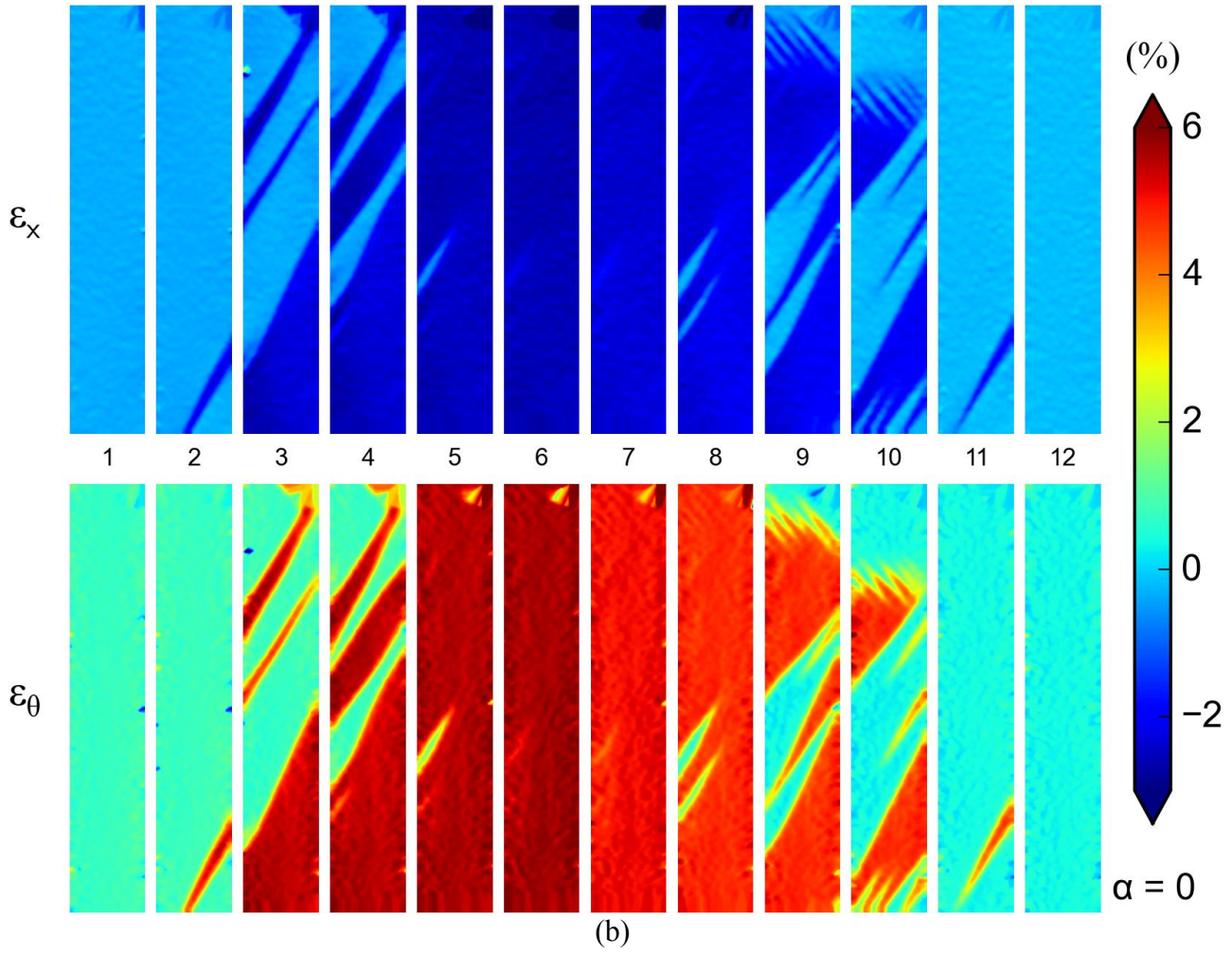

Fig. 4.13b Results from a uniaxial hoop tension test. (b) Sequences of axial and hoop strain contours from DIC corresponding to the numbered bullets marked on the responses in (a).

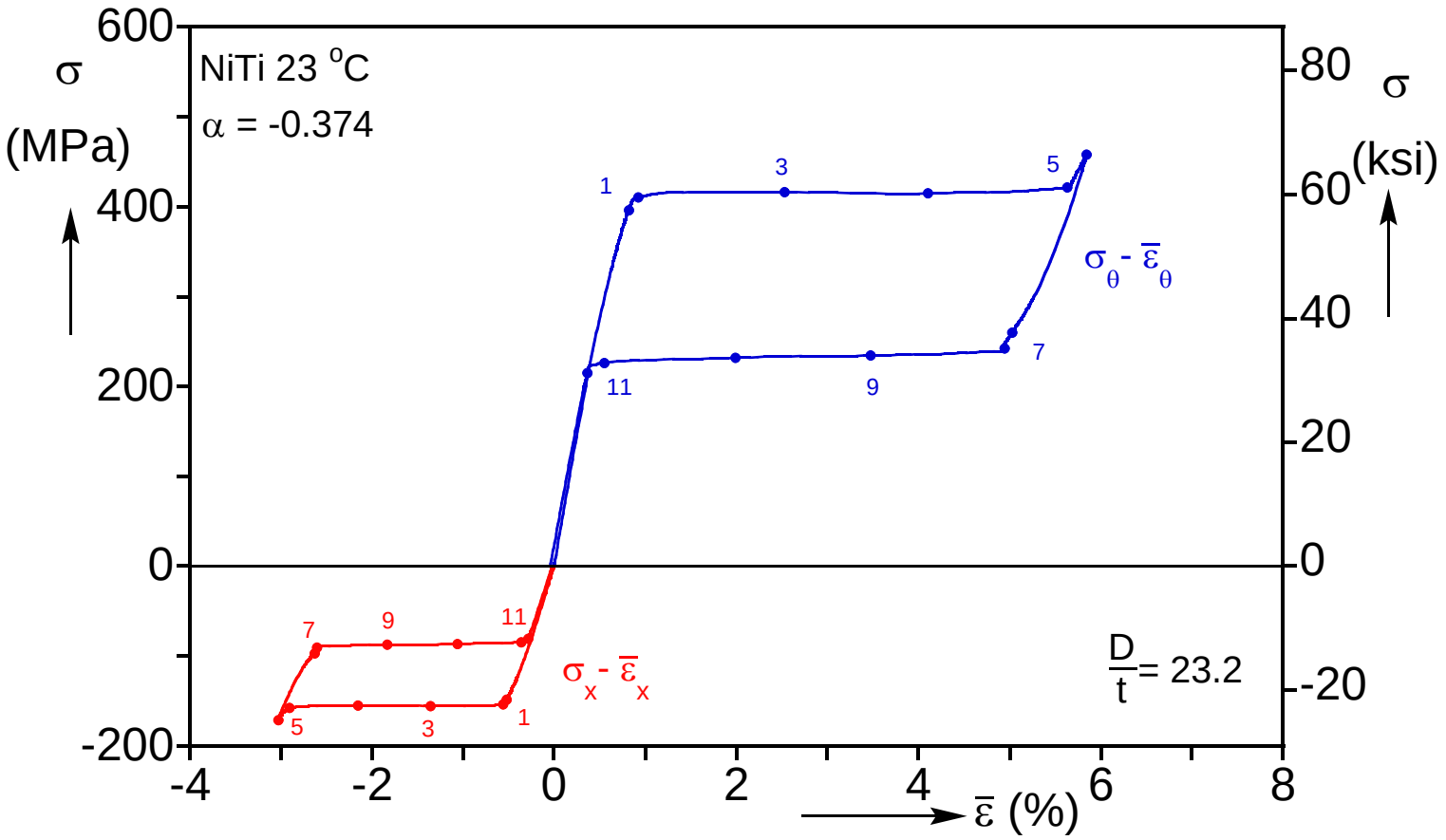

(a)

Fig. 4.14a Results from a biaxial test with $\sigma_x = -0.374\sigma_\theta$. (a) Stress-average strain responses.

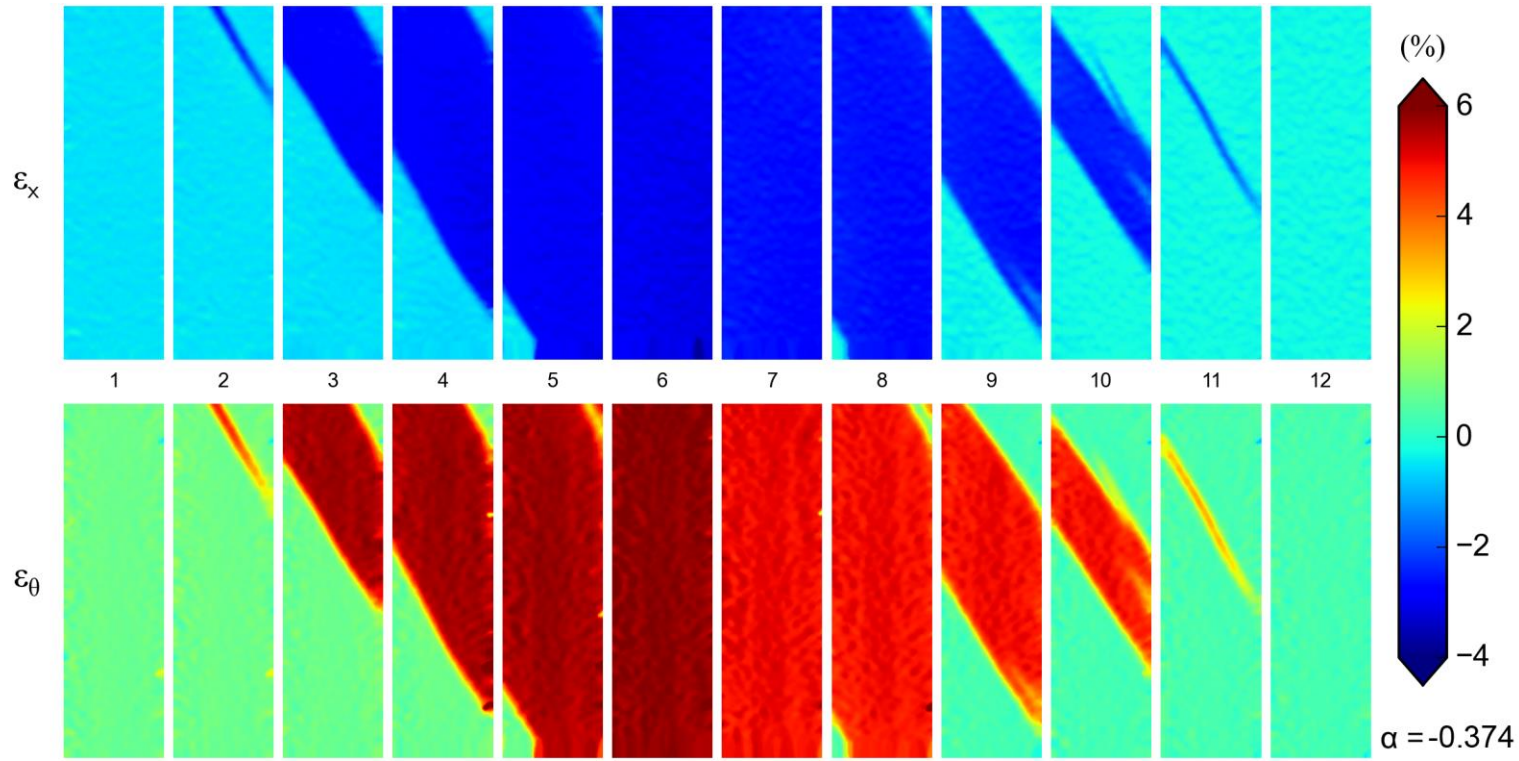

Fig. 4.14b Results from a biaxial test with $\sigma_x = -0.374\sigma_\theta$. (b) sequences of axial and hoop strain contours from DIC corresponding to the numbered bullets marked on the responses in (a).

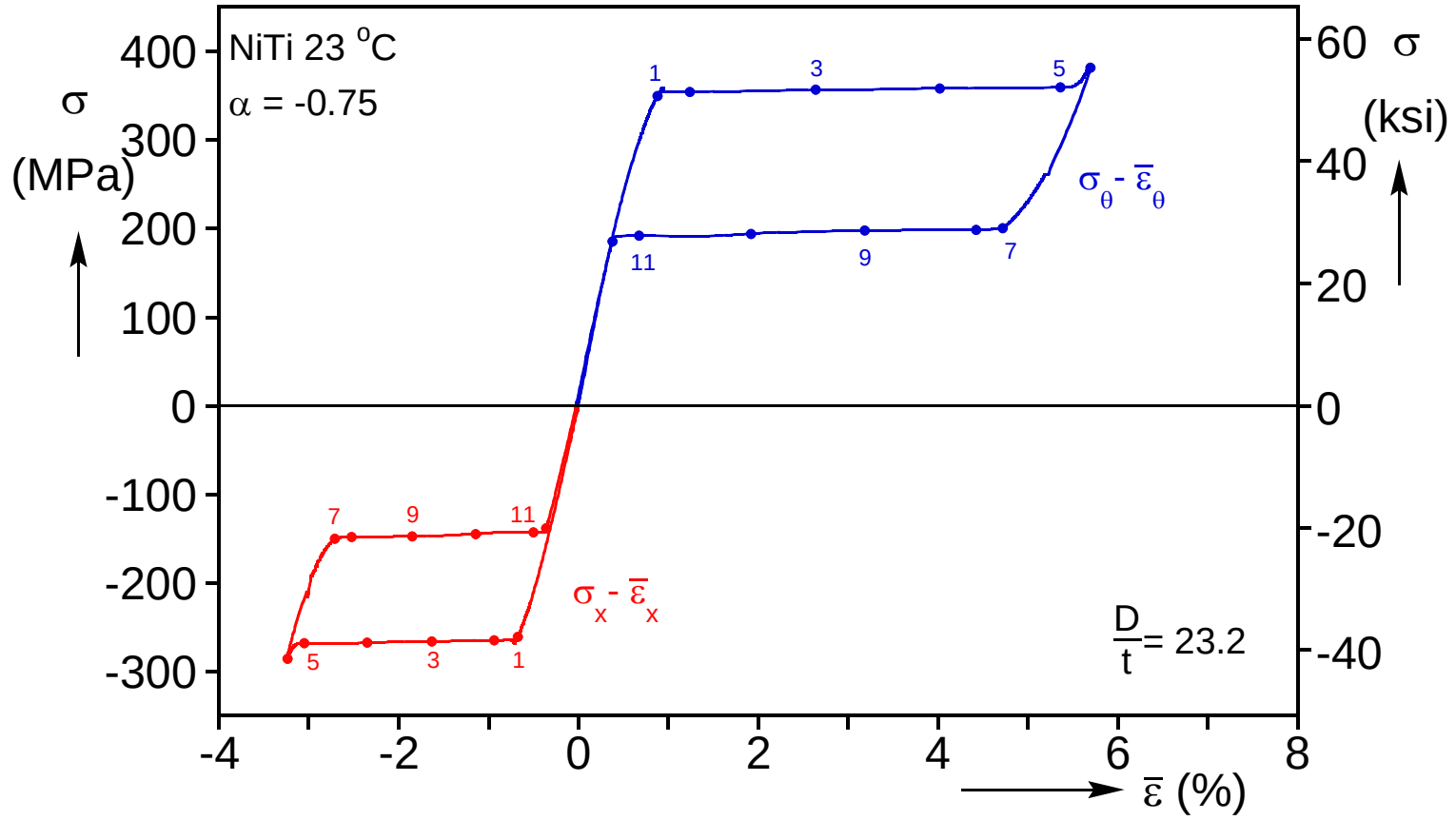

(a)

Fig. 4.15a Results from a biaxial test with $\sigma_x = -0.75\sigma_\theta$. (a) Stress-average strain responses.

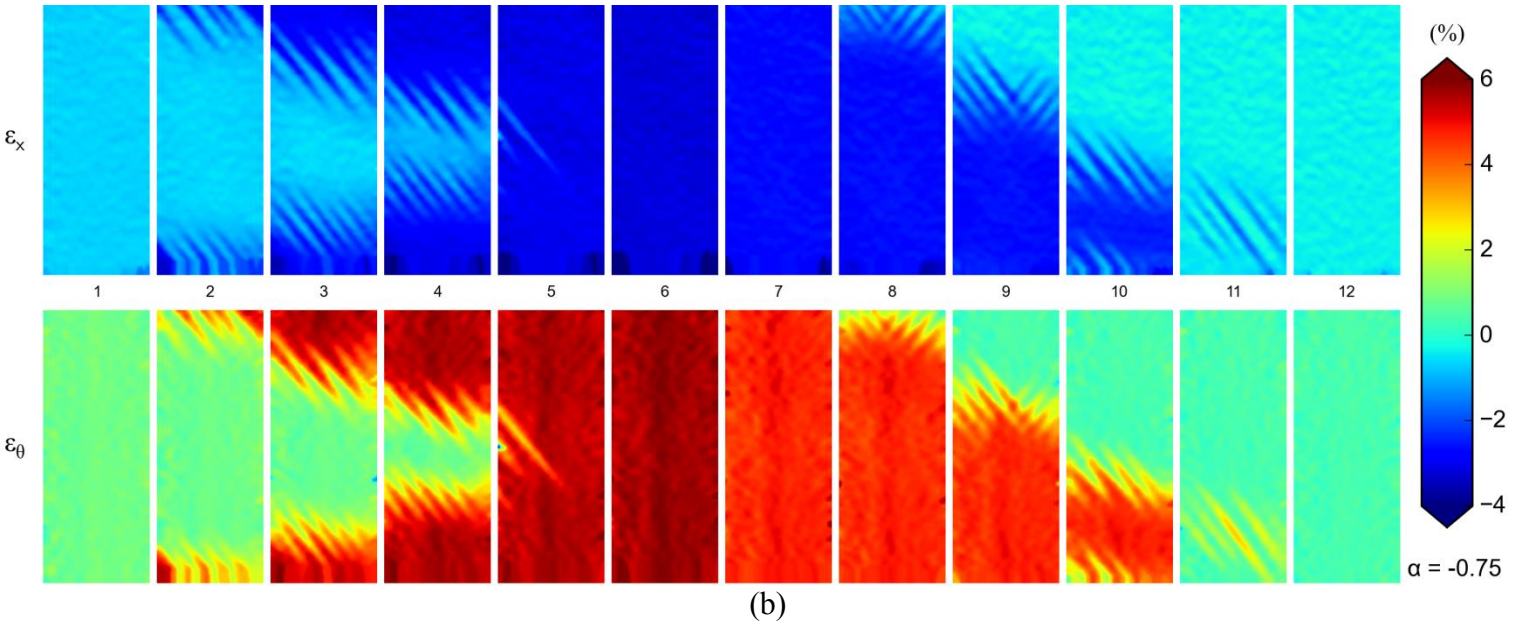

(b)

Fig. 4.15b Results from a biaxial test with $\sigma_x = -0.75\sigma_\theta$. (b) sequences of axial and hoop strain contours from DIC corresponding to the numbered bullets marked on the responses in (a).

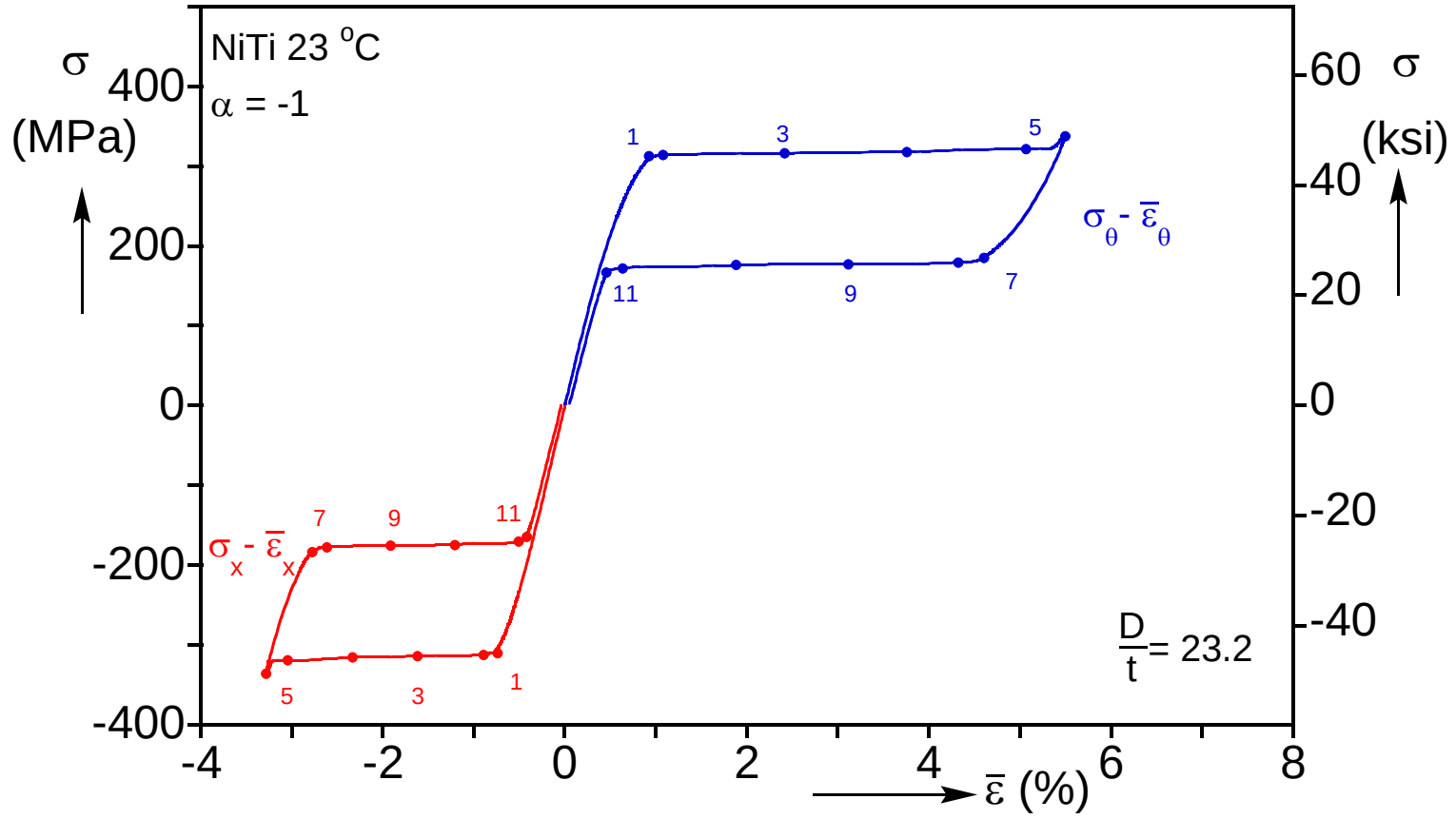

(a)

Fig. 4.16a Results from a biaxial test with $\sigma_x = -1.0\sigma_\theta$. (a) Stress-average strain responses.

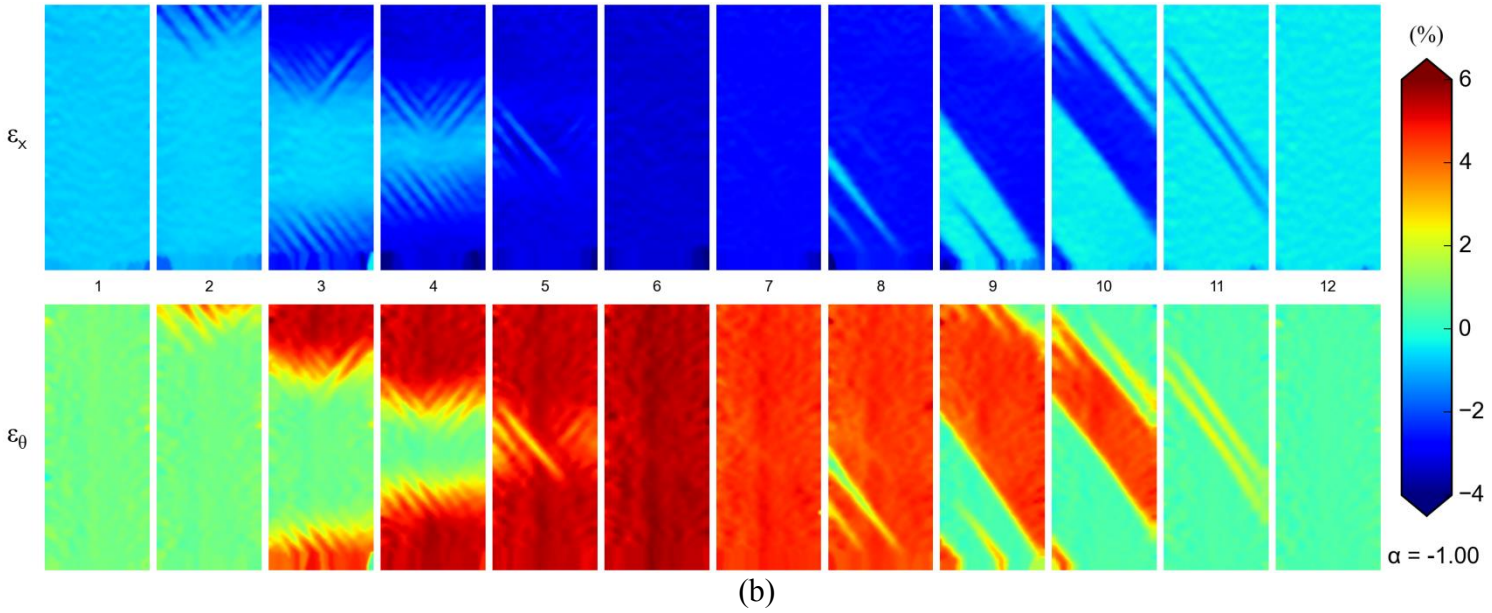

(b)

Fig. 4.16b Results from a biaxial test with $\sigma_x = -1.0\sigma_\theta$. (b) sequences of axial and hoop strain contours from DIC corresponding to the numbered bullets marked on the responses in (a).

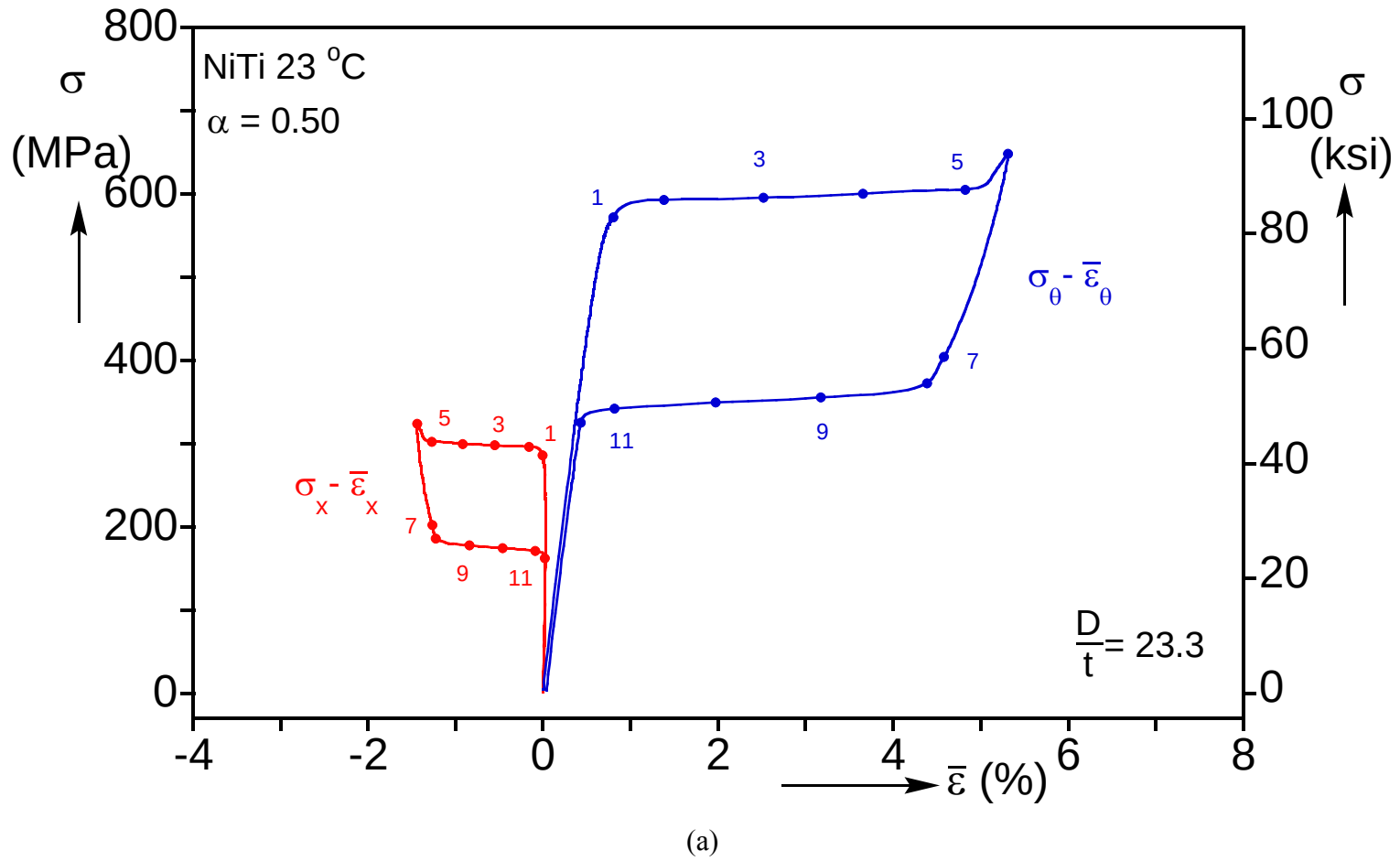

(a)

Fig. 4.17a Results from a biaxial test with $\sigma_x = 0.50\sigma_\theta$. (a) Stress-average strain responses.

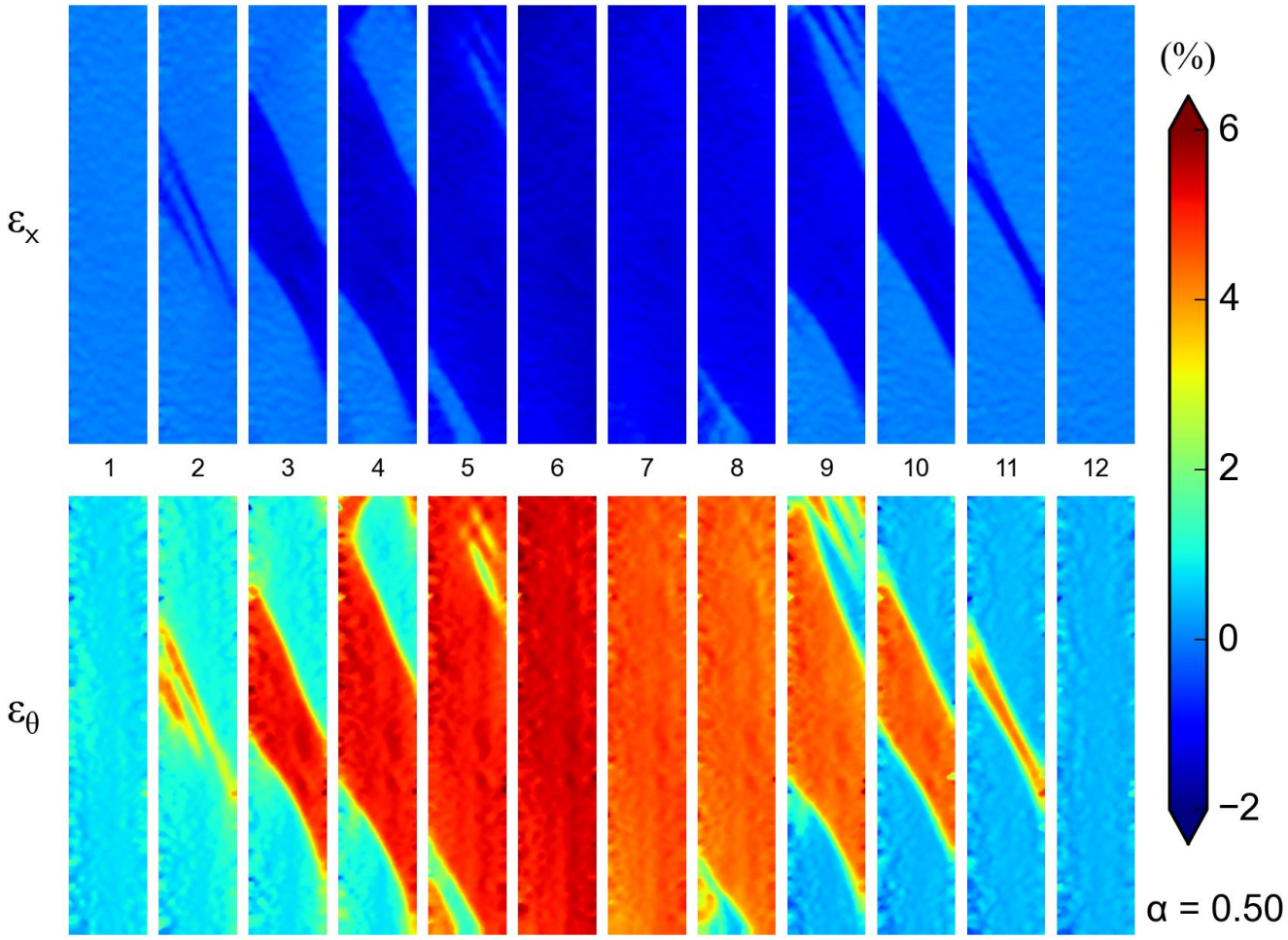

(b)

Fig. 4.17b Results from a biaxial test with $\sigma_x = 0.50\sigma_\theta$. (b) sequences of axial and hoop strain contours from DIC corresponding to the numbered bullets marked on the responses in (a).

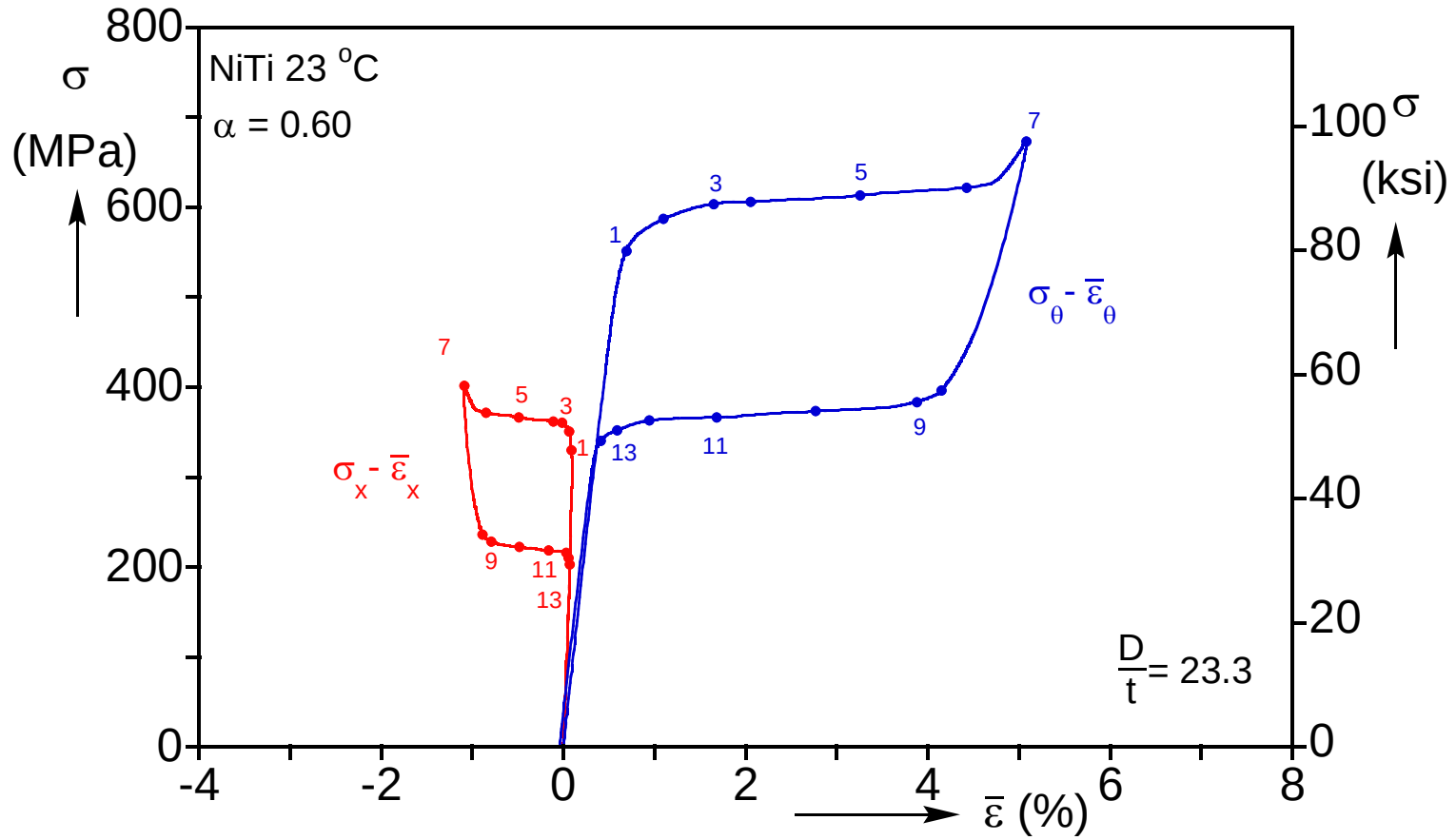

(a)

Fig. 4.18a Results from a biaxial test with $\sigma_x = 0.60\sigma_\theta$. (a) Stress-average strain responses.

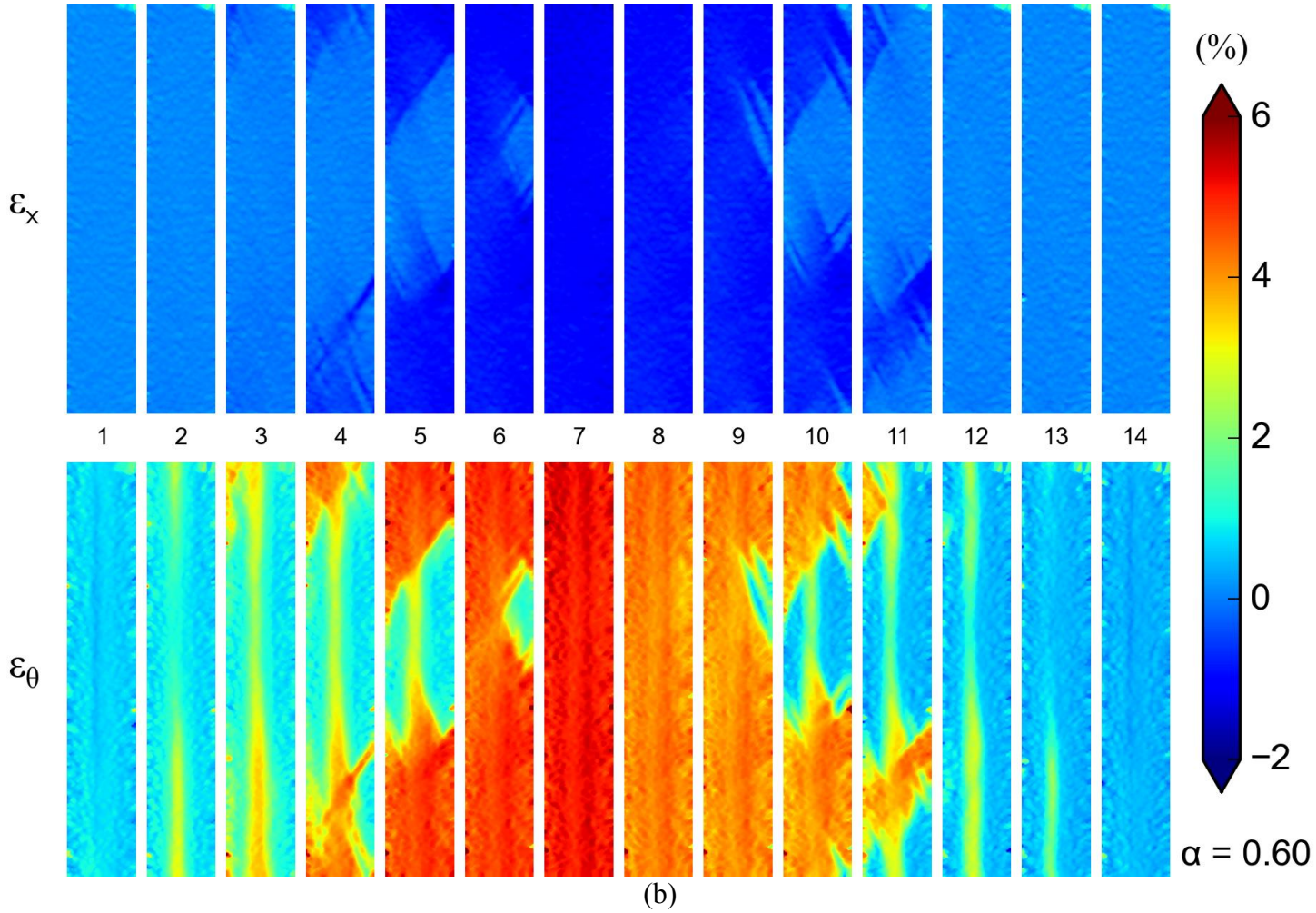

Fig. 4.18b Results from a biaxial test with $\sigma_x = 0.60\sigma_\theta$. (b) sequences of axial and hoop strain contours from DIC corresponding to the numbered bullets marked on the responses in (a).

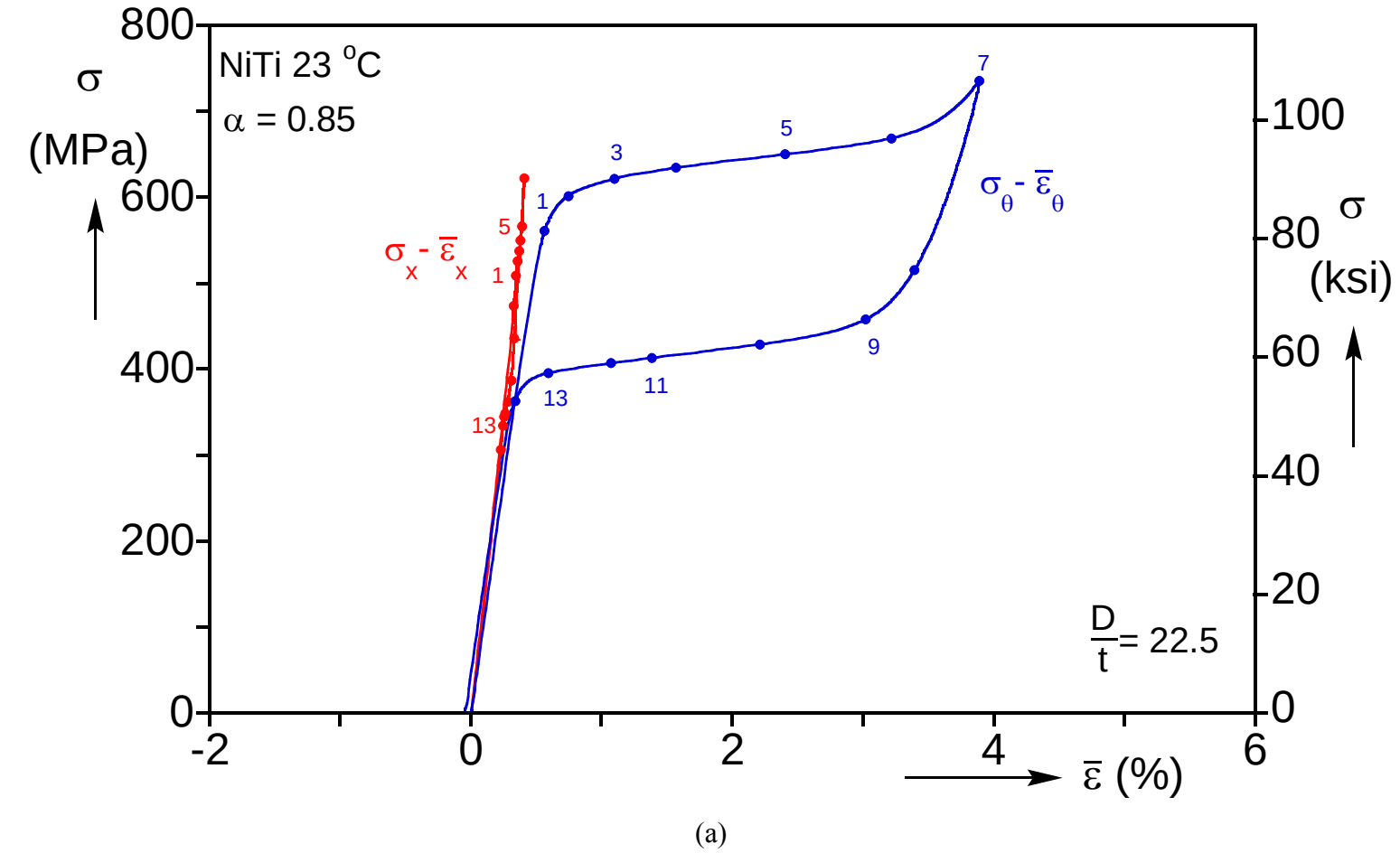

(a)

Fig. 4.19a Results from a biaxial test with $\sigma_x = 0.85\sigma_\theta$. (a) Stress-average strain responses.

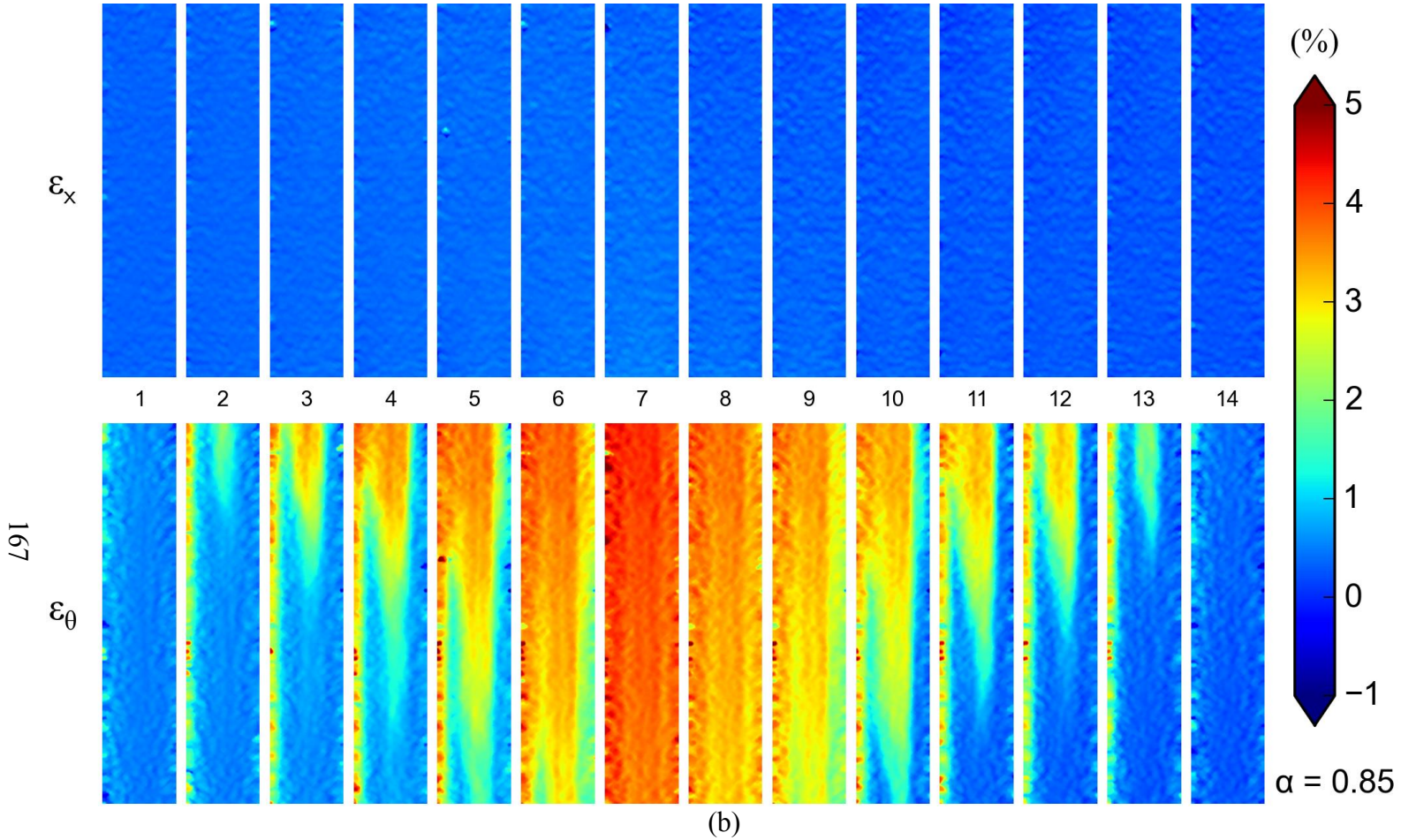

Fig. 4.19b Results from a biaxial test with $\sigma_x = 0.85\sigma_\theta$. (b) sequences of axial and hoop strain contours from DIC corresponding to the numbered bullets marked on the responses in (a).

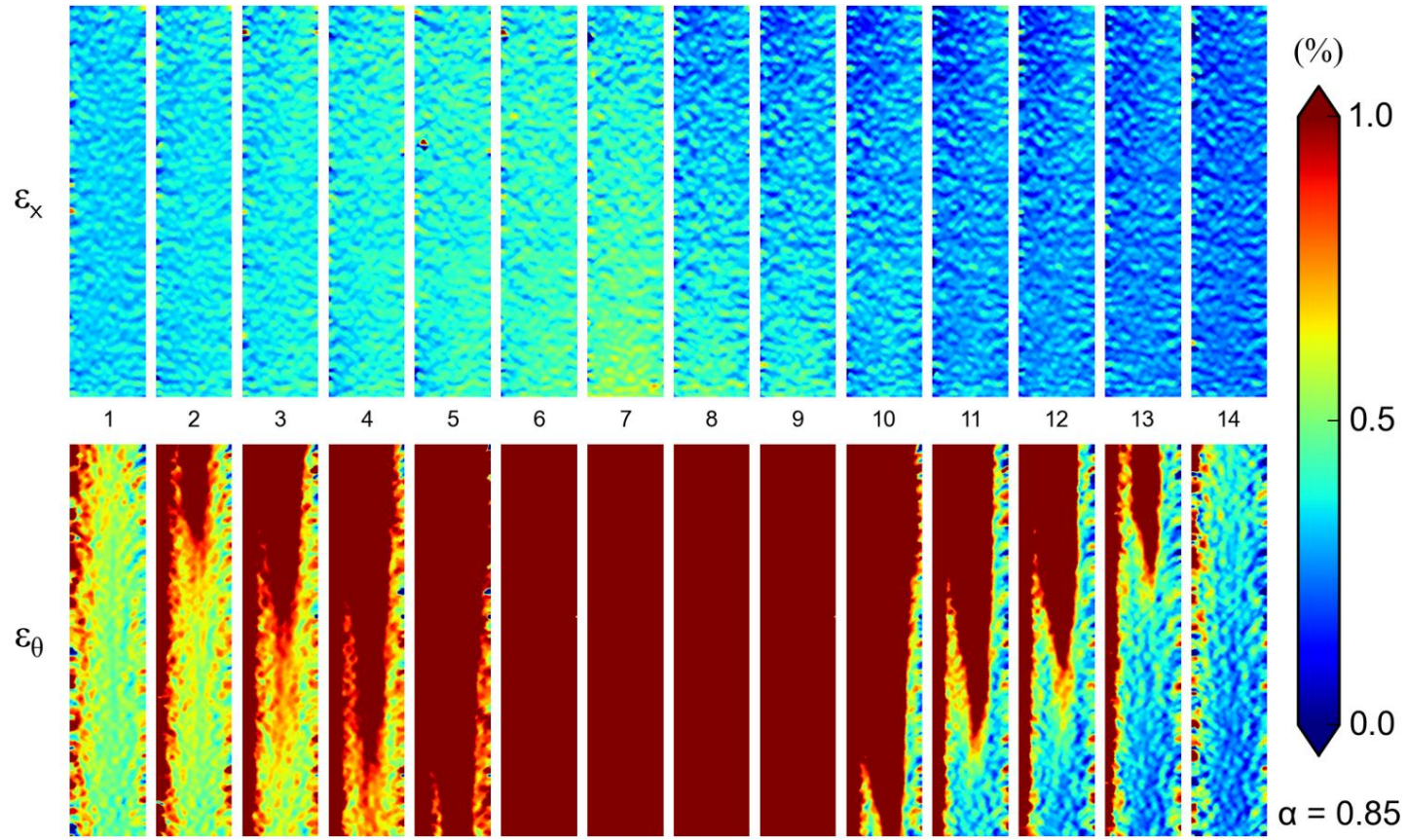

Fig. 4.19c Results from a biaxial test with $\sigma_x = 0.85\sigma_\theta$. (c) sequences of axial and hoop strain contours from (b) with reduced strain scale revealing the lack of localization in the axial component of strain.

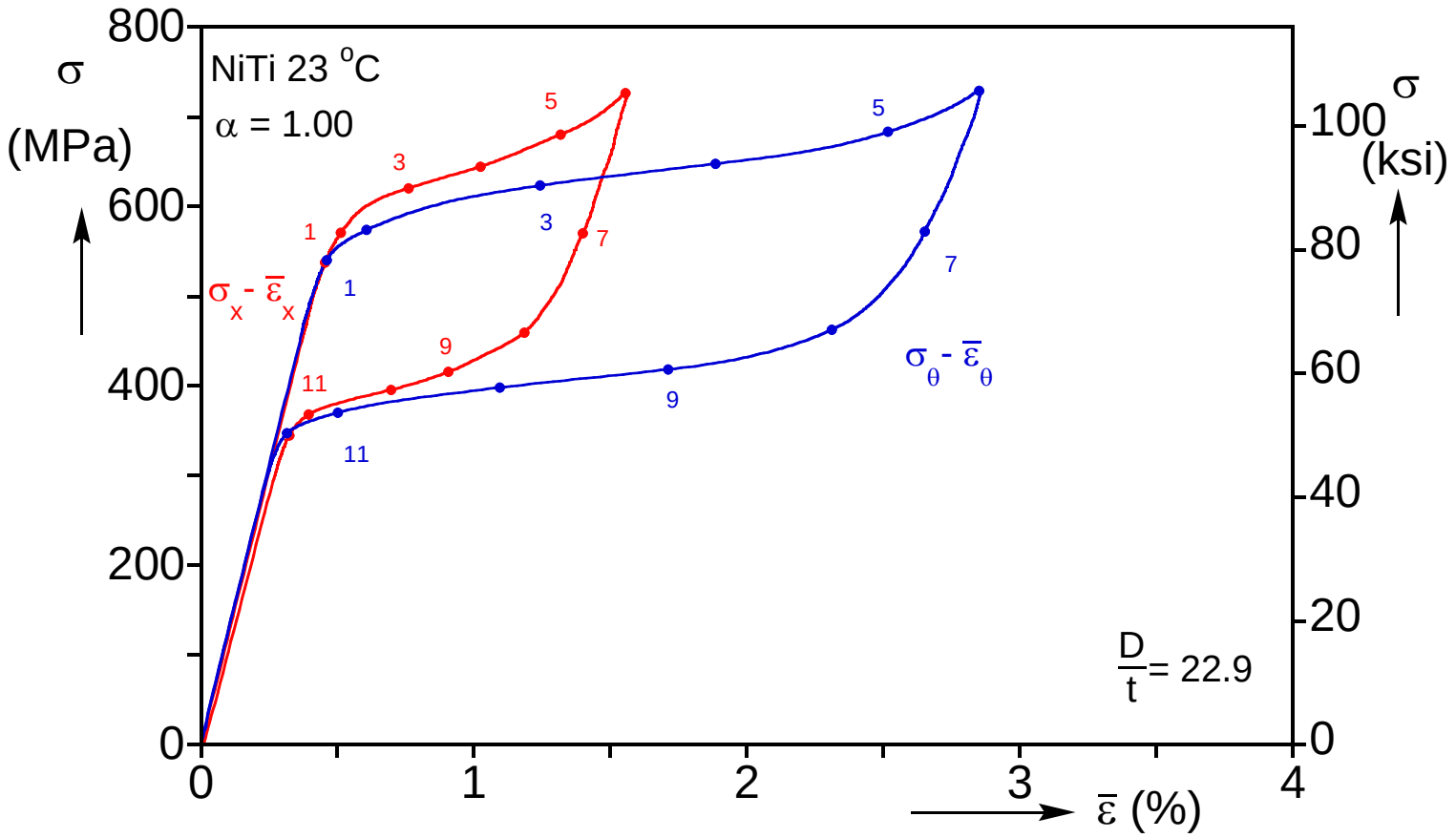

(a)

Fig. 4.20a Results from a biaxial test with $\sigma_x = 1.0\sigma_\theta$. (a) Stress-average strain responses.

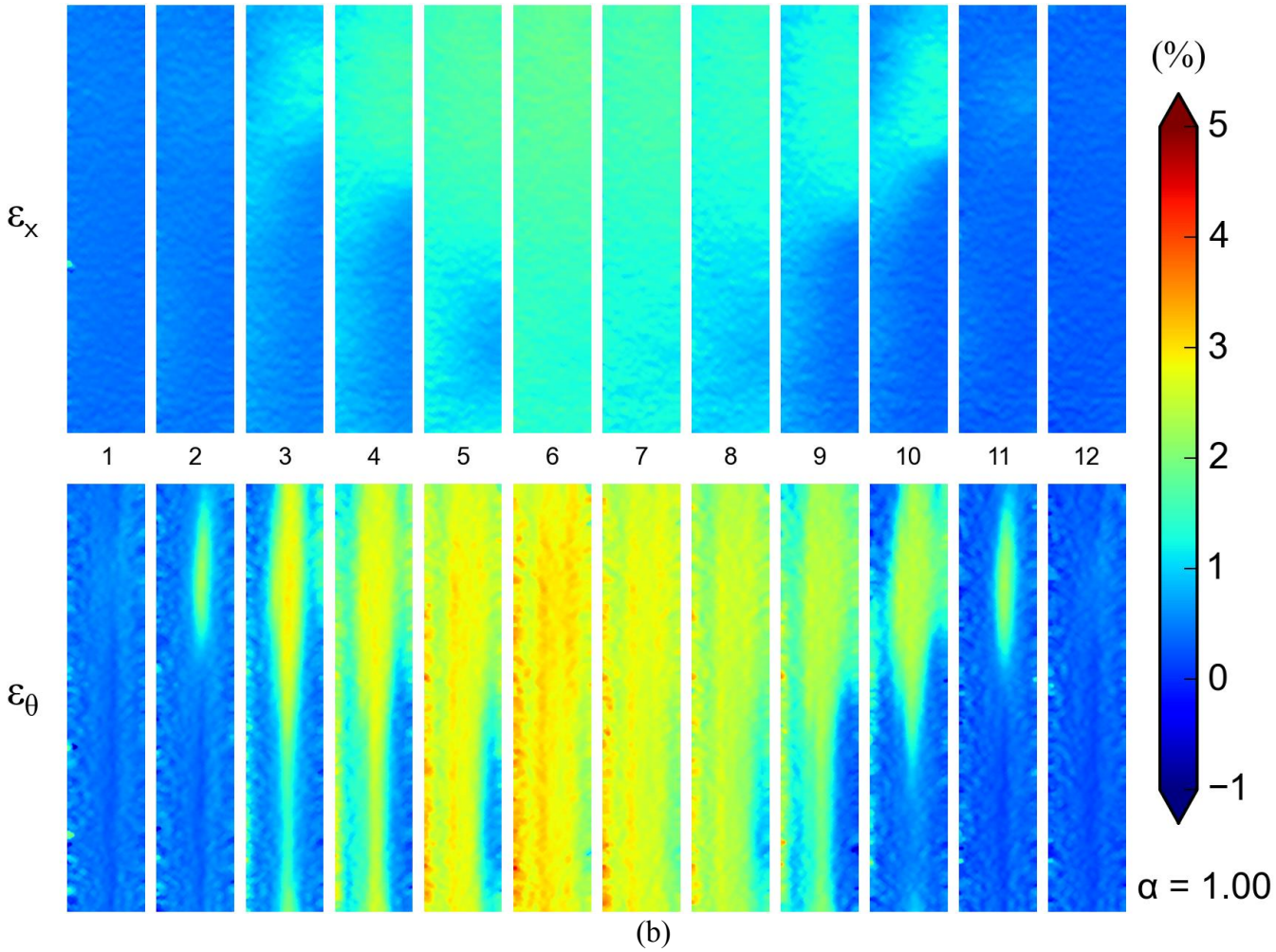

Fig. 4.20b Results from a biaxial test with $\sigma_x = 1.0\sigma_\theta$. (b) sequences of axial and hoop strain contours from DIC corresponding to the numbered bullets marked on the responses in (a).

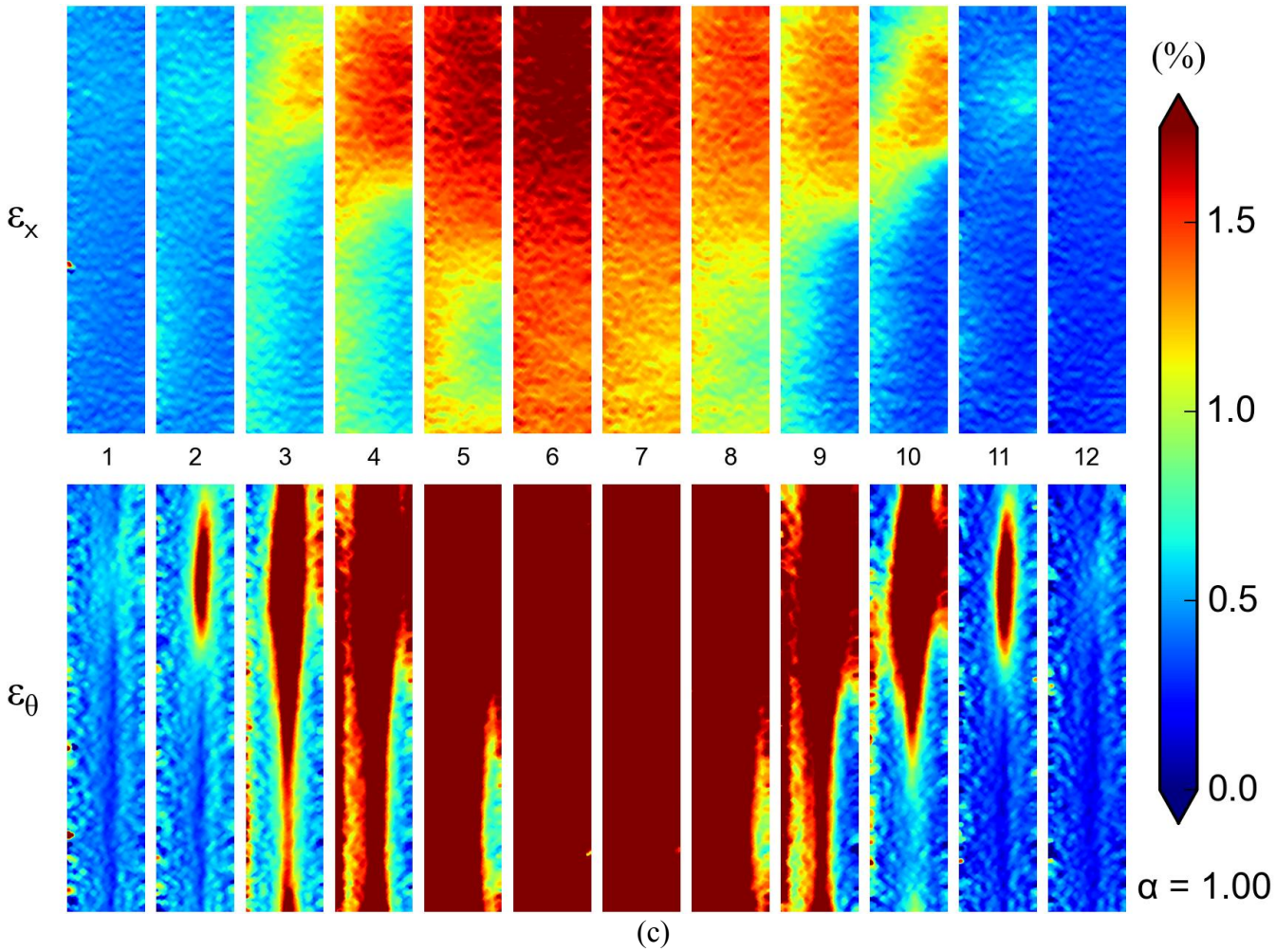

Fig. 4.20c Results from a biaxial test with $\sigma_x = 1.0\sigma_\theta$. (c) sequences of axial and hoop strain contours from (b) with reduced strain scale.

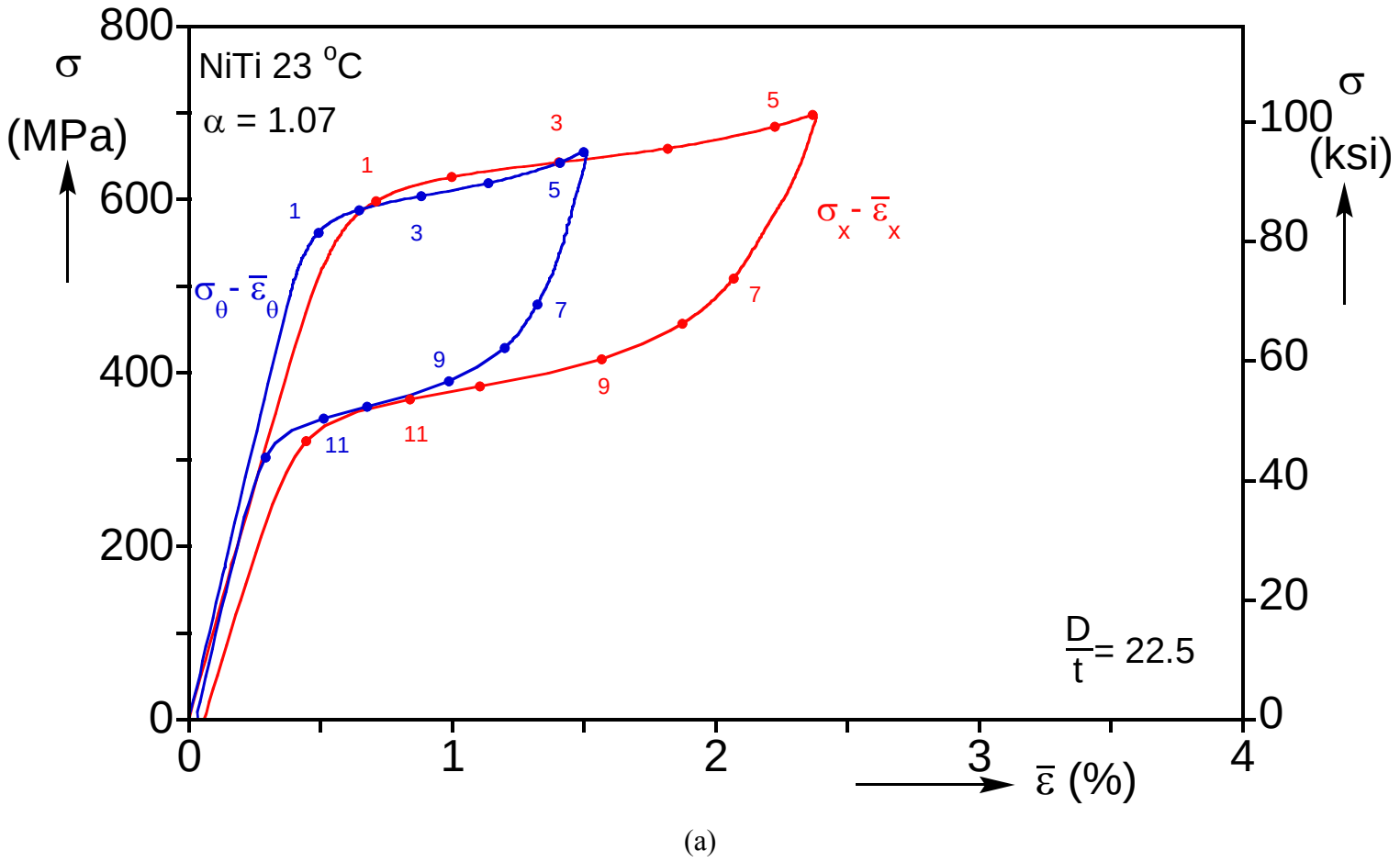

(a)

Fig. 4.21a Results from a biaxial test with $\sigma_x = 1.07\sigma_\theta$. (a) Stress-average strain responses.

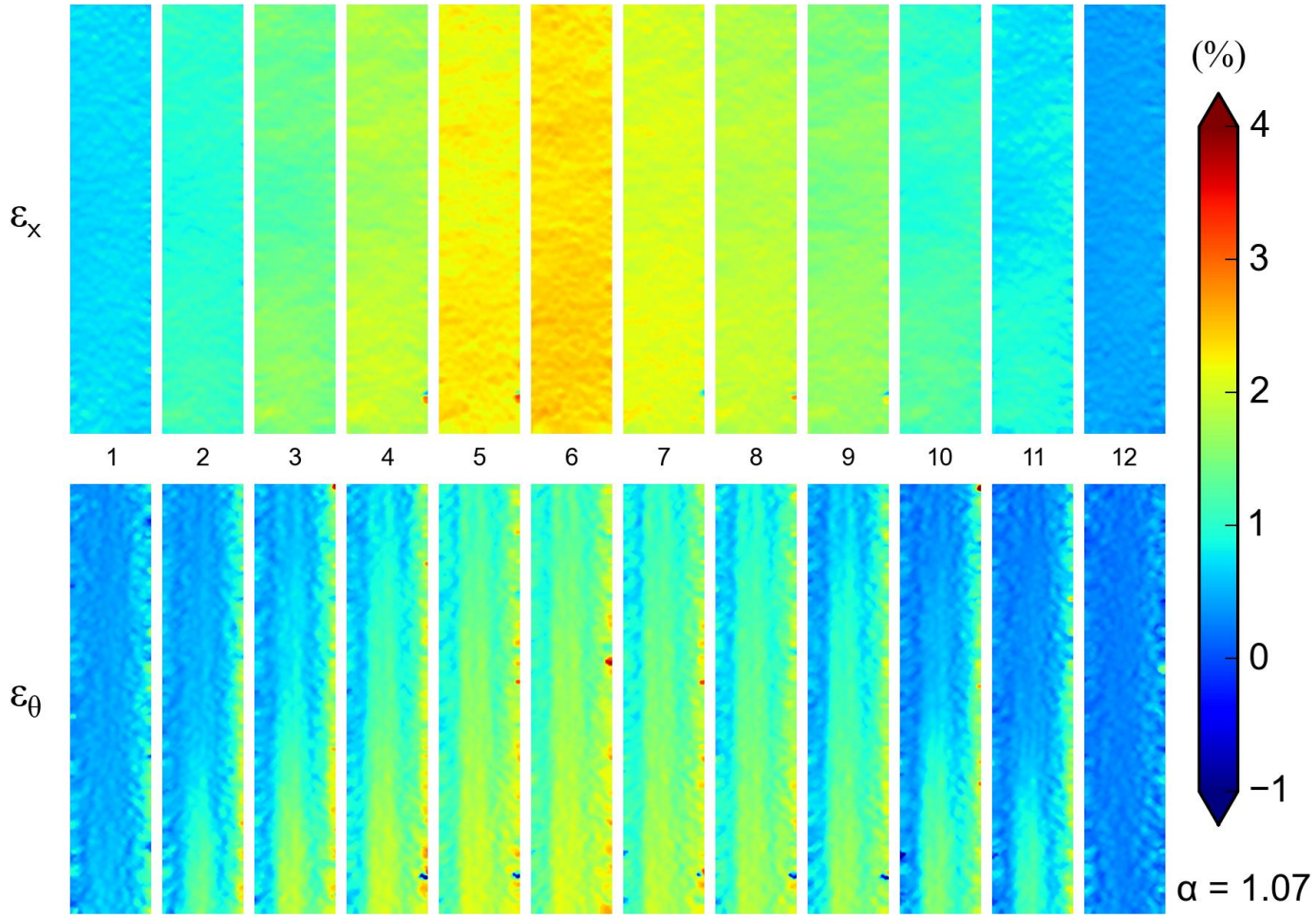

Fig. 4.21b Results from a biaxial test with $\sigma_x = 1.07\sigma_\theta$. (b) sequences of axial and hoop strain contours from DIC corresponding to the numbered bullets marked on the responses in (a).

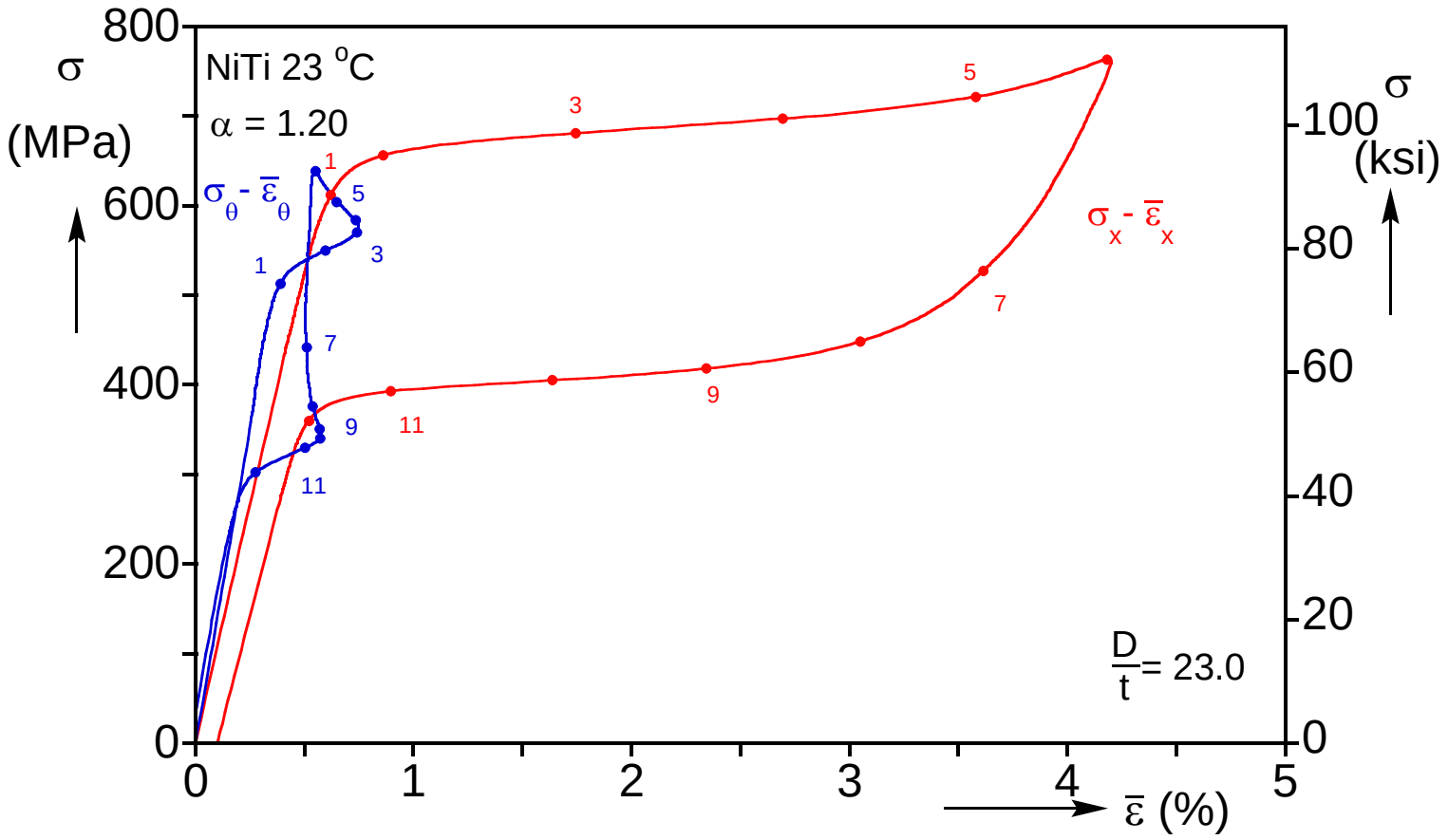

(a)

Fig. 4.22a Results from a biaxial test with $\sigma_x = 1.20\sigma_\theta$. (a) Stress-average strain responses.

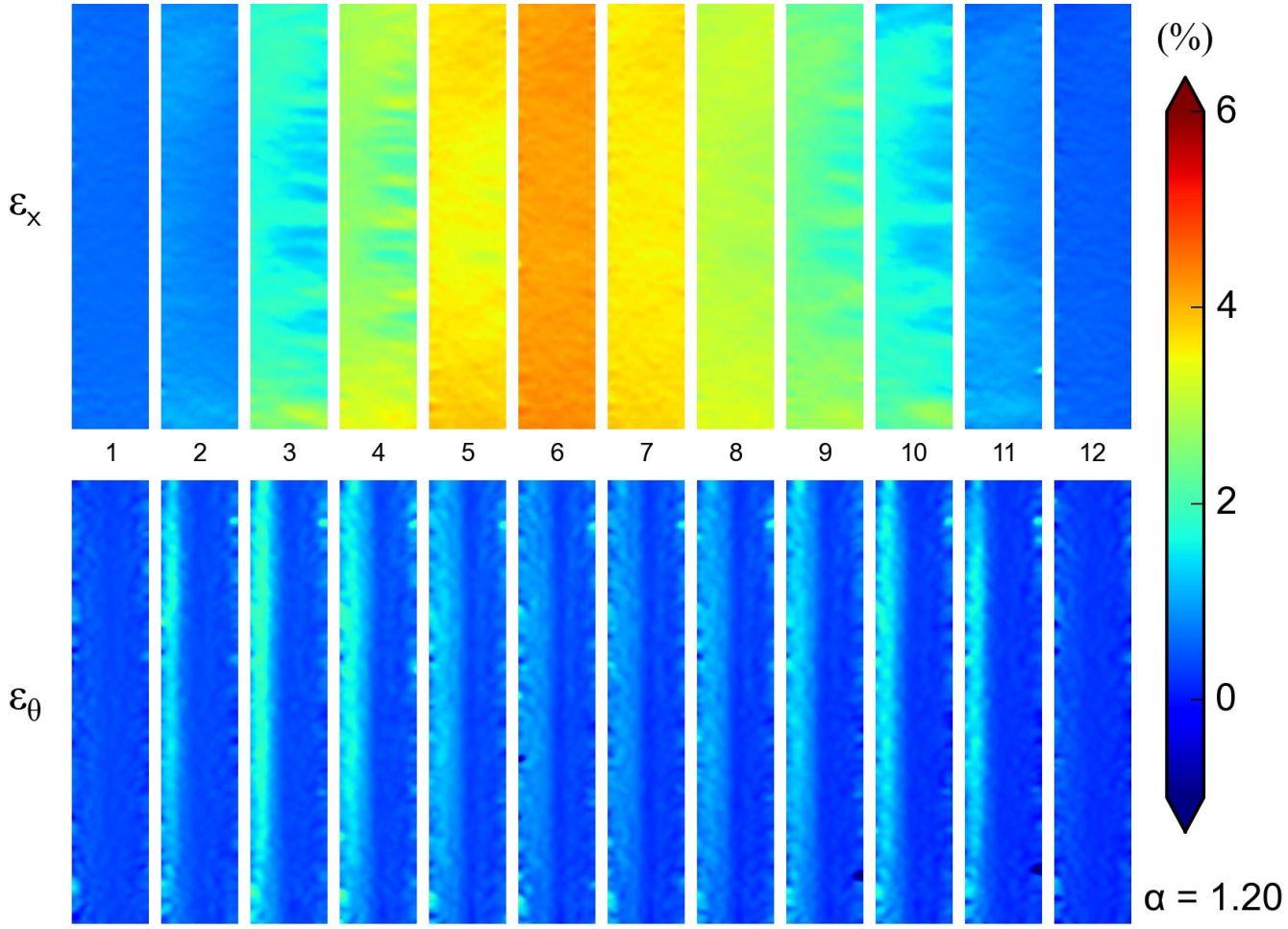

Fig. 4.22b Results from a biaxial test with $\sigma_x = 1.20\sigma_\theta$. (b) sequences of axial and hoop strain contours from DIC corresponding to the numbered bullets marked on the responses in (a).

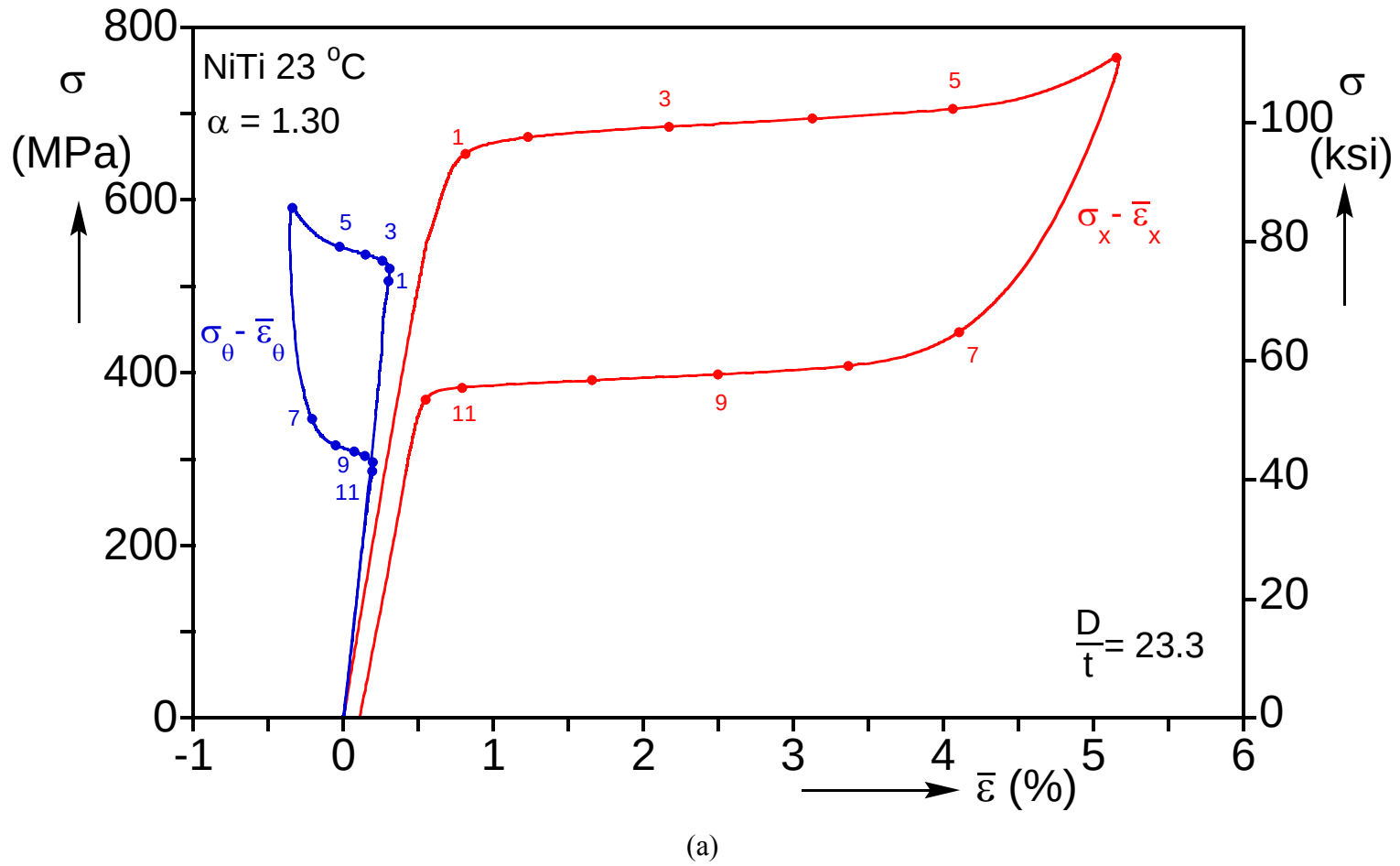

(a)

Fig. 4.23a Results from a biaxial test with $\sigma_x = 1.30\sigma_\theta$. (a) Stress-average strain responses

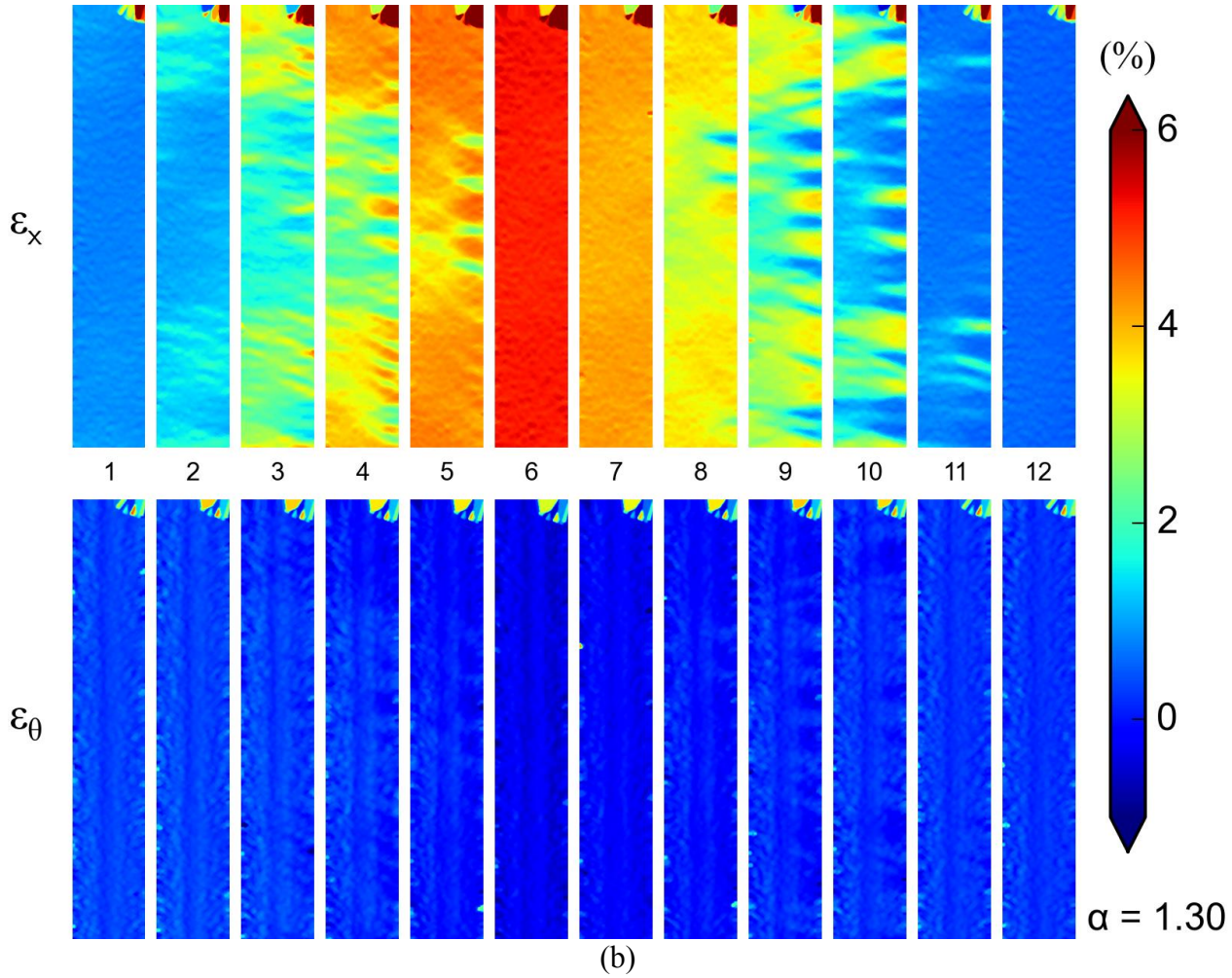

Fig. 4.23b Results from a biaxial test with $\sigma_x = 1.30\sigma_\theta$. (b) sequences of axial and hoop strain contours from DIC corresponding to the numbered bullets marked on the responses in (a).

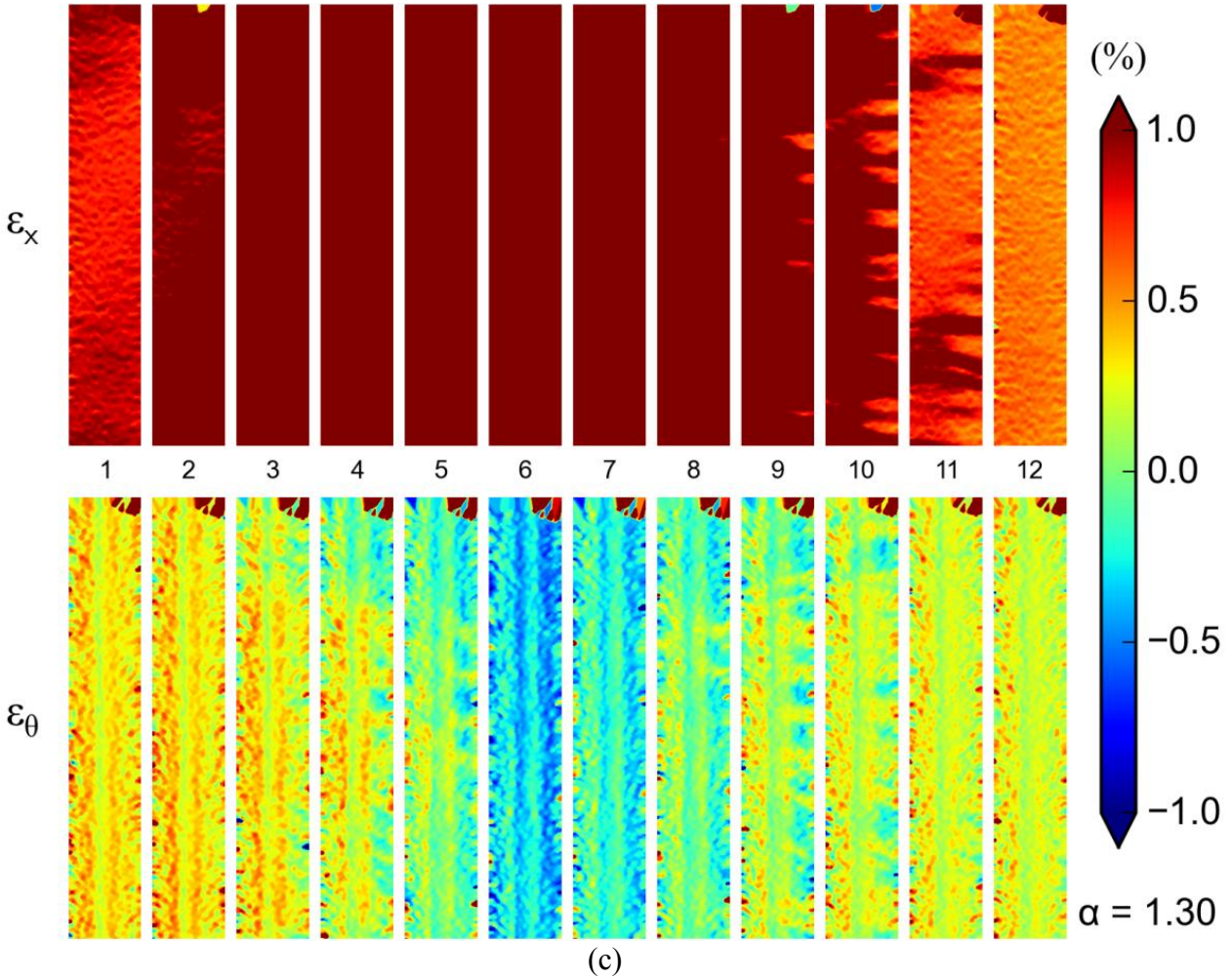

Fig. 4.23c Results from a biaxial test with $\sigma_x = 1.30\sigma_\theta$. (c) sequences of axial and hoop strain contours from (b) with reduced strain scale.

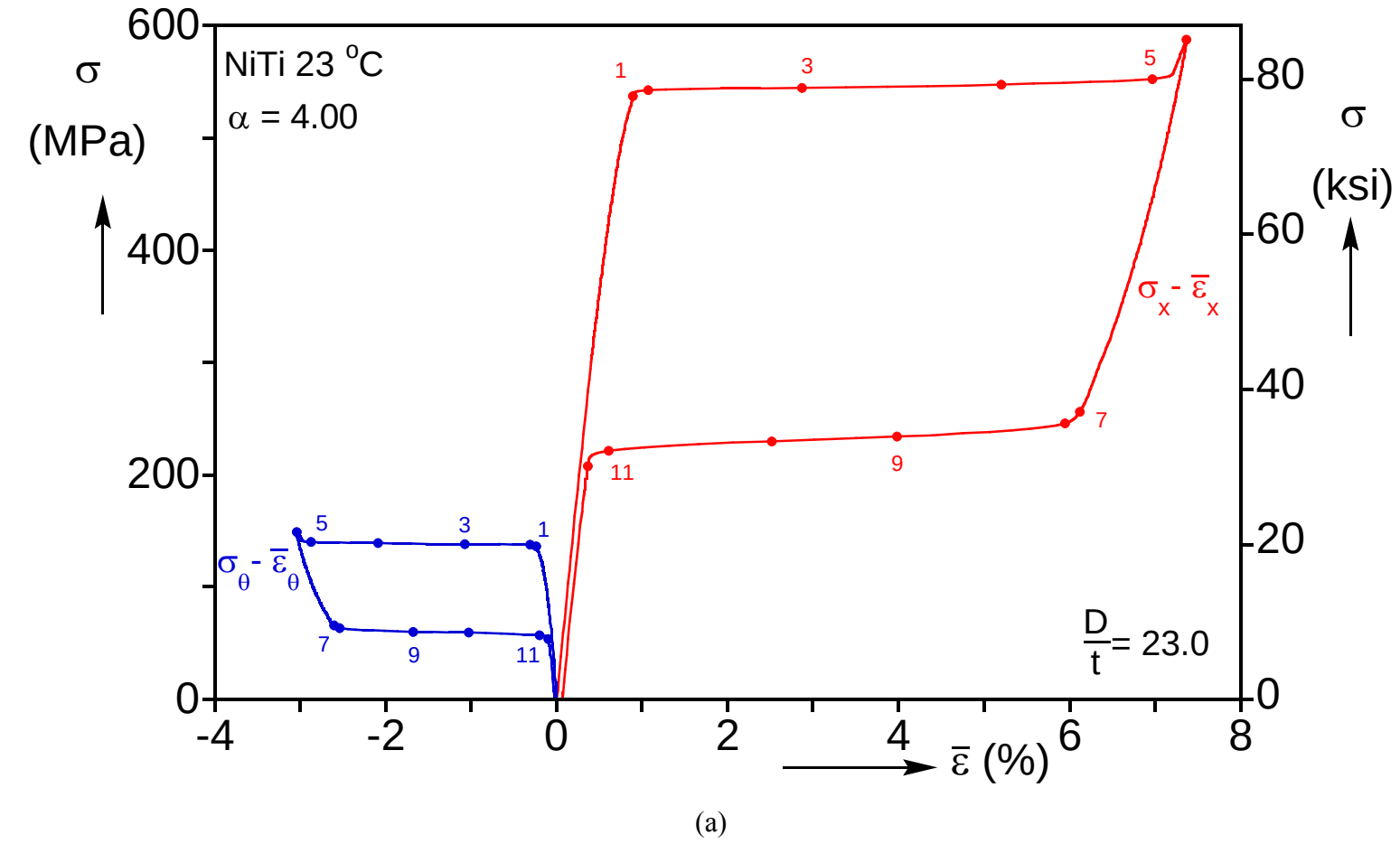

(a)

Fig. 4.24a Results from a biaxial test with $\sigma_x = 4.0\sigma_\theta$. (a) Stress-average strain responses.

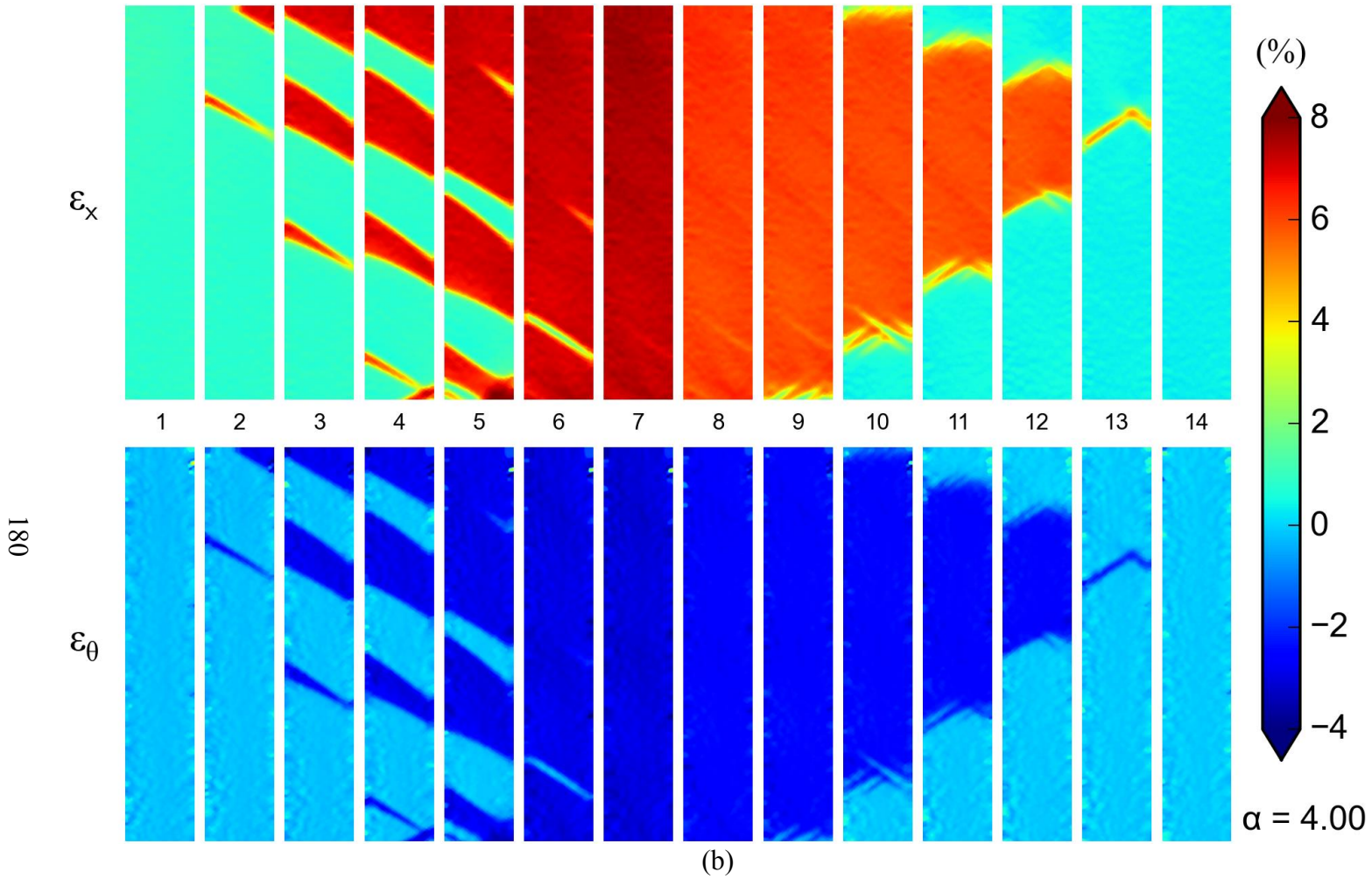

Fig. 4.24b Results from a biaxial test with $\sigma_x = 4.0\sigma_\theta$. (b) sequences of axial and hoop strain contours from DIC corresponding to the numbered bullets marked on the responses in (a).

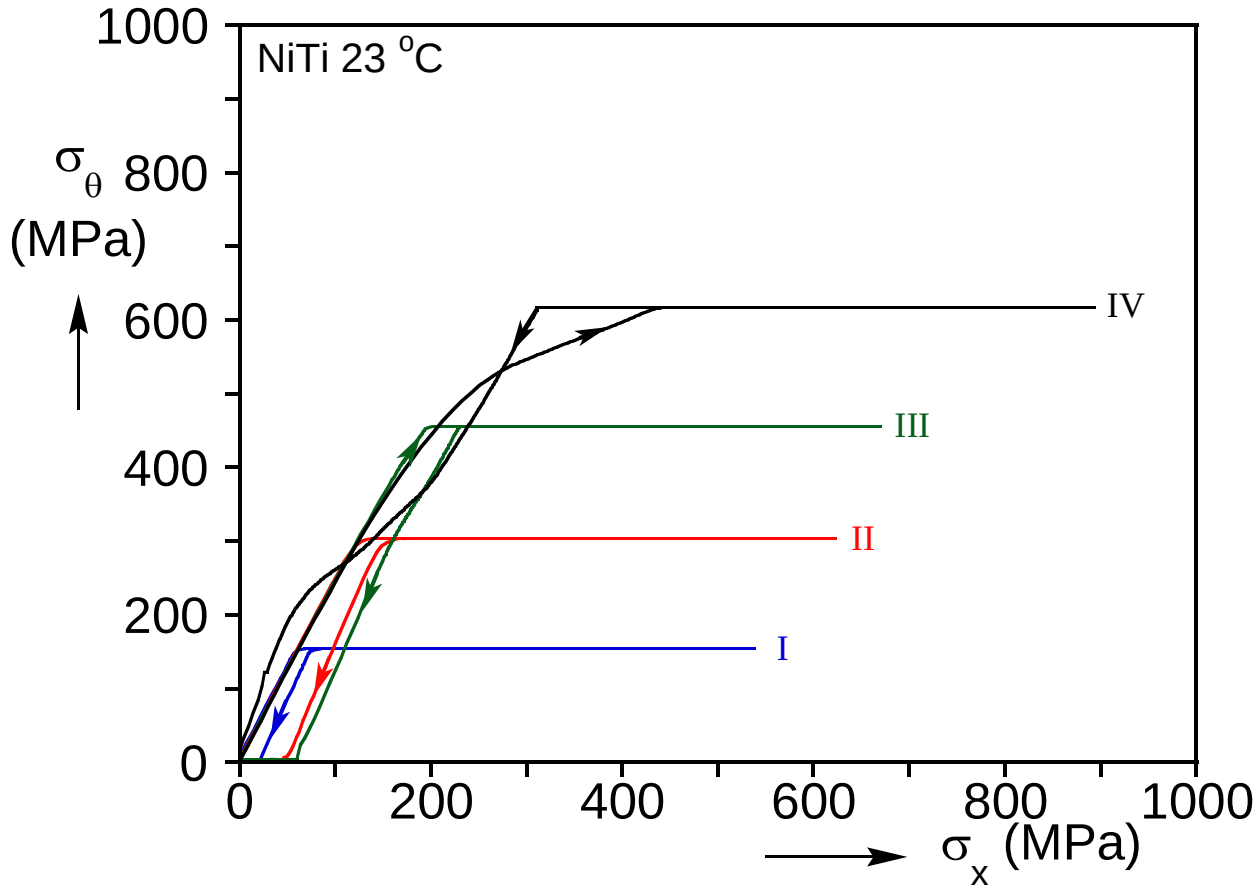

Fig. 4.25 Measured non-radial stress paths for biaxial experiments on NiTi tubes.

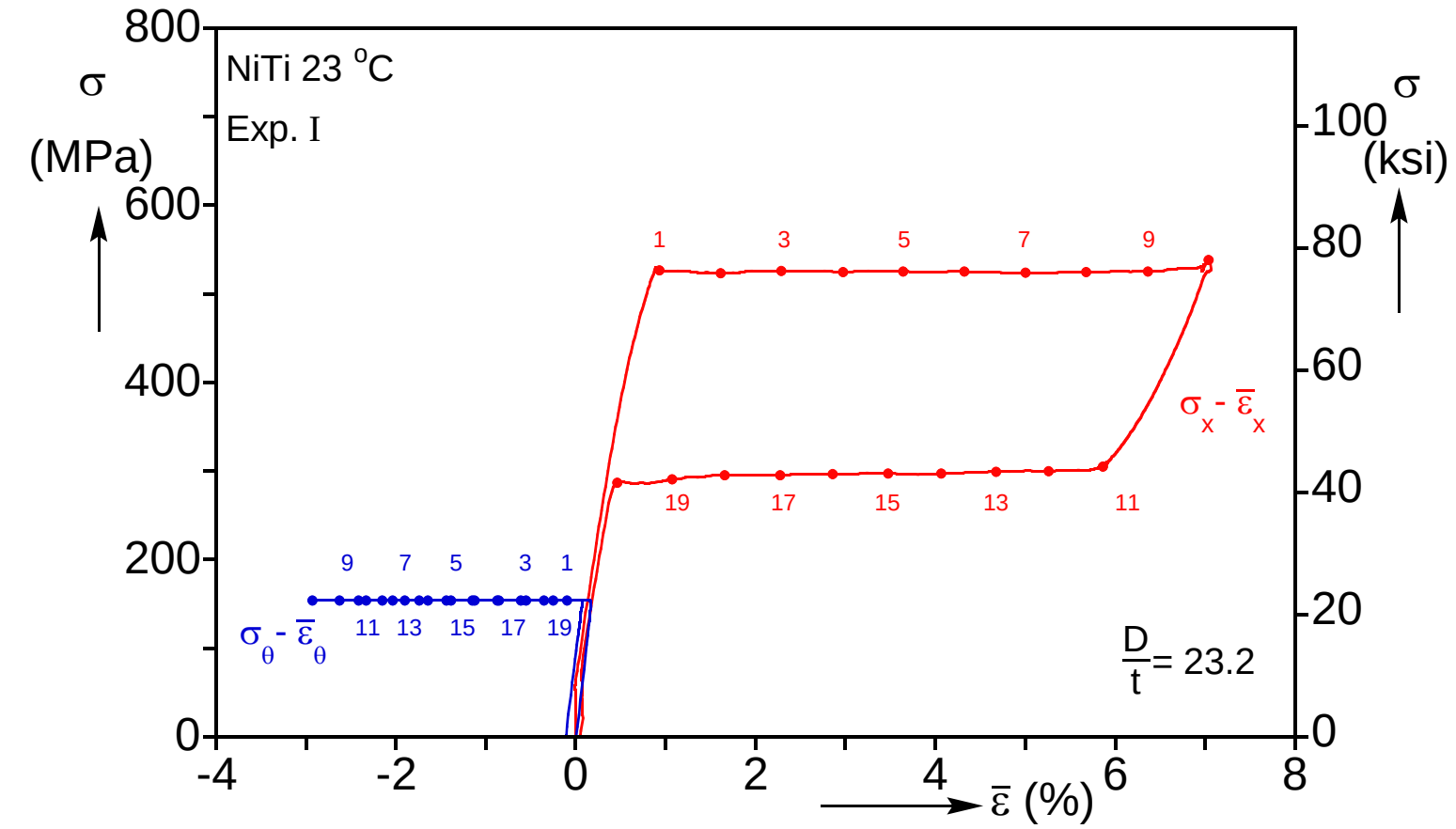

(a)

Fig. 4.26a Results from a non-radial biaxial test with stress path I from Fig. 4.25. (a) Stress-average strain responses.

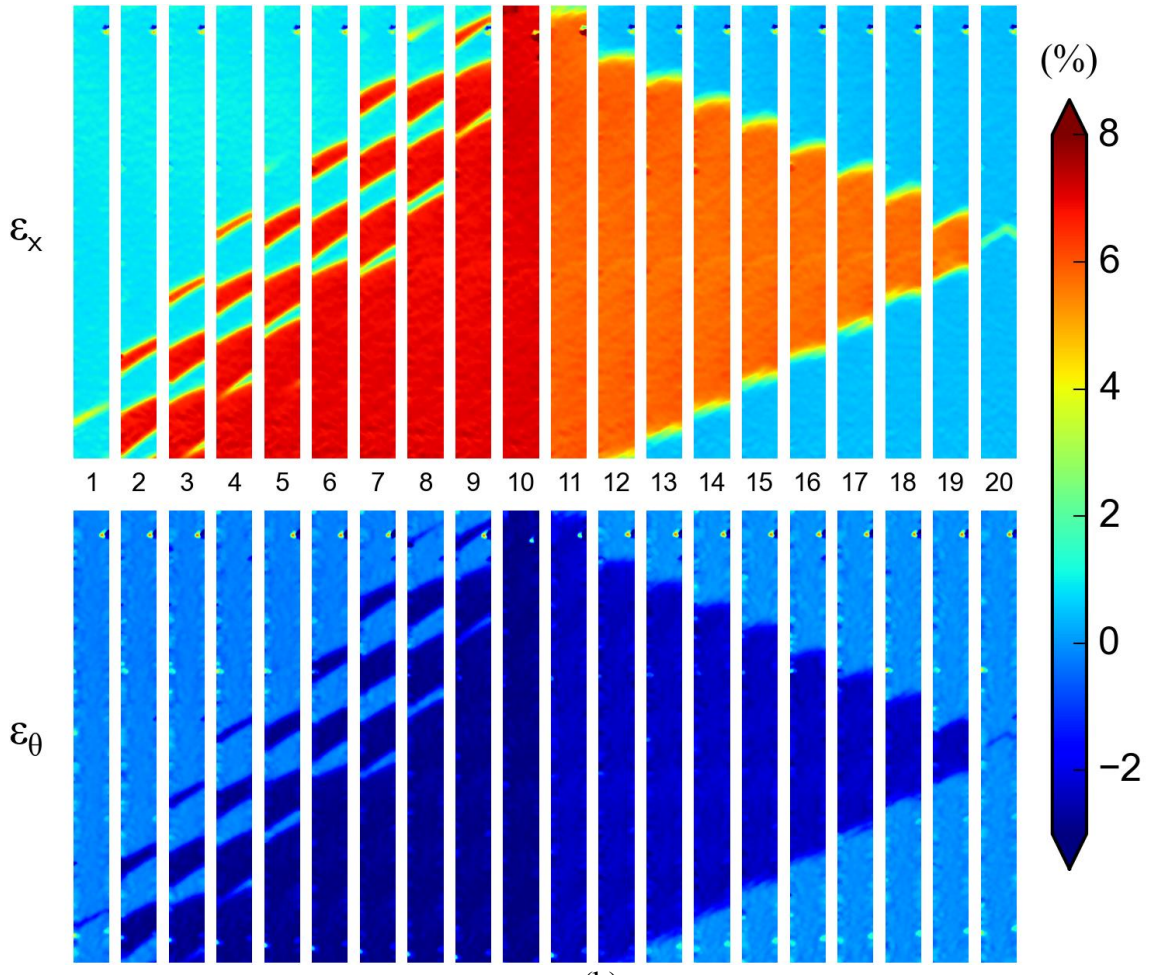

Fig. 4.26b Results from a non-radial biaxial test with stress path I from Fig. 4.25. (b) sequences of axial and hoop strain contours from DIC corresponding to the numbered bullets marked on the responses in (a).

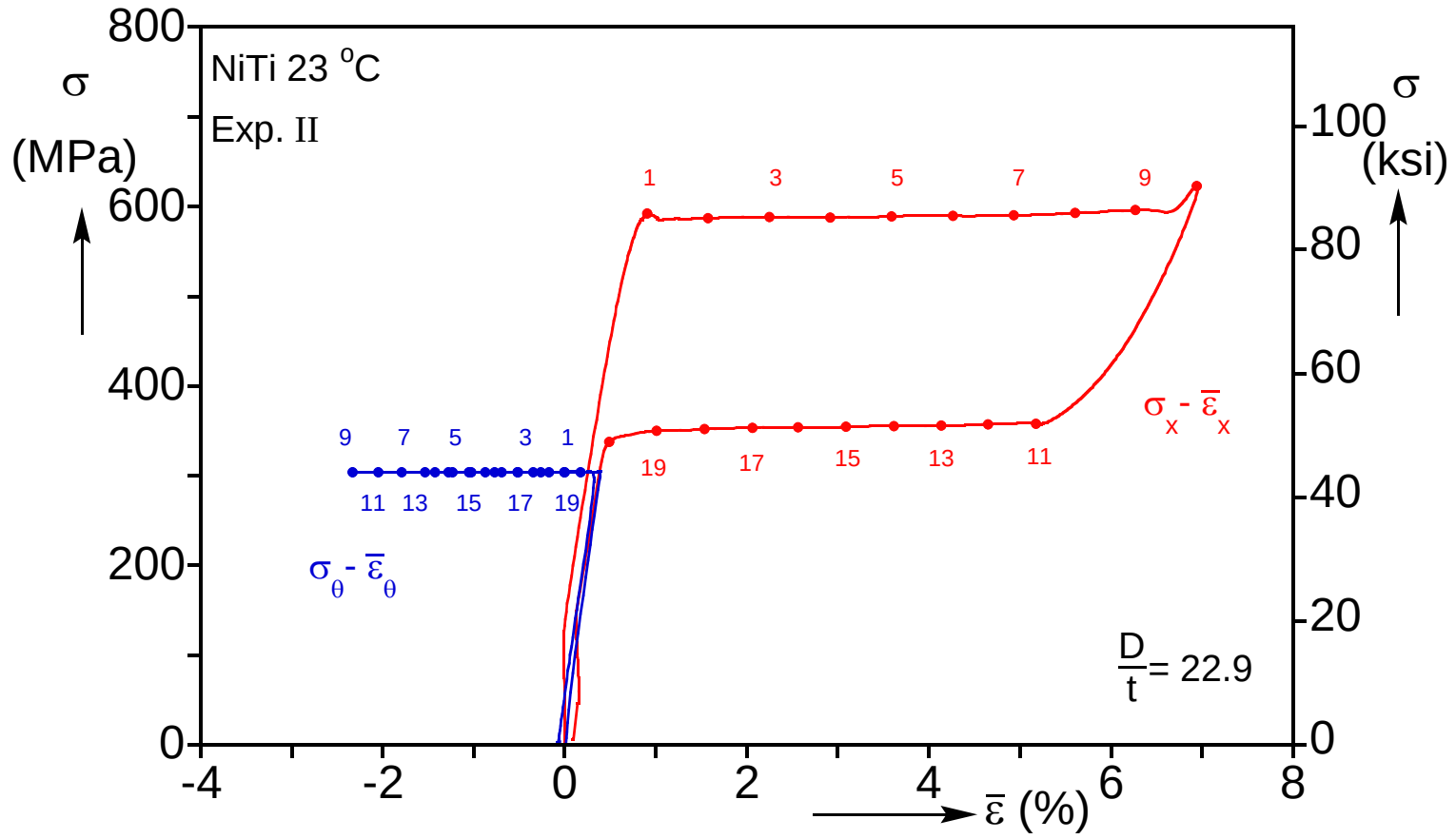

(a)

Fig. 4.27a Results from a non-radial biaxial test with stress path II from Fig. 4.25. (a) Stress-average strain responses.

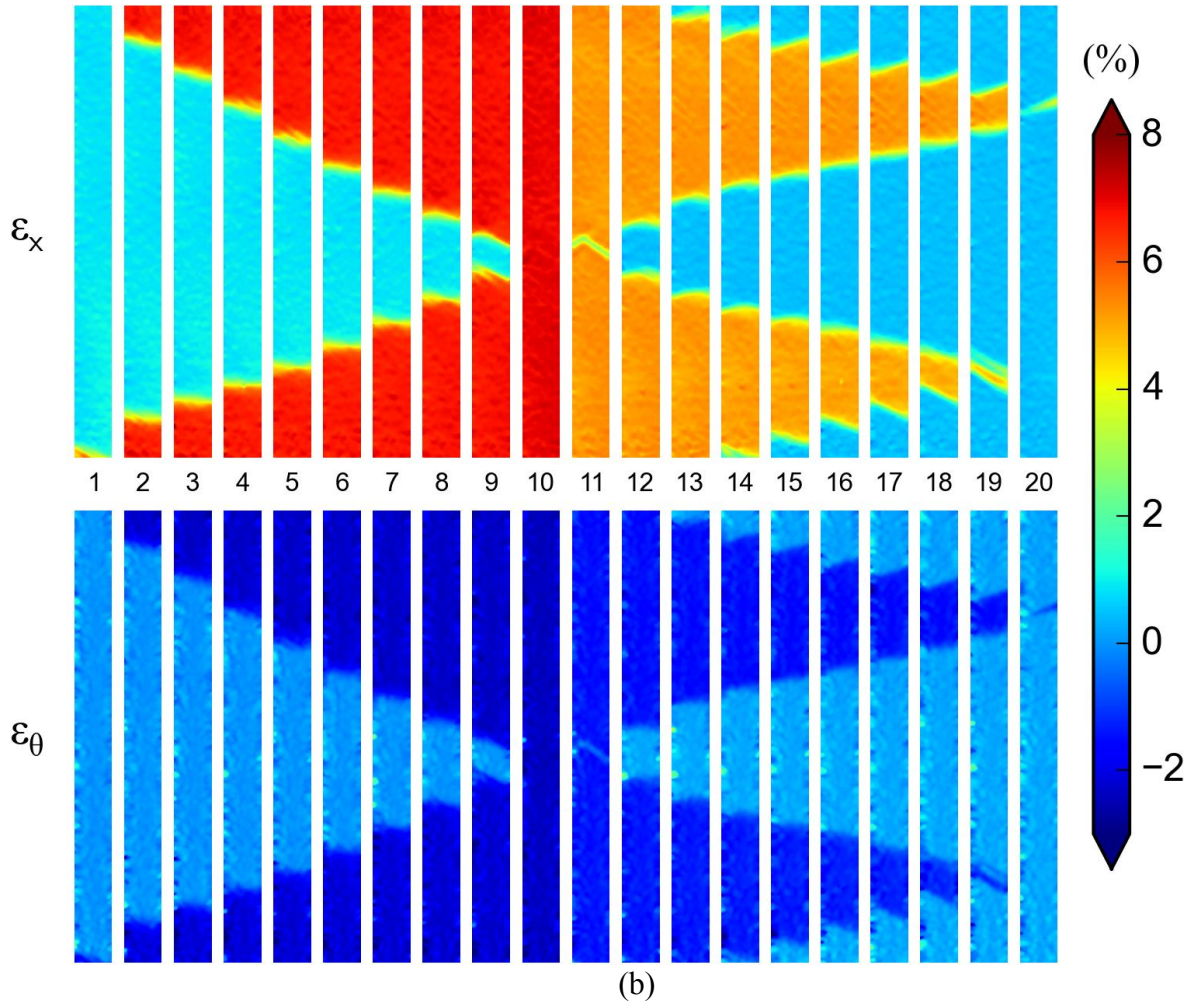

Fig. 4.27b Results from a non-radial biaxial test with stress path II from Fig. 4.25. (b) sequences of axial and hoop strain contours from DIC corresponding to the numbered bullets marked on the responses in (a).

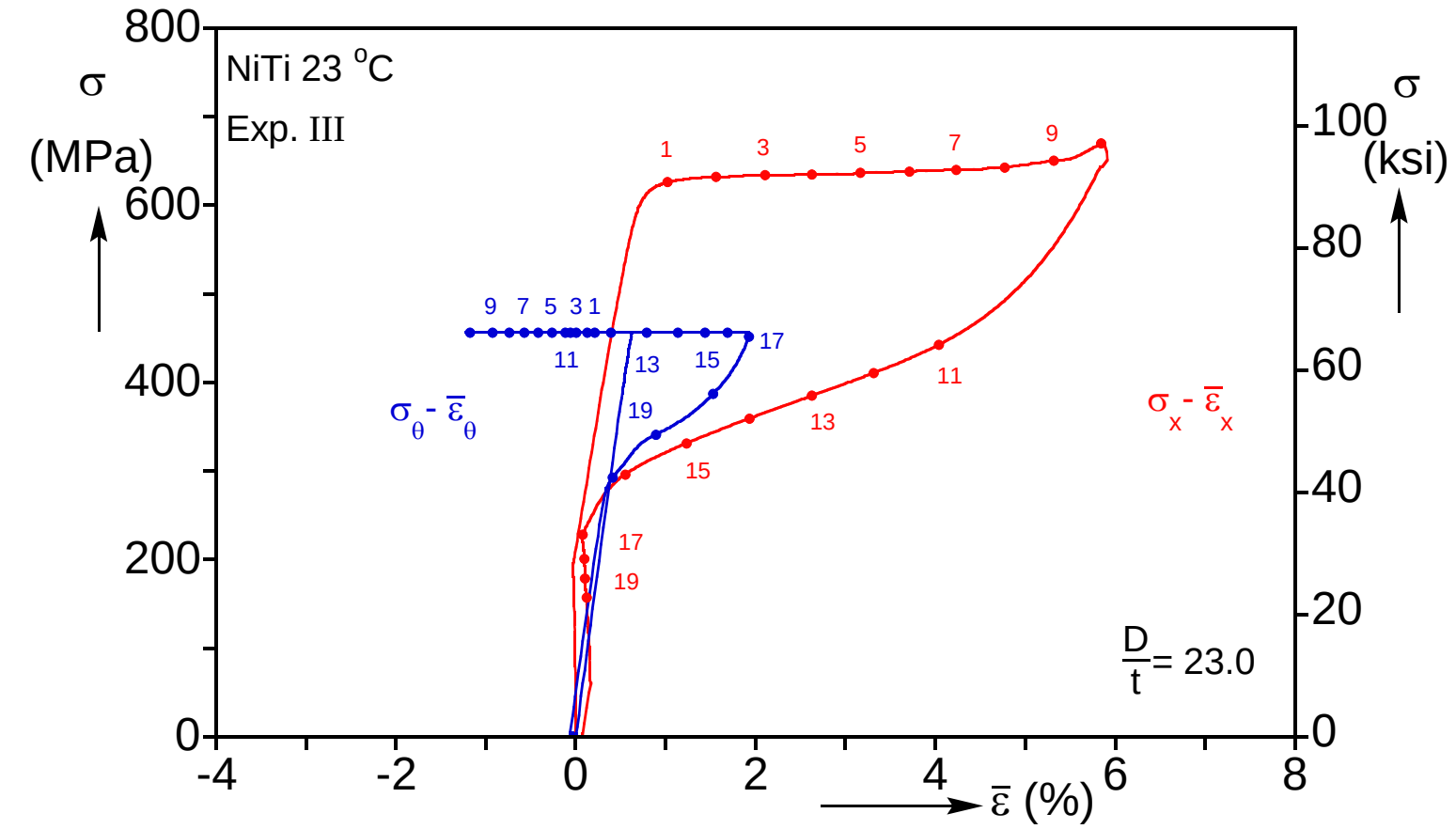

(a)

Fig. 4.28a Results from a non-radial biaxial test with stress path III from Fig. 4.25. (a) Stress-average strain responses.

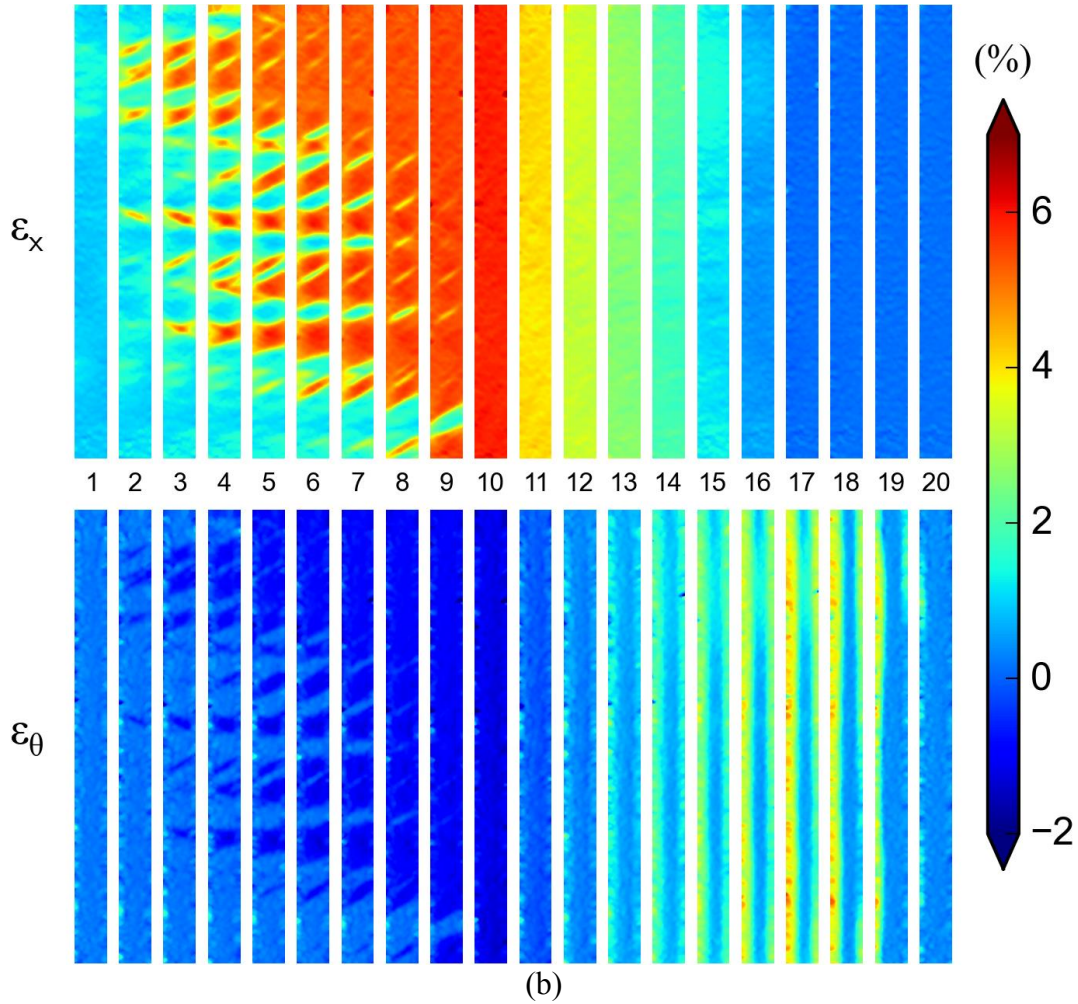

Fig. 4.28b Results from a non-radial biaxial test with stress path III from Fig. 4.25. (b) sequences of axial and hoop strain contours from DIC corresponding to the numbered bullets marked on the responses in (a).

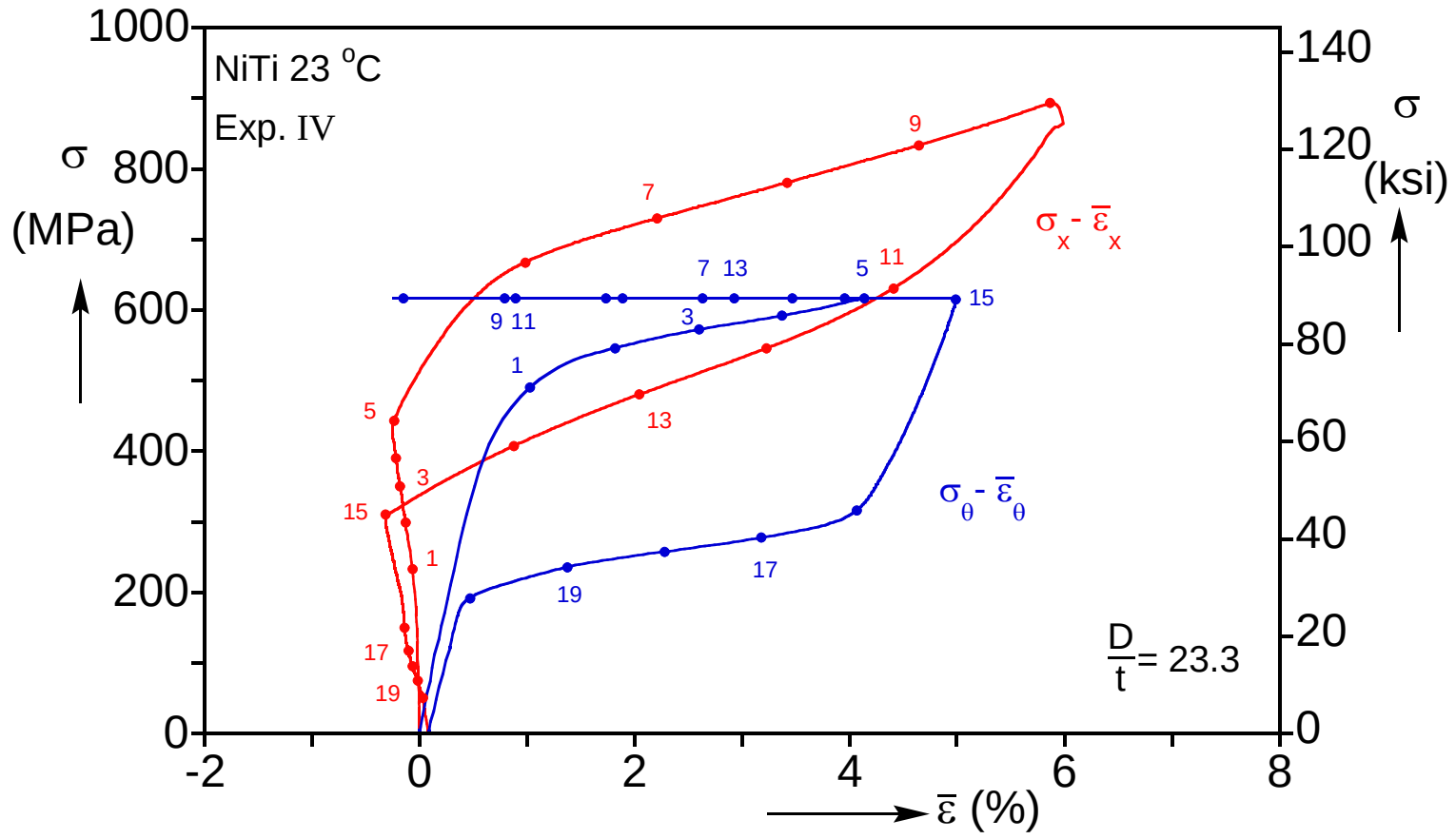

(a)

Fig. 4.29a Results from a non-radial biaxial test with stress path IV from Fig. 4.25. (a) Stress-average strain responses.

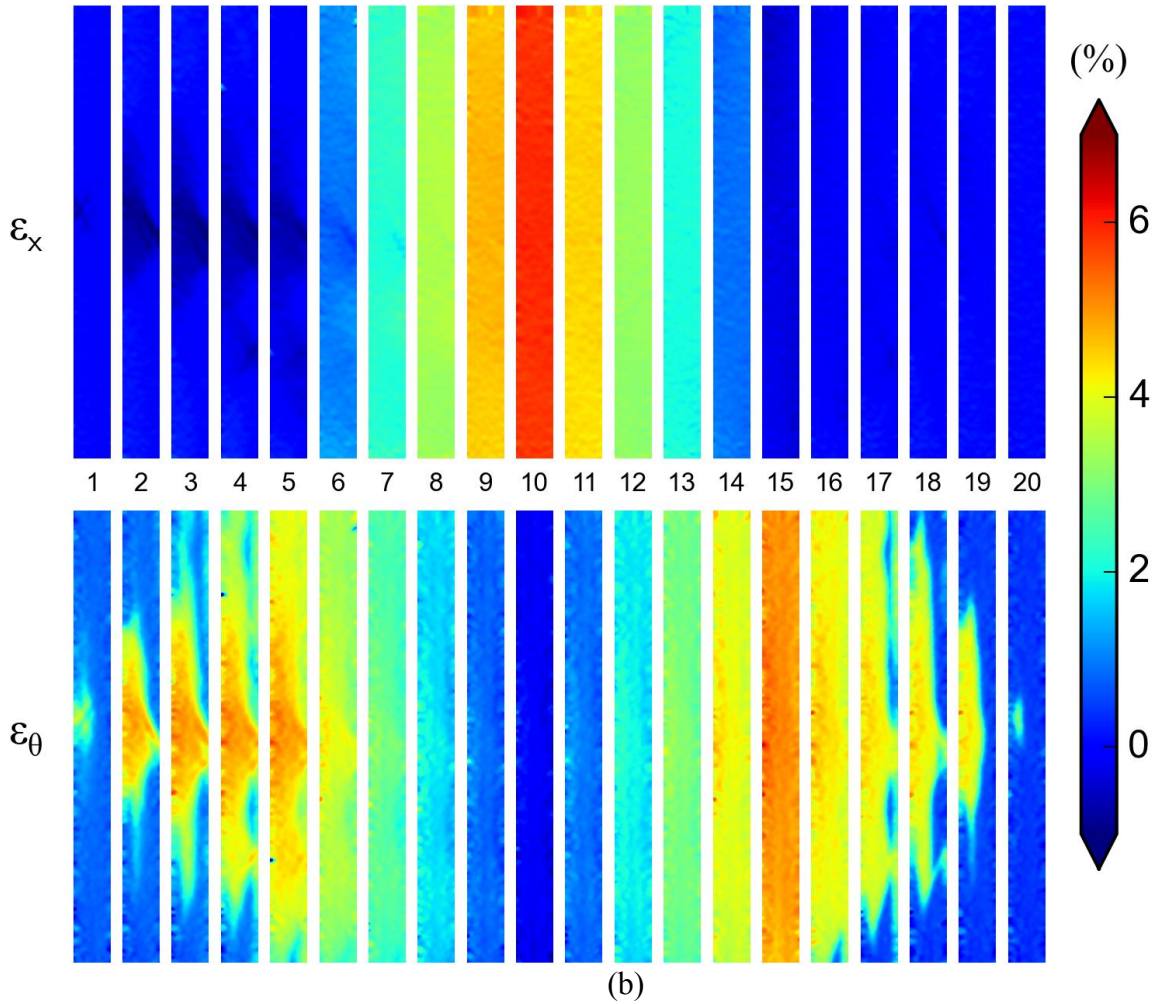

Fig. 4.29b Results from a non-radial biaxial test with stress path IV from Fig. 4.25. (b) sequences of axial and hoop strain contours from DIC corresponding to the numbered bullets marked on the responses in (a).

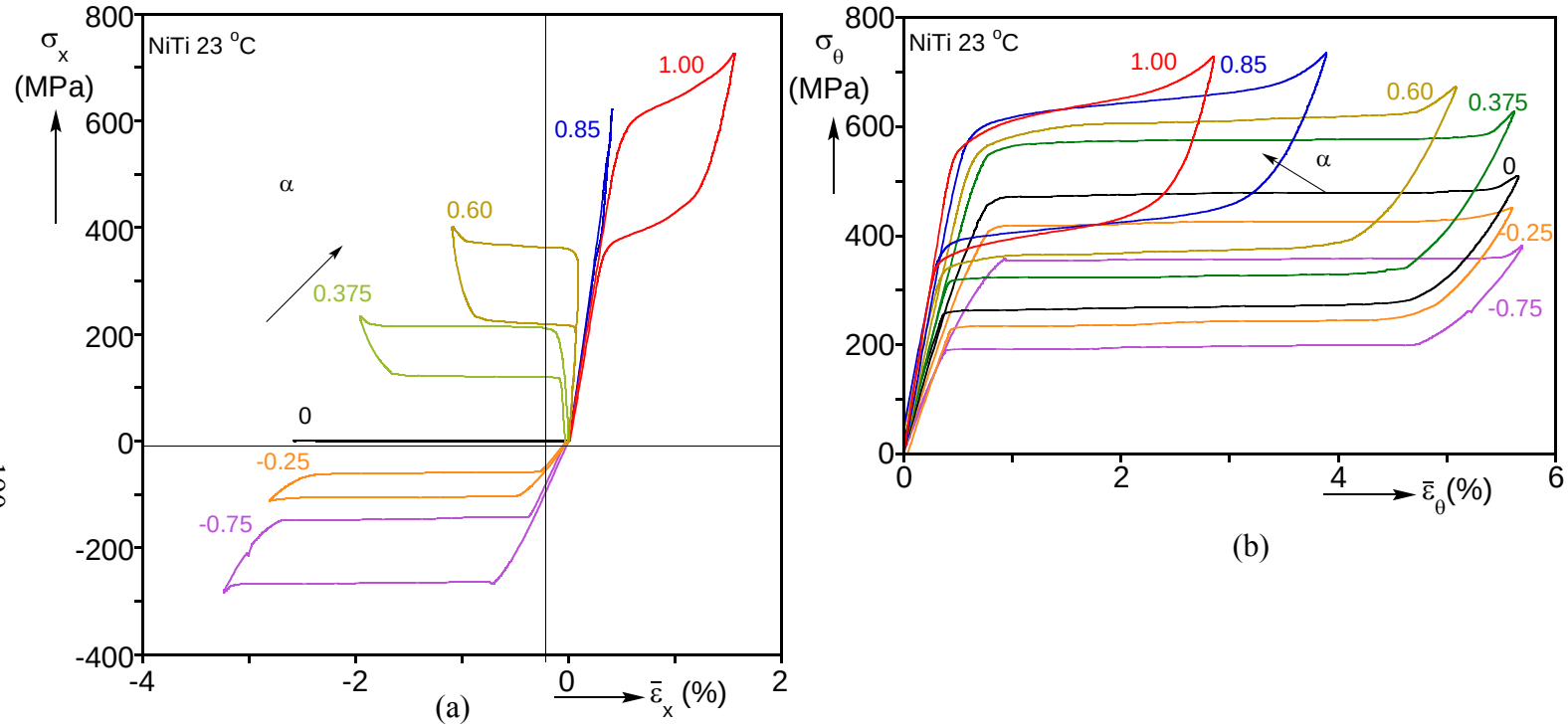

Fig. 4.30 Representative stress-average strain responses for biaxial stress states with $\alpha \le 1.0$. (a) $\sigma_x - \bar{\varepsilon}_x$ and (b) $\sigma_\theta - \bar{\varepsilon}_\theta$.

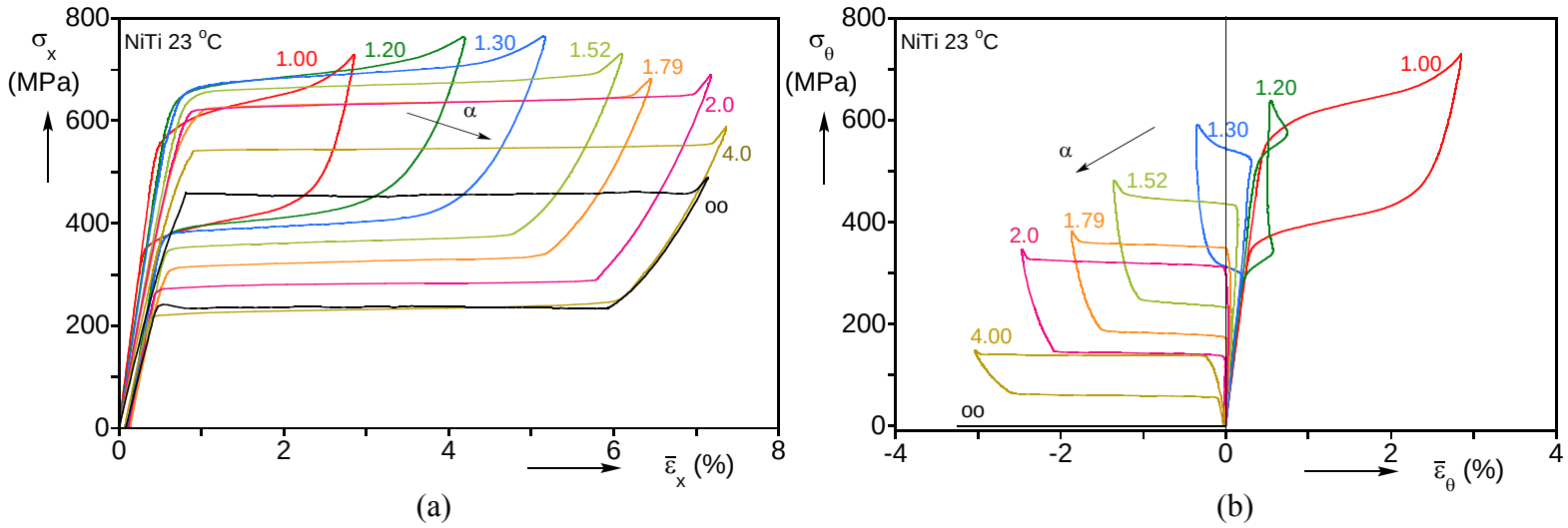

Fig. 4.31 Representative stress-average strain responses for biaxial stress states with $\alpha \geq 1.0$. (a) $\sigma_x - \bar{\varepsilon}_x$ and (b) $\sigma_\theta - \bar{\varepsilon}_\theta$.

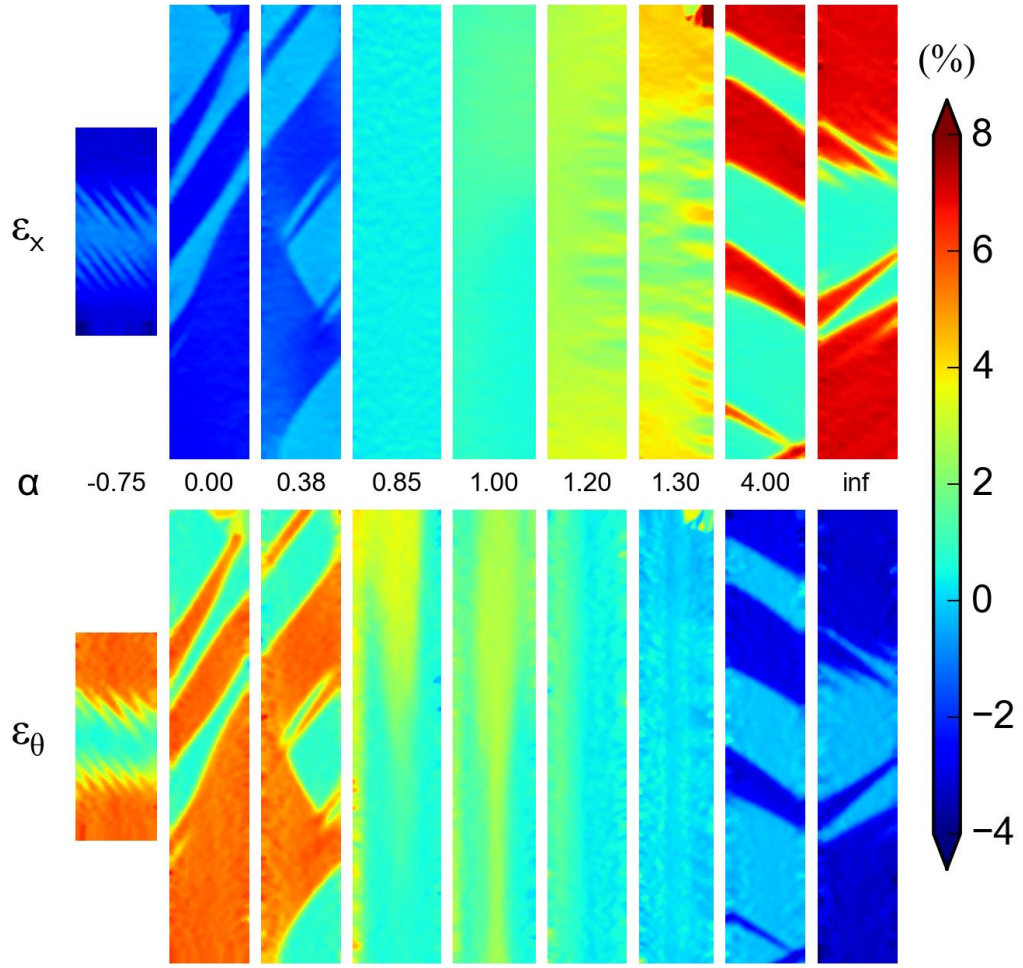

(a)

Fig. 4.32a (a) Sequence of strain contours along the A→M transformation plateau for nine stress ratios showing the transition from hoop dominant inhomogneneous to homogeneous to axially dominant inhomogeneous deformation.

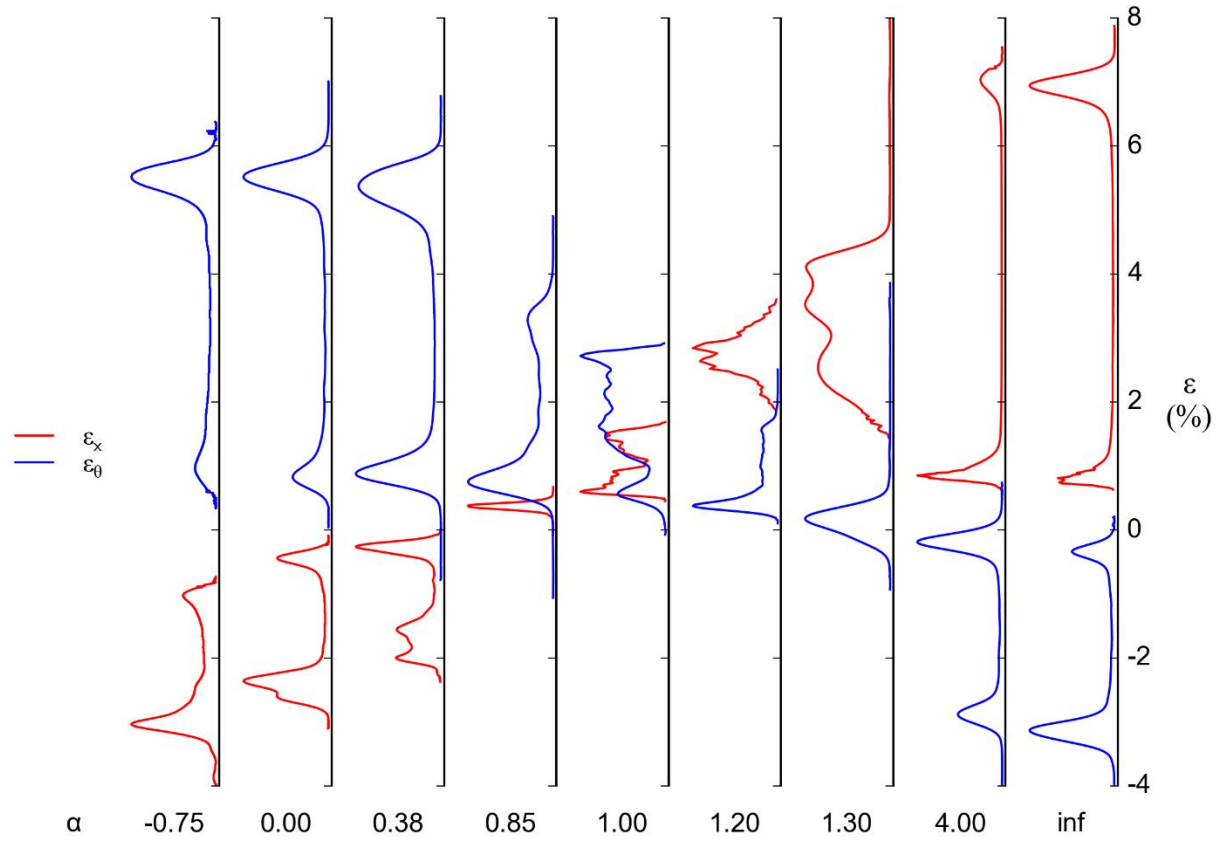

(b)

Fig. 4.32b (b) Sequence of strain histograms along the A→M transformation plateau for nine stress ratios quantifying the degree of inhomogeneity.

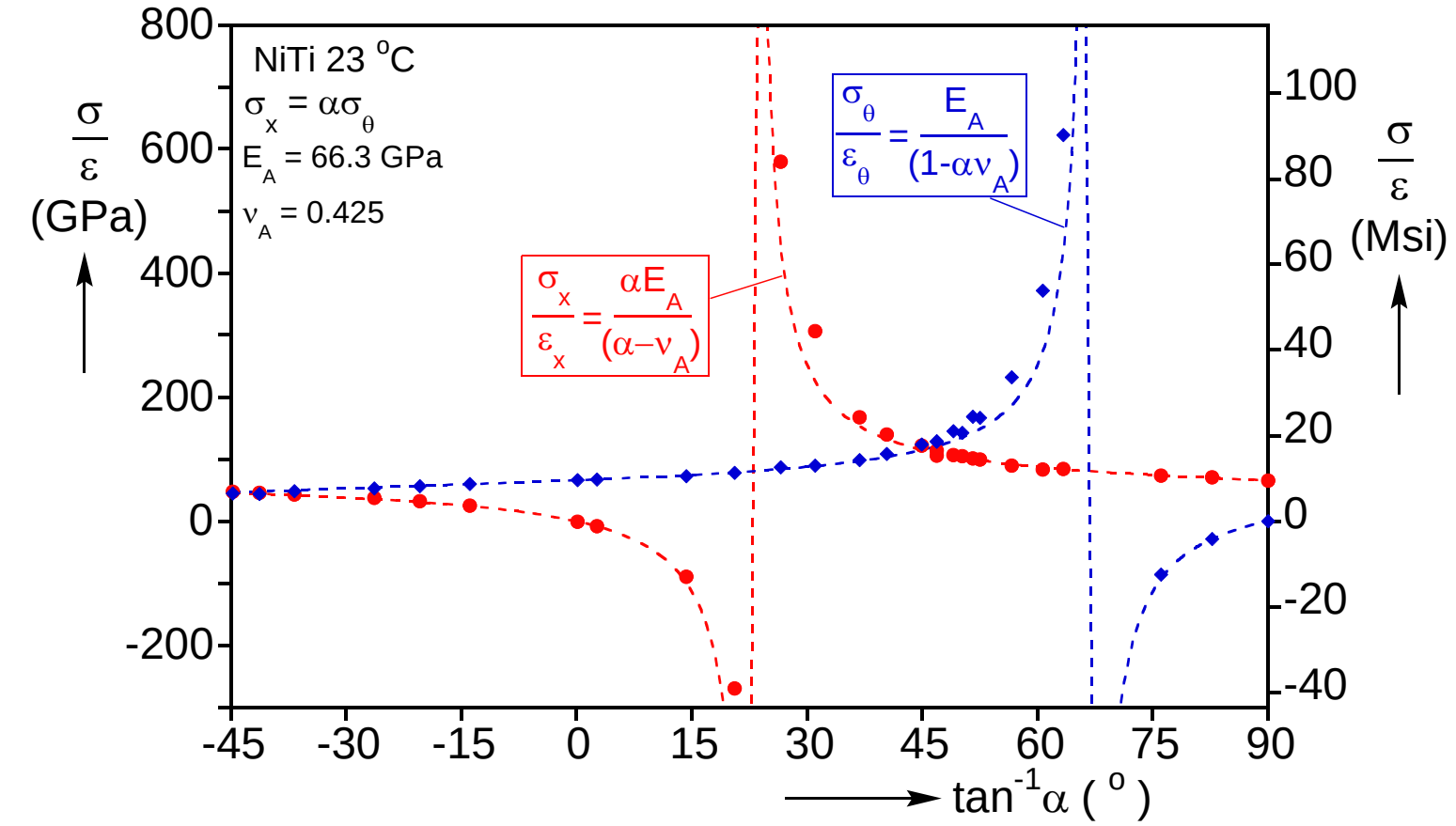

Fig. 4.33 The measured initial stiffness of each of the radial stress path axial and hoop stress-strain response vs. the arctangent of the stress ratio plotted against an isotropic linearly elastic prediction.

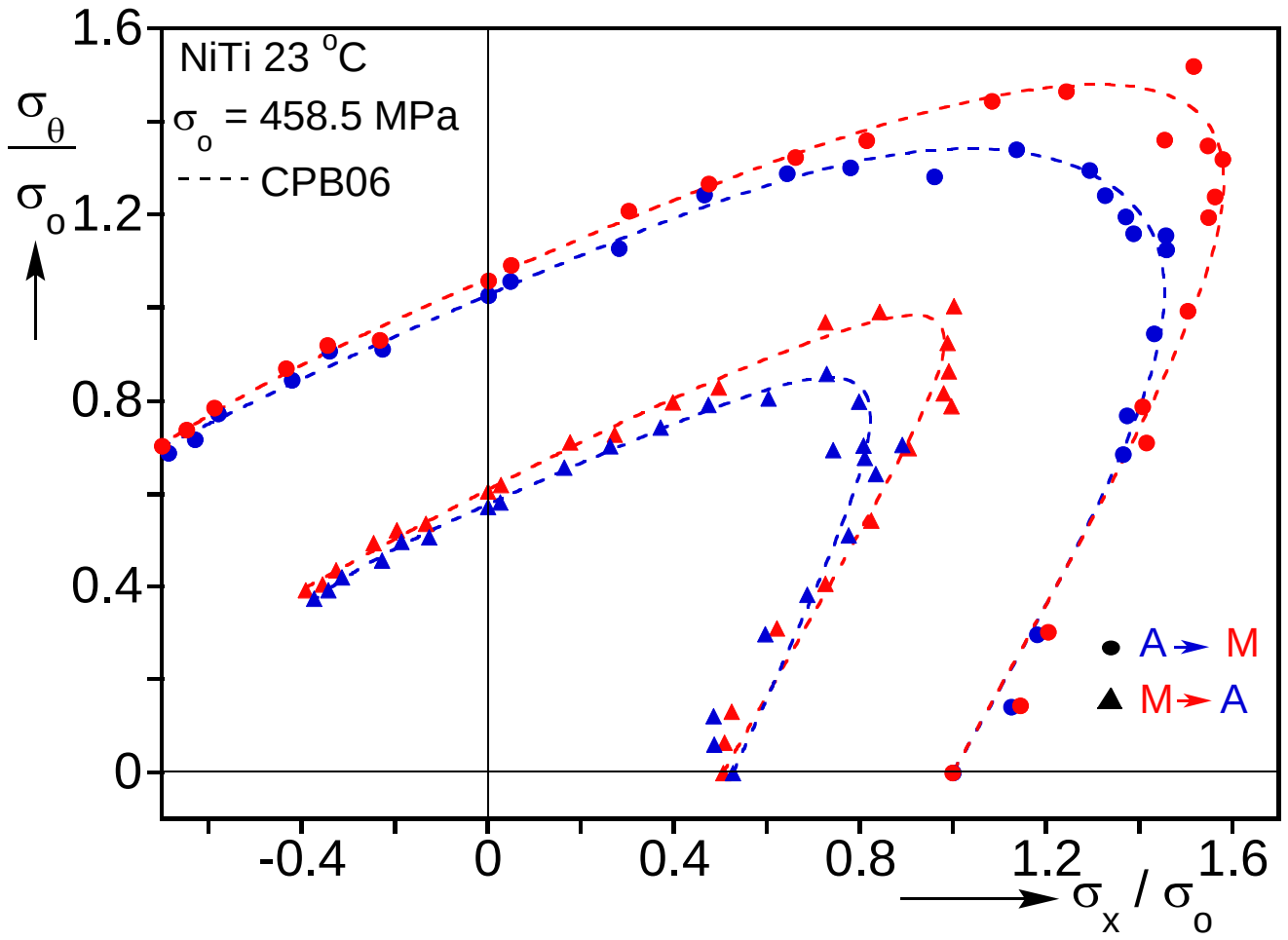

Fig. 4.34 Loci of measured stresses at the nucleation and "completion" of M and A transformations and fitted surfaces.

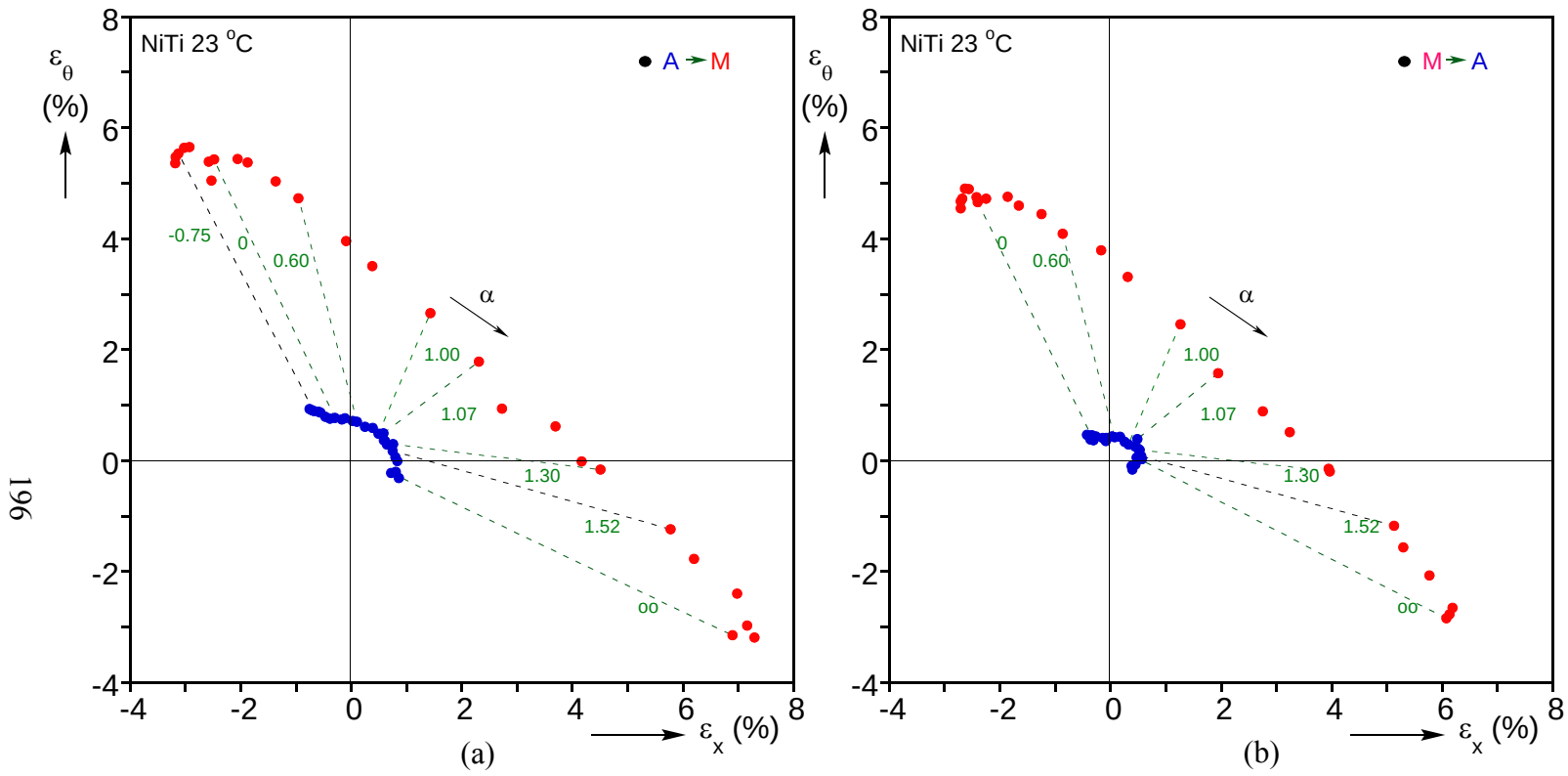

Fig. 4.35 Measured axial vs. hoop strains at the nucleation and "completion" of (a) M and (b) A transformations.

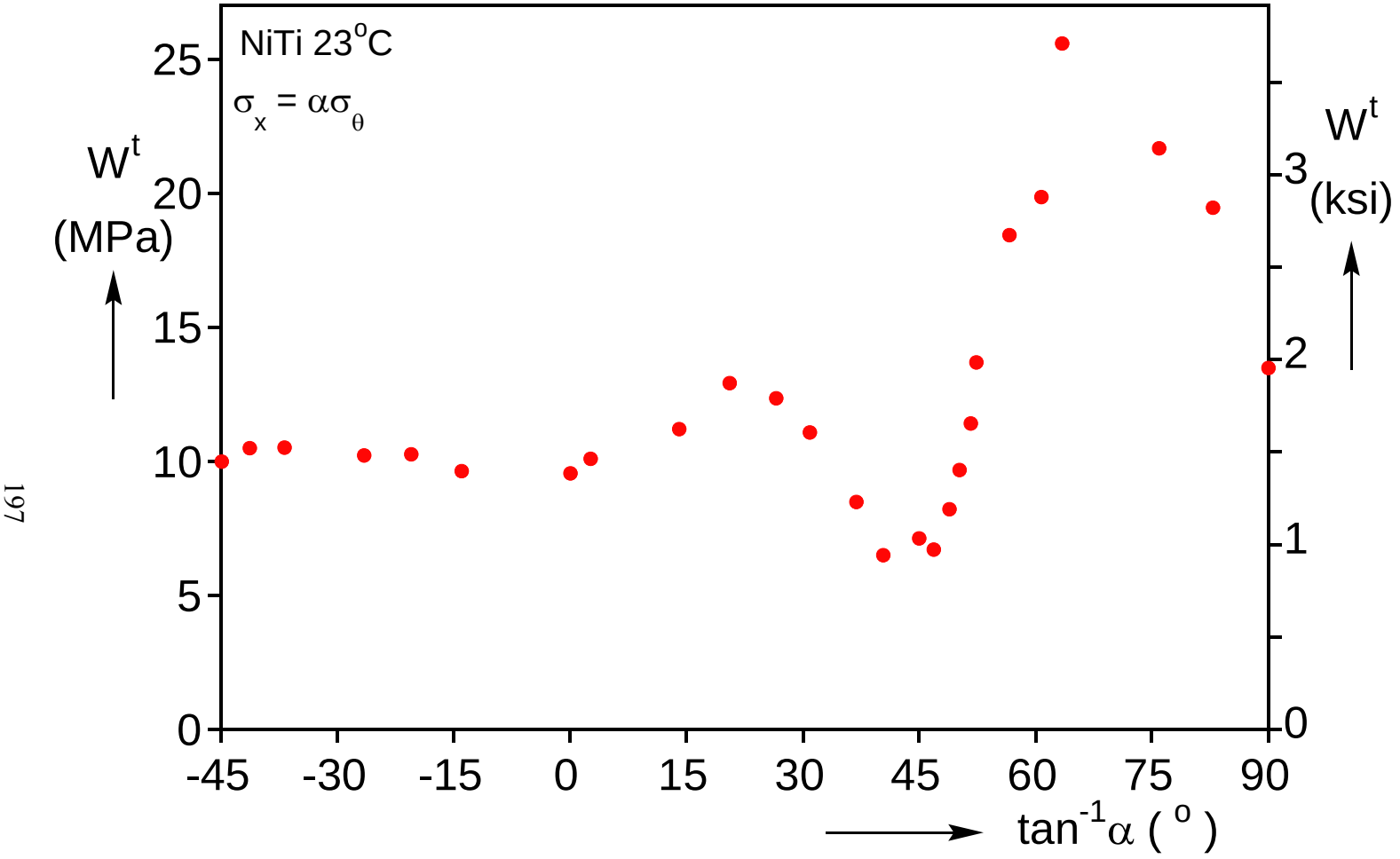

Fig. 4.36 Measured transformation dissipation energy vs. stress ratio angle.

Chapter 5: MULTIAXIAL MATERIAL BEHAVIOR–ANALYSIS[5] [6]

This chapter analyzes the multiaxial results presented in Chapter 4 and uses them to generate and calibrate a transformation surface, study the inclination of the onset of localization bands, and perform a more detailed examination of the thermomechanical interactions associated with latent heats of transformation.

5.1 TENSION-COMPRESSION ASYMMETRY AND ANISOTROPIC "YIELDING"

One of the more important features for any SMA constitutive model is the representation of the transformation criterion. The most common method involves handling transformation in a similar manner to a yield criterion for plastic deformations. To this end, we sought a yield function that would capture the unique material behaviors observed in Chapter 4.

To address tension-compression asymmetry in yielding observed for some metal alloys, Cazacu et al. [2006] (CPB06, see also Plunkett et al. [2008]) proposed the following isotropic yield function:

$$\left(|s_1| - hs_1\right)^k + \left(|s_2| - hs_2\right)^k + \left(|s_3| - hs_3\right)^k = const., \tag{5.1}$$

where s_i are the principal deviators of the Cauchy stress $\boldsymbol{\sigma}$, the exponent k is a positive integer, and h is a constant determined from the ratio of yield stresses in uniaxial tension and compression. Anisotropy is introduced through the following linear transformation

$$\Sigma = \boldsymbol{C}\boldsymbol{s} = \boldsymbol{C}\boldsymbol{T}\boldsymbol{\sigma} \tag{5.2a}$$

---

[5] Bechle, N.J., Kyriakides, S. (2016 *in press*). Evolution of localization in pseudoelastic NiTi tubes under biaxial stress states. *Int'l J. Plasticty*. (Designed and performed experiments, analyzed data, and wrote the paper)

[6] Bechle, N.J., Kyriakides, S. (2016 *in press*). Evolution of phase transformation fronts and associated thermal effects in a NiTi tube under a biaxial stress state. *Extreme Mechanics Letters*. (Designed and performed experiments, analyzed data, and wrote the paper)

producing the following orthotropic version of (5.1):

$$\Phi = \left(|\Sigma_1| - h\Sigma_1\right)^k + \left(|\Sigma_2| - h\Sigma_2\right)^k + \left(|\Sigma_3| - h\Sigma_3\right)^k \tag{5.2b}$$

where Σ_i are the principal values of $\boldsymbol{\Sigma}$. For a plane stress state in a reference Cartesian frame (x, y, z), the relevant values of Σ_{ij} are related to the in-plane stresses as follows:

$$\begin{Bmatrix} \Sigma_{xx} \\ \Sigma_{yy} \\ \Sigma_{zz} \end{Bmatrix} = \frac{1}{3}\begin{bmatrix} C_{11} & C_{12} & C_{13} \\ C_{12} & C_{22} & C_{23} \\ C_{13} & C_{23} & C_{33} \end{bmatrix}\begin{bmatrix} 2 & -1 & -1 \\ -1 & 2 & -1 \\ -1 & -1 & 2 \end{bmatrix}\begin{Bmatrix} \sigma_{xx} \\ \sigma_{yy} \\ 0 \end{Bmatrix} \tag{5.3}$$

and $\Sigma_{xy} = C_{66}\sigma_{xy}$. Σ_{ij} in (5.3) are then used to establish the principal values Σ_i.

The M nucleation stresses from the biaxial experiments in Table 4.1 were used to develop a fit for the CPB06 function (5.2). For the purposes of this exercise the transformation stresses were established using an inelastic work criterion of $\Delta W^t = 0.7$ MPa (ΔW^t is a measure of the nonlinearity in the initial response of NiTi, similar to plastic work). The transformation stress under uniaxial compression for the same tube stock is also included (from Section 3.2). The RHS of (5.2) is assigned a constant value corresponding to the transformation stress under pure tension in the *x*-direction (see Eq. (12) in Cazacu et al. [2006]). The fitting was performed using the minimize algorithm included in the *SciPy.optimize* library based on the conjugate gradient method.

The transformation surface using the parameters listed in Table 5.1 is plotted in the $\sigma_x - \sigma_\theta$ plane in Fig. 5.1 together with the measured transformation stresses. The von Mises (vM) surface is included in the figure for comparison. The CPB06 surface develops the elongated trend exhibited by the data for $0.5 < \alpha < 2.0$ and captures the tension-compression asymmetry, albeit with the limited available compressive data. By contrast, the von Mises surface is seen to deviate significantly from the measured transformation stresses.

It is worth noting that because the data only partially covers the $\sigma_x - \sigma_\theta$ stress plane, similar fits to the one shown in Fig. 5.1 were obtained using different exponents, *k*, resulting in different constants. Adoption of alternate fits changed the shape of the stress surface, especially in regions where data was not available. Clearly, a more unique fit of the transformation surface, will require data in the rest of the stress space.

5.2 BAND ANGLE

For a significant number of the stress ratios of the radial biaxial experiments conducted, the nucleation of M consistently resulted in the formation of a narrow band of higher strain material. The band is inclined to the axis of the tube by an angle ϕ (see Fig. 4.7). Similar bands of discontinuous deformation are commonly observed at the onset of Lüders banding in mild steels and in other materials (e.g., Kyriakides and Miller [2000]; Hallai and Kyriakides [2013]). In a plane stress setting, Hill [1952] examined the conditions that will allow the perfectly plastic material inside a band to develop velocity $\underline{\dot{u}}$ that is different from that of the material on either side of it as shown in Fig. 5.2 (see also Bijlaard [1940]). This velocity vector is at an angle ψ relative to the band. The constraint provided by the material on either side of the band dictates that the strain rate induced by $\underline{\dot{u}}$ along the band is zero (direction *t*). Using the kinematics of the band, the angle ψ is shown to be related to the principal strain rates inside it, $\dot{\varepsilon}_1$ and $\dot{\varepsilon}_2$, through

$$\sin\psi = \frac{\dot{\varepsilon}_1 + \dot{\varepsilon}_2}{\dot{\varepsilon}_1 - \dot{\varepsilon}_2}. \tag{5.4}$$

Adopting an appropriate yield function, $\Phi(\sigma_1, \sigma_2) = const.$, and an associative flow rule, the angle ψ is related to the principal stresses through

$$\sin\psi = \frac{(\partial\Phi/\partial\sigma_1 + \partial\Phi/\partial\sigma_2)}{(\partial\Phi/\partial\sigma_1 - \partial\Phi/\partial\sigma_2)}. \tag{5.5}$$

Thus, for isotopic yielding, uniaxial tension leads to $\dot{\varepsilon}_1 = -2\dot{\varepsilon}_2$ and

$$\psi = \sin^{-1}(1/3) = 19.47^\circ \text{ and } \phi = \frac{\pi}{4} + \frac{\psi}{2} = 54.74^\circ. \tag{5.6}$$

Although transformation to M is not strictly incompressible, this value of ϕ is close to that measured in the uniaxial tension experiment ($\sigma_\theta = 0$ in Table 4.1) on NiTi tubes (see similar results on NiTi strips in Shaw and Kyriakides [1998]).

Motivated by this success we explore what angle this criterion predicts for the radial biaxial experiments presented in Chapter 4 using the anisotropic transformation function Φ (5.2) calibrated to the M nucleation stresses $(\sigma_x, \sigma_\theta)_{NM}$ as outlined in Section 5.1 using an exponent of 6.

The CPB06 transformation surface was used in Eq. (5.5) to develop predictions for the band angles, ϕ. The predicted values of ϕ are plotted against the arctangent of the stress ratio ($\tan^{-1}\alpha$) in Fig. 5.3 together with the measured angle of inclination from the experiments. Included for comparison are corresponding angles predicted if the transformation surface Φ is represented by the von Mises function. The predictions based on CPB06 are seen to follow the trend of the angles measured in the experiments reasonably well for the entire range of stress ratios that develop localized bands. For stress ratios $0.780 \le \alpha \le 1.412$ Eq. (5.5) has no solution, a result that agrees better with the observed behavior than the von Mises bounds of $0.5 \le \alpha \le 2.0$. The lack of prediction accuracy by the von Mises function is directly related to its inaccurate fit of the transformation stress surface. Adoption of alternate fits, as described in Section 5.1, had only small effects on the calculated band inclinations in Fig. 5.3.

5.3 THERMOMECHANICAL INTERACTIONS FOR $\alpha = 2.0$

As was mentioned in Section 4.1, the volume controlled loading scheme employed for the radial biaxial experiments resulted in strain rates during transformation

that were somewhat higher than optimal. As a consequence, the latent heat associated with transformation could not be adequately accomodated, which had an impact on the measured stresses. In this section, we present results from the radial stress path $\alpha = 2.0$ in which, in addition to the DIC diagnostics, the surface temperature of the specimen was also monitored with infrared thermography. This was achieved by having the two sets of imagery on opposite sides of the specimen. Results from this experiment are presented in the following figures and are discussed accordingly.

5.3.1 Loading

Figure 5.4a shows the two recorded stress-mean strain responses ($\sigma - \bar{\varepsilon}$) where $\bar{\varepsilon}_x$ and $\bar{\varepsilon}_\theta$ represent the spatial average of the strain in each direction over the full field of view recorded by DIC (FOV has an axial span of about 6*D* or 38 mm and a hoop span of about 6 mm of the unwrapped circumference). Figure 5.4b shows 38 sets of full-field DIC contours of axial and hoop strain recorded during loading taken at 5 s intervals. The images numbered 1 to 38 correspond to the numbered bullets on the responses in Fig. 5.4a. Bullet and images 1 correspond approximately to the onset of M transformation and 38 to the point at which unloading commences. Included in Fig. 5.4b is a set of recorded infrared (IR) thermograms with color contours representing the change in temperature, ΔT, over the base temperature of 24 °C. The images very closely correspond to the same times as the strain contours in the same figure (the IR images span an axial length of about 7D and a projected width of 1D; i.e., in the transverse direction the DIC contours represent a mapping of about one third of the tube circumference while the IR thermograms are displaying the projected image of the back half of the specimen).

The results collectively clearly indicate that transformation occurs with modest change in stress, leads to inhomogeneous deformation, and to small but tractable changes

of temperature. We discuss the events associated with loading through Fig. 5.4 with supporting results presented in Figs. 5.5-5.7. The A phase initially deforms in a linearly elastic manner. The deformation is homogeneous and the temperature remains uniform and essentially unchanged at 24 °C as depicted in images 1. In this neighborhood, the modulus starts to decrease with a sharp knee developing at an axial stress of 615 MPa. This is an indication that transformation to M has commenced. In fact, the DIC images following 1 show that higher strain localized deformation is entering the FOV from the RHS. Simultaneously, a somewhat higher temperature front has appeared on the right and, interestingly, a weaker one on the left. It appears that transformation nucleated nearly simultaneously at both ends due to the stress concentrations associated with the clamping of the specimen. However, initially these zones lie outside the DIC FOV, and no strain is recorded by the DIC until the transforming material enters the FOV.

Localized deformation patterns enter the FOV first on the RHS in the form of a multi-helical transformation front with sinistral bands. These can be seen in more detail in an expanded view of image 7 included in Fig. 5.5. Such a front is preferred as it tends to minimize structural distortions of the tubular specimen (see Feng and Sun [2006]). The mainly transformed M has an axial strain of just under 7%, a value that corresponds to the end of the stress plateau in the response in Fig. 5.4a. The corresponding hoop strain is at about -2.3% as it is mainly driven by the Poisson effect. The IR images in Fig. 5.4b show that the latent heat released by the transforming material has resulted in an increase in the temperature behind the front (see also Favier *et al.* [2007]). Figure 5.6 displays a more quantitative view of the evolution of temperature in the test specimen. Plotted are axial temperature change profiles at different times during loading along the centerline of the tube. In concert with the IR images, the $\Delta T - x/L$ profiles show that both ends of the

specimen experience local heating from the beginning of the stress plateau. This occurs before any deformation fronts enter the DIC FOV and continues once the front on the right appears. This supports the notion that transformation nucleated first at the ends outside the DIC FOV. The thermal fronts are somewhat diffuse and become visible ahead of the transformation front.

In images 2-12 the multi-helical transformation front on the right propagates towards the center of the specimen and concurrently a thermal front is seen in the IR images to follow suit. The thermal front has a finite width as some of the heat released by the transforming front gets dissipated behind it. In images 5 the transformation front on the left has also entered the DIC FOV. It is also multi-helical but with less pronounced prongs. The two fronts propagate towards each other in a nearly steady-state manner supported by the approximately linear time trajectories of both the strain and thermal fronts in Fig. 5.4b. With the propagation of the fronts the overall temperature of the specimen increases in the manner shown in Fig. 5.6 with the temperature at the location of transformation being higher. Consequently the stress of transformation increases causing the nearly linear increase in the recorded stresses observed in Fig. 5.4a.

As the two fronts approach each other, approximately from images 24 onwards, the transformation front evolves from a multi-pronged shape nearly perpendicular to the tube axis to a single inclined front with no prongs. This, for example, can be observed in the expanded view of the RHS front from images 24 in Fig. 5.5. At some point the helical bands disappear as shown in the expanded view of one of the fronts from images 29 in Fig. 5.5. This takes place first on the left end and then on the right, leaving behind two fronts that form ellipses along inclined planes of constant angle (see images 28-34). The fronts interact thermally with the two temperature peaks eventually coalescing as shown

in in Figs. 5.4b and 5.6. The nearly linear increase in the stresses continues until images 34 with the axial stress reaching 647 MPa, which represents about a 30 MPa increase over the stress measured at the onset of transformation. The maximum ΔT of about 5.75 °C is recorded in images 34 that also corresponds to the completion of transformation close to the end of the top stress plateau in Fig. 5.4a. Although the specimen loading continues until an axial stress of 689 MPa is reached at point 38, the specimen temperature in subsequent images is decreasing.

5.3.2 Unloading

Unloading the specimen is achieved by reversing the flow of water into the specimen maintaining the same volume flux rate as that during loading. Figure 5.4c shows 33 sets of DIC contours of axial and hoop strain taken again at 5 s intervals. Included is a set of IR images of the specimen corresponding to the same times. The mainly M phase material initially unloads homogeneously (see images 39) but follows a rather nonlinear stress-strain trajectory similar to that observed in unloading under uniaxial tension. At a stress of about 290 MPa, sharp knees develop in the responses in Fig. 5.4a indicating that transformation to A has commenced, albeit initially outside the DIC FOV. This transformation again leads to inhomogeneous deformation with the strain behind it being at the level of A at this stress (end of stress plateau ~0.34%). A lower strain transformation front appears on the right starting in images 41, and is seen to propagate towards the center of the specimen in subsequent images. This front is also multi-pronged, but has both sinistral and dextral finger-like features (see expanded view of image 50 in Fig. 5.7; see Shaw and Kyriakides [1998] for similar features in strips). The symmetry of this front minimizes structural distortions. The nucleation of A at the ends of the specimen is unusual as in most biaxial experiments reported in Chapter 4 A

tended to nucleate at the sites at which M transformed last during loading, which in this case is near the center of the specimen. This difference may have been caused by non-uniform temperature outside the IR FOV when unloading commenced. Since the A transformation is endothermic, transformation at the ends has a local cooling effect that is discernible in the IR images, and is even more clearly seen in the $\Delta T - x/L$ profiles plotted in Fig. 5.8. The temperature reduction is smaller than the increase during loading, but it still leads to a gradual but noticeable decrease in the recorded stresses in Fig. 5.4a. In images 46 a second multi-pronged front enters the DIC FOV from the left. It also propagates towards the center and is followed by a cooling front (Figs. 5.4c and 5.8). As a result of the dual propagation of transformation fronts from the two ends, the center of the specimen remains at about 2 °C higher temperature (Fig. 5.8). Consequently, in images 49 transformation nucleates at a third site near the center of the specimen. It appears to be in the form of a helical band as its front end enters the FOV further on the right in images 51 (see Fig. 5.4c). This end subsequently intersects the first multi-prong front and stops while the rest of the helical band widens. The local cooling associated with the multiple propagating fronts results in the undulations observed in the $\Delta T - x/L$ profile of thermogram 50 and in subsequent ones in Fig. 5.8 and in axial temperature variations in the corresponding IR images in Fig. 5.4c.

By images 58 the multiple transformation fronts have reduced the remaining M to what appear as two "islands" near the middle of the FOV (may be part of a helical band). The M zones are close enough for them to interact thermally as seen in Fig. 5.8. Transformation continues and by images 67 the whole FOV has returned back to A and any further deformation is homogeneous. Although transformation has been completed, cooling of the central part of the specimen continues for a while longer, an indication that

heat transfer occurs at a slower rate than transformation. The stress is down to 264 MPa or 26 MPa lower than the level at which M nucleated. Further unloading occurs with the elastic modulus of A (a small residual strain remains after unloading).

5.3.3 Thermomechanical Interaction

The data presented provide a vehicle for quantifying the thermomechanical interaction that has taken place. Concentrating on loading, in Fig. 5.9 we plot with bullets the maximum temperature increase time history for the 38 images in Fig. 5.4b. It is observed that following an initial transient, ΔT increases nearly linearly with time. Thus between images 13 and 31 the temperature increases at an essentially constant rate of 0.0192 °C/s. Between points 31 and 34, which represents the end of transformation, the temperature experiences a sudden increase due to thermal front interaction and is followed by a decay in ΔT .

We will connect the stress-temperature thermomechanical interaction of this biaxial test to the transformation stress-temperature relationship from uniaxial tests by converting the biaxial stress into an equivalent stress. The stress at which M nucleates at 23 °C for this NiTi alloy under biaxial stress states has been shown to trace an unconventional trajectory in the $\sigma_x - \sigma_\theta$ plane (see Fig. 4.34, Fig. 5.1; see also tension/torsion results in Sun and Li [2002]). These transformation stresses were shown to be well represented using the Cazacu et al. [2006] anisotropic "yield" function that also accounts for the tension-compression asymmetry exhibited by the NiTi tubes studied (Section 5.1). The calibrated function was adopted here to evaluate the equivalent stress (σ_e) recorded in the present biaxial experiment as a function of time. The σ_e time history plotted in Fig. 5.10 is seen to increase nearly linearly from the onset of M transformation at point 1 to the end of transformation at 34. The rate of increase of σ_e

between points 13 and 31 is 0.147 MPa/s ($\dot{\sigma}_e$). We aim to correlate this increase in stress to the temperature increase. To this end we use results on the variation of transformation stresses with temperature reported in Chapter 2 from sets of isothermal uniaxial tension and compression experiments on tube of the same alloy (see Fig. 2.8). In the temperature range of interest here, the M transformation stress under tension, σ_{NM}, has a slope of 5.9 MPa/°C. Using this slope and the measured rate of change of temperature, the rate of change of equivalent stress in our experiment is calculated to be 0.113 MPa/s ($\dot{\sigma}_{eca}$). Included in Fig. 5.10 is a plot of equivalent stress vs. time between points 13 and 31 yielded by this calculation. Although this prediction yields slightly lower stress than what was measured, the general trend confirms the influence of latent heat on the measured stress-strain results for SMAs. The difference can be attributed to the fact that the temperatures reported are surface temperatures, which may be influenced by heat losses.

5.4 CONCLUSIONS

The transformation stresses from 26 radial biaxial experiments exhibited a mild anisotropy, but trace a surface that is elongated along the equibiaxial direction and deviates significantly from a von Mises representation. This trend was well represented using the anisotropic yield function of Cazacu et al. [2006] that also captures the tension/compression asymmetry exhibited by the tubes used in the experiments. A more complete representation will have to await experiments that complement the stress states covered.

In many of the presented biaxial stress experiments, transformation nucleated by the sudden appearance of a narrow band of higher strain. Hill's [1952] condition for such discontinuities to develop in a perfectly plastic material was used to establish estimates of the band inclination for different values of the stress ratio α. This was achieved by

replacing the yield function in Hill's criterion with the CPB06 transformation function. The band angle dependence on α produced by this idealized model was found to yield results that follow the measured inclinations quite well, including the lack of solution for a relatively narrow range of stress ratios around the equibiaxial stress state.

The thermomechanical interaction associated with latent heat effects of transformation was investigated for a radial stress biaxial experiment with an axial-to-hoop stress ratio of 2.0. In this experiment, now the rate of loading was somewhat higher than optimal, and the latent heats of transformation caused a small amount of heating during transformation to M and cooling when the material reverted back to A. Infrared thermography showed heating and cooling fronts that develop to follow the transformation fronts. The local rise in temperature during loading resulted in a nearly linear increase in the transformation stresses and a similar decrease during unloading. The changes in stresses were shown to correlate quite well with the temperature dependence of the transformation stress established in independent experiments. The results illustrate the influence of latent heats on recorded stress-deformation responses. They also support the notion that in order to avoid this thermomechanical interaction, material characterization experiments are best performed under isothermal conditions.

C_{11}	C_{12}	C_{13}	C_{22}	C_{23}	C_{33}	C_{66}	h	k
0.9615	0.1079	0.1489	0.9063	0.0378	1.138	1.0	-0.2394	6

Table 5.1 Anisotropy and asymmetry parameters in CPB06 for NiTi in the $\sigma_x - \sigma_\theta$ space.

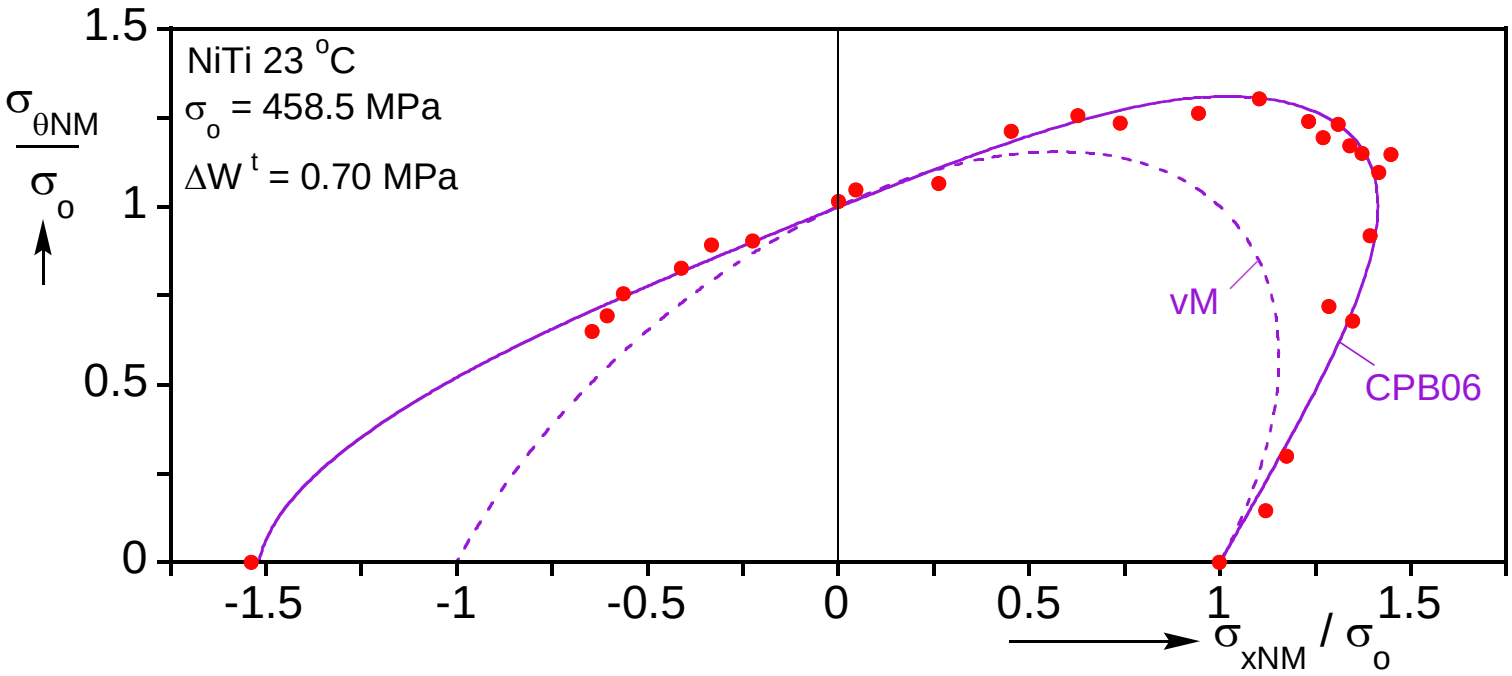

Fig. 5.1 Locus of martensite transformation stresses from the biaxial experiments performed and a fit based on CPB06 (Cazacu et al. [2006]).

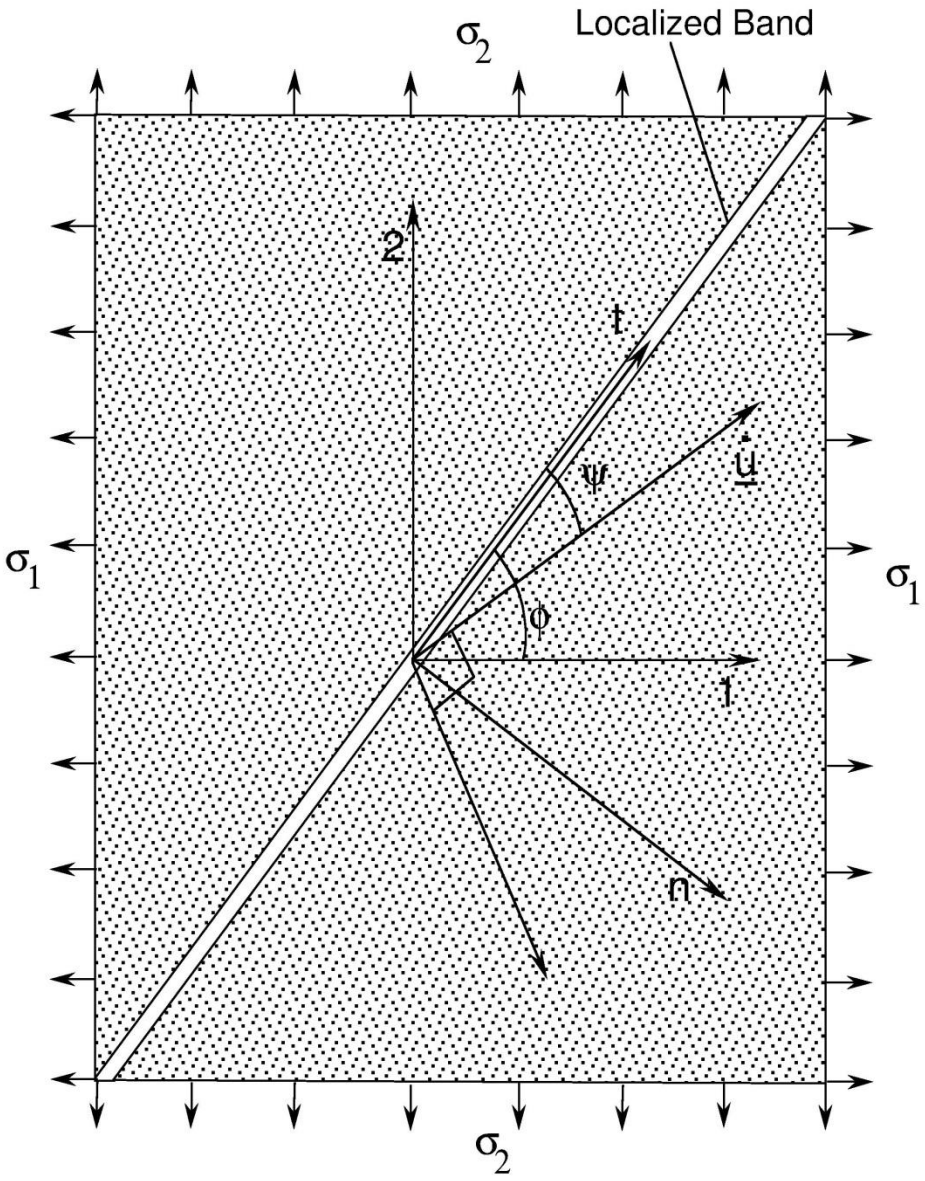

Fig. 5.2 Localization band in a plastic material under plane stress.

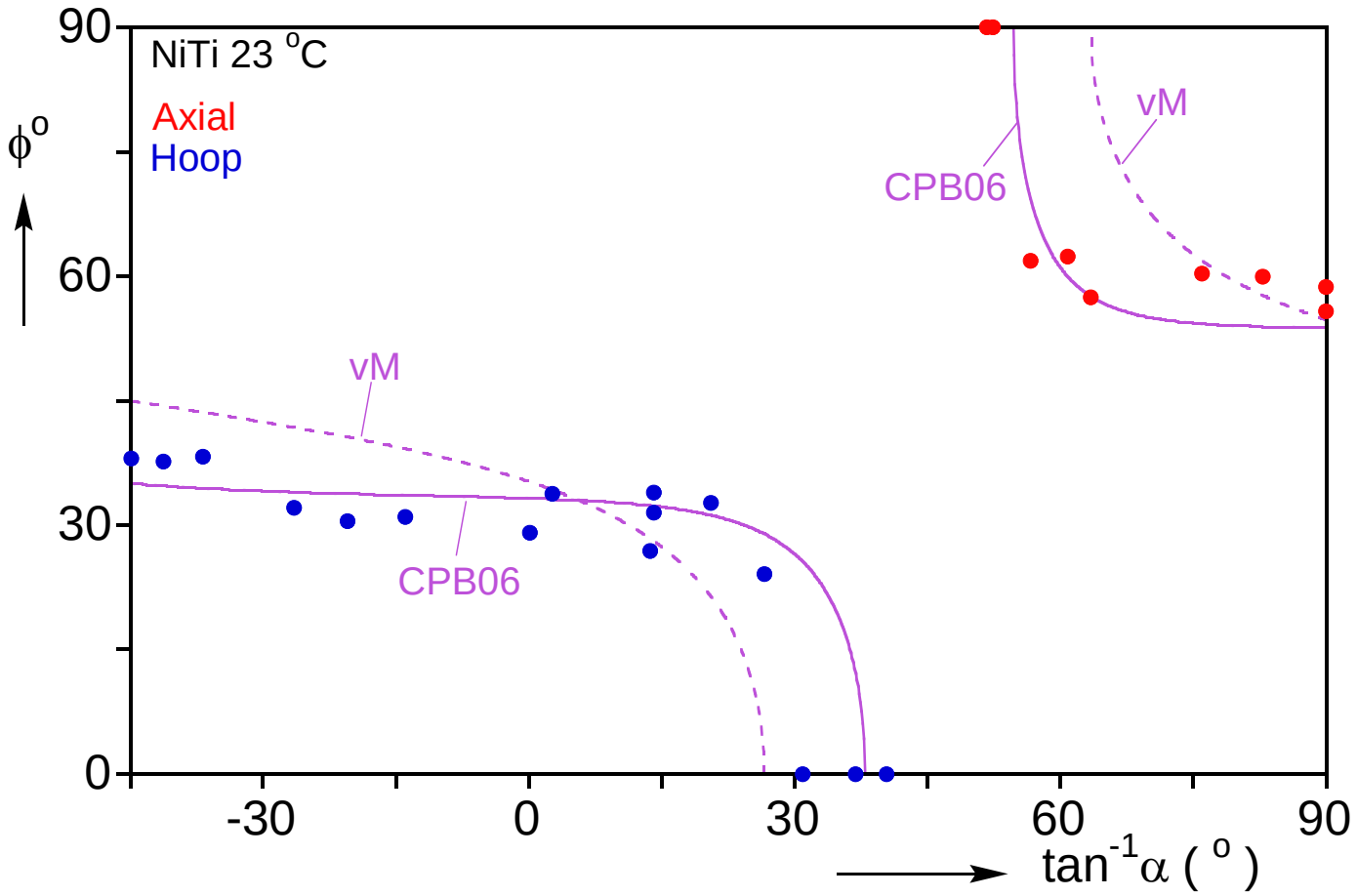

Fig. 5.3 Measured inclination of martensitic localization band to axial direction vs. stress ratio angle. Included are predictions based on Eq. (4.5) for the CPB06 and von Mises transformation surfaces.

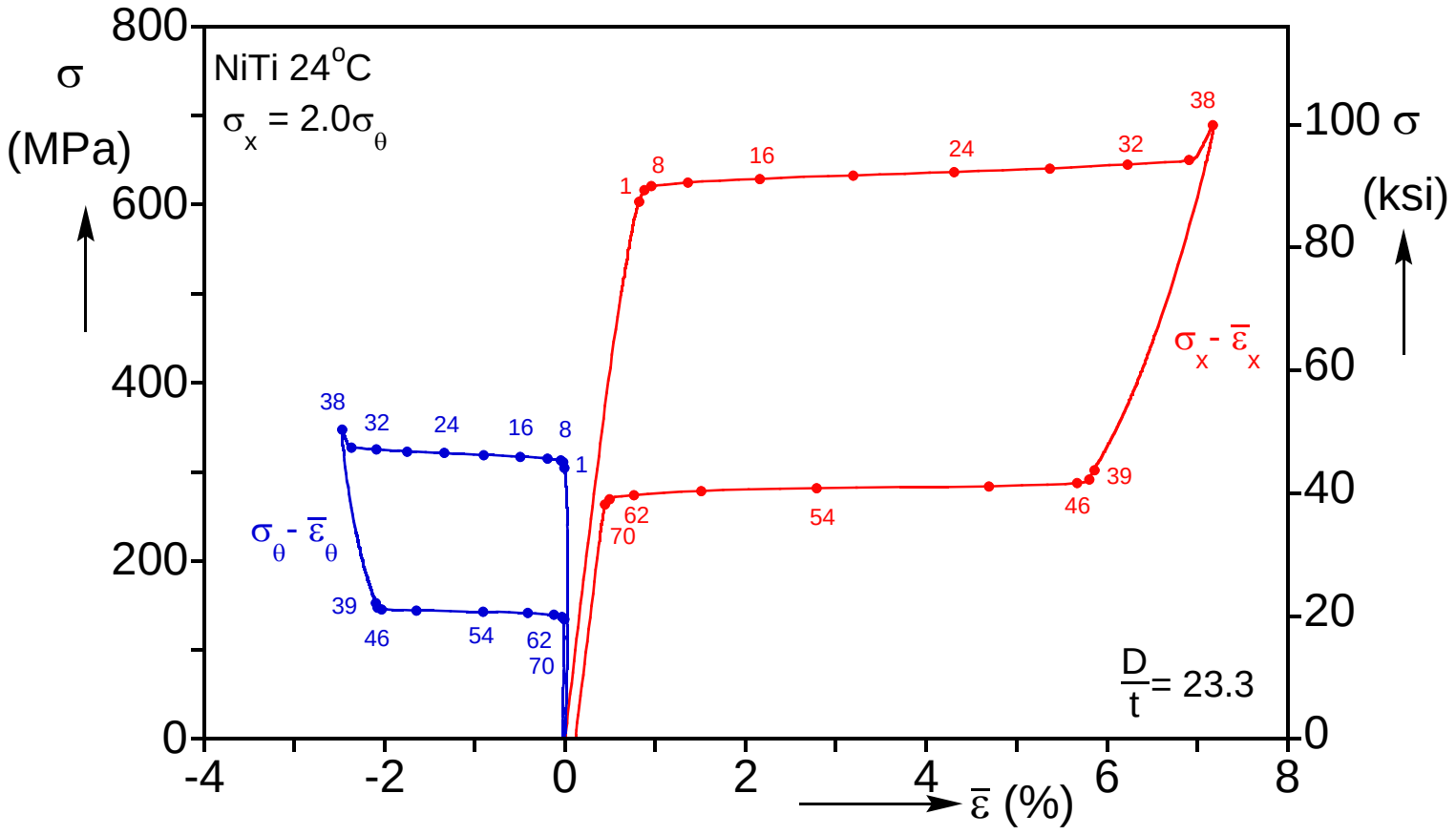

(a)

Fig. 5.4a Results from a biaxial test with $\sigma_x = 2.0\sigma_\theta$. (a) Stress-average strain responses.

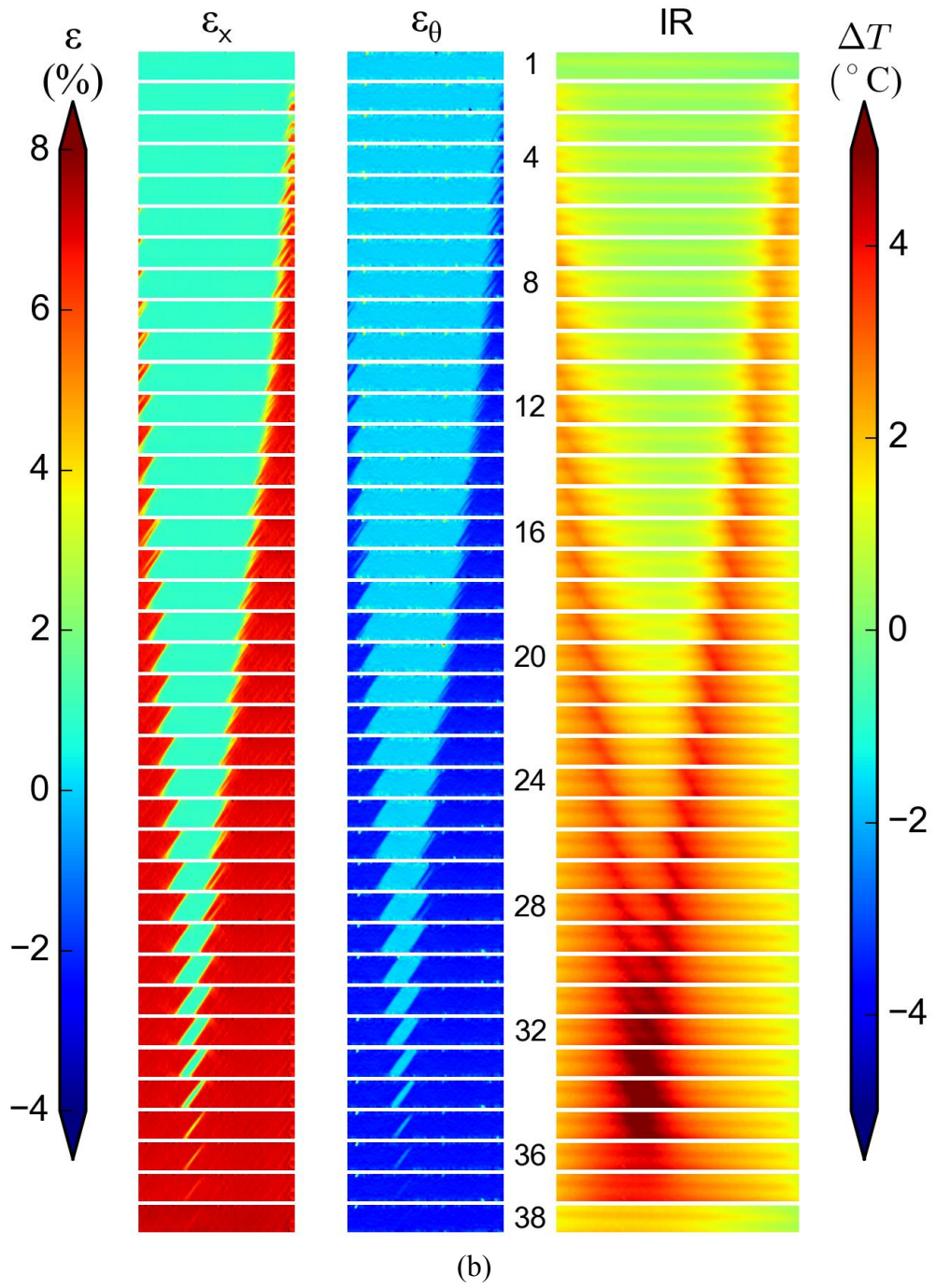

(b)

Fig. 5.4b Results from a biaxial test with $\sigma_x = 2.0\sigma_\theta$. (b) sequences of axial and hoop strain contours from DIC and infrared thermograms corresponding to the numbered bullets marked on the responses in (a) during loading.

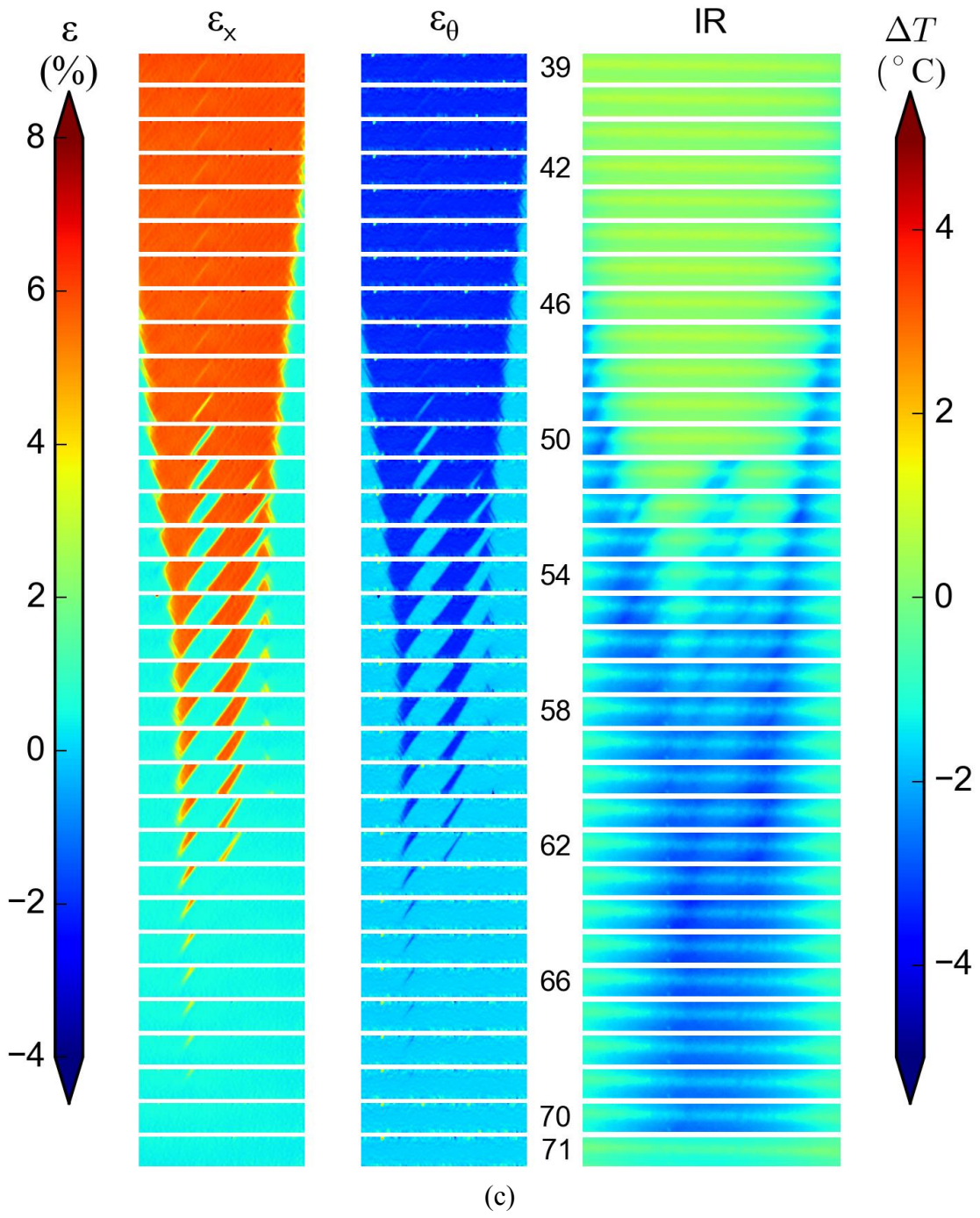

(c)

Fig. 5.4c Results from a biaxial test with $\sigma_x = 2.0\sigma_\theta$. (c) sequences of axial and hoop strain contours from DIC and infrared thermograms corresponding to the numbered bullets marked on the responses in (a) during unloading.

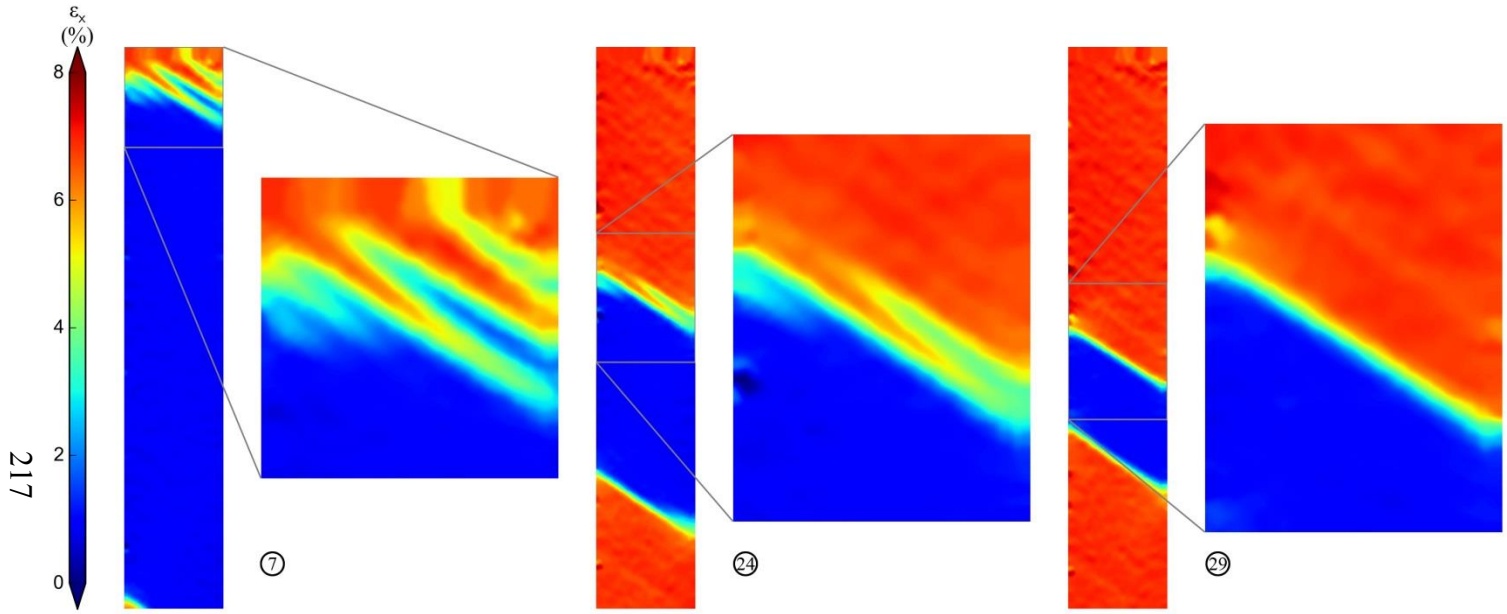

Fig. 5.5 Expanded views of martensitic transformation fronts during loading.

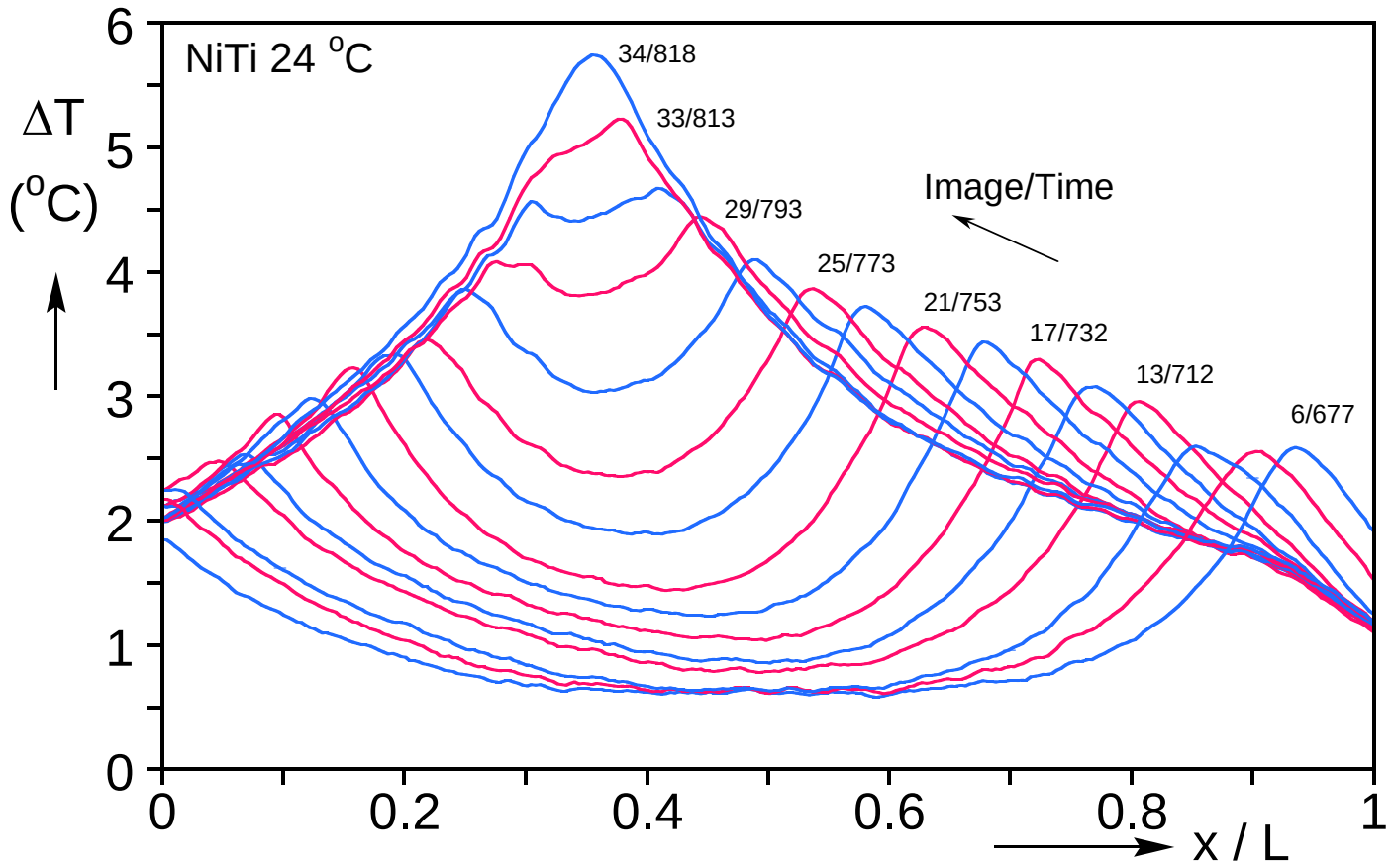

Fig. 5.6 Axial profiles of temperature changes at different times during loading.

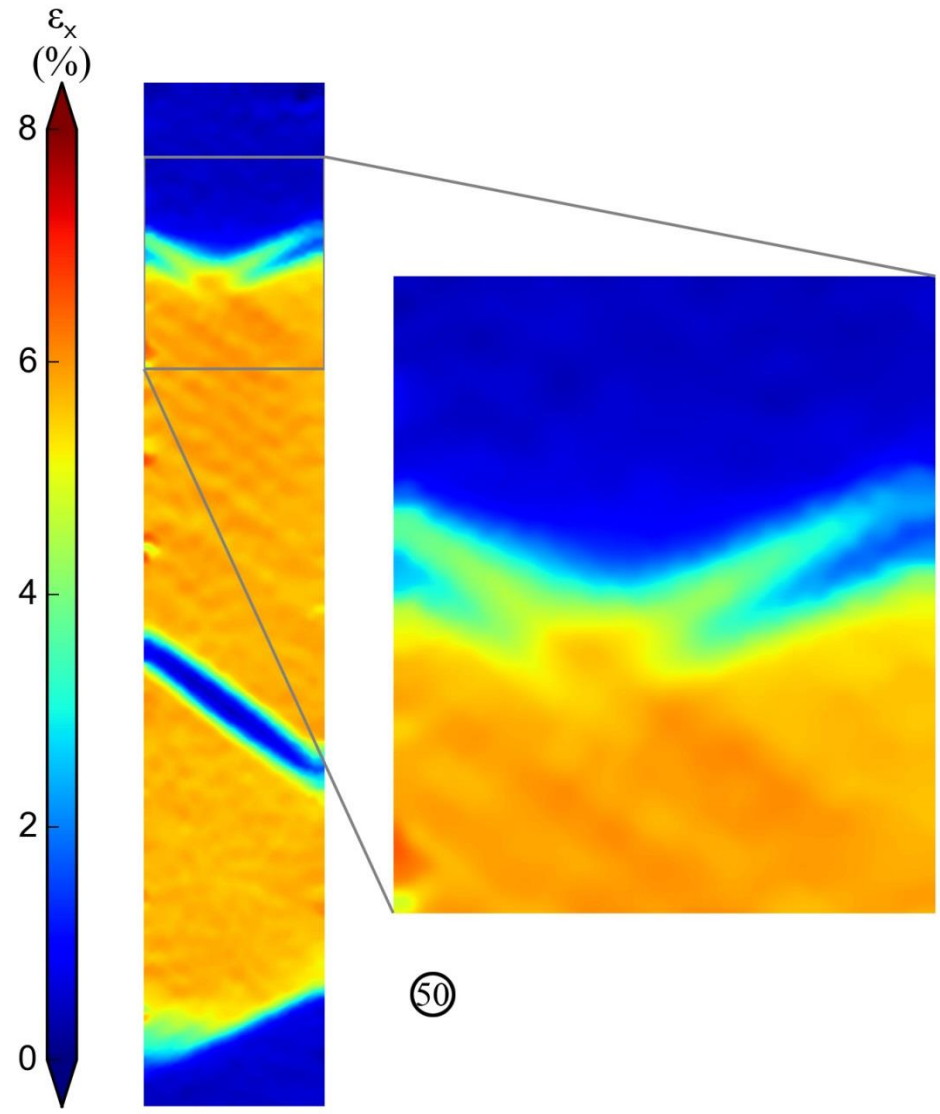

Fig. 5.7 Expanded view of austenitic transformation front during unloading..

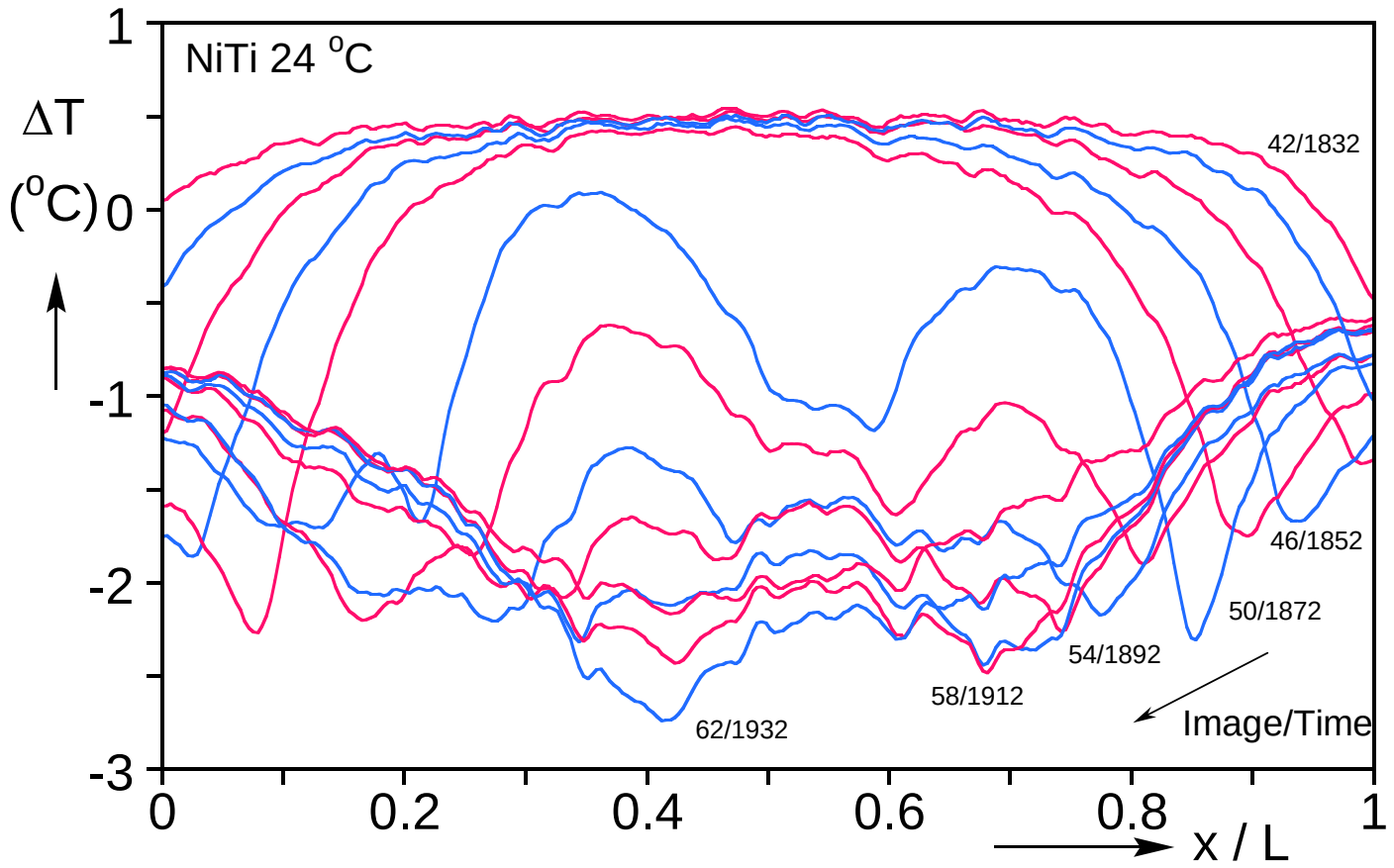

Fig. 5.8 Axial profiles of temperature changes at different times during unloading.

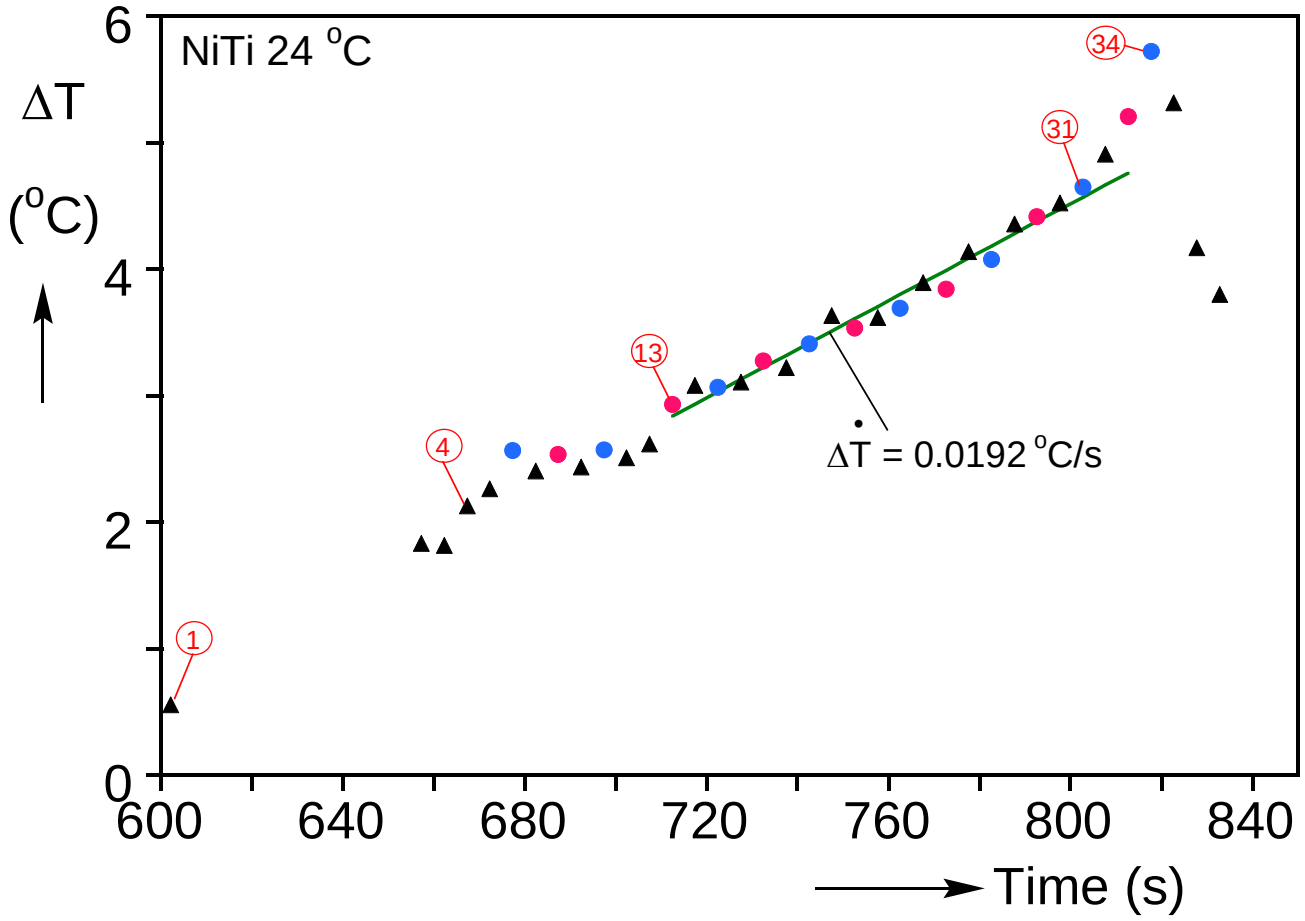

Fig. 5.9 Maximum temperature in specimen and vs. time during loading, with bullets corresponding to the images in Fig. 5.4b. The red and blue color scheme matches those of the profiles in Fig. 5.6.

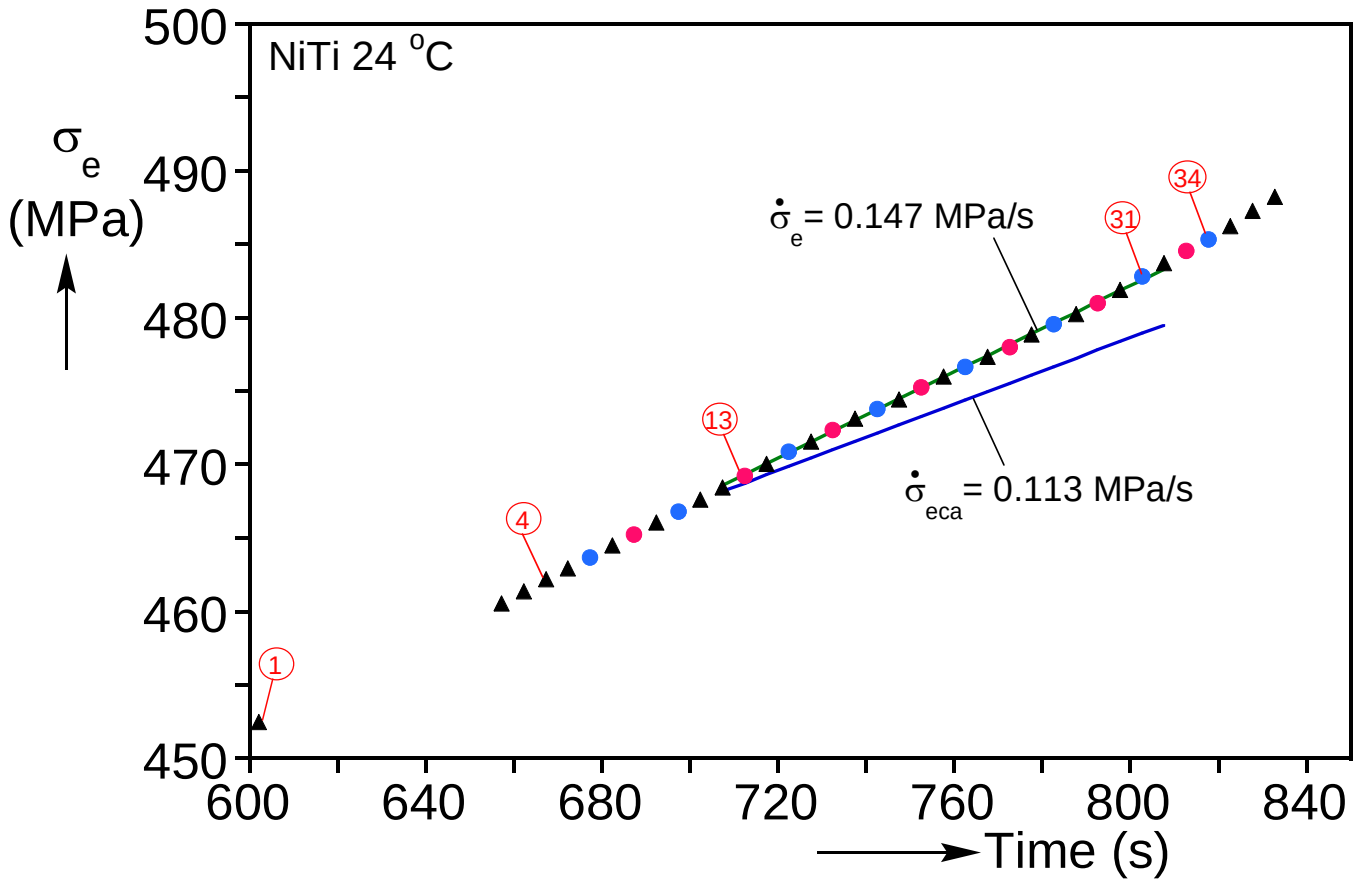

Fig. 5.10 Measured equivalent stress (based on CPB06) vs. time during loading, with bullets corresponding to the images in Fig. 5.4b. The red and blue color scheme matches those of the profiles in Fig. 5.6.

Chapter 6: SUMMARY AND CONCLUSIONS

This dissertation presents the results of an extensive experimental study on the material behavior of NiTi in the pseudoelastic temperature regime. Particular emphasis is placed on the evolution of localized deformation during stress induced phase transformation and its consequences on structural behavior. To this end, experiments have been conducted on NiTi tubes under a variety of stress states and temperatures. Additionally, experiments were conducted on two structures, a tube under pure bending and axial compression of a shell. The main conclusions of those efforts will be outlined in the following sections.

6.1 Uniaxial Material Behavior

To quantify material nonlinearities and begin to establish the foundation of a constitutive model, the uniaxial material response of NiTi was experimentally investigated. Transformation stresses for NiTi have been shown to be highly sensitive to temperature, thus experiments with material characterization as a prime objective are best conducted isothermally. It was also desirable to investigate the dependence of the transformation stress on temperature. To this end, uniaxial tension and compression experiments were conducted on NiTi tubes under isothermal conditions in a temperature range approximately ±20 °C from the austenitic finish temperature, A_f. For all temperatures considered, uniaxial tension resulted in localization in the form of helical bands that propagated along the length of the tubular specimens at an essentially constant stress. Compression on the other hand, exhibited significantly different behavior. The stress at the onset of transformation was significantly higher than that of tension, and the strain extent of transformation was nearly half. More interestingly, the compression

response was monotonic and the deformation was essentially homogeneous. In the temperature regime considered, transformation stresses in both tension and compression were found to be linearly dependent upon temperature, with the rate nearly double in compression compared to tension. Both tension and compression responses deviated from pseudoelasticity at 43 °C, associated with hystereses that did not close fully.

Experiments to track the onset and evolution of plasticity in compression were conducted isothermally on NiTi rods. Overall, pseudoelastic behavior was observed for stresses nearly 2.5 times the onset of transformation. Loading M to higher stresses resulted in a lower M→A transformation stress upon unloading, and increasingly more permanent deformation. Upon unloading after even higher stresses, the material would fully unload prior to the onset of A transformation. A NiTi rod was loaded to failure in compression, which occurred at 2.9 GPa and about 15% strain.

6.2 Structural Behavior

One of the main objectives of this study was to investigate the effect of the aforementioned material nonlinearities on the response of NiTi structures. To this end, two structures were tested, and in both cases, the material instabilities lead to localization and, in turn, structural instabilities.

6.2.1 Pure Bending of NiTi tubes

Bending experiments were conducted on NiTi tubes (nominal D/t = 8) from the same tube stock as the material used for the uniaxial behavior investigation in Chapter 2 under isothermal conditions. The experiments were conducted in a custom-built miniature bending device that was designed and fabricated to the needs of the investigation. Material instabilities led to localization which took the form of localized

curvature in bending. During transformation, the response traced a nearly constant moment plateau accompanied by the coexistence of two curvature regimes corresponding to the onset and termination of the moment plateau. Curvature associated with transformation propagated along the length of the specimen, which was followed by a saturation and upswing in the moment with increased deformation. Localized deformation took the form of narrow bands inclined to the tube axis on the tensioned side, which would coalesce into periodic diamond patterns. No localization occurred on the compressed side, which was confirmed with DIC. Similar behavior was observed for experiments at all temperatures, with the response at 43 °C deviating from pseudoelasticity as was observed in the tension and compression results.

Bending of tubes induces ovalization of the cross-section, which together with localization, can result in collapse for thinner shells as has been seen in bending of steel tubes with Lüders bands. To investigate this effect on NiTi, isothermal bending experiments were conducted on tubes with a nominal D/t of 19. Transformation led to localization on the tensioned side which was followed by the formation and growth of a dimple on the compressed side. The growth of the dimple caused the cross-section to fold which resulted in abrupt collapse and fracture of the specimen. Despite the catastrophic failure, on unloading the specimen returned to the undeformed configuration. Localization and collapse was observed in isothermal bending at 3, 13, and 23 °C.

6.2.2 Axial Compression of NiTi Cylindrical Shell

Pseudoelastic NiTi tubes with a nominal D/t of 25 were compressed between two parallel steel platens. Experiments were conducted at room temperature in a slow enough manner to maintain isothermal conditions. The onset of M transformation led to a reduction in stiffness that induced a stable axisymmetric wrinkling buckling mode during

a short stress plateau. The wrinkling eventually instigated a mode-3 unstable buckling mode which led to the formation of three circumferential lobes and collapse. The nominal stress stabilized during the growth of the first set of lobes eventually forming an additional mode-3 buckle inducing further collapse. This response is in stark contrast to typical shell buckling of elastoplastic metal shells, which results in concertina folding and stress undulations during collapse. The stiffening effect of the M saturation stabilizes the mode-3 buckling mode eventually inducing additional buckling lobes to form and arresting the growth of current ones. In several experiments, prior to the growth of a third mode-3 buckle, the material fractured along the axial direction at one of the extrados of a three-lobe buckle.

6.3 MULTIAXIAL MATERIAL BEHAVIOR

The unique nonlinearities of NiTi observed under uniaxial tension and compression prompted a further investigation into the material behavior under multiaxial stress states. Previous efforts on multiaxial NiTi material responses have primarily focused on the onset of M transformation through tension-torsion experimentation. This work focused on: (a) developing dependable transformation surfaces—both for onset and saturation of A and M transformations; (b) characterizing the evolution of deformation during phase transformations; (c) determining and quantifying any inherent material anisotropies; (d) and evaluating the multiaxial energy absorbing capabilities of NiTi.

To this end, NiTi tubes with a nominal D/t of 25 were subjected to combined internal pressurization and axial loading at room temperature. For the evolution of deformation, full-field displacements were measured using stereo DIC. Experiments were primarily conducted for radial stress paths using a prescribed volume flux rate and a feedback control system to main the stress ratio. A select number of non-radial stress path

experiments are also reported in this study. The radial stress paths were carried out on axial to hoop stress ratios ($\alpha = \sigma_x / \sigma_\theta$) ranging from $-1.0 \leq \alpha \leq \infty$. Inhomogeneous deformation was observed in all stress states except for a small region around equibiaxial tension. Localization primarily took the form of inclined helical bands whose angle with respect to the tube axis is dependent upon the stress state. Forward and reverse stress transformation surfaces exhibited significant deviations from von Mises behavior, with transformation stress values highly dependent on biaxiality. Transformation surfaces were captured accurately by the Cazacu et al. [2006] (CPB06) yield function, proposed for metals that exhibit tension/compression asymmetry and material anisotropy. The CPB06 yield function was employed in the Hill [1952] method for determining localization criterion. The method accurately predicted the inclination of the helical bands at the onset of transformation and the region around equibiaxial tension where no localization was recorded.

The neighborhood around equibiaxial tension also exhibited pronounced hardening with the smallest transformation strains measured. While all transformation stresses were found to have a very mild anisotropy, the transformation strains were strongly anisotropic. Transformation strains were larger in the axial direction compared to hoop, and were highly dependent on biaxiality. The strain anisotropy influenced the energy absorption as the strain energy consumed in the nominal stress-mean strain hysteresis was much larger in axially dominant experiments compared to hoop, and also was highly dependent upon biaxiality with the lower energy absorbing capacity recorded in the region around equibiaxial tension.

6.4 Future Work

This dissertation presents an experimental investigation into the evolution of material nonlinearities due to phase transformations in NiTi and their effects on structures. The results should play an important role in ongoing efforts to develop robust constitutive models for NiTi. The first generation of such a constitutive model has appeared in Jiang et al. [2016], where it was used to simulate the buckling and recovery experiments presented in Section 3.2. The addition of more features of the material behavior reported is expected to further improve the model performance.

Other areas for future work include multiaxial experiments that span larger regions of the stress space. Shaw et al. [2013] presented promising work on tension-torsion experiments of pseudoelastic NiTi tubes, but these results have not yet been published. Once the ambient temperature stress space has been well understood, the temperature dependence of phase transformation induced deformation under multiaxial stress states will be an interesting area of research. Additionally, the response of more NiTi structures will both reveal information about the material, but also provide future benchmarks for constitutive modeling.

Appendix A: SUBMERSIBLE EXTENSOMETER

Tensile experiments were conducted isothermally by submerging the specimen and gripping apparatus into a fluid-filled chamber connected to a temperature controlled circulating bath. The chamber had a window which allowed for the use of DIC measurements for full-field displacements. A submersible extensometer was used for redundancy in deformation measurements and to quantify any error due to the glass window and fluid in the line of sight of the images used for DIC. A custom designed submersible extensometer was fabricated for this purpose.

The design consisted of a spring stainless steel top arm, an anodized aluminum frame, and connected to the specimen with hardened steel "knife" edges (see machine drawings in Figs. A1-A4 for dimensional detail). Vertical displacement of the "knife" edges were determined using the bending strains in the spring steel measured with four strain gages mounted in a full-bridge arrangement. The strain gages and lead wires were protected against moisture with Micro-Measurements M-Coat FBT. The strain signal was read into a signal conditioner to be balanced and amplified. Calibration was conducted using a precision gage block. See Fig. A5 for calibration results.

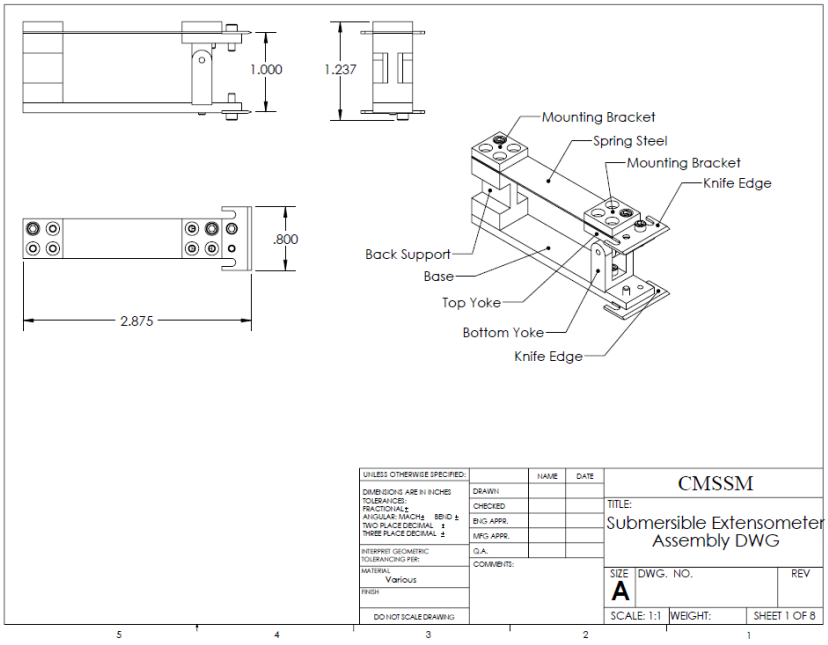

(a)

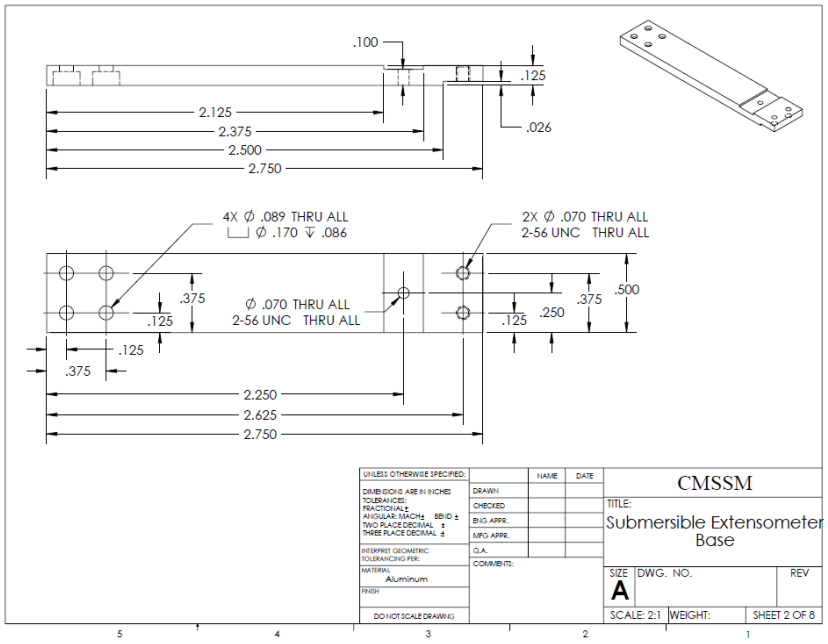

(b)

Fig. A1 Drawings of custom submersible extensometer for submerged tensile experiments: (a) isometric view of assembly, (b) anodized aluminum base plate.

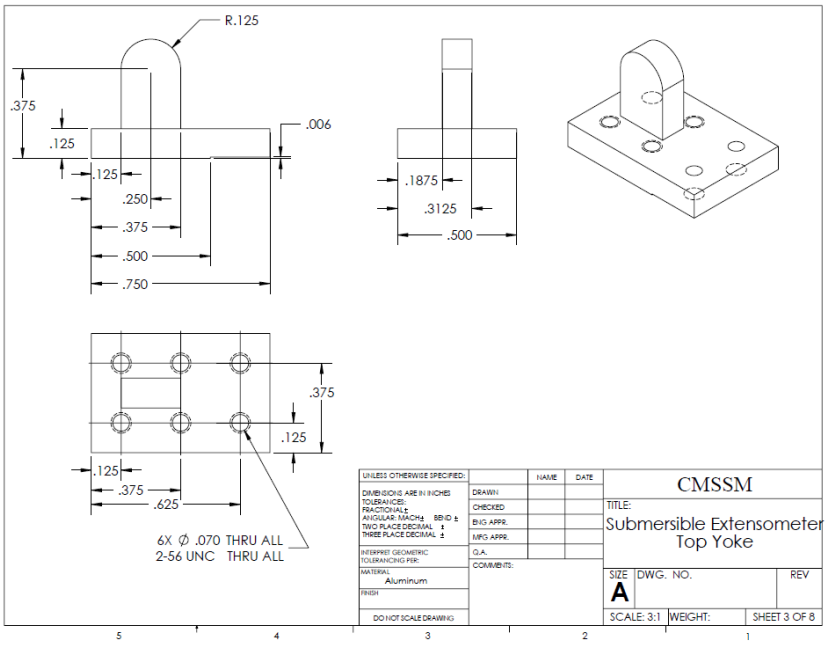

(a)

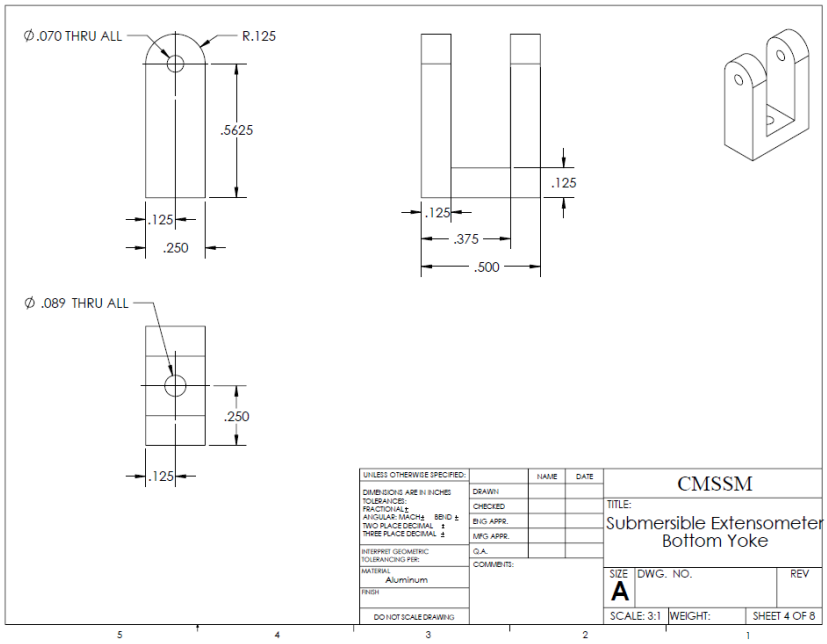

(b)

Fig. A2 Drawings of custom submersible extensometer for submerged tensile experiments: (a) anodized aluminum top yoke, (b) anodized aluminum bottom yoke.

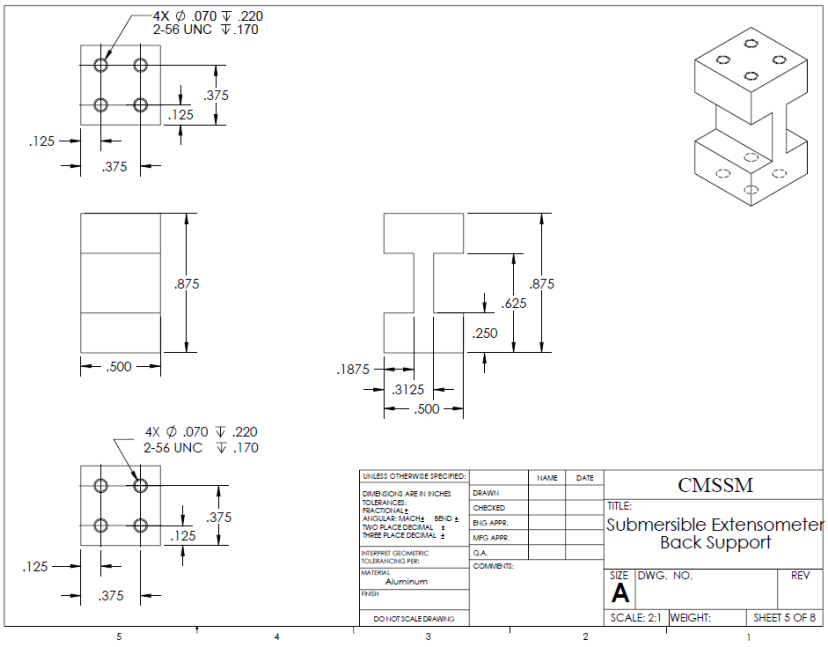

(a)

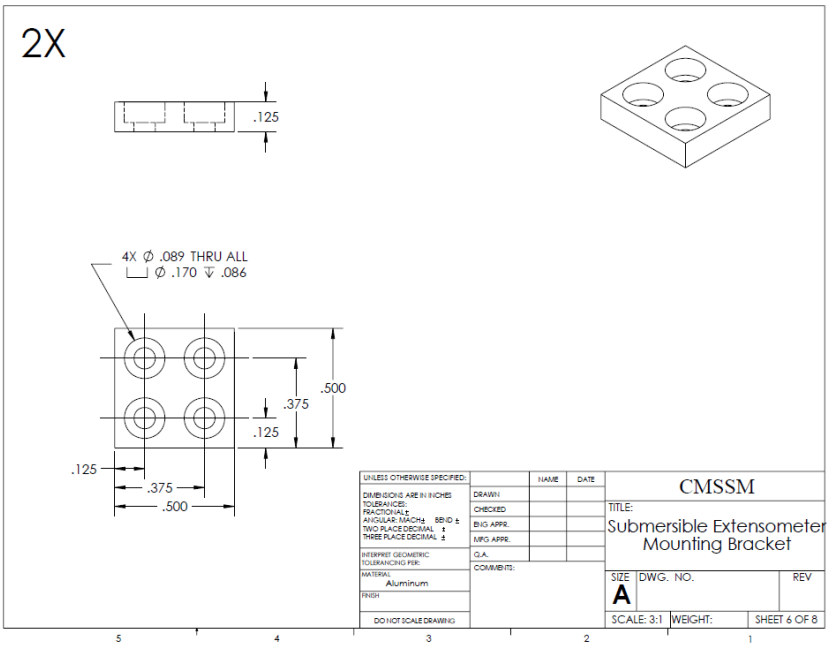

(b)

Fig. A3 Drawings of custom submersible extensometer for submerged tensile experiments: (a) anodized aluminum back support frame, (b) anodized aluminum mounting bracket plate.

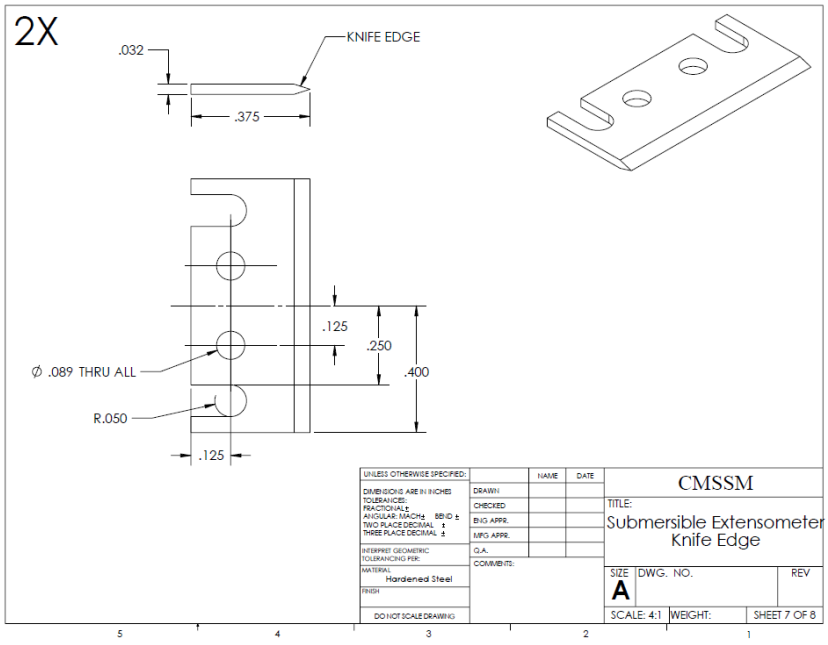

(a)

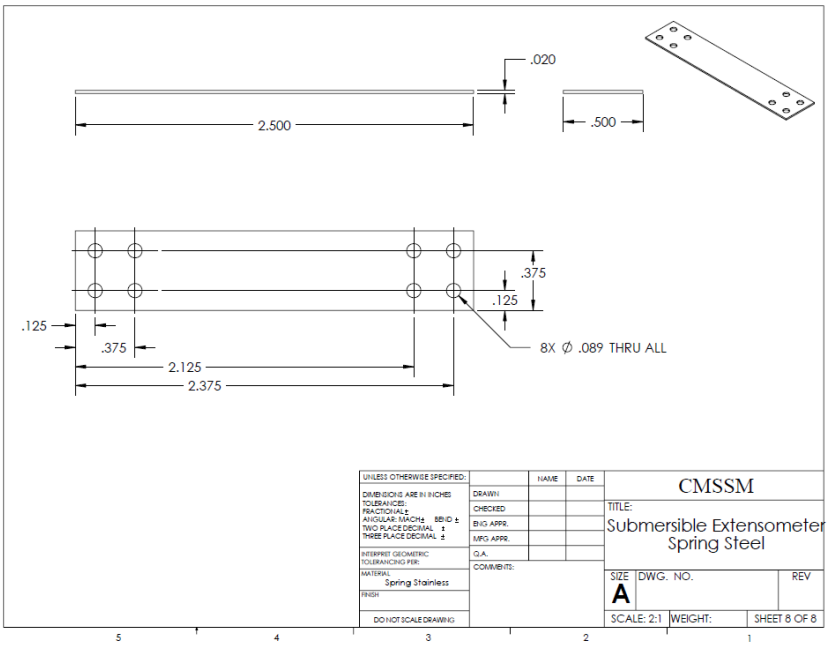

(b)

Fig. A4 Drawings of custom submersible extensometer for submerged tensile experiments: (a) steel knife edges, (b) spring stainless steel for top of submersible extensometer where strain gages were mounted.

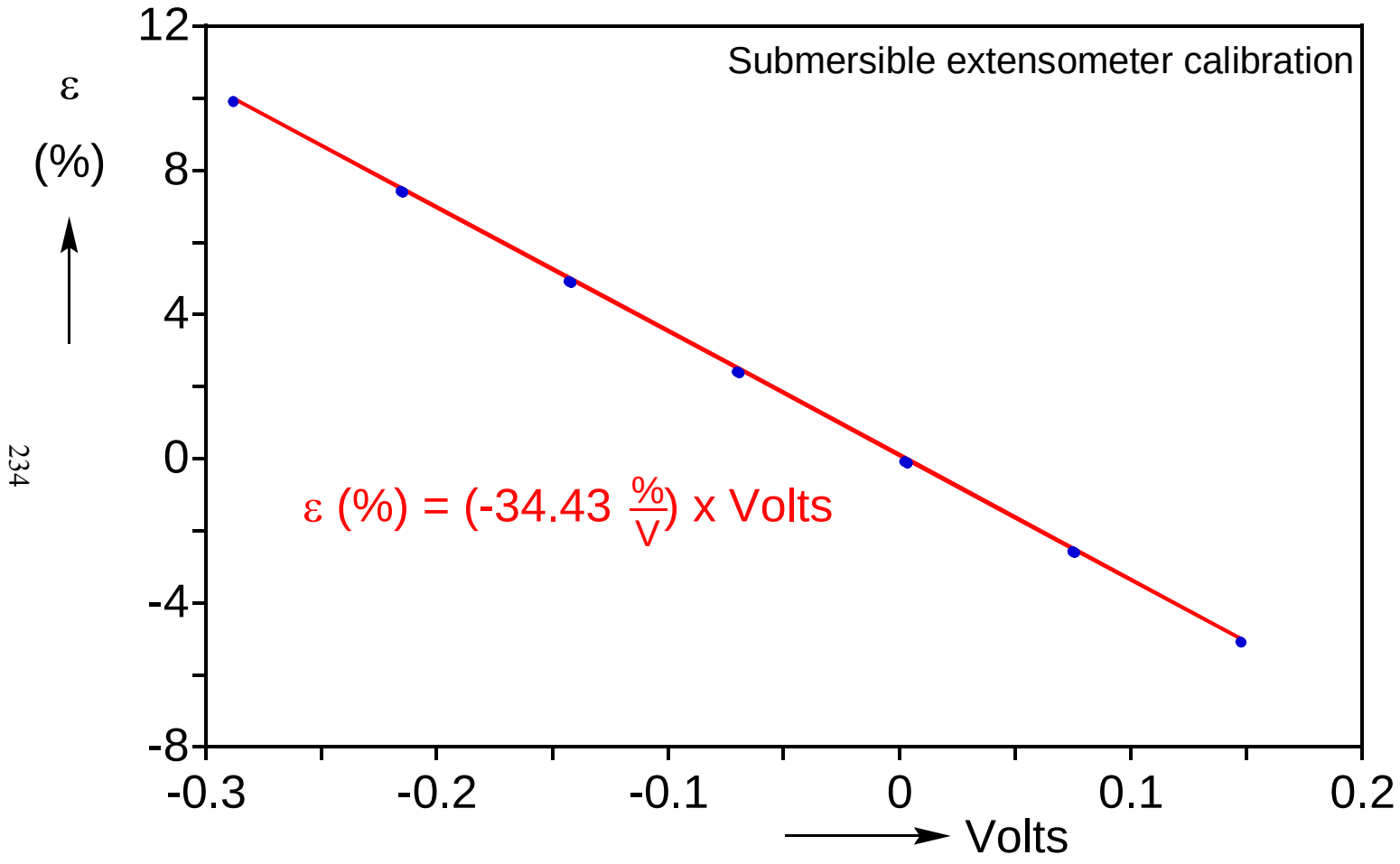

Fig. A5 Strain vs. voltage output from the calibration of the custom-built submersible extensometer.

Appendix B: MINIATURE BENDING DEVICE

Bending experiments were conducted isothermally on a custom miniature bending device. Motion was supplied by a stepper motor which was controlled using NI Motion Assistant Software integrated with LabVIEW. The stepper motor was geared up to a "turnbuckle" assembly which converted the rotary motion into linear motion which actuated the equal contraction/extraction of a roller chain. The roller chain wrapped around idler sprockets and terminated at a hub sprocket assembly. Mounted to the hub sprocket assembly were four Pacific Bearing FL06 PTFE linear bearings secured in steel pillow blocks. NiTi tube specimens were snugly inserted into precision ground steel tubes which traveled through the linear bearings which allowed for the large deformation necessary to complete the phase transformation on the extreme fibers of the specimen. The tension in the roller chain was recorded and used to compute the applied moment. The equal and opposite rotation of the hub sprockets subjected the tubes to pure bending, where the end rotations were recorded using RVDT's. The bending device accommodated isothermal conditions by being capable of operation at very slow rates or the inclusion of a circulating fluid bath to maintain constant specimen temperature at faster loading rates.

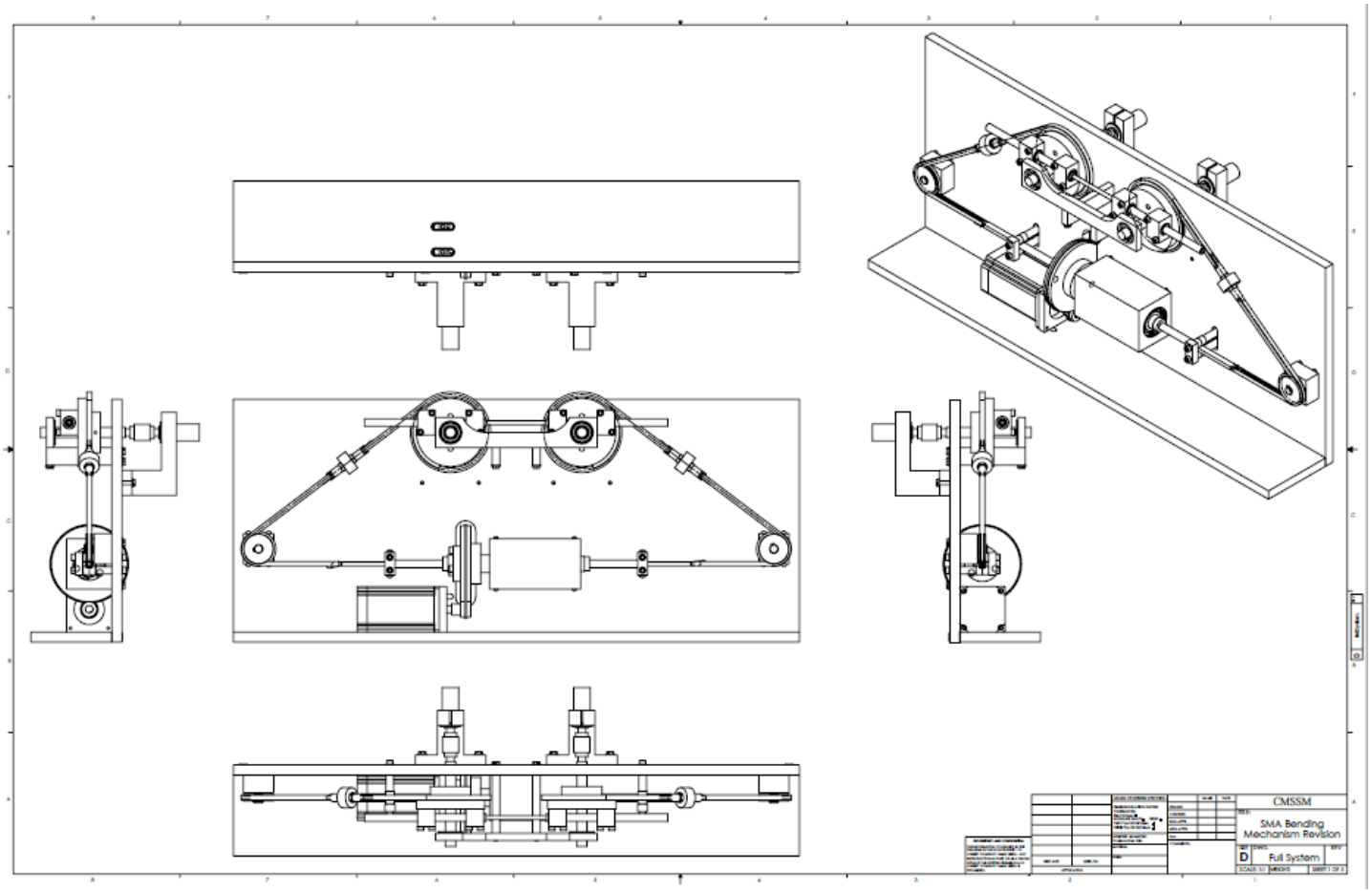

Fig. B1 Drawing of miniature bending device for isothermal pure bending experiments on NiTi tubes.

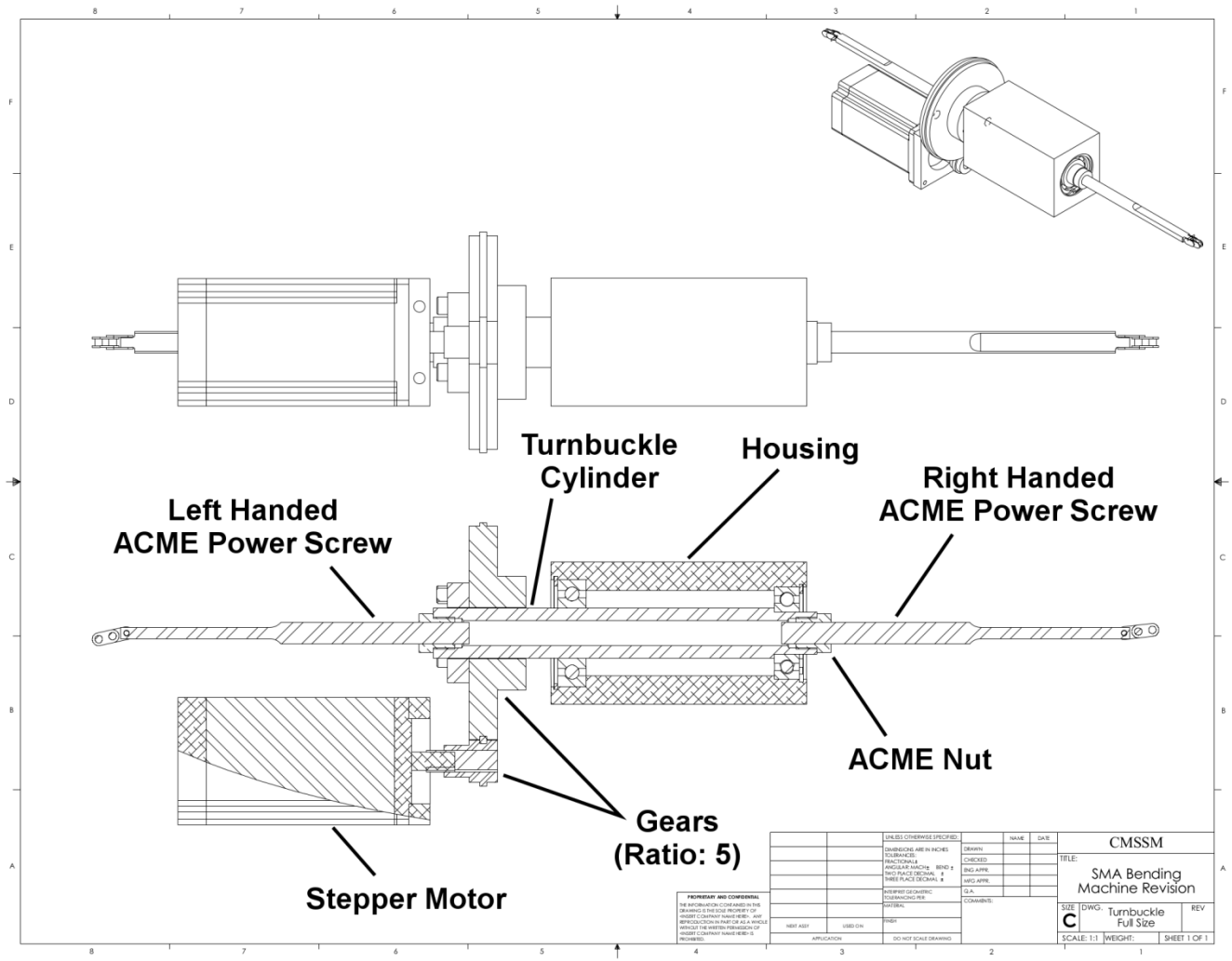

Fig. B2 Drawing of "turnbuckle" assembly which converts rotary motion provided by the stepper motor into linear motion through the simultaneous extension/contraction of ACME power screws restrained against rotation.

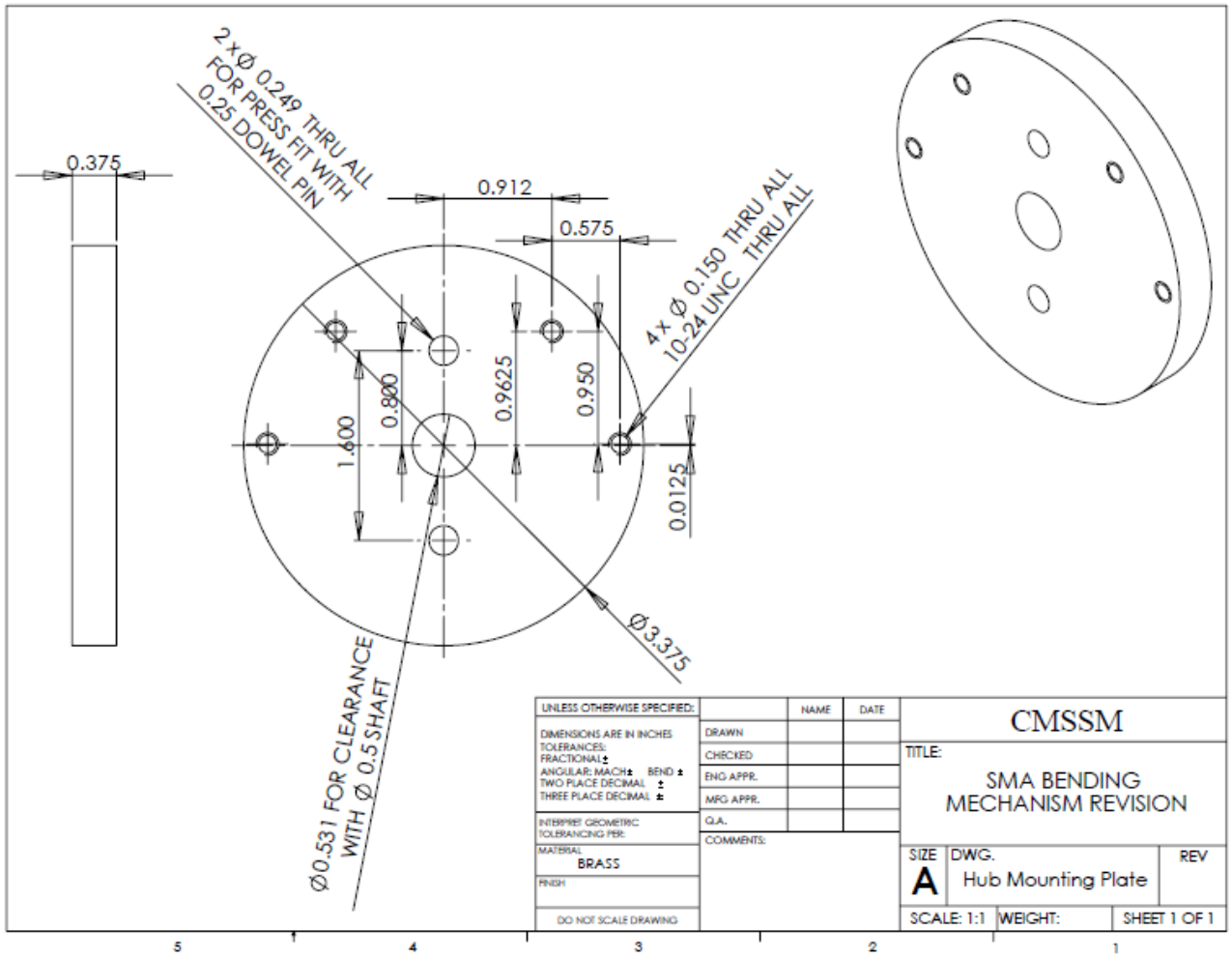

Fig. B3 Drawing of hub sprocket plate where pillow blocks housing the linear bushings are mounted.

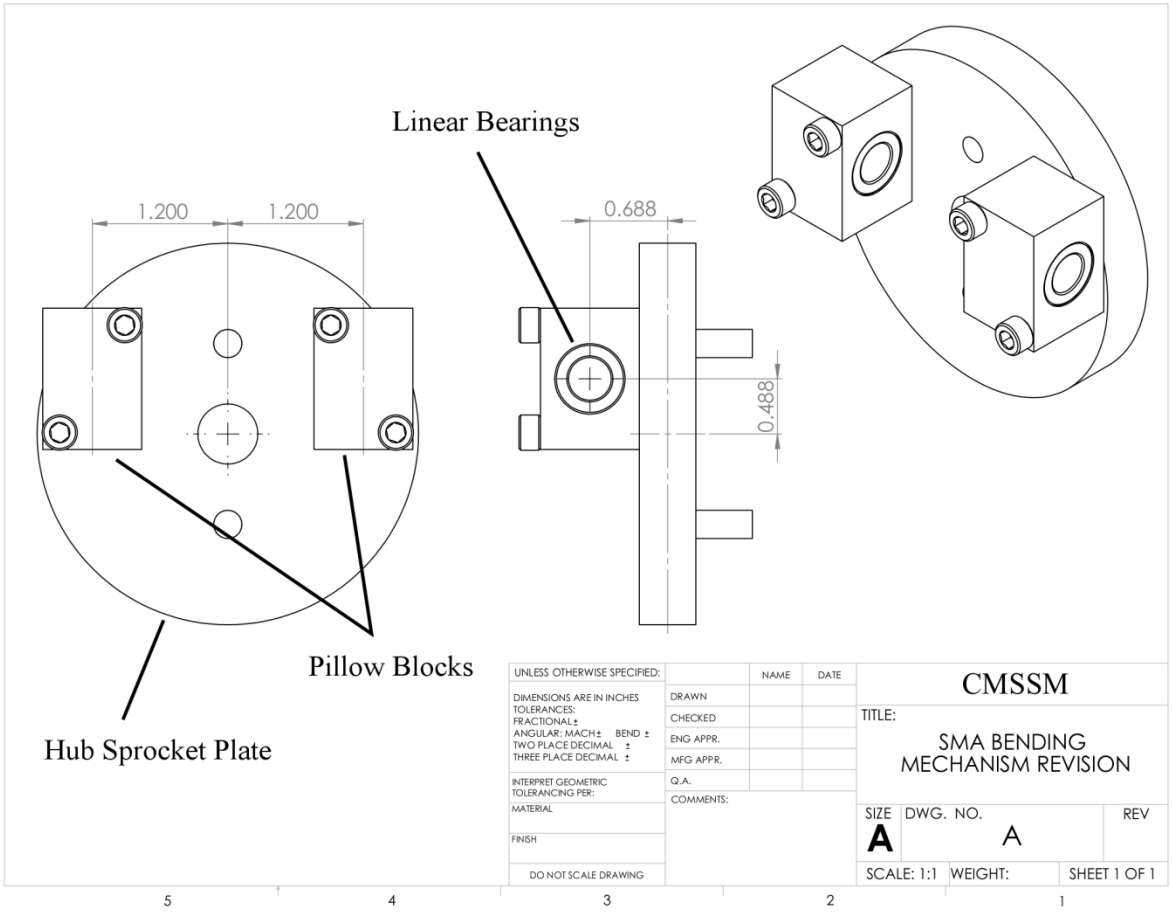

Fig. B4 Drawing of the hub sprocket assembly with mounted pillow blocks housing the linear bearings through which the bending moment is applied to the specimen.

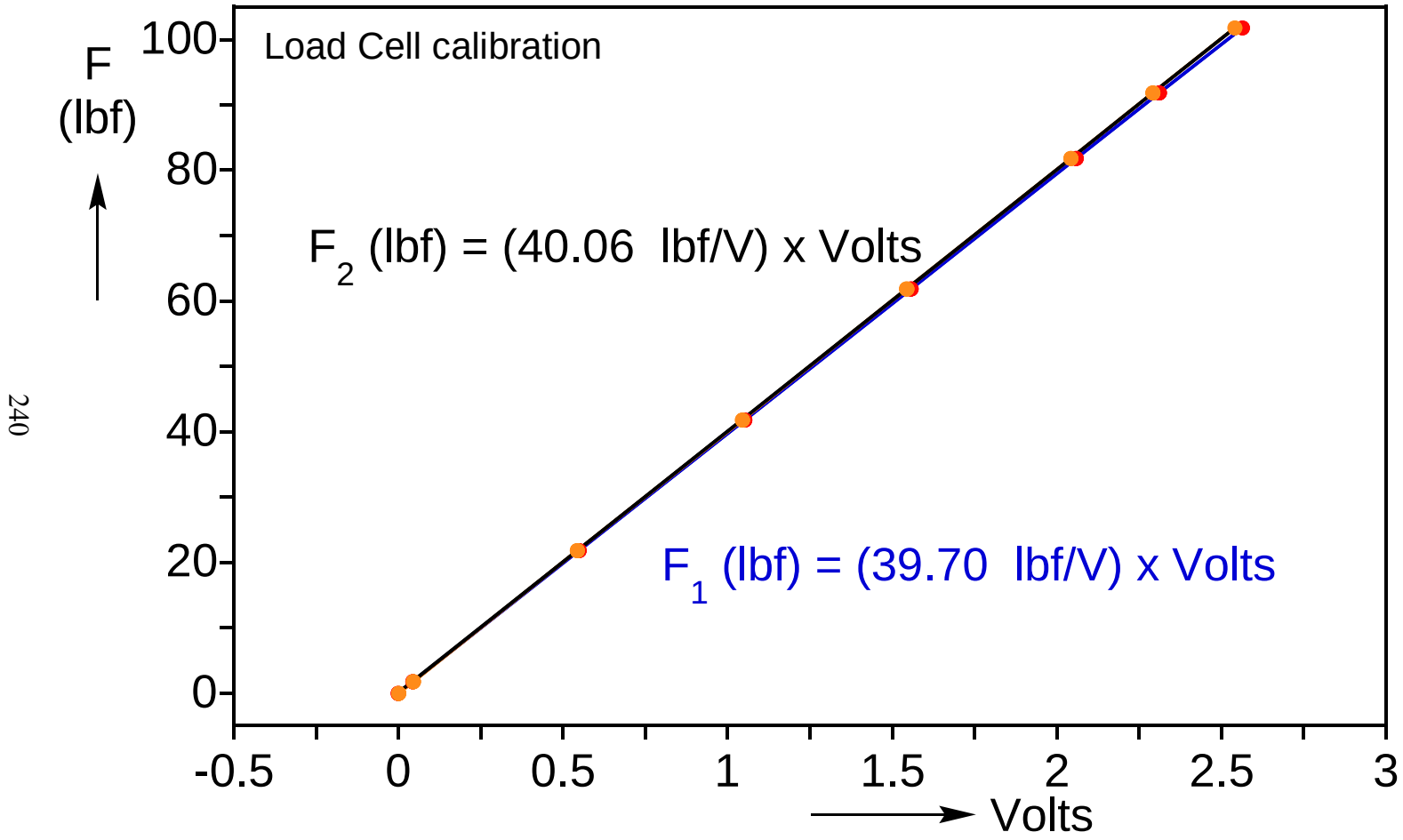

Fig. B5 Load vs. voltage output for calibration of two load cells used in miniature bending device.

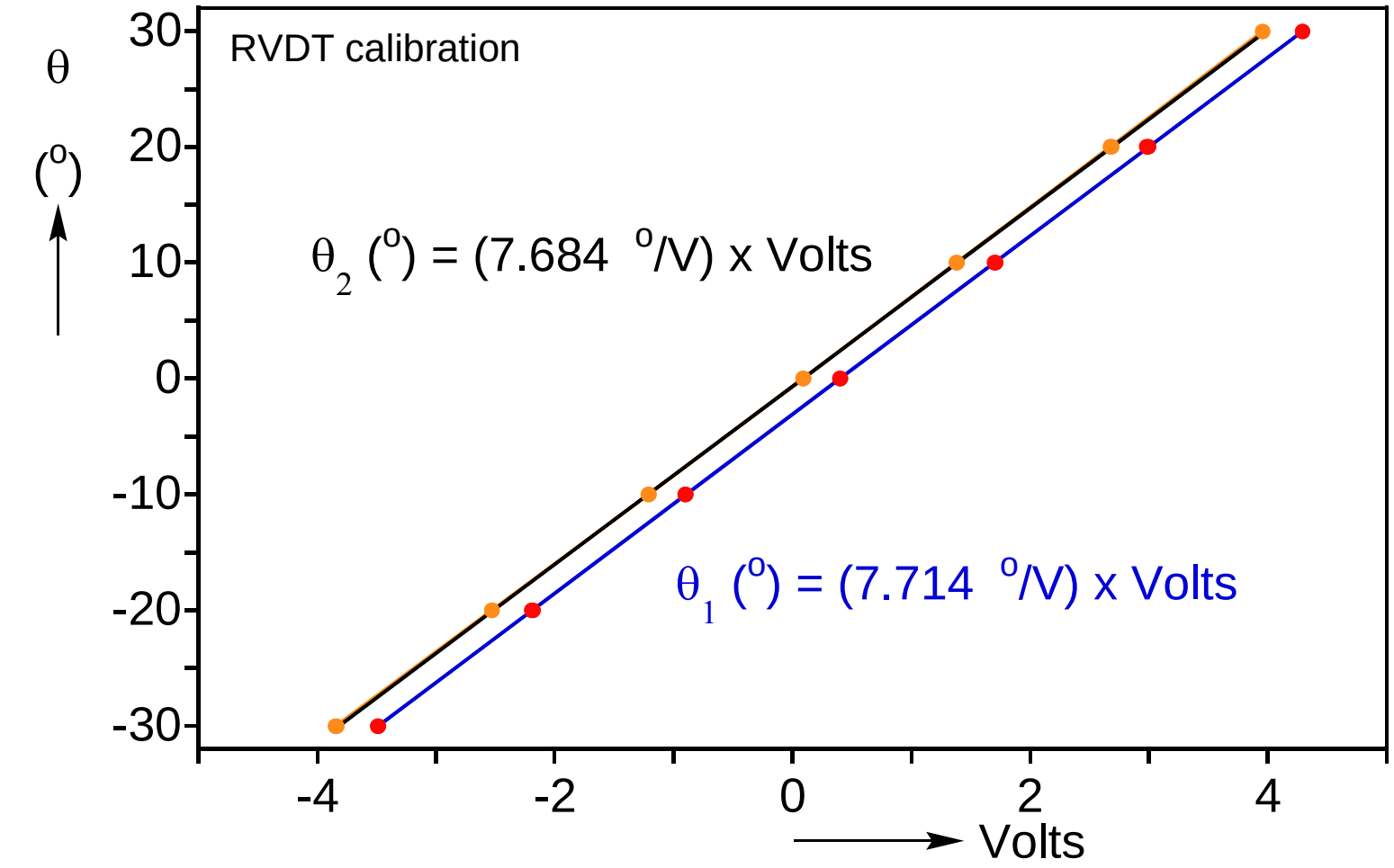

Fig. B6 Rotation vs. voltage output for calibration of two RVDT's used in miniature bending device.

Appendix C: MOMENT CORRECTION

The measured moment-rotation responses were corrected for friction and other inaccuracies of our set up as follows. A series of calibration bending experiments were conducted on steel and aluminum tubes and rods involving loading the specimens to various levels and unloading. The expected moment-curvature responses were determined by numerical integration of measured uniaxial stress-strain results on specimens from the same stock as those used for the bending calibration. The flexibility of extension rods and small errors introduced by the way the specimen is inserted into the ends of the rods are corrected for by requiring that:

$$\kappa = \frac{\bar{\theta}}{L} = \frac{EI_{meas.}}{EI_{calc.}}\left(\frac{\theta_1 + \theta_2}{2L}\right) \tag{C.1}$$

In addition, friction effects introduced to the measured moment by the linear bearings were corrected by generating a moment correction function ($\Delta M_{correc.}$) from the calibration experiments as follows:

$$\Delta M_{correc.} = A\kappa^m M^n\Big|_{meas.} \tag{C.2}$$

where where A, m, and n are constants. See Fig. C1 for the comparison between the raw experimental data and the correction using equations C.1 anc C.2.

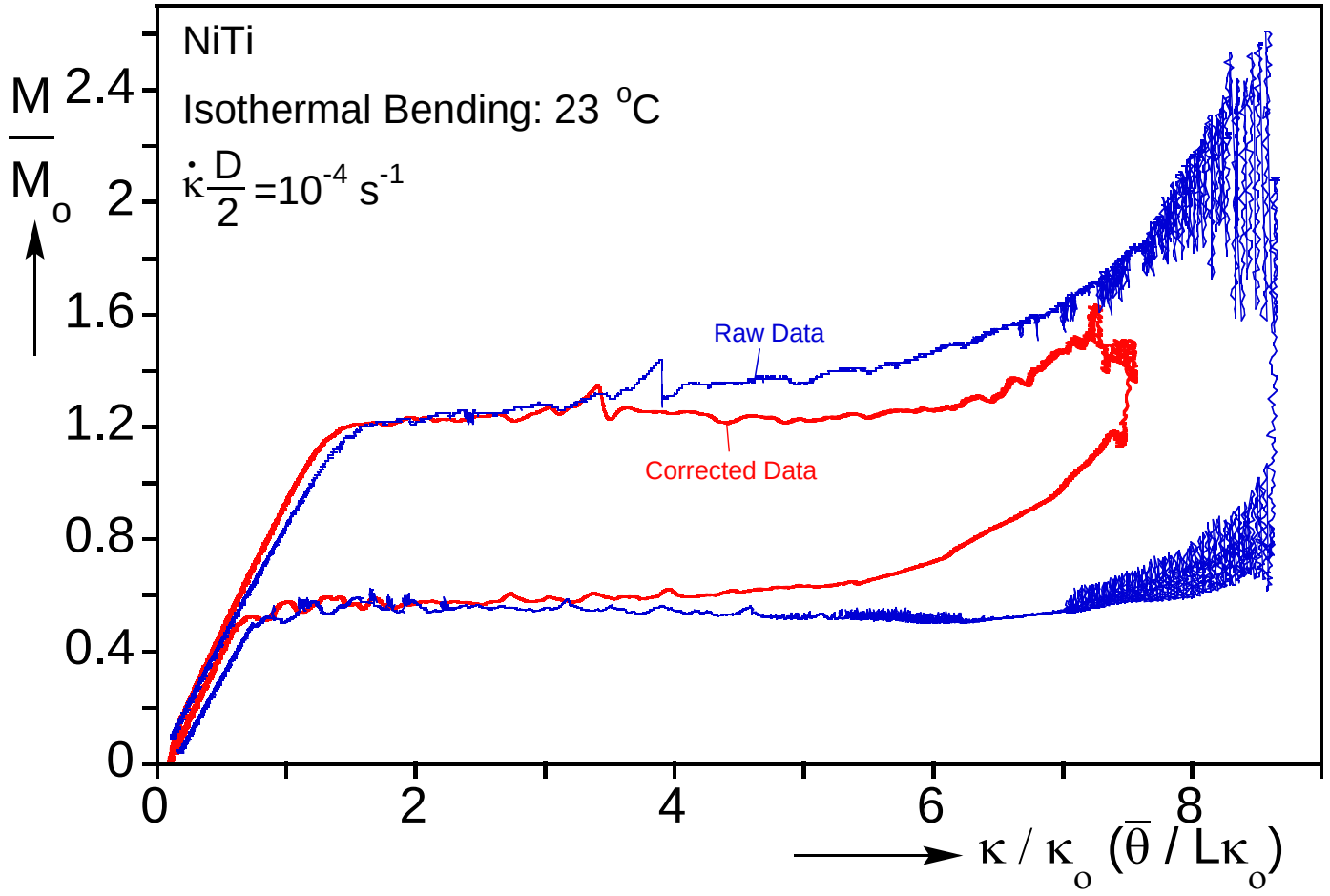

Fig. C1 Comparison of raw experimental data with curvature and moment corrections.

Appendix D: BIAXIAL TEST FACILITY STIFFNESS

The biaxial loading experiments reported in this work were performed by prescribing the fluid volume flux pumped into the system (volume-controlled pressurization) and the testing machine operating under load control. A feedback control loop was used to ensure the axial load followed a prescribed constant relationship to the induced internal pressure. The system consists of the specimen, the initial volume of water in the system, the pump, and accessories like hydraulic tubes, valves, transducers, etc. Although the setup was consciously designed as a "stiff" system, the small changes of volume involved in the experiments meant that the volumetric stiffness of the system influenced the strain rate induced to the specimen. The changes in volume of the main components for a pressure change of ΔP are as follows:

1. *Specimen:* $$\Delta V_s = \frac{\pi D_i^2 L}{4}\left[(1+\Delta\varepsilon_\theta)^2(1+\Delta\varepsilon_x)-1\right], \tag{D1a}$$

where $(\Delta\varepsilon_x, \Delta\varepsilon_\theta)$ are the measured changes in the strains for a pressure increase of ΔP.

2. *Water:* $$\Delta V_w = V_o \frac{\Delta P}{\kappa_w}, \tag{D1b}$$

where V_o is the volume of water in the system and κ_w is the bulk modulus of water at 23 °C (see Table D1).

3. *Pump:* $$\Delta V_p = \frac{\Delta P}{k_p}, \tag{D1c}$$

where k_p is the volumetric stiffness of the pump measured in a series of pressure-controlled experiments performed on the sealed pump up to 700 bar—excludes the contribution of the water compressibility. The main contributor to k_p is the expansion of the active part of the syringe cylinder and is inversely proportional to the initial volume of fluid in the pump. Thus the net volumetric stiffness of the system is given by:

$$\Delta V = \Delta V_s(\Delta P) + V_o \frac{\Delta P}{\kappa_w} + \frac{\Delta P}{k_p(V_o)}. \tag{D2}$$

Figure D1 shows the initial pressure-change in volume response measured in the pure hoop stress experiment (α = 0). Included are the calculated contributions of the specimen, pump and water. The specimen change in volume is very small but the other two contributions are significant. Included in the figure is the system $\Delta P - \Delta V$ response calculated using (D.2) and the parameters listed in Table D1. The calculated system response is seen to be very close to the measured response.

V_o ml	$\frac{\pi D_i^2 L}{4}$ ml	κ_w MPa/ml	k_p MPa/ml
28.2	1.67	89.1	101

Table D1 Pressurization system parameters

In this experiment water was pumped into the system at the rate of 0.02 ml/min. The measured strain rate $\dot{\varepsilon}_\theta$ was 4×10^{-6} s^{-1}. This value is about an order of magnitude smaller than it would have been in a perfectly rigid pressurization system in which the flux of pressurizing fluid goes exclusively to deform the specimen.

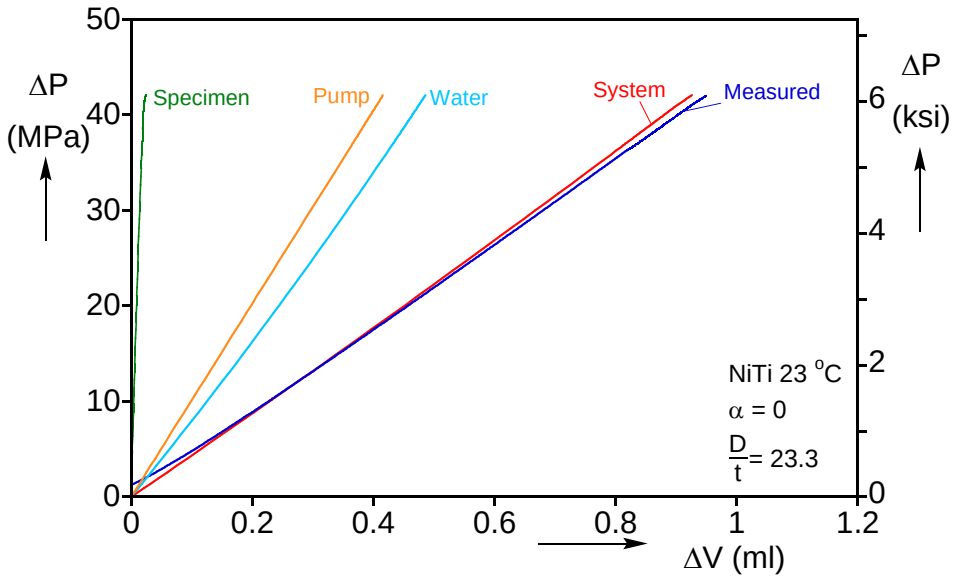

Fig. D1 Pressure change vs. volume change during loading of biaxial experiment on NiTi tube indicating the contribution of the system compliance to the measured volume change.

Appendix E: JOURNAL PUBLICATIONS

Bechle, N.J., Kyriakides, S. (2014). Localization in NiTi tubes under bending. *Int'l J. Solids Struct*. **51**, 967-980.

Jiang, D., Bechle, N.J., Landis, C.M., Kyriakides, S. (2016). Buckling and recovery of NiTi tubes under axial compression. *Int'l J. Solids & Struct.* **80**, 52-63.

Bechle, N.J., Kyriakides, S. (2016). Evolution of localization in pseudoelastic NiTi tubes under biaxial stress states. *Int'l J. Plasticty*. (in press).

Bechle, N.J., Kyriakides, S. (2016). Evolution of phase transformation fronts and associated thermal effects in a NiTi tube under a biaxial stress state. *Extreme Mechanics Letters*. (in press).

References

Abeyaratne, R., Knowles, J.K. (1993). A Continuum Model of a Thermoelastic Solid Capable of Undergoing Phase Transitions. *J. Mech. and Phys. Solids* **41**, no. 3, 541–571.

Abeyaratne, R., Knowles, J.K. (2006). Evolution of phase transformations: A continuum theory. Cambridge University Press, New York.

Aguirre, F., Kyriakides, S., Yun, H.D. (2004). Bending of steel tubes with Lüders bands. *Int. J. Plast.* **20**, 1199-1225.

Arghavani, J., Auricchio, F., Naghdabadi, R., Reali, A. and Sohrabpour, S. (2010). A 3-D phenomenological constitutive model for shape memory alloys under multiaxial loadings. *Int'l J. Plasticity* **26**, 976-991.

Asgarian, B., Moradi, S. (2011). Seismic response of steel braced frames with shape memory alloy braces. *J. Constructional Steel Research*. **67**, 65-74.

Auricchio, F. and Petrini, L. (2004). A three-dimensional model describing stress-temperature induced solid phase transformations: solution algorithm and boundary value problems. *Int'l J. Num. Meth. Eng.* **61**, 807-836.

Auricchio, F., Bonetti, E., Scalet, G., and Ubertini, F. (2014). Theoretical and Numerical Modeling of Shape Memory Alloys Accounting for Multiple Phase Transformations and Martensite Reorientation. *Int'l J. Plasticity* **59**, 30–54.

Bardi, F.C. and Kyriakides, S. (2006). Plastic buckling of circular tubes under axial compression. Part I Experiments. *Int'l J. Mechanical Sciences* **48**, 830-841.

Bardi, F.C., Kyriakides, S. and Yun, H.D. (2006). Plastic buckling of circular tubes under axial compression. Part II Analysis. *Int'l J. Mechanical Sciences* **48**, 842-854.

Bechle, N.J., Kyriakides, S. (2014). Localization in NiTi tubes under bending. *Int'l J. Solids Struct.* **51**, 967-980.

Berg, B. T. (1995a). Bending of superelastic wires, Part I: Experimental aspects. *J. Appl. Mech.* **62**, 459-465.

Berg, B. T. (1995b). Bending of superelastic wires, Part II: Application to three-point bending. *J. Appl. Mech.* **62**, 466-470.

Bijlaard, P.P. (1940). Theory of local plastic deformations. *Publication of the International Association of Bridge and Structural Engineers* **6**, 27–44.

Bouvet, C., Calloch, S., Lexcellent, C. (2002). Mechanical behavior of a Cu-Al-Be shape memory alloy under multiaxial proportional and nonproportional loadings. *J. Eng. Mater. Technol.* **124**, 112–124.

Bouvet, C., Calloch, S., Taillard, K., Lexcellent, C. (2004a). Experimental determination of initial surface of phase transformation of SMA. *J. Physique IV - Proc.* **115**, 29-36.

Bouvet, C., Calloch, S. and Lexcellent, C. (2004b). A Phenomenological Model for Pseudoelasticity of Shape Memory Alloys under Multiaxial Proportional and Nonproportional Loadings. *European J. Mech. A/Solids* **23**, no. 1, 37–61.

Boyd, J.G., and Lagoudas, D.C. (1996). A Thermodynamical Constitutive Model for Shape Memory Materials. Part I. The Monolithic Shape Memory Alloy. *Int'l J. of Plasticity* **12**, no. 6, 805–842.

Brinson, L.C. (1993). One-Dimensional Constitutive Behavior of Shape Memory Alloys: Thermomechanical Derivation with Non-Constant Material Functions and Redefined Martensite Internal Variable. *J. Intelligent Mat. Sys. and Struct.* **4**, no. 2, 229–242.

Butler, J.F. (1962). Lüders front propagation in low-carbon steels. *J. Mech. Physics of Solid* **10**, 313-334.

Cazacu, O., Plunkett, B., Barlat, F. (2006). Orthotropic yield criterion for hexagonal closed packed metals. *Int. J. Plast.* **22**, 1171-1194.

Chau, E.T.F., Friend, C.M., Allen, D.M., Hora, J., Webster, J.R (2006). A technical and economic appraisal of shape memory alloys for aerospace applications. *Materials Science and Eng: A*, **438**, 589-592

Corona, E. and Kyriakides, S. (1988). On the collapse of inelastic tubes under combined bending and pressure. *Int'l J. Solids Struct*. **24**, 505-535.

Corona, E., Shaw, J.A. and Iadicola, M.A. (2002). Buckling of steel bars with Lüders bands. *Int. J. Solids Struct.* **39**, 3313-3336.

Daly, S., Ravichandran, G., Bhattacharya, K. (2007). Stress-induced martensitic phase transformation in thin sheets of Nitinol. *Acta Mat.* **55**, 3593–3600.

Duerig, T, Pelton, A., Stöckel, D. (1999). An Overview of Nitinol Medical Applications. *Materials Science and Engineering: A* 273–275, 149–160.

Favier, D., Louche, H., Schlosser, P., Orgéas, L., Vacher, P., Debove, L. (2007). Homogeneous and heterogeneous mechanisms in an austenitic polycrystalline Ti-50.8 at.% Ni thin tube under tension. Investigation via temperature and strain fields measurements. *Acta Mat.* **55**, 5310-5322.

Feng, P., Sun, Q.P. (2006). Experimental investigation on macroscopic domain formation and evolution in polycrystalline NiTi microtubing under mechanical force. *J. Mech. Physics Solid* **54**, 1568-1603.

Gall, K., Sehitoglu, H., Chumlyakov, Y.I. & Kireeva, I.V. (1999). Tension-compression asymmetry of the stress-strain response in aged single crystals and polycrystalline NiTi. *Acta Mater.* **47**, 1203-1217.

Gall, K., Sehitoglu, H. (1999). The role of texture in tension-compression asymmetry in polycrystalline NiTi. *Int'l J. Plasticity* **15**, 69-92.

Govindjee, S. and Kasper, E.P. (1999). Computational Aspects of One-Dimensional Shape Memory Alloy Modeling with Phase Diagrams. *Computer Methods in Applied Mechanics and Engineering* **171**, no. 3–4, 309–326.

Govindjee, S., Hall, G.J. (2000). A computational model for shape memory alloys. *Int'l. J. Solids Struct.* **37**, 735-760.

Govindjee, S., Miehe, C. (2001). A multi-variant martensitic phase transformation model: formulation and numerical implementation. *Comp. Meth. Appl. Mech. Eng.* **191**, 215-238.

Grabe, C., Bruhns, O.T. (2009). Path dependence and multiaxial behavior of a polycrystalline NiTi alloy within the pseudoelastic and pseudoplastic temperature regimes. *Int'l J. Plasticity* **25**, 513–545.

Grolleau, V., Louche, H., Delobelle, V., Penin, A., Rio, G., Liu, Y. and Favier, D. (2011). Assessment of tension–compression asymmetry of NiTi using circular bulge testing of thin plates. *Scripta Mat.* **65**, 347–350.

Hallai, J.F., Kyriakides, S. (2011a). On the effect of Lüders bands on the bending of steel tubes: Part I experiments. *Int'l J. Solids & Structures* **48**, 3275-3284.

Hallai, J.F., Kyriakides, S. (2011b). On the effect of Lüders bands on the bending of steel tubes: Part II analysis. *Int'l J. Solids & Structures* **48**, 3285-3294.

Hallai, J.F., Kyriakides, S. (2013). Underlying material response for Lüders-like instabilities. *Int'l J. Plasticity* **47**, 1-12.

Hartl, D.J. and Lagoudas, D.C. (2009). Constitutive modeling and structural analysis considering simultaneous phase transformation and plastic yield in shape memory alloys. *Smart Mater. Struct.* **18**, 104017.

Hartl, D.J., Lagoudas, D.C., Calkins, F.T., and Mabe, J.H. (2010). Use of a Ni60Ti shape memory alloy for active jet engine chevron application: I. Thermomechanical characterization. *Smart Materials and Struct* **19**, 015020.

Helm, D., Haupt, P., (2001). Thermomechanical behavior of shape memory alloys. *Proc. SPIE Int'l Symposium on Smart Struct. and Materials* **8**, 302-313.

Hill, R. (1952). On discontinuous plastic states, with special reference to localized necking in thin sheets. *J. Mech. Phys. Solids* **1**, 19–30.

Iadicola, M.A., Shaw, J.A. (2002). An Experimental setup for measuring unstable thermo-mechanical behavior of shape memory alloy wire. *J. Intel. Mat. Syst. Struct.* **13**, 157–166.

Iadicola, M.A., Shaw, J.A. (2004). Rate and thermal sensitivities of unstable transformation behavior in a shape memory alloy. *Int'l J. Plasticity* **20**, 577–605.

Jackson, C. M., Wagner, H. J., and Wasilewski, R. J. (1972). 55-Nitinol--the Alloy with a Memory: Its Physical Metallurgy, Properties, and Applications. *NASA Report*. NASA-SP-5110.

Jacobus, K., Sehitoglu, H. and Balzer, M. (1996). Effect of stress state on the stress-induced martensitic transformation of polycrystalline Ni-Ti Alloy. *Metallu. Mater. Trans. A* **27,** 3066-3073.

Jiang, D., Bechle, N.J., Landis, C.M., Kyriakides, S. (2016). Buckling and recovery of NiTi tubes under axial compression. *Int'l J. Solids & Struct.* **80**, 52-63.

Kauffman, G.B., Mayo, I. (1997). The Story of Nitinol: The Serendipitous Discovery of the Memory Metal and Its Applications. *The Chemical Educator* **2**, 1–21.

Kyriakides, S., Miller, J.E. (2000). On the propagation of Lüders bands in steel strips. *ASME J. Appl. Mech.* **67**, 645-654.

Kyriakides, S., Ok, A. and Corona, E. (2008). Localization and propagation of curvature under pure bending in steel tubes with Lüders bands. *Int'l J. Solids & Structures* **45**, 3074-3087.

Lagoudas, D., Hartl, D., Chemisky, Y., Machado, L., and Popov, P. (2012). Constitutive Model for the Numerical Analysis of Phase Transformation in Polycrystalline Shape Memory Alloys. *Int'l J. Plasticity* **32–33**: 155–183.

Leclercq, S., and Lexcellent, C. (1996). A General Macroscopic Description of the Thermomechanical Behavior of Shape Memory Alloys. *J. Mech. Physics Solids* **44**, no. 6, 953–980.

Lexcellent, C., Vivet, A., Bouvet, C., Calloch, S., Blanc, P. (2002). Experimental and numerical determinations of the initial surface of phase transformation under biaxial loading in some polycrystalline shape-memory alloys. *J. Mech. Physics Solids* **50**, 2717–2735.

Lexcellent, C., Blanc, P. (2004). Phase transformation yield surface determination for some shape memory alloys. *Acta Mat.* **52**, 2317–2324.

Li, Z.Q., Sun Q.P. (2002). The initiation and growth of macroscopic martensite band in nano-grained NiTi microtube under tension. *Int'l J. Plasticity* **18**, 1481-1498.

Liang, C. and Rogers, C.A. (1990). One-Dimensional Thermomechanical Constitutive Relations for Shape Memory Materials. *J. Intelligent Material Systems and Structures* **1**, no. 2 , 207–234.

Liang, C. and Rogers, C.A. (1992). A Multi-Dimensional Constitutive Model for Shape Memory Alloys. *J. Eng. Math.* **26**, no. 3, 429–443.

Lim, T.J., McDowell, D.L. (1999). Mechanical behavior of a Ni-Ti shape memory alloy under axial-torsional proportional and nonproportional loading. *J. Eng. Mater. Tech.* **121**, 9–18.

Liu, Y., Liu, Y., and Van Humbeeck, J. (1998) Lüders-like Deformation Associated with Martensite Reorientation in NiTi. *Scripta Materialia* **39**, no. 8, 1047–1055.

Liu, Y., Hoover, I., Xiang, H., Bataillard, L., and Miyazaki, S. (1999). Strain dependence of pseudoelastic hysteresis of NiTi. *Metal. Mat. Trans.* **30A**, 1275-1282.

Mao, S.C., Han, X.D., Tian, Y.B., Luo, J.F., Zhang, Z., Ji, Y., Wu, M.H., (2008). In situ EBSD investigations of the asymmetric stress-induced martensitic transformation in TiNi shape memory alloys under bending. *Mat. Scie. Eng. A* **498**, 278-282.

Mao, S., Luo, J., Zhang, Z., Wu, M., Liu, Y., Han, X. (2010). EBSD studies of the stress-induced B2-B19' martensitic transformation in NiTi tubes under uniaxial tension and compression. *Acta Mat.* **58**, 3357-3366.

Matsumoto, O., Miyazaki, S., Otsuka, K., and Tamura, H. (1987). Crystallography of Martensitic Transformation in Ti-Ni Single Crystals. *Acta Metallurgica* **35**, 2137–2144.

McNaney, J.M., Imbeni, V., Jung, Y., Papadopoulos, P., Ritchie, R.O. (2003). An experimental study of the superelastic effect in a shape-memory Nitinol alloy under biaxial loading. *Mech. Materials* **35**, 969–986.

Michailidis, P.A., Triantafyllidis, N., Shaw, J.A., Grummon, D.S. (2009). Superelasticity and stability of a shape memory alloy hexagonal honeycomb under in-plane compression. *Int'l J. Solids & Structures* **46**, 2724-2738.

Miyazaki, S., Otsuka, K., and Suzuki, Y. (1981a). Transformation Pseudoelasticity and Deformation Behavior in a Ti-50.6 at% Ni Alloy. *Scripta Metallurgica* **15**, no. 3, 287–292.

Miyazaki, S., Imai, T., Otsuka, K., and Suzuki, Y. (1981b). Lüders-like Deformation Observed in the Transformation Pseudoelasticity of a Ti-Ni Alloy. *Scripta Metallurgica* **15**, no. 8, 853–856.

Miyazaki, S., Kimura, S., Otsuka, K. and Suzuki. Y. (1984). The Habit Plane and Transformation Strains Associated with the Martensitic Transformation in Ti-Ni Single Crystals. *Scripta Metallurgica* **18**, 883–888.

Mohd Jani, J., Leary, M., Subic, A., and Gibson, M.A. (2014). A Review of Shape Memory Alloy Research, Applications and Opportunities. *Materials & Design* **56**, 1078–1113.

Nacker, J. C. (2009). The evolution of phase transformations in pseudoelastic NiTi tubes under pure bending. MS Thesis, Engineering Mechanics, Univ. Texas at Austin.

Nemat-Nasser, S., Choi, J.Y, Isaacs, J.B., Lischer, D.W. (2006). Quasi-static and dynamic buckling of thin cylindrical shape-memory shells. *ASME J. Applied Mech.* **73**, 825-833.

Orgéas, L. and Favier, D. (1998). Stress-induced martensitic transfomation of a NiTi alloy in isothermal shear, tension and compression. *Acta Mat.* **46**, 5579-5591.

Ozbulut, O.E., Hurlebaus, S., and Desroches, R. (2011). Seismic Response Control Using Shape Memory Alloys: A Review. *J. Intelligent Material Systems and Structures* **22**, no. 14, 1531–1549.

Patoor, E., El Armani, M., Eberhardt, A., Berveiller, M. (1995). Determination of the origin for the dissymmetry observed between tensile and compression tests on shape memory alloys. *J. Physique IV* **05**, C2–495–C2–500.

Plunkett, B., Cazacu, O., Barlat, F. (2008). Orthotropic yield criteria for description of anisotropy in tension and compression in sheet metalshexagonal closed packed metals. *Int. J. Plast.* **24**, 847-866.

Poncet, P.P. (1994). Applications of Superelastic Nitinol Tubing. *Proc. Int'l Conf. on Shape Memory and Superelastic Tech.*, 1-7.

Popov, P., Lagoudas, D.C. (2007). A 3-D constitutive model for shape memory alloys incorporating pseudoelasticity and detwinning of self-accommodated martensite. *Int'l J. Plasticity* **23**, 1679-1720.

Qidwai, M.A., and Lagoudas, D.C. (2000). On Thermomechanics and Transformation Surfaces of Polycrystalline NiTi Shape Memory Alloy Material. *Int'l J. Plasticity* **16**, no. 10–11 1309–1343.

Rahman, M.A, Qiu, J., Tani, J. (2001). Buckling and postbuckling characteristics of the superelastic SMA columns. *Int'l J. Solids & Structures* **38**, 9253-9265.

Raniecki, B. and Lexcellent, C. (1998). Thermodynamics of Isotropic Pseudoelasticity in Shape Memory Alloys. *European J. Mech. A/Solids* **17**, no. 2, 185–205.

Reedlunn, B., Daly, Shaw, J.A. (2013). S.H.Superelastic shape memory alloy cables: Part I – Isothermal tension experiments. *Int'l J. Solids & Structures* **50**, 3009-3026.

Reedlunn, B., Churchill, C.B., Nelson, E.E., Shaw, J.A., Daly, S.H. (2014). Tension, compression and bending of superelastic shape memory tubes. *J. Mech. Physics Solids* **63**, 506-537.

Rogueda, C., Lexcellent, C., Bocher, L. (1996). Experimental study of pseudoelastic behaviour of a Cu Zn AI polycrystalline shape memory alloy under tension-torsion proportional and non-proportional loading tests. *Archives Mech.* **48**, 1025 – 1047.

Sehitoglu, H., Karaman, I., Anderson, R., Zhang, X., Gall, K., Maier, H.J. and Chumlyakov, Y. (2000). Compressive response of NiTi single crystals. *Acta Mat.* **48**, 3311-3326.

Sharabash, A.M. and Andrawes, B.O. (2009). Application of Shape Memory Alloy Dampers in the Seismic Control of Cable-Stayed Bridges. *Engineering Structures* **31**, no. 2, 607–616.

Shaw, J.A. and Kyriakides, S. (1995). Thermomechanical aspects of NiTi. *J. Mechanics Physics Solids* **43**, 1243-1281.

Shaw, J.A. and Kyriakides, S. (1997). On the nucleation and propagation of phase transformation fronts in a NiTi alloy. *Acta Mat.* **45**, 683-700.

Shaw, J.A. and Kyriakides, S. (1998). Initiation and propagation of localized deformation in elasto-plastic strips under uniaxial tension. *Int'l J. Plast*. **13**, 837–871.

Shaw, J.A. (2002). A Thermomechanical Model for a 1-D Shape Memory Alloy Wire with Propagating Instabilities. *Int'l J. Solids Struct.* **39**, no. 5, 1275–1305.

Shaw, J.A. Churchill, C.B., and Iadicola, M.A. (2008). Tips and Tricks for Characterizing Shape Memory Alloy Wire: Part 1Differential Scanning Calorimetry & Basic Phenomena. *Experimental Techniques*, 55-62.

Shaw, J.A., Reedlunn, B., Daly, S. (2013). Instabilities during tension-torsion of superelastic NiTi tubes. Oral presentation at SES 50th annual Technical Meeting and AMD-ASME Summer Meeting. Brown University, Providence, RI, July 28-Aug. 1, 2013.

Sun, Q.P., Li, Z.Q. (2002). Phase transformation in superelastic NiTi polycrystalline micro-tubes under tension and torsion—from localization to homogeneous deformation. *Int'l J. Solids & Structures* **39**, 3797-3809.

Tang, Z., Li, D. (2012). Quasi-static axial buckling behavior of NiTi thin-walled cylindrical shells. *Thin Walled Structures* **51**, 130-138.

Tas, H., Delaey, L., and Deruyttere, A. (1972). Stress-Induced Transformations and the Shape-Memory Effect. *Journal of the Less Common Metals* **28**, 141–151.

Thamburaja, P., Anand, L. (2002). Superelastic behavior in tension–torsion of an initially-textured Ti–Ni shape-memory alloy. *Int'l J. Plasticity* **18**, 1607–1617.

Vacher, P. and Lexellent, C. (1992). Study of the pseudoelastic behavior of polycristallin shape memory alloys by resistivity measurements and acoustic emission. *Mech. Behav. Mat'ls*. **VI 3**, 231-236.

Van Humbeeck, J. (1999). Non-medical applications of shape memory alloys. *Mat'l Sci. & Eng*. **A273-275**, 134-148.

Wasilewski, R.J. (1971). The effects of applied stress on the martensitic transformation in NiTi. *Metallu. Trans.* **2**, 2973-2981.

Wu, M.H., Schetky, L.M. (2000). Industrial applications for shape memory alloys. *Proc. Int'l Conf. on Shape Memory and Superelastic Tech.*, 171-182.

Yoneyama, T., and Miyazaki, S. (2008). Shape Memory Alloys for Biomedical Applications. Woodhead Publishing Limited, Cambridge, England.

Vita

Nathan Joseph Bechle entered the University of Wisconsin—Madison in 2003 and graduated with a B.S. (2007) in Civil & Environmental Engineering. He subsequently entered the Graduate School at the University of Wisconsin—Madison and graduated with a M.S. (2009) in Civil & Environmental Engineering with a thesis entitled "The Characterization of Wood Plastic Composites Over Multiple Time Domains." He then entered the Graduate School at The University of Texas at Austin to pursue a Ph. D. in Engineering Mechanics. In the process, he made several presentations at national and international conferences, and co-authored the journal publications listed in Appendix E.

Permanent email: nathan.bechle@gmail.com

This dissertation was typed by the author.